

# Table of content

Abstract .....	i
Acknowledgments.....	iii
Publications.....	v
Table of content.....	vi
List of Figures .....	xii
List of Tables .....	xvi
Abbreviations .....	xix
Co-Authorship forms .....	xx
<b>CHAPTER 1 Introduction .....</b>	<b>1</b>
1.1. Background.....	2
1.1.1 Climate change .....	2
1.1.2 Hydrological response to climate change .....	2
1.1.2.1. Frequency and magnitude of extreme precipitation .....	3
1.1.2.2. Evaporation paradox .....	4
1.1.2.3. Catchment water balance .....	5
1.2. Motivation and novelty of the research .....	6
1.2.1 Motivation of the research .....	6
1.2.2 Major Contributions of the thesis .....	7
1.3. Research Objectives .....	7
1.4. Thesis Outline.....	9
<b>CHAPTER 2 Literature Review .....</b>	<b>12</b>
2.1. Climate change .....	13
2.1.1. Historical observed climate change .....	14
2.1.2. IPCC SRES scenarios .....	15
2.1.3. Projected climate change .....	18
2.2. New Zealand and Waikato climate change and its impacts .....	21
2.2.1. New Zealand climate change and impacts .....	21
2.2.2. Waikato climate change and impacts .....	22
2.3. Climate change impacts analysis .....	23
2.3.1. Global Circulation Models (GCMs) .....	23
2.3.2. Regional Climate Models (RCMs) .....	26

2.3.3.	Statistical downscaling .....	28
2.4.	Climate change impacts on hydrology and water resources.....	30
2.4.1	Extreme precipitation and induced-flooding .....	30
2.4.1.1.	Extreme precipitation.....	30
2.4.1.2.	Extreme precipitation induced floods .....	31
2.4.2	Evapotranspiration.....	32
2.4.3	Catchment water balance.....	34
2.5.	Regional hydrologic and water resources impact assessment of climate change .....	36
2.5.1.	Frequency and regionalization of daily precipitation .....	36
2.5.2.	FAO-56 method coupled with GCM/RCM data .....	42
2.5.3.	Water balance model .....	45
2.5.3.1.	Future projections of catchment water balance .....	47
2.6.	Summary.....	50
CHAPTER 3 Study sites and data .....		51
3.1.	Study region.....	52
3.1.1.	North Island of New Zealand .....	52
3.1.2.	Waikato catchment .....	58
3.1.3.	Representatives of forest and grass sub-catchments.....	62
3.2.	Data collection and processing .....	72
3.2.1.	Observed meteo-hydrological data.....	73
3.2.2.	Global and Regional Climate Model (GCM/RCM) data.....	75
3.2.3.	Soil type and landuse maps .....	78
3.3.	Summary.....	78
CHAPTER 4 Extraction of extreme precipitation .....		79
4.1.	Introduction .....	80
4.1.1.	Overview of Partial Duration Series by Peak-Over-Threshold (POT).....	80
4.1.1.1	Characteristics of PDS .....	80
4.1.1.2	Significance of threshold value.....	81
4.1.2	GP-Poisson distribution and parameter estimators .....	82
4.1.2.1.	The Poisson distribution of peak occurrences .....	82
4.1.2.2.	The GP distribution of peak magnitudes .....	82
4.1.2.3.	Parameter estimators.....	83
4.2.	Data .....	84

4.3.	Methods .....	85
4.3.1.	Randomness Test and Trend Test.....	86
4.3.1.1.	Randomness Detection using Autocorrelation Coefficients.....	86
4.3.1.2.	Trend Detection using Mann-Kendall Test .....	87
4.3.2.	Validation of the Poisson-GP distribution.....	88
4.3.2.1	Verification of the Poisson distribution using Dispersion measure.....	88
4.3.2.2	Suitability of GP distribution based on L-MOM ratios and sensitivity analysis.....	90
4.4.	Results and discussions .....	91
4.4.1.	Random test and trend test.....	91
4.4.2.	Verification of the Poisson distribution for the changes in peak occurrences .....	93
4.4.2.1	Fisher test.....	93
4.4.2.2	Variance-to-Mean ratio test .....	93
4.4.3.	Selection of a frequency distribution.....	97
4.4.3.1	Stability of distribution parameters.....	103
4.5.	Summary.....	107
CHAPTER 5 Regional extreme precipitation analysis.....		109
5.1.	Introduction .....	110
5.2.	Methods and techniques .....	110
5.2.1.	Identification of homogeneous regions .....	111
5.2.1.1.	Discordancy Measure ( $D_i$ ) .....	111
5.2.1.2.	Heterogeneity Measure (H) .....	112
5.2.2.	Regional frequency distribution .....	113
5.2.2.1.	Regionalization .....	114
5.2.2.2.	Goodness-of-Fit test using L-MOM ratio diagram and Z-statistic .....	114
5.2.2.3.	Robustness Test .....	116
5.3.	Results and discussions .....	119
5.3.1.	Overview on partial duration series (PDS) and its frequency distribution.....	119
5.3.2.	Identification of homogenous region.....	121
5.3.3.	Identification of a regional frequency distribution .....	125
5.3.3.1.	Goodness-of-fit test.....	125
5.3.3.2.	Regional quantile estimation .....	127
5.3.3.3.	Robustness test.....	130

5.3.4.	Comparison of PDS4/GP and PDS5/GP results .....	134
5.4.	Summary.....	136
CHAPTER 6 Statistical downscaling of daily precipitation.....		137
6.1	Introduction.....	138
6.2	Study region and data.....	138
6.3	Methods and Techniques .....	143
6.3.1	Statistical downscaling methods.....	143
6.3.2	Selection of large-scale predictor variables.....	145
6.3.3	Model Calibration and Validation .....	146
6.3.4	Evaluation for model performance .....	147
6.4	Results and Discussions .....	148
6.4.1	Selection of large-scale predictor variables.....	148
6.4.2	Model Calibration and validation .....	151
6.4.2.1	Model Calibration .....	151
6.4.2.2	Model Validation .....	157
6.5	Summary .....	162
CHAPTER 7 Future projections on extreme precipitation.....		164
7.1	Introduction .....	165
7.2	Data sets and methods .....	165
7.2.1.	Data sets.....	166
7.2.1.1	Precipitation station data.....	166
7.2.1.2	Downscaled precipitation data.....	166
7.2.1.3	Gridded precipitation data .....	166
7.2.2.	Methods .....	167
7.2.2.1.	Downscaling and extracting daily precipitation time series .....	167
7.2.2.2.	Evaluation of point and areal precipitation data .....	168
7.2.2.3.	Simulation and projection of future extreme precipitation.....	169
7.3	Results and Discussions.....	170
7.3.1.	Daily precipitation time series generated from GCMs/RCM.....	170
7.3.2.	Extreme precipitation estimation.....	175
7.3.3.	Projection of future extreme precipitation.....	177
7.3.4.	Future projection of extreme precipitation from AMS and PDS.....	178
7.4	Summary.....	179
CHAPTER 8 Future projections on potential evapotranspiration .....		181

8.1.	Introduction .....	182
8.2.	Data sets and methods .....	182
8.2.1.	Data sets.....	183
8.2.2.	Mann-Kendall trend test .....	183
8.2.3.	A combined FAO-RCM approach and EToCal model .....	184
8.2.3.1.	FAO-56 method .....	184
8.2.3.2.	EToCal model.....	185
8.2.3.3.	Evaluation of catchment PET simulation .....	186
8.2.4.	Future projection of PET .....	187
8.3.	Results and Discussions.....	188
8.3.1.	Long-term daily pan evaporation data sets.....	188
8.3.2.	Trends in daily pan evaporation data.....	189
8.3.3.	Potential evapotranspiration estimation and FAO-RCM model validation .....	190
8.3.4.	Future projections of daily potential evapotranspiration of different sub- catchments .....	194
8.4.	Summary.....	198
CHAPTER 9 Assessment of climate change impacts on catchment water balance ...		200
9.1.	Introduction .....	201
9.2.	Data and methods .....	201
9.2.1.	Data.....	201
9.2.2.	Materials and Methods .....	202
9.2.2.1.	Bias-corrected potential evapotranspiration .....	203
9.2.2.2.	Lumped and conceptual model.....	204
9.2.2.3.	Modelling of future runoff production and assessment of catchment water balance .....	208
9.3.	Results and Discussions.....	208
9.3.1.	The MIKE-NAM calibration and validation .....	208
9.3.2.	Projected changes in future water balance .....	214
9.3.3.	Errors in a combined modelling of future streamflow .....	222
9.3.3.1.	Uncertainty embedded in regional climate model .....	222
9.3.3.2.	Uncertainty adds from future scenarios .....	223
9.3.3.3.	Uncertainty caused by observation and usage .....	223
9.3.3.4.	Uncertainty created by hydrological models and other programs .....	223
9.3.3.5.	Uncertainty caused by study assumptions .....	224

9.4.	Summary.....	225
CHAPTER 10 Conclusions and recommendations .....		227
10.1.	Conclusion remarks .....	228
10.1.1.	Future projection of extreme precipitation .....	228
10.1.1.1.	Extreme precipitation definition .....	228
10.1.1.2.	Validity of statistically downscaled daily precipitation for present climate.....	230
10.1.1.3.	Validity of downscaled extreme precipitation for future climate .....	230
10.1.2.	Future projections of potential evapotranspiration .....	231
10.1.3.	Combined effects of changing precipitation and PET on catchment surface water.....	233
10.2.	Contributions to knowledge.....	234
10.3.	Possibilities for further research .....	234
APPENDIX A Long term mean daily precipitation for the 1960-90 period for 36 stations .....		236
APPENDIX B Long term mean daily evaporation for the 1961-90 period for 7 stations .....		255
APPENDIX C.1 Predictor-predictand $R^2$ values for 14 stations for CGCM3.1/T47 model .....		260
APPENDIX C.2 Predictor-predictand $R^2$ values for 5 stations for GCM HadCM3 model .....		262
APPENDIX D Monthly precipitation, evaporation and discharge observed in selected sub-catchments .....		264
APPENDIX E List of publications .....		264
REFERENCES .....		268

# List of Figures

Figure 2.1 Observed changes in global average surface temperature, global average sea level and Northern Hemisphere snow cover for the period 1961-1990 .....	15
Figure 2.2 GHG emissions with six SRES scenarios from 2000 to 2100.....	16
Figure 2.3 Schematic representations of the SRES scenarios.....	17
Figure 2.4 Change in global surface temperature is projected for a single SRES emissions scenario. ....	19
Figure 2.5 Change in global surface temperature is projected for a range of SRES emissions scenarios. ....	19
Figure 2.6 Description of GCM models .....	24
Figure 2.7 A downscaling of GCM to RCM for the Waikato catchment .....	27
Figure 2.8 Concept of spatial downscaling.....	28
Figure 2.9 The World’s surface water .....	34
Figure 2.10 Definition of AMS of precipitation .....	37
Figure 2.11 The concept of PET estimation using FAO-56 method .....	43
Figure 3.1 Maps of North Island region and its Waikato catchment .....	53
Figure 3.2 Long-term mean annual precipitation over New Zealand during the 1961-2001 period .....	55
Figure 3.3 Long-term mean annual temperature over New Zealand during the 1971-2000 period .....	56
Figure 3.4 Long-term mean annual Penman potential evapotranspiration over New Zealand during the 1961-2001 period .....	57
Figure 3.5 Waikato catchment and its river network .....	59
Figure 3.6 Waikato median annual sunshine hours total based on the 30 year period from 1981 to 2010 .....	60
Figure 3.7 Waikato median annual wind speed based on the 30 year period from 1981 to 2010 .....	

.....

Figure 3.8 Waikato catchment and its landuse..... 63

Figure 3.9 Waikato catchment and its representative sub-catchments ..... 64

Figure 3.10 Map of Mangatawhiri sub-catchment and meteo-hydrological stations..... 65

Figure 3.11 Map of Whangamarino sub-catchment and meteo-hydrological stations .... 66

Figure 3.12 Map of Mangaonua sub-catchment and meteo-hydrological stations ..... 66

Figure 3.13 Graphs of monthly precipitation, evaporation and discharge at stations in Mangatawhiri sub-catchment ..... 67

Figure 3.14 Graphs of monthly precipitation, evaporation and discharge at stations in Mangaonua sub-catchment..... 68

Figure 3.15 Map of Mangatawhiri sub-catchment’s landuse and soil types..... 69

Figure 3.16 Map of Whangamarino sub-catchment’s landuse..... 70

Figure 3.17 Map of Whangamarino sub-catchment’s soil type ..... 70

Figure 3.18 Map of Mangaonua sub-catchment’s land use ..... 71

Figure 3.19 Map of Mangaonua sub-catchment’s soil type..... 71

Figure 3.20 GCMs and RCM data with different spatial resolutions ..... 77

Figure 4.1 Geographic location of selected stations ..... 84

Figure 4.2 Data record lengths at 36 selected stations ..... 85

Figure 4.3 Correlogram of the computed autocorrelation coefficients corresponding to  $r_1$  ..... 92

Figure 4.4 R curve produced from ratio of observed variance and observed mean..... 96

Figure 4.5 L-MOM diagram, expressing the suitability of PDS with different distribution models ..... 100

Figure 4.6 L-MOM diagram, expressing the sensitivity of  $C_s$  against  $C_k$  in GP at selected stations..... 102

Figure 4.7 Plot of variation of the PDS mean and $C_v$ (a); dimensionless frequency curve (b); and frequency curve (c) for different values of $\lambda$ .....	106
Figure 5.1 PDS5 extracted from daily hyetograph at station 1155 with the threshold value $u = 36.878$ mm .....	119
Figure 5.2 $D_i$ statistic results for different PDS4, 5 .....	123
Figure 5.3 Regional L-MOM ratio diagram for PDS4 and PDS5.....	127
Figure 5.4 Comparison of regional quantile estimates for PDS4 and PDS5 for different return periods, $T$ .....	130
Figure 5.5 Comparison of estimated quantile using at-site (point) and regional (line) GP model for PDS4.....	131
Figure 5.6 Comparison of estimated quantile using at-site (point) and regional (line) GP model for PDS5	132
Figure 5.7 Box plot of growth factor computed for different return periods for PDS4 across 32 stations.....	133
Figure 5.8 Box plot of growth factor computed for different return periods for PDS5 across 32 stations.....	134
Figure 6.1 Geographical locations of the study region and selected stations .....	139
Figure 6.2 The closest grid box to the Waikato catchment (in red) extracted from Australia and New Zealand Window .....	142
Figure 6.3 Estimation of regional precipitation using spatial interpolation Thiessen method.....	150
Figure 6.4 Model calibration: Observed and simulated daily precipitation at station 2101 from CGCM3/T47 (upper) and GCM HadCM3 (lower) over period of 1961-1980 .....	155
Figure 6.5 Model validation: Observed and the simulated daily precipitation at station 2101 from CGCM3/T47 (upper) and GCM HadCM3 (lower) over period of 1981-1990.....	158
Figure 6.6 Model validation: Bias (percentage difference between observed and simulated monthly precipitation) from CGCM3/T47 over period 1981-1990.....	160

Figure 6.7 Model validation: Bias (percentage difference between observed and simulated monthly precipitation) from GCM HadCM3 over period 1981-1990.....	161
Figure 7.1 Gridded precipitation data from GCM and RCM models: CGCM3/T47 (left) and RCM HadCM3 (right) over the Waikato catchment.....	166
Figure 7.2 Graphs of areal precipitation simulation from different models against observation over the 1971-1980 period.....	174
Figure 7.3 Frequency curves developed for regional observation and model simulation over the period 1971-1990.....	175
Figure 7.4 Frequency curves developed for regional observation and model simulation corresponding to the 2011-40 and 2041-70 future scenarios.....	178
Figure 7.5 Frequency curves developed for AMS and PDS5 corresponding to 2041-70 and 2041-70 future periods.....	179
Figure 8.1 Monthly pan evaporation distributions for different stations.....	192
Figure 8.2 Monthly simulated PET distribution for different stations.....	193
Figure 8.3 Projection of mean daily PET for different sub-catchments.....	196
Figure 8.4 Variation coefficient of mean daily PET projections for different sub-catchments.....	197
Figure 9.1 NAM model structure.....	205
Figure 9.2 Calibrated hydrograph for Mangatawhiri catchment during the 1973-78 period.....	212
Figure 9.3 Validated hydrograph for catchment during the 1979-80 period.....	212
Figure 9.4 Calibrated hydrograph for Mangaonua catchment during the 1981-93 period.....	213
Figure 9.5 Validated hydrograph for Mangaonua catchment during the 1994-96 period.....	213
Figure 9.6 Runoff volumes for the Mangatawhiri catchment for the periods 2001-30, 2031-60 and 2061-90.....	215
Figure 9.7 Runoff volumes for the Whangamarino catchment for the periods 2001-30, 2031-60 and 2061-90.....	216

Figure 9.8 Runoff volumes for the Mangaonua catchment for the periods 2001-30, 2031-60 and 2061-90.....	217
Figure 9.9 River flow computed from unbiased-corrected PET (upper) and bias-corrected PET (lower) the Mangatawhiri catchment for the 2001-30, 2031-60 and 2061-90 periods .....	220
Figure 9.10 River flow computed from unbiased-corrected PET (left) and bias-corrected PET (right) the Whangamarino catchment for the 2001-30, 2031-60 and 2061-90 periods .....	220
Figure 9.11 River flow computed from unbiased-corrected PET (left) and bias-corrected PET (right) the Mangaonua catchment for the 2001-30, 2031-60 and 2061-90 periods	221

## List of Tables

Table 2.1 Projected average surface warming at the end of the 21 <sup>st</sup> century (at 2090-1099 relative to 1980-1999) .....	20
Table 3.1 Information on selected precipitation stations in North Island .....	74
Table 3.2 Information about selected evaporation stations.....	75
Table 3.3 Information on selected discharge stations .....	75
Table 3.4 The number of grid cells from RCM HadCM3 found for selected stations and selected sub-catchments .....	77
Table 4.1 Summary on the acceptance of the Poisson hypothesis based on the Fisher dispersion (F) test (in percentage, %) .....	95
Table 4.2 Summary on the acceptance of the Poisson hypothesis based on the Variance-to-mean ratio (R) test (in percentage, %) .....	95
Table 4.3 The PDS mean and $C_v$ values as well as GP distribution parameters estimated for different $\lambda$ values for selected stations in the Northern North Island.....	104
Table 5.1 L-MOM ratios of PDS4 and PDS5 for 32 stations .....	120
Table 5.2 Discordance ratio ( $D_i$ ) computed for PDS4 and PDS5 at station with 500 Monte-Carlo simulations.....	122

Table 5.3 Heterogeneity measures, H, for a homogenous region with 500 Monte-Carlo simulations .....	124
Table 5.4 Regional L-MOM estimator for PDS4 and PDS5 (for $\lambda =4$ and 5) for the homogenous North Island region .....	125
Table 5.5 Goodness-of-fit measures with 500 Monte-Carlo simulations for different 3-parameter distributions tested with PDS4 and PDS5 .....	126
Table 5.6 Estimates of the GP distribution parameters for PDS 4 and PDS5.....	128
Table 5.7 T-year quantile estimation from the regional GP distribution for PDS 4 and PDS5 accepted at the 90% confidence level .....	129
Table 5.8 Results of discordance, heterogeneity, goodness-of-fit and robustness tests for PDS4 and PDS5 (for $\lambda =4$ and $\lambda=5$ ).....	135
Table 6.1 Information about meteorological station in the study region .....	140
Table 6. 2 26 large-scale CGM and NCEP predictor variables and their description ....	141
Table 6.3 Predictor variables selected for different stations .....	149
Table 6.4 List of 8 large-scale predictors and results of cross-correlation analysis for both GCMs .....	151
Table 6.5 Model assessment for daily and seasonal precipitation simulations from CGCM3/T47 model .....	152
Table 6.6 Model assessment for daily and seasonal precipitation simulations from GCM HadCM3 model.....	153
Table 6.7 Assessment of the model performance for daily mean areal precipitation using Thiessen polygon method .....	154
Table 7.1 Criteria for assessing the RCM precipitation simulation against observed precipitation between 1971 and 1990 .....	171
Table 7.2 Assessment of the downscaling performance for areal daily precipitation over the 1971–1990 period.....	172
Table 7.3 Extreme precipitation events recorded at stations from 1971 to 1990.....	173
Table 7.4 Quantile estimated for regional observed and RCM precipitation .....	175

Table 8.1 Statistical characteristics of daily evaporation observed at stations .....	188
Table 8.2 Mann-Kendall test results for different locations .....	189
Table 8.3 Statistical characteristics of daily PET simulation for the 1971-2000 periods .....	190
Table 8.4 Assessment of daily PET simulation against observation, and for different methods .....	191
Table 8.5 Summary on characteristics of future PET projections for different sub- catchments .....	195
Table 9.1 Summary on historical data used in the study .....	202
Table 9.2 Model calibration and validation periods for different catchments .....	206
Table 9.3 Summary on NAM model parameters .....	206
Table 9.4 NAM parameters for different catchments .....	209
Table 9.5 Model evaluation for different catchments .....	211
Table 9.6 Future projections of catchment water balance .....	218

# Abbreviations

AMS	Annual Maximum Series
CGCM3.1/T47	Canadian Global Climate Model version 3.1/T47
DHI	Danish Hydraulic Institute
FAO	Food and Agriculture Organization
GCM	Global Circulation Model or Global Climate Model
GP	Generalized Pareto distribution
HadCM3	The United Kingdom Hadley Centre Coupled Model version 3
IPCC	Intergovernmental Panel on Climate Change
LRIS	Landcare Research Institute
MfE	Ministry of Environment
NAM	Nedbør-Afstrømnings-Model
NARCCAP	North American Regional Climate Change Assessment Program
NCSA	National Centre for Supercomputing Application
NECP	National Centre of Environmental Prediction
NIWA	National Institute of Water and Atmospheric Research
PDS	Partial Duration Series
PET	Potential Evapotranspiration
POT	Peak Over Threshold
RCM	Regional Circulation Model or Regional Climate Model
RFA	Regional Frequency Analysis
SDSM	Statistical Downscaling Model
SRES	Special Report on Emission scenarios
WMO	World Meteorological Organization
WRC	Waikato Regional Council
WWF	World Wildlife Fund

## Co-Authorship Form

This form is to accompany the submission of any PhD that contains research reported in published or unpublished co-authored work. **Please include one copy of this form for each co-authored work.** Completed forms should be included in all copies of your thesis submitted for examination and library deposit (including digital deposit), following your thesis Acknowledgements.

Please indicate the chapter/section/pages of this thesis that are extracted from a co-authored work and give the title and publication details or details of submission of the co-authored work.

Chapter 4 includes partial reproduction from the paper titled "Pham, H. X., Shamseldin, A. Y. and Melville, B. W. (2014). Statistical properties of partial duration series - A case study of North Island of New Zealand. J. Hydrol. Eng., 19, 807-815"

Nature of contribution by PhD candidate	Lead author, conducted study and wrote the text
Extent of contribution by PhD candidate (%)	92%

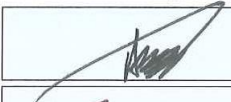
### CO-AUTHORS

Name	Nature of Contribution
Asaad Y. Shamseldin	Editing
Bruce W. Melville	Editing

### Certification by Co-Authors

The undersigned hereby certify that:

- ❖ the above statement correctly reflects the nature and extent of the PhD candidate's contribution to this work, and the nature of the contribution of each of the co-authors; and
- ❖ in cases where the PhD candidate was the lead author of the work that the candidate wrote the text.

Name	Signature	Date
Asaad Y. Shamseldin		9/5/2014
Bruce W. Melville		23/5/14

## Co-Authorship Form

This form is to accompany the submission of any PhD that contains research reported in published or unpublished co-authored work. **Please include one copy of this form for each co-authored work.** Completed forms should be included in all copies of your thesis submitted for examination and library deposit (including digital deposit), following your thesis Acknowledgements.

Please indicate the chapter/section/pages of this thesis that are extracted from a co-authored work and give the title and publication details or details of submission of the co-authored work.

Chapter 4 includes partial reproduction from the paper titled "Pham, H. X., Shamseldin, A. Y., and Melville, B. W. (2012). Statistical properties partial duration series - Case study: Auckland region, New Zealand, 4th International Conference on Estuaries and Coasts, Hanoi, Vietnam 8-11 October 2012"

Nature of contribution by PhD candidate

Lead author, conducted study and wrote the text

Extent of contribution by PhD candidate (%)

90%

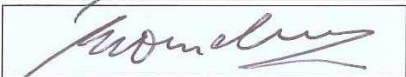
### CO-AUTHORS

Name	Nature of Contribution
Asaad Y. Shamseldin	Editing
Bruce W. Melville	Editing

### Certification by Co-Authors

The undersigned hereby certify that:

- ❖ the above statement correctly reflects the nature and extent of the PhD candidate's contribution to this work, and the nature of the contribution of each of the co-authors; and
- ❖ in cases where the PhD candidate was the lead author of the work that the candidate wrote the text.

Name	Signature	Date
Asaad Y. Shamseldin		9/5/2014
Bruce W. Melville		23/5/14

## Co-Authorship Form

This form is to accompany the submission of any PhD that contains research reported in published or unpublished co-authored work. **Please include one copy of this form for each co-authored work.** Completed forms should be included in all copies of your thesis submitted for examination and library deposit (including digital deposit), following your thesis Acknowledgements.

Please indicate the chapter/section/pages of this thesis that are extracted from a co-authored work and give the title and publication details or details of submission of the co-authored work.

Chapter 5 includes partial reproduction from the paper titled "Pham, H. X., Shamseldin, A. Y. and Melville, B. W. (2013). Statistical properties of partial duration series and its implication in frequency analysis. J. Hydrol. Eng. DOI: 10.1061/ (ASCE) HE.1943-5584.0000916"

Nature of contribution by PhD candidate	Lead author, conducted study and wrote the text
Extent of contribution by PhD candidate (%)	95%

### CO-AUTHORS

Name	Nature of Contribution
Asaad Y. Shamseldin	Editing
Bruce W. Melville	Editing

### Certification by Co-Authors

The undersigned hereby certify that:

- ❖ the above statement correctly reflects the nature and extent of the PhD candidate's contribution to this work, and the nature of the contribution of each of the co-authors; and
- ❖ in cases where the PhD candidate was the lead author of the work that the candidate wrote the text.

Name	Signature	Date
Asaad Y. Shamseldin		9/5/2014
Bruce W. Melville		23/5/14

## Co-Authorship Form

This form is to accompany the submission of any PhD that contains research reported in published or unpublished co-authored work. **Please include one copy of this form for each co-authored work.** Completed forms should be included in all copies of your thesis submitted for examination and library deposit (including digital deposit), following your thesis Acknowledgements.

Please indicate the chapter/section/pages of this thesis that are extracted from a co-authored work and give the title and publication details or details of submission of the co-authored work.

Chapter 6 includes partial reproduction from the paper titled "Pham, H. X, Shamseldin, A. Y. (2013). Statistical downscaling of daily precipitation using UKSDSM model, 6th Thailand-Japan International Academic Conference, Osaka, Japan 9-11 November 2013"

Nature of contribution by PhD candidate	Lead author, conducted study and wrote the text
Extent of contribution by PhD candidate (%)	97%

### CO-AUTHORS

Name	Nature of Contribution
Asaad Y. Shamseldin	Editing

### Certification by Co-Authors

The undersigned hereby certify that:

- ❖ the above statement correctly reflects the nature and extent of the PhD candidate's contribution to this work, and the nature of the contribution of each of the co-authors; and
- ❖ in cases where the PhD candidate was the lead author of the work that the candidate wrote the text.

Name	Signature	Date
Asaad Y. Shamseldin		9/5/2014

## Co-Authorship Form

This form is to accompany the submission of any PhD that contains research reported in published or unpublished co-authored work. **Please include one copy of this form for each co-authored work.** Completed forms should be included in all copies of your thesis submitted for examination and library deposit (including digital deposit), following your thesis Acknowledgements.

Please indicate the chapter/section/pages of this thesis that are extracted from a co-authored work and give the title and publication details or details of submission of the co-authored work.

Chapter 7 includes partial reproduction from the paper titled "Pham, H., Shamseldin, A. and Melville, B. (2014). Downscaling of daily precipitation and projection of future extreme precipitation. J. Hydrol. Eng. (ASCE)" - under reviewing.

Nature of contribution by PhD candidate	Lead author, conducted study and wrote the text
Extent of contribution by PhD candidate (%)	97%

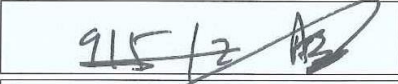
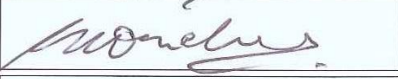
### CO-AUTHORS

Name	Nature of Contribution
Asaad Y. Shamseldin	Editing
Bruce W. Melville	Editing

### Certification by Co-Authors

The undersigned hereby certify that:

- ❖ the above statement correctly reflects the nature and extent of the PhD candidate's contribution to this work, and the nature of the contribution of each of the co-authors; and
- ❖ in cases where the PhD candidate was the lead author of the work that the candidate wrote the text.

Name	Signature	Date
Asaad Y. Shamseldin		9/5/2014
Bruce W. Melville		23/5/14

## Co-Authorship Form

This form is to accompany the submission of any PhD that contains research reported in published or unpublished co-authored work. **Please include one copy of this form for each co-authored work.** Completed forms should be included in all copies of your thesis submitted for examination and library deposit (including digital deposit), following your thesis Acknowledgements.

Please indicate the chapter/section/pages of this thesis that are extracted from a co-authored work and give the title and publication details or details of submission of the co-authored work.

Chapter 8 includes partial reproduction from the paper titled "Pham, H., Shamseldin, A. and Melville, B. (2014). Projection of potential evapotranspiration under climate change over forest and grass catchments. J. Theor. Appl. Clima." - under reviewing.

Nature of contribution by PhD candidate	Lead author, conducted study and wrote the text
Extent of contribution by PhD candidate (%)	97%

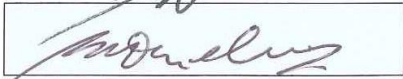
### CO-AUTHORS

Name	Nature of Contribution
Asaad Y. Shamseldin	Editing
Bruce W. Melville	Editing

### Certification by Co-Authors

The undersigned hereby certify that:

- ❖ the above statement correctly reflects the nature and extent of the PhD candidate's contribution to this work, and the nature of the contribution of each of the co-authors; and
- ❖ in cases where the PhD candidate was the lead author of the work that the candidate wrote the text.

Name	Signature	Date
Asaad Y. Shamseldin		9/5/2014
Bruce W. Melville		23/5/14

## Co-Authorship Form

This form is to accompany the submission of any PhD that contains research reported in published or unpublished co-authored work. **Please include one copy of this form for each co-authored work.** Completed forms should be included in all copies of your thesis submitted for examination and library deposit (including digital deposit), following your thesis Acknowledgements.

Please indicate the chapter/section/pages of this thesis that are extracted from a co-authored work and give the title and publication details or details of submission of the co-authored work.

Chapter 9 includes partial reproduction from the paper titled "Pham, H., Shamseldin, A. and Melville, B. (2014). The assessment of climate change impact on water balance of forested and farmed catchments. J. Hydrol. Eng. (ASCE)" - under reviewing.

Nature of contribution by PhD candidate	Lead author, conducted study and wrote the text
Extent of contribution by PhD candidate (%)	97%

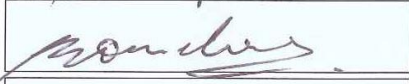
### CO-AUTHORS

Name	Nature of Contribution
Asaad Y. Shamseldin	Editing
Bruce W. Melville	Editing

### Certification by Co-Authors

The undersigned hereby certify that:

- ❖ the above statement correctly reflects the nature and extent of the PhD candidate's contribution to this work, and the nature of the contribution of each of the co-authors; and
- ❖ in cases where the PhD candidate was the lead author of the work that the candidate wrote the text.

Name	Signature	Date
Asaad Y. Shamseldin		9/5/2014
Bruce W. Melville		23/5/14

# CHAPTER 1

## Introduction

This chapter provides brief information about this research thesis. The first section of the chapter introduces the background to the research. The second section presents the motivation for the research together with the major contributions of this thesis towards current studies on catchment water balance modelling under climate change. The specific objectives of the research are presented in the third section. The last section of the chapter describes the organization of the thesis.

## **1.1. Background**

### **1.1.1 Climate change**

The impacts of climate change on water resources have been the focus of attention for many decades because climate change has been associated with many disasters around the globe. Floods have amplified in some regions while droughts have intensified in others. This could be the direct impacts of climate change on hydrological cycle disturbing water resources (Sanderson, 2010; Zhang et al., 2010). The most vulnerable regions are identified as the low-lying areas where flooding has become more frequent and severe as the result of extreme precipitation effect (Fowler and Kilsby, 2003; IPCC, 2008; Guhathakurta et al., 2011). In contrast, the forested and farmed areas encounter water insufficiency caused by extreme droughts (IPCC, 2008; Tanaka et al., 2008; Sangmanee et al., 2011). These events have become a major concern because of their current and potential causes and effects such as increasing frequency, magnitude and persistence (Delgado, 2010; Kjeldsen, 2000; Pryce, 2009).

The greatest evidence of climate change is believed to be increasing global average surface temperature and rising global average sea level and will tend to continue to occur in the future with increasing greenhouse gas (GHGs) emissions. In addition, an increase in extreme events like heavy precipitation, storms and heat waves are observed in many regions, and is predicted to be more severe and frequent in the future (IPCC, 2007).

### **1.1.2 Hydrological response to climate change**

Hydrologic components are likely to respond to the changing climate. In general, precipitation and especially extreme precipitation is very sensitive to increases in temperature (Changchun et al., 2010; European-Commission, 2005; IPCC, 2008). Despite

the observed decrease in evaporation, the rate of evaporation is to increase with increasing temperature and heat waves (Cong and Yang 2008; IPCC, 2008; Bell et al., 2011). Thus, surface runoff is subject to change as a result of increasing precipitation, temperature and evaporation (Gleick, 1993; Roy et al., 2001).

### **1.1.2.1. Frequency and magnitude of extreme precipitation**

Extreme precipitation is considered as the most reliable representative of typical local weather and the most sensitive indicator of climate change (Francis and Hengeveld, 1998; Chiew et al., 2010; Furcolo, Villani et al., 1995; Mason et al., 1999; Im et al., 2010; Lavers et al., 2010; Pal and Tabbaa, 2009; Mason et al., 1999). Moreover, floods associated with extreme precipitation have been identified in many countries, such as United Kingdom, America and Canada, India, Bangladesh and China over past decades (Fowler and Kilsby, 2003; Guhathakurta et al., 2011; Roy et al., 2001). As a result, these events are very important in terms of design aspects and risk mitigation (Furcolo et al., 1995; Driouech et al., 2010; Lamb, 2001; Pocatello, 2000).

In practice, flood prediction and infrastructure design depend significantly on the analysis of extreme precipitations that is commonly used to develop synthetic design storms. This requires an accurate and adequate estimation of quantiles from observations. Under the changing climate, the design storm is used to mathematically represent a precipitation event that reflects conditions in a given area for designing infrastructure (Pocatello, 2000). The accuracy of design storm estimation depends on the magnitude and frequency of extremes. A regional frequency analysis (RFA) is normally used in this regard which depends on the accuracy of extreme event extracted from observed time series (Norbiato et al., 2007; Trefry et al., 2005).

Annual maximum series (AMS) and Partial duration series (PDS) are two main models for defining extreme events. The former uses only the one largest event of each year which may not be fully representative of extreme precipitations from historical record. The later involves more subsequent large events in a year which would provide more reliable results of simulated extremes (Norbiato et al., 2007; Hosking and Wallis, 1997; Zvi, 2009). However, the PDS model is still underused relative to the AMS model which is constrained by the selection of peaks in each year and the resulting frequency distributions (Cunnane, 1973; Claps and Laio, 2003; Begueria, 2005; Adamowski, 2009; Takeuchi, 1984). Different studies have suggested specific values of peaks per year ranging from 1.6 to 15 depending on the study areas (Cunnane, 1973; Hosking and Wallis, 1987; Claps, 2003). In fact, the validity of these peak numbers was not tested when the climate change takes place (García-Cueto, 2012).

### **1.1.2.2. Evaporation paradox**

Evaporation has become a major concern in assessment and management of water resources, especially under changing climatic conditions. About 35% to 45% of continental precipitation turns to surface runoff while the rest is lost due to evaporation (Peter, 1993). There was a decrease in evaporation during the past 50 years which has occurred in many regions over the globe (Gifford 2004; Szilagyi and Jozsa, 2008). However, recent studies argue that evaporation rates are believed to increase with rising temperature. This gives rise the evaporation paradox.

The evaporation paradox has been argued, is one indicator of the most significant climate change variables. In theory, it expresses the contrast between the expectation and observation of evaporation rate (Cong and Yang 2008; Szilagyi and Jozsa, 2008). Evaporation rate is conventionally measured by a pan while evaporation estimation is carried out using different methods ranging from empirical to physical-based (Chun et al,

2010; Douglas et al., 2009; IIASA, 1994; Palutikof et al., 1994; Penman, 1947; Thornthwaite, 1948). The evaporation paradox may result in inaccurate estimates of future evaporation prediction because linkages between evaporation and climate change have not been fully understood.

The combined Penman-Monteith method developed by the Food and Agriculture Organization (FAO), also known as FAO-56 method, is considered to be the most reliable method for estimating potential evapotranspiration (PET) that is widely used to indirectly estimate actual evaporation (IIASA, 1994; Zotarelli et al., 2010). In the context of climate change, there is no study dealing with evaporation or/and PET using FAO-56 method coupled with Global Climate Model (GCM) and Regional Climate Model (RCM) data. Only a few studies employed Penman and/or Monteith methods and GCM/RCM data. However, these studies did not suggest which GCM/RCM is the most reliable for estimating PET.

### **1.1.2.3. Catchment water balance**

Climate change impacts directly on water resources in altering the volume and runoff with time (Changchun, 2010; Engen-Skaugen et al., 2005; Middelkoop et al., 2001). In general, a rise in runoff and volume is consistent with increasing temperature and precipitation (Guo et al., 2002; Middelkoop et al., 2001; Mpelasoka, 2000). A decrease in runoff and volume is also affected by increasing temperature and decreasing precipitation (Strzepek and McCluskey, 2007). In a changing climate, changes in precipitation directly and remarkably impact on water resources (Archer et al., 2010; Esqueda et al., 2011; Kim and Kaluarachchi, 2009; Pike et al., 2010). Water resources can also be impacted by changes in soil, vegetation and evapotranspiration (Iturbe et al., 1999; Marks et al., 1993; Pike et al., 2010; Yates, 1994).

Different water balance models were used to deal with modelling of water balance under changing climate together with GCM/RCM data. This includes conceptual and distributed models at daily and monthly time scale (Brauer, 2007; Madsen et al., 2002; Mauser and Bach, 2009; Mauser and Bach, 2009; White et al., 2011). However, current water balance modelling is mainly dependent on precipitation while evapotranspiration is fixed as a proportion of precipitation (Zhang et al., 2008). Moreover, these models do not fully take into account the interaction of the various phases of rainfall-runoff transformation within the soil, causing the inaccuracy of modelled water balance components of a catchment (Andrew and Dymond, 2007; Jiang et al., 2007; Marks et al., 1993). Moreover, at the catchment scale water balance modelling under different climate change scenarios is not fully studied (Ha, 2009; Marks et al., 1993; Mauser and Bach, 2009).

## **1.2. Motivation and novelty of the research**

### **1.2.1 Motivation of the research**

The focus of this research is to study the impacts of climate change on catchment hydrology, using catchments in New Zealand as case studies. Potential evapotranspiration and precipitation are two key inputs which are used in water balance calculations. Under climate change, it is envisaged that significant variability in precipitation and evapotranspiration will take place which would undoubtedly affect the catchment water balance.

A common assumption made in previous studies dealing with impacts of climate change on catchment hydrology is that the potential evapotranspiration rates would remain the same as their current and past values (Comnalicer, 2010; Vaitiekuniene, 2005; Zhang et al., 2008). Moreover, so far there is no agreement on climate change impacts on potential

evapotranspiration at the catchment scale. It is clear that if the improved estimation of evapotranspiration is successful, it may assist in more accurate modelling of catchment flows. This research for the first time will study the variation of potential evapotranspiration in different sub-catchments and its effects on catchment runoff and volume for future time. Similarly, recent developments in precipitation estimation under changing climate highlights the need for addressing the variability in extreme precipitation under climate change. The research to date has tended to focus on the frequency analysis of extreme occurrence based on annual maximum series (AMS) rather than on partial duration series (PDS). Likewise, the outperformance of PDS over the AMS has not yet been examined with future data. This study for the first time examines the variation on extreme precipitation events under changing climate conditions using FA/PDS and its comparative FA/AMS.

### **1.2.2 Major Contributions of the thesis**

This research aims to increase general knowledge of evapotranspiration and extreme precipitation as well as their interference in water resources of a catchment due to climate change impacts. This will be a valuable contribution to the understanding of hydrological response subject to changing climate in several regions where study catchments are present. Along this line, the best combined use of different techniques in this research may be helpful for similar regions.

### **1.3. Research Objectives**

The overview and discussion presented in the previous sections has demonstrated that precipitation and potential evapotranspiration (PET) play an equally important role in the hydrologic system. Also, these two key components are very sensitive to changing climate.

Water balance is a unique unit to examine the catchment hydrology and estimate the effects of climate change on catchment water availability. In the context of climate change, the emerging problem is the quantitative estimation of precipitation and PET variability as well as the modelling of catchment water availability from changing precipitation and PET. This research is aimed at taking over the problem in typical catchments in New Zealand.

*The specific objectives of the research are to:*

- Estimate the variability in extreme precipitation due to climate change across the North Island of New Zealand.
- Quantify the change in potential evapotranspiration due to climate change for Waikato catchment in the North Island.
- Compute the catchment water availability under changing climate for three typical forest and grass sub-catchments of the Waikato catchment located in the North Island.
- Evaluate the performance of statistical and dynamic downscaling for obtaining precipitation at station location.
- Assess the performance of frequency analysis using partial duration series (FA/PDS) over annual maximum series (FA/AMS) for estimating extreme precipitations under climate change.
- Evaluate the use of the combined Penman-Monteith method with downscaled climate data for estimating potential evapotranspiration.

## 1.4. Thesis Outline

This research thesis is structured as follows:

**Chapter 1 Introduction** introduces the background, motivation, objectives and outline of the research thesis.

**Chapter 2 Literature review** provides a brief overview of climate changes and their impacts on hydrology and catchment water in relation to the objectives of this research. The relevant methods and techniques are also described with main remarks on their application.

**Chapter 3 Study region and data** gives information on characteristics of selected catchments and sub-catchments and their data availability. Data collection and processing are presented including data types and sources. This chapter also introduces different software and programs used in this thesis dealing with data extraction, processing and analysis.

**Chapter 4 Extraction of extreme precipitation** explains the novel approach to extract extreme events from daily precipitation series. This chapter further investigates the most reliable partial duration precipitation series (PDS) for the whole North Island region including the studied Waikato catchment. This was tested at 25 single observation stations across the North Island region.

**Chapter 5 Regionalized extreme precipitation** examines the validity of the PDS obtained from Chapter 4 and regionalizes it for the North Island region. This was then used as a reference for estimating daily precipitation and extreme precipitation.

**Chapter 6 Downscaling of daily precipitation** aims to compute the daily precipitation at station location and areal mean precipitation over the Waikato catchment from Global

Climate Models (GCMs). Two different GCMs were used to give a better assessment of daily precipitation variability from present to the future.

**Chapter 7 Future projection of extreme precipitation** predicts future extreme precipitation as well as to confirm the preferable use of Regional Climate Model (RCM) over the GCMs for climate change studies.

**Chapter 8 Future projection of potential evapotranspiration** first answers the question whether or not evaporation paradox exists in the Waikato catchment by computing the change in evapotranspiration rate from present to the future. This chapter then gives more detailed information on the variation of water losses due to evapotranspiration that occurs in different forest and grass land sub-catchments.

**Chapter 9 Assessment of climate change impacts on catchment water balance** qualifies the effects of changing precipitation and potential evapotranspiration on the catchment surface runoff and volume for both present and future time.

**Chapter 10 Conclusions and recommendations** summaries the findings of this research thesis. A recap of the gaps identified by the research is shown. This chapter also presents limitations of the thesis and proposes possibilities for further studies in this field.

**Appendices** provide materials related to this research in detail.

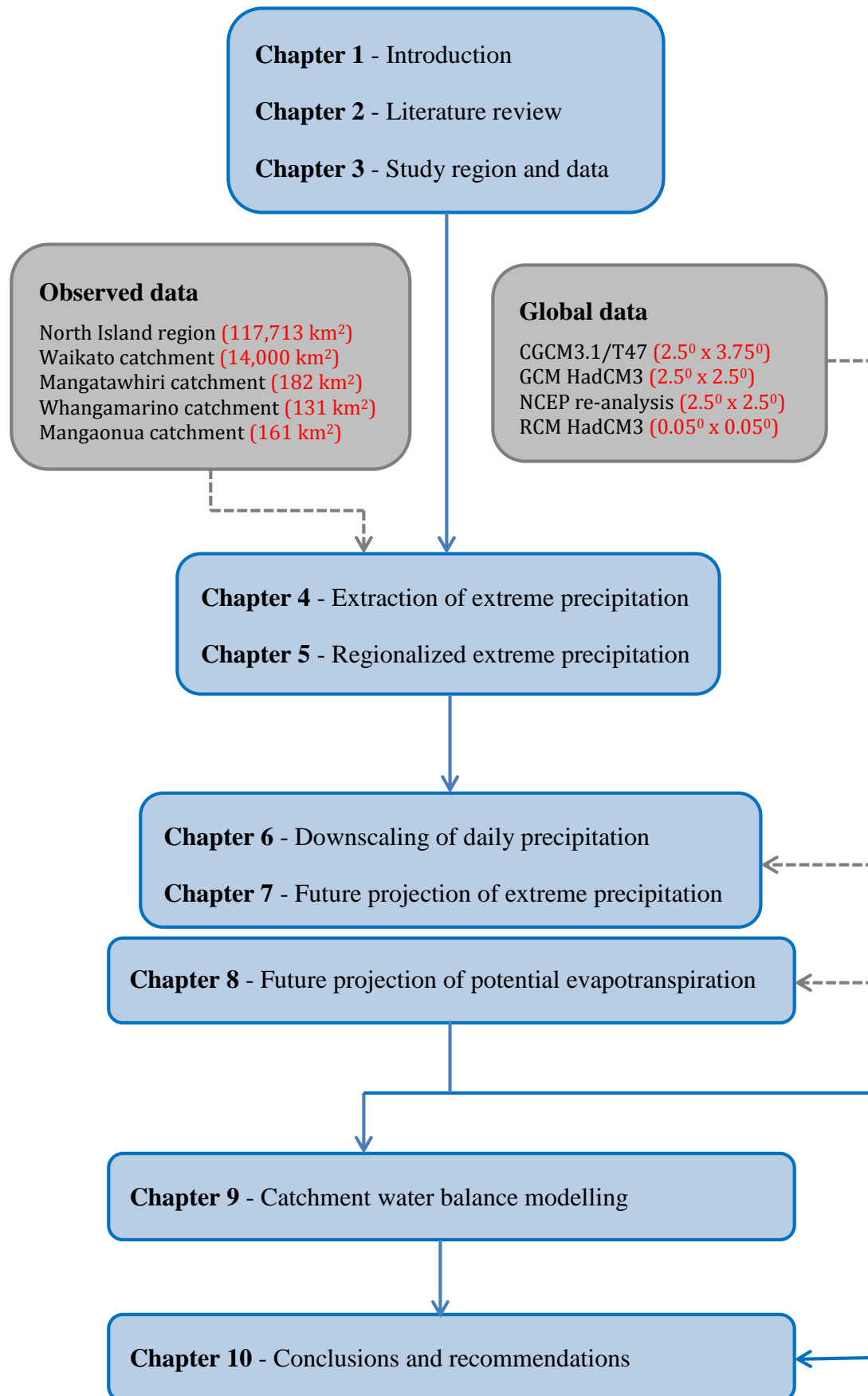


Figure 1.1 Organization of the thesis

## CHAPTER 2

# Literature Review

This chapter introduces a brief overview of past studies relevant to the research in this thesis. The initial sections of the chapter present the basic knowledge about climate changes and their impacts on hydrology and catchment water. The explanation of relevant methods and techniques is also presented in the following sections.

## 2.1. Climate change

The long-term change in the state of climate is known as climate change which is mainly caused by both natural and man-made forces. The former includes natural changes in the Earth's climate system components and their interactions, volcanic eruptions and variability in solar radiation, while the latter includes industrial, agricultural and deforestation activities. Both natural and man-made disturbance could affect the energy budget on the surface, resulting in the increase in globally averaged temperatures which has been observed since the mid-20th century (Sweeney, 2009).

Greenhouse gases (GHG) are essential to maintain a stable climate of the Earth by warming it with the sun's heat trapped around its atmosphere. GHG are carbon dioxide (CO<sub>2</sub>), methane (CH<sub>4</sub>), nitrous oxide (N<sub>2</sub>O) and chlorofluorocarbons (CFCs) which mainly come from volcanic eruptions and human activities. The level of GHG has rapidly increased resulting in too much heat trapped around the Earth. This causes the so-called 'Greenhouse Effect' which could lead to global warming (Mitchell, 1989).

Over the last 200 years normal climate are being affected, such as more frequent occurrence of extremes events with rising temperature including heat-waves, extreme precipitations, extreme droughts and intensive tropical cyclones (IPCC, 2007 and 2008).

The following sub-sections give more details on the observed climate change as well as the future projection of climate change until late 21<sup>st</sup> century.

### 2.1.1. Historical observed climate change

The increasing global temperature is the most clear evidence symptom of climate change which has been occurring across the globe and most notably in Northern Hemisphere at high latitudes (Figure 2.1). According to IPCC (2007), climate change was observed as follows:

- Global surface temperature increased by  $0.74^{\circ}\text{C}$  during the 1906-2005 period. In particular, average Northern Hemisphere temperatures during the second half of the 20th century were likely the highest in at least the past 1300 years.
- Arctic sea ice has shrunk by 2.7% per decade, with larger decreases in summer of 7.4% per decade. Mountain glaciers and snow cover on average have declined in both hemispheres.
- From 1900 to 2005, precipitation increased significantly in eastern parts of North and South America, northern Europe and northern and central Asia but declined in the Sahel, the Mediterranean, southern Africa and parts of southern Asia. Globally, the area affected by drought has likely increased since the 1970s.
- Over the past 50 years in most land areas, hot days and hot nights have become more frequent. Likewise, the frequency of heavy precipitation events has also increased.
- Since about 1970, intense tropical cyclone activity has increased in the North Atlantic, but there is no clear trend in the annual numbers of tropical cyclones.

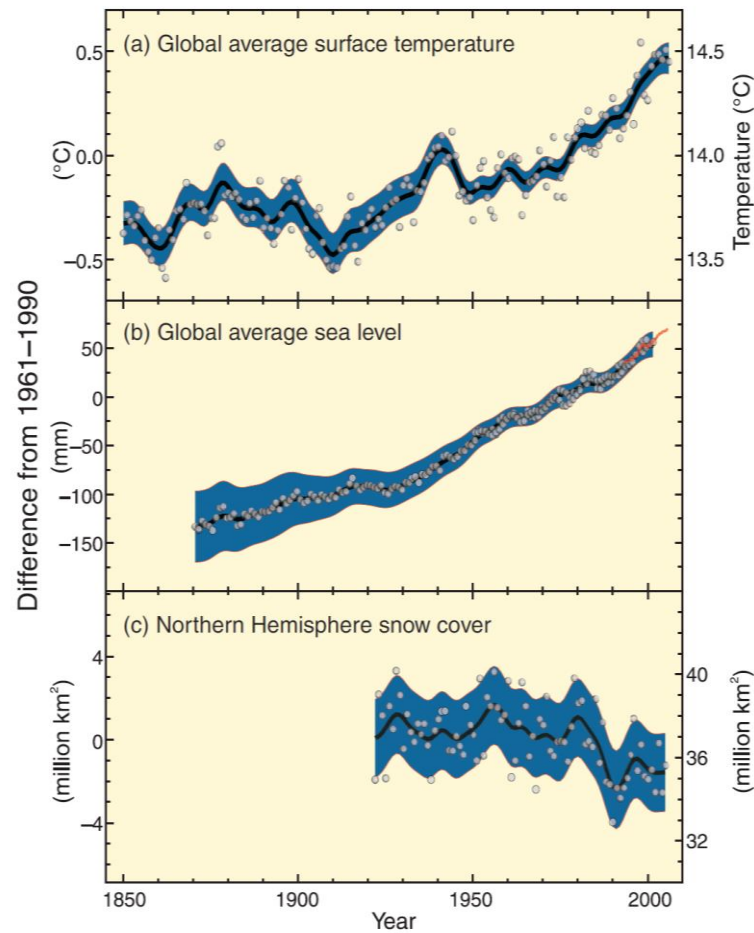


**Figure 2.1** Observed changes in global average surface temperature, global average sea level and Northern Hemisphere snow cover for the period 1961-1990 within 5%-80% uncertainty range (shaded areas) (from IPCC, 2007)

### 2.1.2. IPCC SRES scenarios

The Intergovernmental Panel on Climate Change developed several scenarios and described them in the Special Report on Emissions Scenarios. They are known as IPCC SRES scenarios which are widely used in many recent climate change vulnerability and impact assessments. These scenarios describe a developed world from demographic, economic and technological driving forces and resulting GHG emissions, in the absence of additional climate policies (IPCC, 2000).

According to IPCC (2000 and 2007), the SRES scenarios are based on the assumption that CO<sub>2</sub> emissions are projected to increase from 40% to 110% during 2000-2030 period as a result of a projected rise in global GHG emissions from 9.7 to 36.7 GtCO<sub>2</sub>-eq (25% to 90%) in which fossil fuels would remain dominant in the global energy mix over that period (Figure 2.2).

Therefore, emissions projections, with CO<sub>2</sub> concentration as the driving forces, are used as standard inputs to Global and Regional Circulation Models (GCMs/RCMs) to assess the impacts of climate change (IPCC, 1999, 2000 and 2007).

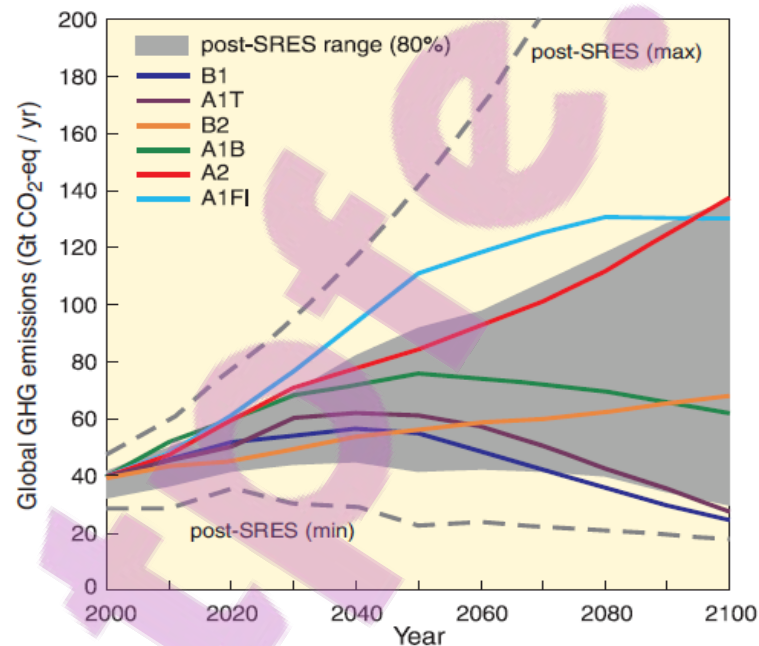


**Figure 2.2** GHG emissions with six SRES scenarios from 2000 to 2100 (IPCC, 2007)

SRES scenarios are grouped into four basic families, namely A1, B1, A2 and B2. Each scenario implicitly presents the driving forces (Figure 2.3).

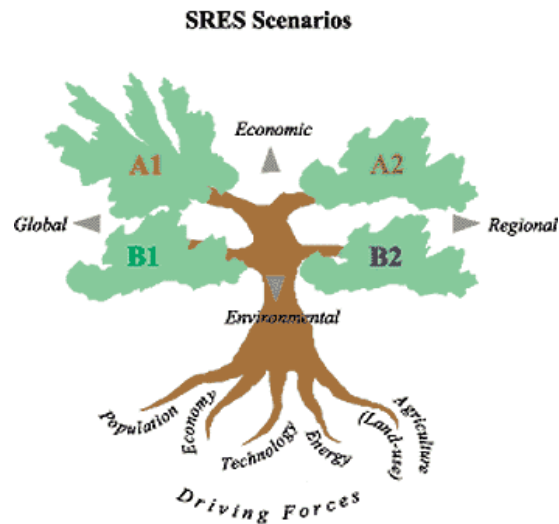


**Figure 2.3** Schematic representations of the SRES scenarios (from IPCC, 2007)

- |  |   |
|--|---|
| - <b>A1</b> : globalization, emphasis on human wealth<br>Globalized, intensive (market forces).              | - <b>A2</b> : regionalization, emphasis on human wealth<br>Regional, intensive (clash of civilizations) |
| - <b>B1</b> : globalization, on sustainability and equity<br>Globalized, extensive (sustainable development) | - <b>B2</b> : regionalization, on sustainability and equity<br>Regional, extensive (mixed green bag)    |

According to IPCC (2000 and 2007), the details of the four SRES scenario families are:

- The A1 family describes a future world of very rapid economic growth, global population that peaks in mid-century and declines thereafter, and the rapid introduction of new and more efficient technologies.
- The B1 family describes a convergent world with the same global population as in the A1, but with rapid changes in economic structures toward a service and information economy, with reductions in material intensity, and the introduction of clean and resource-efficient technologies.
- The A2 family describes a very heterogeneous world which focuses on local and regional levels with the slow converge of fertility patterns across regions, the growth of regionally oriented economic development, and slow fragment change in technology.

- The B2 family describes a world in which the emphasis is on local solutions to economic, social, and environmental sustainability. It is a world with continuously increasing global population at a rate lower than A2, intermediate levels of economic development, and less rapid and more diverse technological change than in the B1 and A1 families.

### 2.1.3. Projected climate change

The projected rise in global mean temperature for single and for a range of SRES emissions scenarios is shown in Figures 2.4 and 2.5.

About 0.2°C per decade is projected for a range of SRES emissions scenarios between 2000 and 2030. In case of GHGs and aerosol concentrations at year 2000 level are assumed to be constant through the century; it is expected that global mean temperature would still increase by around 0.1°C per decade. From 2031 onwards, increasing temperature is projected depending on specific emissions scenarios. Projected global mean temperature increase is 1.80 to 4.00 by the end of this century from B1 to AF1 scenarios (Table 2.1).

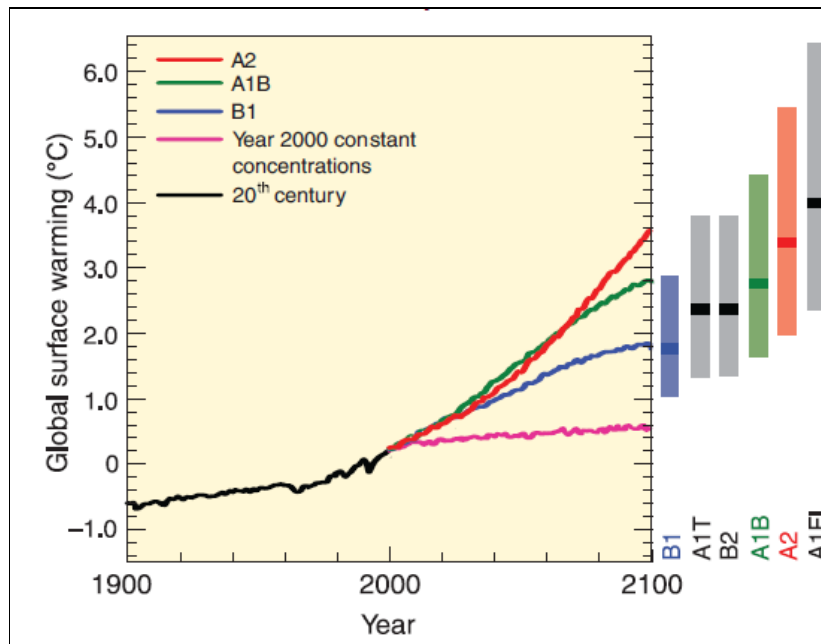


**Figure 2.4** Change in global surface temperature is projected for a single SRES emissions scenario (from IPCC, 2007).

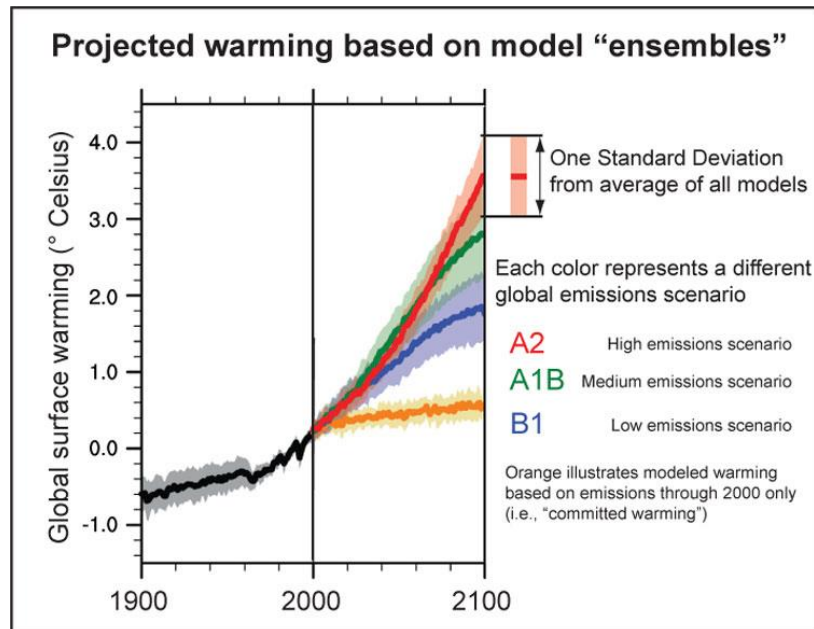


**Figure 2.5** Change in global surface temperature is projected for a range of SRES emissions scenarios (from IPCC, 2007).

**Table 2.1** Projected average surface warming at the end of the 21<sup>st</sup> century (at 2090-2099 relative to 1980-1999) (*from IPCC, 2007*)

No.	RSES scenarios	Temperature change (°C)		Sea level rise (m)
		Best estimate	Scenario range	
1	B1	1.8	1.1 – 2.9	0.18 – 0.38
2	A1T	2.4	1.4 – 3.8	0.20 – 0.45
3	B2	2.4	1.4 – 3.8	0.20 – 0.43
4	A1B	2.8	1.7 – 4.4	0.21 – 0.48
5	A2	3.4	2.0 – 5.4	0.23 – 0.51
6	A1F	4.0	2.4 – 6.4	0.26 – 0.59

The SRES scenarios published in IPCC (2007) overcame some GCM limitation to project a more reliable temperature and sea level rise in IPCC (2000). Projected climate change in the 21<sup>st</sup> century with a high degree of probability is presented below:

- Warming is expected to be greatest over land and at most high northern latitudes, and least over the Southern Ocean (near Antarctica) and northern North Atlantic, continuing recent observed trends.
- Sea ice is projected to shrink in both the Arctic and Antarctic under all SRES scenarios.
- It is very likely that hot extremes, heat waves and heavy precipitation events will become more frequent.
- It is likely that future tropical cyclones (typhoons and hurricanes) will become more intense, with larger peak wind speeds and more heavy precipitation associated with ongoing increases of tropical sea-surface temperatures.
- Extra-tropical storm tracks are projected to move poleward, with consequent changes in wind, precipitation and temperature patterns.
- And increases in the amount of precipitation are very likely in high-latitudes, while decreases are likely in most subtropical land regions.

## 2.2. New Zealand and Waikato climate change and its impacts

### 2.2.1. New Zealand climate change and impacts

For most developed countries, human originated greenhouse gases are thought to be the major cause of climate change. However, New Zealand is only one developed country producing more than 55% of likely GHG emissions, CH<sub>4</sub> and N<sub>2</sub>O, from agriculture (MfE, 2008; NIWA, 2005; WRC, 2011).

As reported by the IPCC 4<sup>th</sup> Assessment Report (2007) and WWF (2007), observed climate change in New Zealand as follows:

- Mean air temperatures have risen 1.0 °C from 1855-2004, and 0.4°C since 1950.
- There have been more heat waves, fewer frosts.
- There has been more rain in the south-west, less rain in the north-east.
- And sea level has since arisen by about 70 mm.

As a consequence,

- Floods, landslides, droughts and storm surges are very likely to become more frequent and intense, and snow and frost are likely to become less frequent.
- The 1997-1998 and 1998-1999 droughts had agricultural losses of US\$800 million.
- Coastal inundation and erosion increased, especially in regions exposed to cyclones and storm surges. Coastal development is exacerbating the climate risks (from the Bay of Plenty to Northland).
- Eastern New Zealand is likely to have less soil moisture, although the western part is likely to receive more rain (medium confidence).

- Ice volume of glaciers decreased from 100 km to 50 km over past century. Losses of at least a quarter of glacier mass since 1950. Mass balance of Franz Josef glacier decreased 0.02 m/year from 1894-2005.
- Various bio-ecosystems have been disturbed and changed, such as alpine species which are likely to be at risk of extinction. The tree line has shifted to higher altitudes; earlier egg laying in Welcome Swallow; kiwifruit varieties likely to become uneconomic in Northland by 2050.
- And the hydro-system has altered, with for example, reduction in water supply for irrigation, cities, industry and riverine environment in those areas where streamflow declines (e.g. Northland and eastern lowlands).

### **2.2.2. Waikato climate change and impacts**

As reported in WRC (2011), the potential climate change and impacts in the Waikato

Region include:

- Changes in weather patterns – differences in rainfall, temperature and microclimates could affect agriculture and horticulture. The location of some industries, agriculture, horticulture and tourism may change.
- More turbulent weather - extreme weather can increase flooding, erosion, droughts and damage ecosystems.
- Sea level rise - higher sea levels will affect coastal communities increasing coastal flooding and erosion.

As a consequence,

- Threats to biodiversity - species that are already under threat or at the limit of their climatic range may not be able to survive.

- New diseases and pests may take hold. Tropical pests and tropical diseases like malaria may become established in areas where they currently do not exist.

## **2.3. Climate change impacts analysis**

Climate change can be tested by changes in the mean and/or the variability of its properties for decades or longer periods, and the causes of climate change also need to be accounted for (IPCC, 2007). In practice, it is essential to study the Earth's climate system components and their interaction along with atmospheric and anthropogenic gases emissions. In this case, Global Circulation Models (GCMs) and its embedded SRES scenarios are the option. This section presents the techniques that are commonly used to qualify the impacts of climate change for both past and future times.

### **2.3.1. Global Circulation Models (GCMs)**

With advances in technology, Global Climate Models (GCMs), also known as Global Circulation Models, were developed and have been improved considerably over time. The GCM outputs are a useful data source for investigating any variation in each climate element of the Earth's climate system, such as atmosphere, cryosphere, biosphere and ocean as well as their interaction for both current and future time (Baguis et al., 2010; Ishak et al., 2010).

Based on the synthesis report by the Intergovernmental Panel on Climate Change (IPCC, 2007), the GCMs are a very powerful tool which is able to simulate the response of the earth's climate system to the changing concentrations of greenhouse gases (GHGs). In principle, a GCM is designed to simulate the thermodynamics and the physics of atmosphere, land surface and ocean as well as their interaction and reaction to the changing climate. In addition, the geographical effect on climate system is likely to be simulated in

this GCM. Basically, the climate is represented in GCMs as a three dimensional (3D) grid cell over the globe with a horizontal resolution of between 250 km and 600 km, their vertical resolution is from 10 to 20 layers in the atmosphere and up to 30 layers in the ocean (Figure 2.6). These models are run from daily to decadal time step.

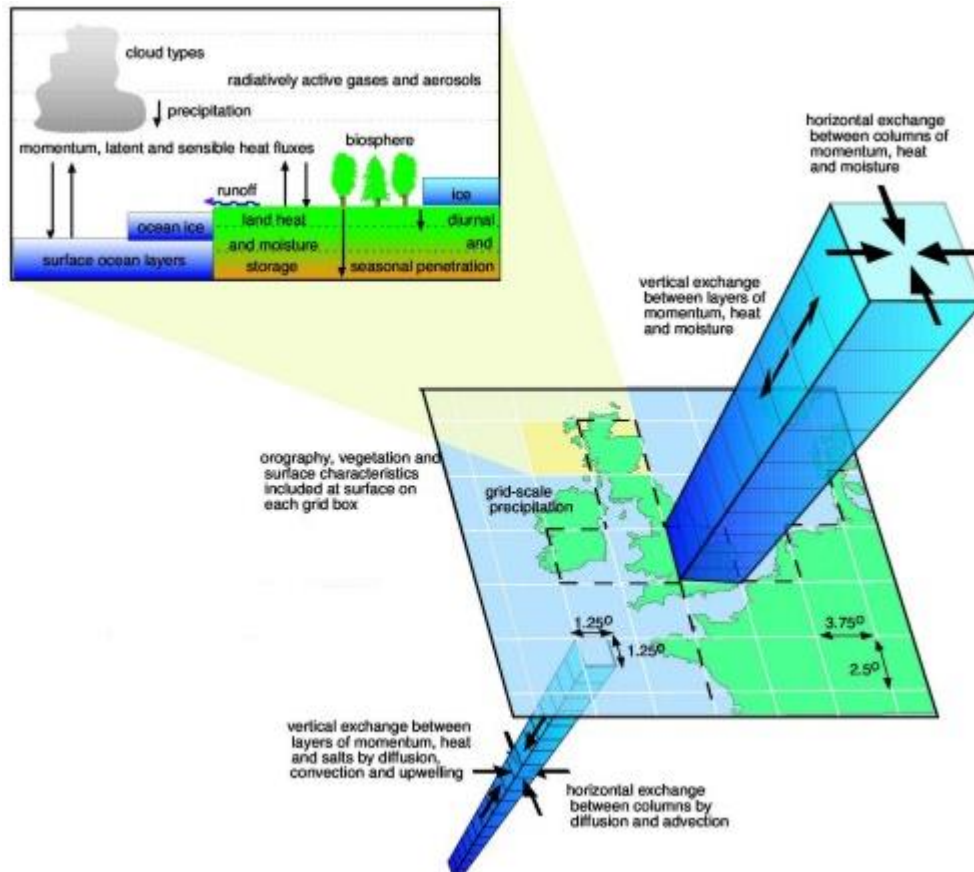


**Figure 2.6** Description of GCM models (*David Viner, Climatic Research Unit, University of East Anglia, the United Kingdom*)

There are numerous GCMs developed by different national centres which range from atmospheric (AGCMs) or oceanic (OGCMs) to coupled atmosphere-ocean general circulation models (AOGCMs) (IPCC, 2007). The AGCMs and OGCMs only simulate either atmospheric or oceanic movements, while the most recently developed AOGCM can incorporate atmosphere to ocean interactions with other additional components (such as a sea ice model or a model for evapotranspiration over land) (Randall, 2007). At present, the AOGCM is considered as a full climate model being most effective for studies dealing with climate change impacts (Hamish, 2012).

However, there is a variation in the model structures and each AOGCM has its own features on the representation, the interaction and the parameterization of the processes. According to Randall (2007), the performance of each model is based on the numerical methods used to solve the model equations as well as the resolution at which the model is run. More importantly during parameterization, all properties of geophysical processes of global change are averaged over the large scale even though many physical processes occur at much smaller scales. This gives rise to the GCM uncertainties associated with the intermodel and intramodel variability (Chun, 2010; Dubrovsky, 2009; Im et al., 2010; Jeong et al., 2012; Wilby et al., 1999). Furthermore, AOGCM only focuses on natural systems, but do not include socio-economic systems and their interaction. This could cause uncertain future scenarios (Mujumdar and Ghosh, 2008).

### 2.3.2. Regional Climate Models (RCMs)

Even though GCMs are very powerful, they are only sufficient for studies dealing with global climate change over large-scale regions, global or continental scales (Mujumdar and Ghosh, 2008; Naoum and Tsanis, 2003; Willems and Vrac, 2011). The coarse spatial resolution constrains the model performance in simulating processes at individual or sub-grid cell, such as processes in the hydrological cycle (Wilby et al., 1999).

In order to give more detail on local climate system, a regional climate model (RCM) is developed from its driving GCMs. This RCM is considered as a comprehensive, consistent and physical interpolation at the local, sub-GCM grid scale (Rummukainen, 2010) which simulates local climate over an area of interest in a GCM (Giorgi, 1990).

Fundamentally, a RCM is based on the same physical-dynamic description of climate processes which are used in the GCM (Baguis et al., 2010; Ishak et al., 2010). A nesting modelling technique is used to simulate realistic large-scale atmospheric behaviour over a nested area which uses initial and lateral boundary conditions from the GCM output considering the effects of local forcings (Giorgi, 1990) with varying-time intervals to generate a higher resolution RCM (Christensen et al., 2001) (Figure 2.7). The driving forces consist of large-scale forcing from a GCM, and mesoscale forcing complex topographic features and surface characteristics that initiate the local climate. To date, this technique lacks a two-way interaction between RCM and the driving GCM (IPCC, 2007; Mearns et al., 2003). The domain size and resolution are the most important parameters driving the downscaling process (Castro, 2005; Denis et al., 2002; Xu, 2007) which requires a lot of computational time.

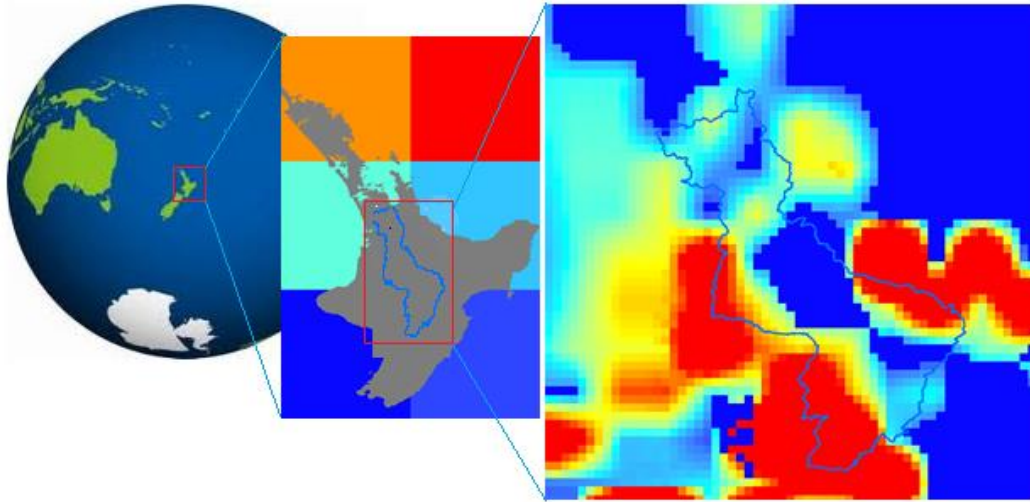


**Figure 2.7** A downsampling of GCM to RCM for the Waikato catchment

In comparison to GCMs, RCMs are much improved to provide the data at finer spatial resolution of 20 km, 10 km or less (Rummukainen, 2010), and higher temporal resolution of 6 hours or less (Drost et al., 2007; Misra et al., 2013; Randall et al., 2007).

More recently, RCMs have been updated by coupling with other climate process models, such as hydrology, ocean, sea-ice, chemistry and land-biosphere models (Bell et al., 2011; Xu and Yang, 2012). However, more advanced techniques employed into RCMs could also create more errors. The more complex the RCMs, the more amplified the error sources they create (Pielke, 2012). This would lead to the difficulty in applying the RCMs because the models themselves do not automatically provide reliable forecasts (Landsea and Knaff, 2010).

For the best use of RCM, statistical bias correction is needed in order to reduce some of the uncertainties as well as to increase the prediction accuracy (Yoon et al., 2012). In addition, the combination of RCM output with observed data sets could be useful for the validation of RCMs as well as for the reduction of explicit errors associated with the models (Mearns et al., 2003).

### 2.3.3. Statistical downscaling

GCMs and RCMs are valuable tools, however they are unable to give more detailed information required for extreme event analysis and risk assessment for a small region or catchment whose extent is less than a single grid cell of GCMs or RCMs (IPCC, 2007; Mujumdar and Ghosh, 2008; Naoum and Tsanis, 2003; Willems and Vrac, 2011). In this regard, downscaling technique is a solution which can fill the gap between the large-scale climate change and the local-scale response (Comnalicer et al., 2010; Coulibaly and Dibike, 2004; Prudhomme et al., 2002). The concept of spatial downscaling is presented in Figure 2.8.

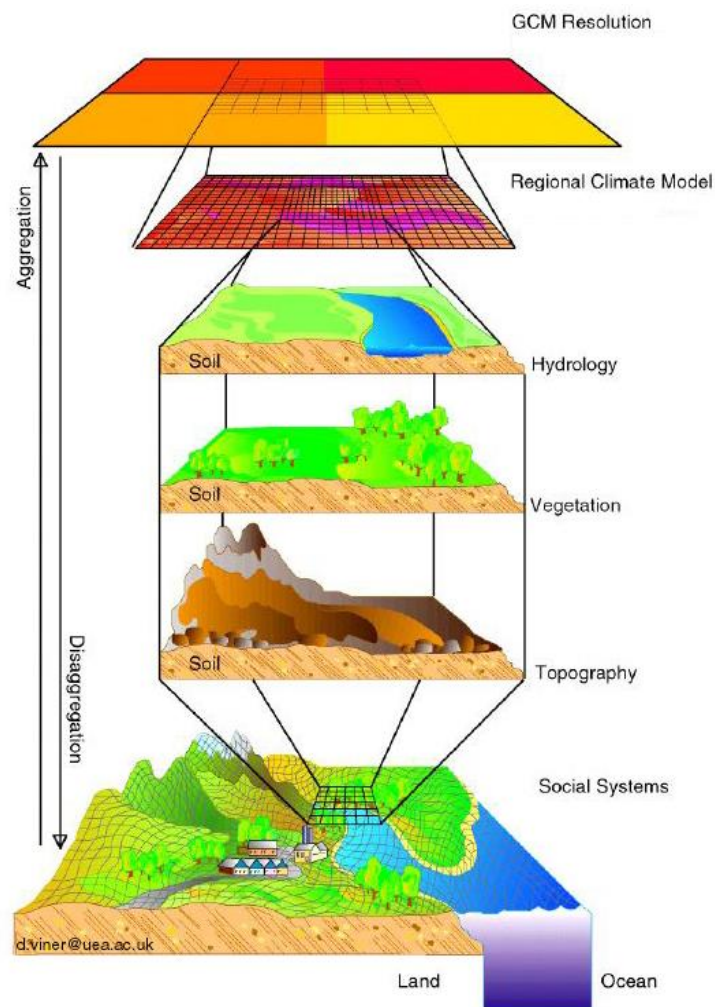


**Figure 2.8** Concept of spatial downscaling

(David Viner, Climatic Research Unit, University of East Anglia, the United Kingdom)

The downscaling technique includes dynamic and statistical downscaling. The former is used to generate RCM with higher spatial resolution as described in the previous section. The latter is used to obtain detailed information over smaller regions or even at a certain location (Chun, 2010; Ferrero et al., 2009; Hashmi, 2010; Li and Qi, 2010; Wilby et al., 1999; Willems and Vrac, 2011) and over non-uniform regions (Mearns et al., 2003).

The statistical downscaling is based on the development of robust direct statistical relationships between large-scale climatic variables (predictors) and the local ones (predictands) utilizing historic data (Timbal et al., 2008). The relationships are normally assumed to be time-invariant. This means that the developed statistical relationships found between predictors and predictands over past decades are assumed to be valid in the future. This assumption is the major uncertainty source because some of the controlling variables are not taken into account when climate changes (Chen et al., 2011; Ferrero et al., 2009; Khan et al., 2006). Likewise, other uncertainty sources in the statistical downscaling stem from the uncertainty in the GCM (Davani et al., 2012; Mujumdar and Ghosh, 2008; Sunyer et al., 2012; Wilby et al., 2004).

Despite its disadvantages, statistical downscaling is still considered as the benchmark due its effectiveness in climate prediction and model sensitivity. In essence, during the downscaling process biases are removed to prevent any uncertainties it may cause to the results (Pham et al., 2013; Wilby et al., 2002). In addition, statistical downscaling requires less computational effort, and offers opportunities for testing scenarios for many decades or even centuries (Charles et al., 1999; Chen et al., 2012; Mearns et al., 2003; Wang et al., 2012; Wilby, et al., 2004). Moreover, statistical downscaling allows users to employ various ensemble GCM results to improve the simulation accuracy (Pham et al., 2013b; Wilby, 1998, 2002).

## **2.4. Climate change impacts on hydrology and water resources**

### **2.4.1 Extreme precipitation and induced-flooding**

Rising sea level and increased frequency and intensity of extreme events namely, heavy rain and drought, are considered to be two major causes that threaten coastal development. Of these the variability of extreme precipitation is the most complex due to its prompt response to changing climate as well as its persistence which may cause disasters such as floods and water work collapse.

#### **2.4.1.1. Extreme precipitation**

In many studies dealing with the impacts of changing climate, extreme precipitation is considered a good indicator of climate change. Observed data over past decades has indicated that variability of extreme precipitation frequency and intensity is consistent with increasing temperature across the North Hemisphere (Francis and Hengeveld, 1998). Trends in temperature and atmospheric circulation have been demonstrably evident in relation to occurrence of extreme precipitation (Chiew et al., 2010). Furthermore, the typical intensity and frequency of extreme precipitation characterizes the local typical climate at certain locations (Furcolo et al., 1995; Mason, Waylen et al., 1999; Im et al., 2010; Lavers et al., 2010; Pal and Tabbaa, 2009). In addition, a change in extreme precipitation is very sensitive to small changes in climate (Mason et al., 1999).

Most land regions over the globe have experienced the increasing frequency of heavy precipitation over the late 20<sup>th</sup> century. This is even worse in the absence of an anthropogenic contribution (IPCC, 2008). The occurrence of heavy precipitation has occurred more frequently across Europe, North America, Asia, Pacific and Africa; however seasonal changes in heavy precipitation vary with location.

Significant increases in frequency in extreme precipitation are identified in the warm season in the USA and Canada without considering the anthropogenic forcing (Kunkel, 2003). In exception, both increase and decrease in intensity of extreme precipitation in winter is observed in different regions of these countries (Zhang et al., 2010).

In cool season, extreme precipitation becomes remarkable across the United Kingdom (UK) (Sanderson, 2010). The most significant changes are observed in autumn and spring (Fowler and Kilsby, 2003).

Significant increases in the intensity of extreme events are observed in most South African regions from 1931 to 1990. For example, the intensity of the 10-year high events has increased by over 10% (Mason et al., 1999).

Intense precipitation during summer monsoon cause serious and recurrent floods in India, Bangladesh, Nepal in recent decades, and is believed to become more frequent in the future as it contributed to the past (Sivakumar and Stefanski, 2011).

As reported in NIWA (2012), heavy rainfall was defined as rainfall greater than 100 mm in 24 hours which is one of the most frequent and widespread severe weather hazards to affect New Zealand, most destructively in North Island region. Flooding and landslides caused by heavy rainfall directly threaten human life, disrupt transport and communications, and cause damage to buildings and infrastructure.

#### **2.4.1.2. Extreme precipitation induced floods**

The dependence of flood risk on the frequency and magnitude of extreme precipitation has been illustrated in many studies. In many regions of the UK, a significant rising flood risk is a consequence of increased precipitation and storminess, more severe and frequent storm surges and rising sea level (Fowler and Kilsby, 2003; Kaya et al., 2006).

In Asian countries likely India, Bangladesh and Nepal, the changes in frequency and intensity of extreme events (i.e., heavy precipitation, storminess, snowmelt) and the occurrence of associated flash flood, ice flood, landslides have increased and tend to be more frequent in the future (Guhathakurta et al., 2011).

The North Island region of New Zealand is the worst affected by heavy rainfall induced floods. Since the most disastrous flood occurred in 2004 in the lower and middle North Island, heavy rainfall had reoccurred in May 2007 and January 2012 at higher intensity (NIWA, 2012).

Testing the dependence of a significant increase in flood risk on the increasing return period of precipitation in the Southern Quebec river basin in Canada, Roy et al. (2001) reported depending upon the soil moisture a 1.4 to 10-year flood event is observed corresponding to a 20-year rainfall event while the return period for the flood event ranges from 4.5 to 160 years for a 100-year precipitation event under current climatic conditions. The study presented an estimate of 13 to 400 years for the return period of the flood event corresponding to a 20-year (2080-2100) rainfall event and 400 to greater than 10,000 years for a 100-year rainfall event defined on the basis of future climatic conditions.

### **2.4.2 Evapotranspiration**

The general declining trend in evaporation is observed in many regions over the globe, such as Soviet Union, Venezuela, Australia, New Zealand, China, etc. over last 50 years (Roderick et al., 2005 and 2009; Stephen et al., 2009). However, evapotranspiration rate is believed to increase with increasing temperature.

The maximum 1, 3, 5, and 7 days evaporation will decrease in winter while increase in other three seasons consistent with the change in temperature. This occurs in many parts of the USA and Canada (Yang et al., 2012).

With increasing temperature and CO<sub>2</sub> concentration, the evapotranspiration rate increases by 3%–7% and by 15%–34% from the current climate across the UK. This is estimated for the presence and absence of vegetation effect, respectively (Bell et al., 2011).

The dependence of evaporation variation on different climatic variables is also addressed which also leads to conflicting results in evaporation.

In the arid regions of China, the statistically significant decrease in pan evaporation was identified as a result of decreasing wind speed and diurnal temperature as well as increasing precipitation (Roderick et al., 2009; Shen et al., 2010).

A study on decreasing evaporation trend in Europe and North America and their projections also show a strong dependence on the main dramatic and intra-annual drivers of radiation, precipitation deficit and runoff (Teuling et al., 2009).

For the South Florida case study, both increasing and decreasing trends in pan evaporation are found in many stations. Meanwhile, evapotranspiration is identified to increase which is consistent with increasing humidity and vapour pressure deficit. This study also highlighted that pan evaporation measurements are prone to too many sources of errors (Abtew et al., 2011).

In Norway for future scenarios, the highest increase in evaporation in spring and autumn, and the lowest increase or in some cases decreased evaporation during summer (Engen-Skaugen et al., 2005).

In New Zealand, a decrease in pan evaporation was observed in all selected regions (Roderick et al., 2005). However, future evapotranspiration projection is not fully investigated. There was only one study dealing with future change in lake evaporation in Canterbury.

### 2.4.3 Catchment water balance

The impacts of climate change on water resources have become more complicated affecting the water resources assessment and management at all levels. The global surface water is dependent on runoff that varies with change in precipitation and evaporation (Figure 2.9). Only 30% to 45% of precipitation turns to surface runoff while the rest is counted for evaporation (Gleick, 1993).

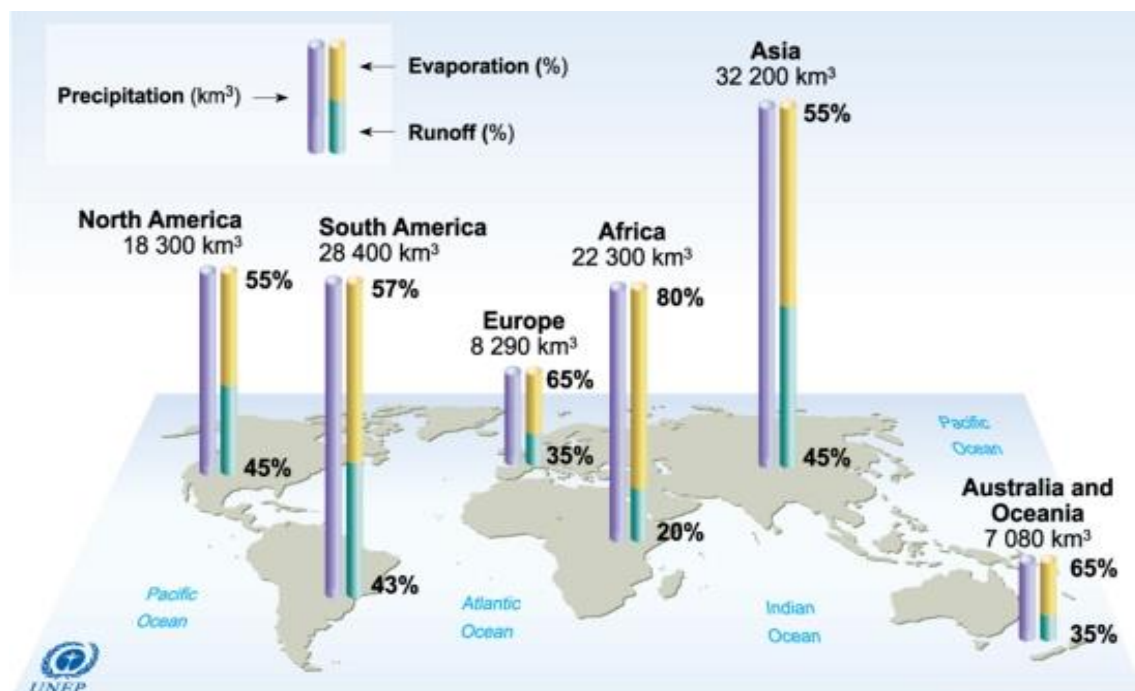


**Figure 2.9** The World's surface water (from Gleick, 1993)

According to the Nature Conservancy (2010), “*climate change is intensifying the circulation of water on, above and below the surface of the Earth, causing droughts and floods to be more frequent, severe and widespread*”. Changchun (2010) also highlighted that the direct impact of climate change on water resources is altering the volume and runoff over time and space.

A decrease in runoffs and runoff volume during dry season and an increase in runoff and runoff volume are identified in different regions. Seasonally spatial variation in runoffs

with locations demonstrated in current studies is strongly dependent on temperature and precipitation and snowmelt.

A seasonal change in the discharge regime in the Rhine basin of Germany is recognised as the consequence of a shift from a combined rainfall-snowmelt regime to a more rainfall dominated regime. The frequency and magnitude of peak flows could increase during winter, while low flow could occur more frequently and last longer (Middelkoop et al., 2001).

In Norway, mean annual and seasonal streamflow are projected for the 2030-49 period from the 1980-99 basis. The changes are especially large in winter and summer (i.e., increase in winter and decrease in summer). The mean annual streamflow increases by 12.8% and 0.386% for year 2030 and 2049, respectively. The summer streamflow will decrease and the winter runoff will increase everywhere (Engen-Skaugen et al., 2005).

Runoffs in semi-dry regions of China are very small or even zero during dry season being very sensitive to increasing temperature and decreasing rainfall. In humid regions, runoffs are perennial and the baseflow occupies a large portion of the total runoff volume which is more sensitive to precipitation change than increasing temperature (Guo et al., 2002).

The Komati basin shared by Swaziland and South Africa faces water scarcity during the period of 2011-2030 because a reduction in water availability of about 10% is projected with a temperature increase of 2°C (Jusoh, 2007). However, many African countries after 2050 would experience a change in streamflow from a decrease of 15% to an increase of 5% above the 1961–1990 period. More notably, for 2100, the change would move from a decrease of 19% to an increase of 14% (Strzepek and McCluskey, 2007).

In New Zealand, a general increase of inflows consistent with increasing precipitation and temperature during past decades. In addition, operational risk is also involved in the change of water resources system (Mpelasoka, 2000).

## **2.5. Regional hydrologic and water resources impact assessment of climate change**

The adequacy of quantification of climate change impacts on water resources depends on the ability to predict the changes in precipitation and potential evapotranspiration (IIASA, 1994). For this reason, the common methods and techniques used to estimate these two key components are explained in considerable detail in the following sub-sections.

### **2.5.1. Frequency and regionalization of daily precipitation**

Frequency analysis is widely used in hydrology to establish a relationship between extreme values and return periods (Meng et al., 2007). There are two main models which can be used for frequency analysis. These models are the Annual Maximum Series (AMS) and the Partial Duration Series (PDS).

#### **2.5.1.1. Annual maximum series (AMS)**

In the AMS model, the maximum values occurring in each water year are used in the analysis. In this way, one extreme event is used to represent each water year (Figure 2.10). This model is commonly used as a conventional tool in hydrology (Adamowski, 2009; Clause and Pearsonb, 1995; Cunnance, 1973; Gottschalk and Krasovskaia, 2002; Jenkinson, 1955; Pearson and Henderson, 1998). However, the model also exhibits some disadvantages.

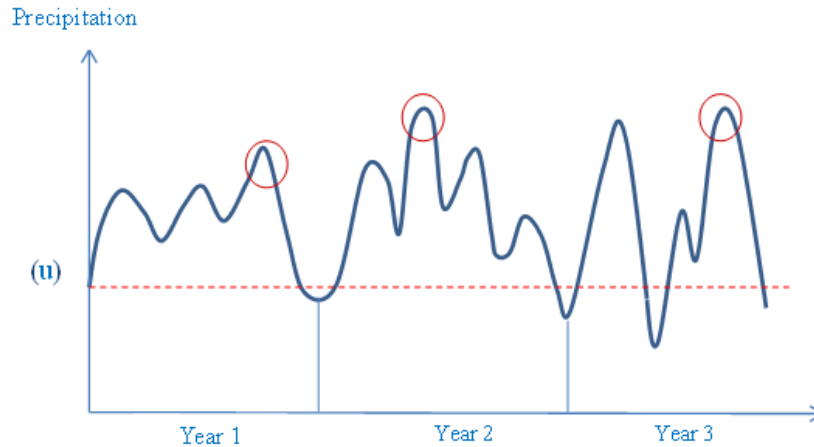


**Figure 2.10** Definition of AMS of precipitation (marked in red)

The AMS requires too much data and for long periods. All its extreme events estimated for return period  $T$  from AMS have high variability. Event estimates from the AMS are least efficient for small  $T$ , but better performance for  $T$  is equal to 1000 years (Madsen et al., 1997).

The AMS also expresses some constraints when it is used in regional frequency of precipitation because it is very difficult to define a parent distribution for a homogeneous region. Different distributions of daily precipitation were defined for each group of stations. The results show that the L-Moment (L-MOM) ratio diagram, which is used to determine the distribution parameters, for the AMS data is scattered (Madsen et al., 1997).

The generalized extreme value (GEV) distribution is fitted to winter season daily maximum precipitation over North America (Zhang et al., 2010).

A study in Korea reveals that extreme daily precipitation of the AMS is best estimated using a Kappa distribution, especially in the context of climate change as well as hydrologic response to climate change (Park and Jung, 2002).

A Gumbel distribution is recommended for the AMS to study the variability of extreme precipitation under changing climate in Germany for different future scenarios (Friederichs, 2010). However in the UK, the Gumbel distribution should be considered as a special case for the AMS because the Gumbel approximation overestimates and underestimates for temperature and rainfall, respectively (Jenkinson, 1955).

Currently, the Generalised Extreme Value distribution of annual maximum events from GCM outputs (downscaled GEV/AMS model) is commonly used for frequency analysis of extreme precipitations (Fowler et al., 2010; García-Cueto and Santillán-Soto, 2012; Huntingford et al., 2003; Park and Jung, 2002; Yang et al., 2010). However, the GEV/AMS model is envisaged to have potential uncertainty for future projections in estimation of extreme events (Furcolo et al., 1995; Lambert et al., 1994), especially for dramatically changing climate (Cavazos, 1998) because these extreme events cannot explicitly describe the physical processes which affect climate (Li and Qi, 2010).

### **2.5.1.2. Partial Duration Series (PDS)**

PDS model considers all the extreme values above a certain threshold value ( $u$ ) in which more than one extreme event per year can be used in the frequency analysis. For example, the PDS contains on average three extreme events in each year (Fig. 2.10). Therefore, it can consider more extreme events in which the highest peaks in any year can be neglected if their magnitudes are less than peaks occurring in other years (Norbiato et al., 2007). Moreover, the PDS model provides more reliable estimates than the AMS model for low return period ( $T$ ) events (i.e.  $T < 10$  years) (Hosking and Wallis, 1997) and also for high return period events (i.e.  $T = 100$  years) (Zvi, 2009). Madsen et al. (1997) conducted a comprehensive comparison between the performance of AMS and PDS. They found that the PDS can provide the most efficient quantile estimates for practical purposes.

Despite the above advantages, the PDS model is still underused relative to the AMS model due to its complexity (Cunnane, 1973; Claps and Laio, 2003; Begueria, 2005; Adamowski, 2009). Basically, the PDS model assumes that the arrival of mutually independent peaks is governed by the Poisson distribution with the resulting frequency distribution of exceedances of peaks above the threshold given by the Generalized Pareto distribution (GP) (Begueria, 2005; Trefry et al., 2005; Yuguo et al., 2008). The exponential distribution which is a special limiting case of the GP distribution has also been used in modelling the exceedance of peaks above the threshold (Ashkar and Rousselle, 1983; Bobee et al., 1993). Satisfaction of the above noted assumptions can be obtained by selecting an optimal threshold value (Madsen et al., 1993). However, the performance of GP/PDS is very sensitive to even a small change in the threshold values leading directly to a quantile estimation uncertainty (Takeuchi, 1984). Therefore, an important feature of GP/PDS is the stability of the threshold value with the shape parameter of the GP remains unchanged or exhibiting only minor changes which can lead to a reduction in uncertainties when using the PDS model.

To date, there is no universal agreement on the selection of the threshold value. One method of dealing with this issue is to set the threshold value equal to the smallest annual peak; and the other method uses the average number of peaks per year ( $\lambda$ ). In principle,  $\lambda$  value can be an integer or a real number. Compared to the first method, the second method is a better option because it can provide unbiased quantile estimates (Buishand, 1989). An early study by Cunnane (1973) suggested that the minimum value of  $\lambda$  should be 1.6 per year and  $\lambda = 2$  is sufficient for flood quantiles estimation, without considering the combined effects of model and sampling errors. According to Hosking and Wallis (1987), increasing the value of  $\lambda$  in the PDS model could improve its performance such as  $\lambda = 5$  for geo-morpho-climatic modelling and  $\lambda = 10$  for wind velocity modelling. Claps (2003)

suggested that the  $\lambda$  value should be chosen between 3 and 15 for homogenous Italian regions. Rosbjerg and Madsen (2004) choose the  $\lambda$  value between 2 and 3 when conducting a precipitation frequency analysis in Denmark using a Bayesian framework for incorporation of imprecise historical data. Begueria (2005) used the method of ordinary moments to estimate the quantile values which is a function of the threshold value. It was concluded that there is no unique optimum threshold value because it is very difficult to consider both changes in the shape and scale parameters of the GP distribution with the changes in the threshold value.

In New Zealand, performance of PDS was compared to AMS for estimating extreme flood at 20 sites in South Island. The results reveals that the PDS ( $\lambda= 2$  and 5) are best for the region which provide fuller picture of the flood hydrograph of the region. In contrast, AMS is only efficient for smaller homogenous sub-regions. In addition, the PDS better capture the underlying structure and processes of flood time series. Moreover, they do not censor much data as the AMS does (Madsen et al., 1997).

Even though the PDS model is more flexible in quantifying extreme events, it is often associated with statistical complexity. Furthermore, there is no universal guideline on modelling of the PDS which results in difficulties when choosing the appropriate distribution coupled with the selection of threshold value. These two elements are very important in satisfying the PDS model assumption as well as in ensuring reliable quantile estimates.

It is envisaged that the novel application of GP/PDS model could give the best prediction of extreme events, however, its performance has not been examined in the context of climate change, particularly when the GP/PDS is coupled with downscaled climatic variables from the GCMs and the RCMs.

### **2.5.1.3. Regional frequency of precipitation**

Through most studied works, the spatial and temporal distribution of extreme precipitation events does not present a consistent trend for a region as a whole. In reality, extreme precipitations vary unevenly over time and space that is very difficult to investigate their patterns, tendency (frequency, magnitude) and persistence. Especially, the extreme event has become more anomalous under different climate changes over last few decades. The most reliable method is recommended to be regional frequency analysis (RFA) as shown in many publications, as it provides a framework for hazard characterization of these extremes (Fowler and Hennessy, 1995; Fowler and Kilsby, 2003; Norbiato et al., 2007).

Basically, the RFA incorporates observed data from nearby or similar sites to derive estimates for any given site in a homogeneous region (Norbiato et al., 2007; Trefry et al., 2005). Frequency analysis is widely used to establish a relationship between extreme values with different given return periods (Pearson and Henderson, 1998; Meng et al., 2007). The future extreme events corresponding to different return periods are predicted by employing the same frequency distribution function that describes extreme precipitations from observation. In practice, it is important to ensure that the estimated extreme precipitations are valid for a whole region rather than only at a single site. For this reason, an effective regional frequency with unbiased distribution parameter estimators needs to be defined for homogenous regions. This is effective not only for estimating accurately the rare occurrence of precipitation extremes (Lettenmaier et al., 1987; Hosking and Wallis, 1988; Potter and Lettenmaier, 1990; Hosking and Wallis, 1997), but also for reducing the uncertainty associated with parameter estimation at gauged sites and for risk assessment at un-gauged sites (Furcolo et al., 1995), and for maximizing the utilization of available data achieved (Mohssen, 2009). Thus, it is important to achieve an appropriate balance between the spatial density of observation and length of the series which should

have a rather homogeneous distribution across the study area. In order to conduct a reliable regionalization procedure, it is very important to involve as many highest events (peaks) as possible into stages of reconstruction, gap filling, quality control and homogenization within a homogenous area (Moreno et al., 2010).

### **2.5.2. FAO-56 method coupled with GCM/RCM data**

The use of potential evapotranspiration (PET) has become more preferable over the use of conventional pan evaporation (Nichols et al., 2004), especially when it is used to detect climate trend (Hobbins and Rami'rez, 2004). This may be due to the fact that the pan evaporation is directly used to measure evaporative water at a certain location which does not fully incorporate numerous possible physical effects of temperature and wind speed on evaporation process (Naoum and Tsanis, 2003; Szilagyi and Jozsa, 2008). In addition, measurement errors, systematically changing errors and instrument errors may result in an inaccurate estimation of evaporation rate in many regions (Gifford, 2004).

PET is widely used in practice to indirectly estimate the actual evaporation rates. Methods used to estimate PET range from empirical to physically-based (Chun et al, 2010; Douglas et al., 2009; IIASA, 1994; Palutikof et al., 1994; Penman, 1947; Thornthwaite, 1948). The former only considers the effects of air temperature  $T$ , on evapotranspiration, while the latter also takes into account the influence of additional climatic variables, such as relative humidity (RH), radiation ( $R_s$ ) and wind speed ( $U_s$ ). The combined Penman-Monteith method developed by the Food and Agriculture Organization (FAO) which is known as FAO-56 method is considered to be the most reliable method for estimating evapotranspiration (IIASA, 1994; Zotarelli et al., 2010). The concept of FAO-56 method for estimating PET is shown in Figure 2.11. This physically-based method involves different climatic variables as well as controlling factors (Brazel et al, 1993; Gifford, 2004;

Meszaros and Miklanek, 2006; Roderick et al., 2009; Teuling et al., 2009). However, this method requires a wide range of input data over long periods when in fact not all of these data are obtainable from observations (Kay and Davies, 2008; Naoum and Tsanis, 2003). This is the main uncertainty source in the estimation of evapotranspiration using the FAO-56 method (Chen, 2011; Chun, 2010; Espadafor et al., 2011).

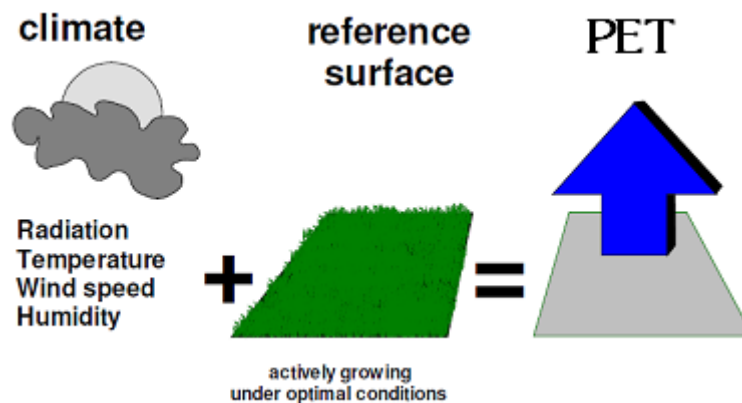


**Figure 2.11** The concept of PET estimation using FAO-56 method (*modified from Zotarelli et al., 2010*)

In the context of climate change, the use of FAO-56 method coupled with GCM/RCM data is preferred but still restricted in application. Only few studies dealing with evapotranspiration estimation use Penman and/or Monteith methods with GCMs/RCMs.

Baguis et al. (2010) employed RCM data at 25 km and 50 km resolutions, and two separate Penman and Monteith methods were used to estimate PET for the central Belgium region. They concluded that uncertainty sources may consist of spatial coarse resolutions, climatic variable selections and climate scenarios.

Another study in China by Chu and Singh (2010) applied a statistical downscaling model (SDSM) to directly downscale evaporation to station locations from GCMs. However, the modelled results were unrealistic because short observed records were used for model

calibration and validation. Moreover, inadequacy of climate predictors' selection (i.e.,  $T_{\max}$ ,  $T_{\min}$ , airflow, vorticity and horizontal wind, sea surface mean pressure, etc.) is another uncertainty source affecting the accuracy of model simulations. These problems also noted in another study in which a numerical weather model version 5 (MM5) model was used for computing PET (Ishak et al., 2010).

The MM5 was also applied by Silva et al. (2010) for a case study in Chile. The study reveals the importance of large lengthy data input and fine spatial resolutions reliable estimation of PET.

A recent study in the United State also demonstrates that estimation of PET by both probabilistic and deterministic models would give better results if finer spatial resolutions and longer observed data were used (Tian et al., 2012).

Obeysekera (2013) used data sets from different RCMs at 50 km resolution to simulate PET using the Penman-Monteith equation for the Florida region. This later study addressed that the PET simulation biases associate with errors in RCMs structure themselves as well as errors in measurements used for model validation. However, the study was unable to suggest which RCM is the best for PET simulation.

In general, the accuracy of PET estimation in the context of climate change studies is dependent on both the methods and the GCMs/RCMs used (Milly and Dunne, 2011). Different methods and GCMs/RCMs could have different uncertainties/errors depending on their own features (Brazel et al., 1993; Kay and Davies, 2008), causing inadequate estimation of spatial and temporal evapotranspiration variability (Andersen, 2008). Those studies also indicate that GCM/RCMs perform differently for different regions.

There is no study on future projections on land evapotranspiration in New Zealand. There is only one study dealing with climate change impact on lake evaporation using GCM data

(NIWA, 2010). Lake Ellesmere (Te Waihora) in Canterbury was selected in which temperature plays an important role in lake process. Future lake evaporation was projected using Penman method which would increase by 110-374 mm/year depending on different selected GCM scenarios. The mean annual PET was predicted to be less than rainfall with their difference of 16-60% that is important because they will have a major influence on the lake water balance.

### **2.5.3. Water balance model**

Water balance models are commonly used for water resources assessment and management. This type of model acts as a valuable tool for assessing the hydrologic characteristics of diverse watersheds and effective evaluation of the hydrologic consequences of climatic change (Xu and Singh, 1998). They could also serve the purpose of quantifying climate change impacts on streamflow from precipitation, temperature, evapotranspiration and soil moisture (Archer et al., 2010; Comnalicer et al., 2010; Esqueda et al., 2011; Ha, 2009; Kim and Kaluarachchi, 2009; Marks et al., 1993; Obeysekera et al., 2011; Vaitiekuniene, 2005).

In the context of climate change, change in precipitation directly and remarkably impacts on water resources (Archer et al., 2010; Esqueda et al., 2011; Kim and Kaluarachchi, 2009; Pike et al., 2010). Water resources can also be impacted by changes in soil, vegetation and evapotranspiration (Iturbe et al., 1999; Marks et al., 1993; Pike et al., 2010; Yates, 1994). However, current water balance modelling is mainly dependent on precipitation while evapotranspiration is fixed as a proportion of precipitation (Zhang et al., 2008). Furthermore, these models do not fully take into account the interaction of the various phases of rainfall- runoff transformation within the soil, causing inaccuracy of modelled water balance components of a catchment (Andrew and Dymond, 2007; Jiang et al., 2007;

Marks et al., 1993). Moreover, at the catchment scale water balance modelling under different climate change scenarios is not fully studied (Ha, 2009; Marks et al., 1993; Mauser and Bach, 2009).

There are numerous methods to model the water balance of a catchment with regard to variation in time scale as well as the degree of model structure complexity. Being categorized by the model structure, the most common used models are conceptual lumped and distributed models. The distributed models partition precipitation into evapotranspiration and runoff, including the mutual corporation of hydrological and atmospheric models (Mauser and Bach, 2009). This type of model requires a wide range of data, such as land cover, soil types, digital elevation model (DEM), climate data, etc., but enables to model runoff over large areas (Andrew and Dymond, 2007), hence a lot of time and effort are required. The most important input data are considered to be precipitation and evaporation (Xu and Singh, 1998; Moreda, 1999). However, the spatially lumped models likely NAM model, are able to represent the land phase of the hydrological cycle including soil moisture and ground water recharge from rainfall, evapotranspiration for smaller areas, and simulated runoffs from overland flow, interflow and base flow (Brauer, 2007; Jiang et al., 2007; Vaitiekuniene, 2005). Therefore, these models can link the soil matrix with atmosphere which importantly contributes to the hydrological system. At present, this type of model is sufficient for rainfall-runoff simulation in combination with other routing models (Madsen et al., 2002). These advantages still remain when climate change impacts take place (Ha, 2009).

Water balance models can also be categorized as daily, monthly and annual models. They may have different requirement on input data, but give similar outputs (Brauer, 2007; Mauser and Bach, 2009; White et al., 2011). The annual water balance model is not suitable in the context of climate change because this type of model only simulates annual

streamflow volumes while it is essential to speculate the prompt hydrological response of climatic change (Moreda, 1999). In practice, monthly water balance models are commonly used because the main purposes are planning water resources and predicting the effects of climate change with their long-term variability. Additionally, monthly hydro-meteorological data are most readily available (Xu and Singh, 1998). These monthly models are particularly valuable for application where monthly, seasonal and annual stream flow volumes are primary interests. In preference, daily water balance models typically emphasise the dynamic aspects of hydrological processes (Wang et al., 2011). Therefore, this reliably assess the impacts of climate change on the catchment water balance, especially for models with five or more parameters (Yates, 1994).

### **2.5.3.1. Future projections of catchment water balance**

To date, there are several studies dealing with the modelling of water balance under changing climate using the outputs of Global Circulation Models (GCMs) and Regional Climate Models (RCMs). A study in the United State used GCM data as input into the regional distributed hydrological model to simulate precipitation and potential evapotranspiration which likely have large effects on water balance. This is carried out for 1xCO<sub>2</sub> and 2xCO<sub>2</sub> scenarios. Inadequacy of this monthly gridded water balance model performance is caused by topographical effect on precipitation, the lack of snow component and the effect of vegetation/water balance interaction (Marks et al., 1993).

Kim and Kaluarachchi (2009) used a two-layer water balance model to simulate runoff of the Upper Blue Nile river basin from temperature and precipitation generated from six GCMs. In this study, the correlation among stations and between temperature and

precipitation were assumed to be constant with time. This is one of the major limitations of the study.

A study in Philippines by Comnalicer et al. (2010) used statistically downscaled output data to input into monthly conceptual hydrological model, BROOK90, to simulate different water balance components of a forest watershed. Even though the results indicate a large amount of rainwater transferred to evaporation, the catchment water was modelled from a change in rainfall rather than in evaporation.

One study in Germany by Brauer (2007) also investigated the effects on different catchment water balance components using Wagenigen and NAM models of which the later outperforms the former with regard to summer discharge, peak discharge and snow simulation. This was examined using observed data from 1971 to 2006.

Another study in Lithuanian assumed that rainfall-runoff model is less sensitive to evaporation, but sensitive to rainfall (Vaitiekuniene, 2005). This is one of the most major uncertainty sources of the model simulations based on observation over period 1993-2000.

Even though the daily lumped models are suited to assess climate change impact as well as predict stream flow, the data input requirement is a major disadvantage of these models. Data on precipitation, evapotranspiration and soil over the long period is necessary but usually insufficient for both model calibration and prediction stages.

In New Zealand, future rainfall-to-river flow modelling is projected using temperature scenarios embedded in GCMs. This means that any change in temperature directly affect the rainfall and its resulting runoff. However, this cause-and-effect relation does not fully represent the actual variation of rainfall and runoff. In particular, the frequency of the extreme storm events does not change with time resulting in an underestimation of extreme runoff events. Moreover, main changes due to the change in temperature are not

considered. They are changes in natural vegetation mechanism, land uses as well as increasing evapotranspiration and freezing levels (NIWA, 2005).

Fowler et al. (2008) investigated the impacts of future natural climate change on the soil water regime for Hawke's Bay, a pastoral area in New Zealand. Precipitation and evapotranspiration data were used to drive a daily water balance model (DWBM) of near surface hydrology to compute pasture productivity. Even though they highlighted the importance of rainfall and evapotranspiration, however the incorporation of these variables in the modelling system is still limited.

Chiew et al. (1994 and 2002) predicted the change in future runoffs under climate change scenarios in 5 GCMS. They proved that changes in rainfall are always amplified in runoff with amplification factor for runoff being higher in drier catchments. The change in rainfall has little effect on the soil moisture in wet catchments but in drier catchments, percentage change in soil moisture levels can be greater than the percentage change in rainfall. Compared to precipitation, temperature increases alone have negligible impacts on the runoff and soil moisture. As a result, annual runoff would increase up to 25% by the year 2030 in the wet tropical catchments. The GCMs do not agree in the direction of rainfall change in south-east Australia resulting changes in runoff up to  $\pm 20\%$  by 2030. Near the western coast of Australia, the simulations show runoff change of up to  $\pm 50\%$ .

Chiew et al. (2009) projected catchment runoff from changing rainfall using 23 GCMs used in IPCC 2AR over southeast Australia. The results indicated that most of GCMs can reproduce the observed spatial mean annual rainfall pattern, but the errors in the mean seasonal and annual rainfall amount can be significant. The future mean annual rainfall projections averaged across the region range from -10% to +3% change per degree global warming, which is amplified as -23% to +4% change in the future mean annual runoff. The

study also concluded that using only the better GCMs or weights to favour the better GCMs give similar runoff impact assessment results as the use of all 23 GCMs.

## **2.6. Summary**

In this chapter, information about observed and projected global climate change and New Zealand climate change were provided. In addition, findings from single studies on regional response of changing climate on precipitation, evapotranspiration and runoff were also presented. The description and implication of GCMs, RCM and statistical downscaling were introduced. Likewise, the methods for estimating potential evapotranspiration and modelling streamflow were described. This information will be used in Chapters 4 to 9 of this thesis.

## CHAPTER 3

# Study sites and data

This chapter gives a brief description of the study region and its data. Different sub-catchments are highlighted because this research aims to test the hypotheses with different catchment characteristics which may reflect the remarks on the findings. The first section presents information on the study region and its sub-catchments. The next section describes the main characteristics of the selected catchments. Data types and sources are explained in the following sections. The chapter summary is presented in the final section, emphasizing the differentiation of data usage for certain sub-catchments.

## 3.1. Study region

### 3.1.1. North Island of New Zealand

The preliminary study region of this study is the North Island of New Zealand. The total area of the North Island is 117,713 km<sup>2</sup> making it the world's 14<sup>th</sup> largest island. It had a population of 3,422,000 by June 2013, accounting for approximately 77% of New Zealand's population. The geographic location of the North Island is between 35<sup>0</sup>S and 42<sup>0</sup>S in latitude and 172<sup>0</sup>E, 179<sup>0</sup>E in longitude and covers the areas of nine administrative regions, namely Northland, Auckland, Waikato, Bay of Plenty, Gisborne, Hawke's Bay, Taranaki, Manawatu-Wanganui and Wellington (Figure 3.1).

The climate of the North Island is characterized as warm subtropical. Climate in the region is dominated by westerly winds and dramatically driven by topographic effects. However, the region can further be divided into different climate zones such as Northern New Zealand (Northland, Auckland), Central North Island, South-West North Island and Eastern North Island.

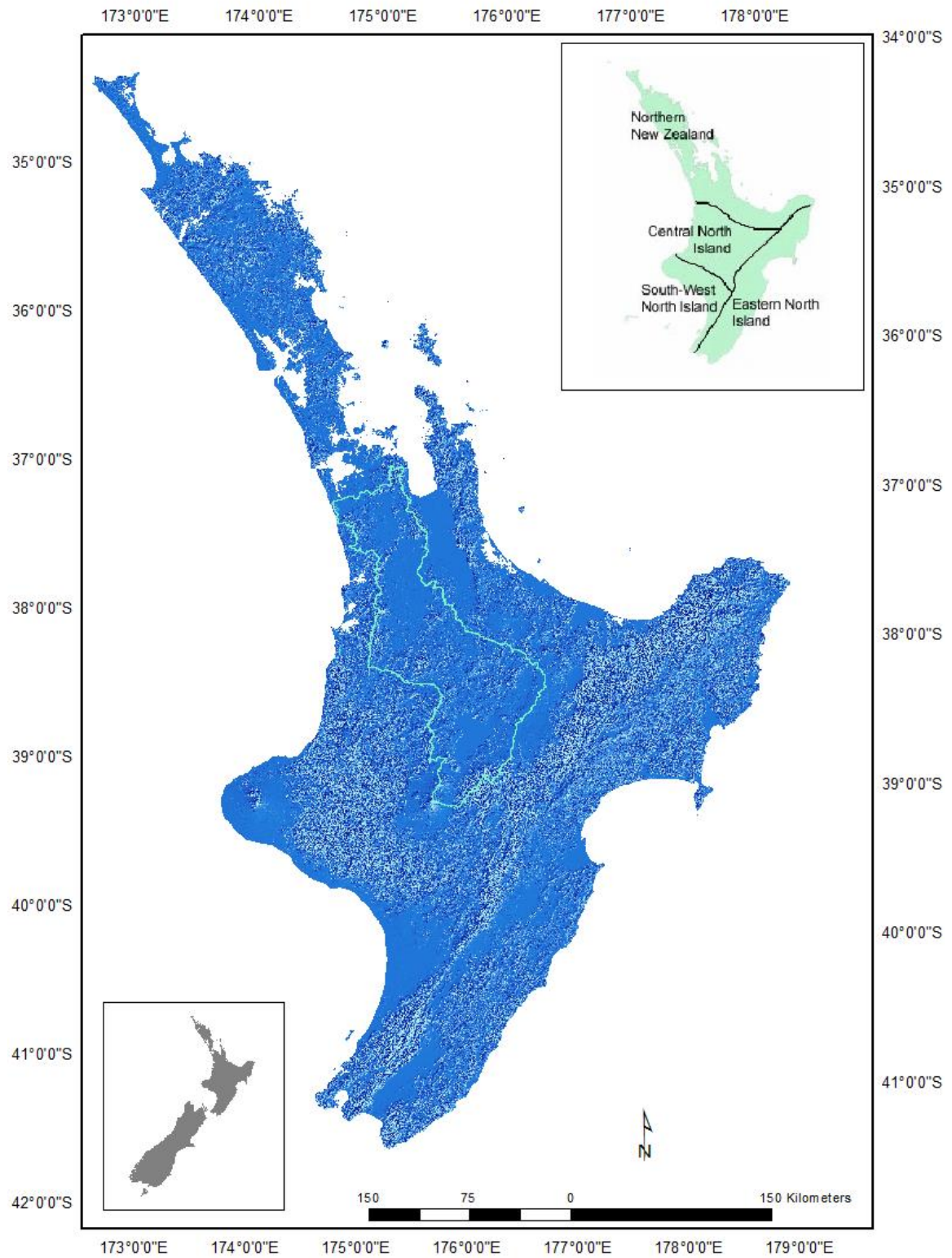


**Figure 3.1** Maps of North Island region and its Waikato catchment

Most areas of New Zealand have between 600 mm and 1600 mm of annual precipitation spread throughout the year with a dry period during the summer. Over the North Island areas, more precipitation falls in winter than in summer. Mean annual temperatures range from 10°C in the south to 16°C in the north of New Zealand. The coldest month is usually July and the warmest month is usually January or February. Temperatures also drop about 0.7°C for every 100 m of altitude. Being consistent with temperature variation, more evaporation is recorded in summer and less evaporative water occurs in winter. Average daily evaporation varies between 0.3 mm/day to 5.1 mm/day for winter and summer days, respectively (Sturman, 2001; NIWA, 2005). The information on spatial variability of mean annual precipitation and potential evaporation along with mean annual temperature over New Zealand is presented in Figures 3.2 -3.4.

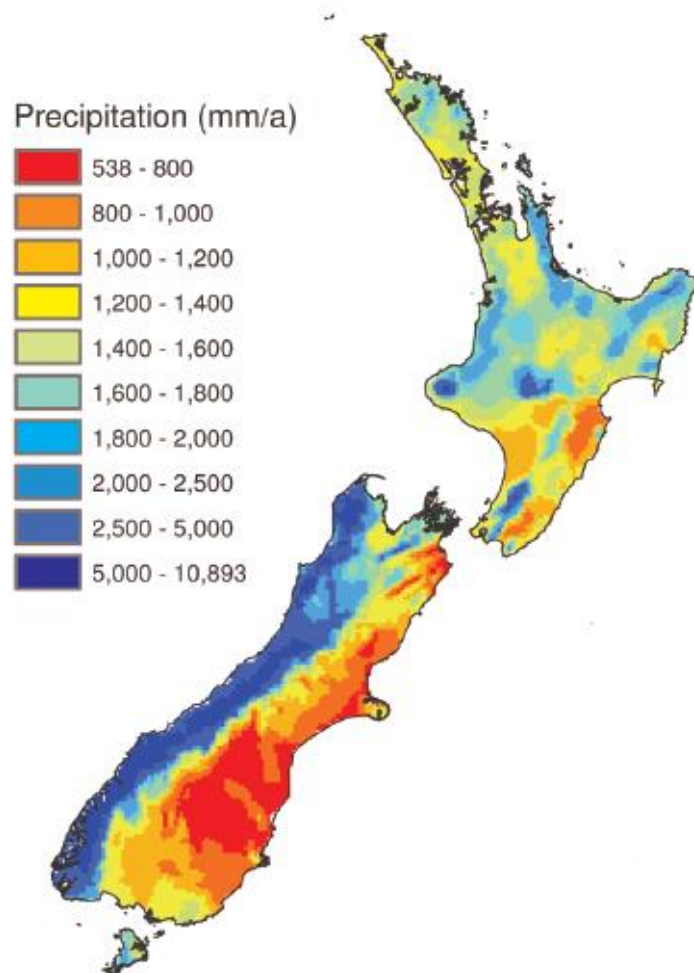


**Figure 3.2** Long-term mean annual precipitation over New Zealand during the 1961-2001 period (from Woods *et al.*, 2006)

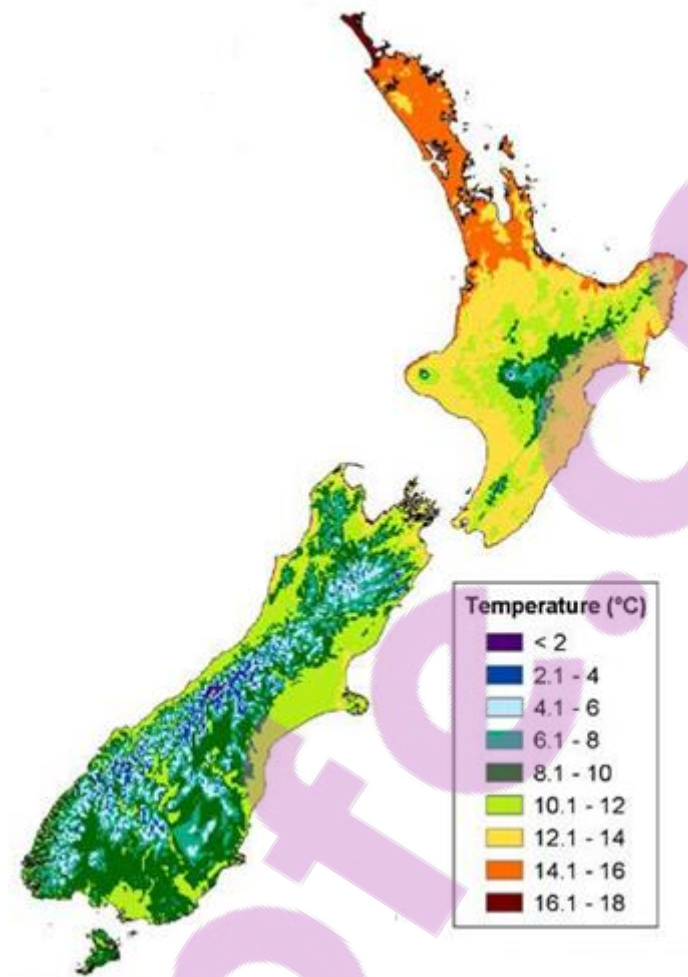


**Figure 3.3** Long-term mean annual temperature over New Zealand during the 1971-2000 period (from NIWA, 2003)

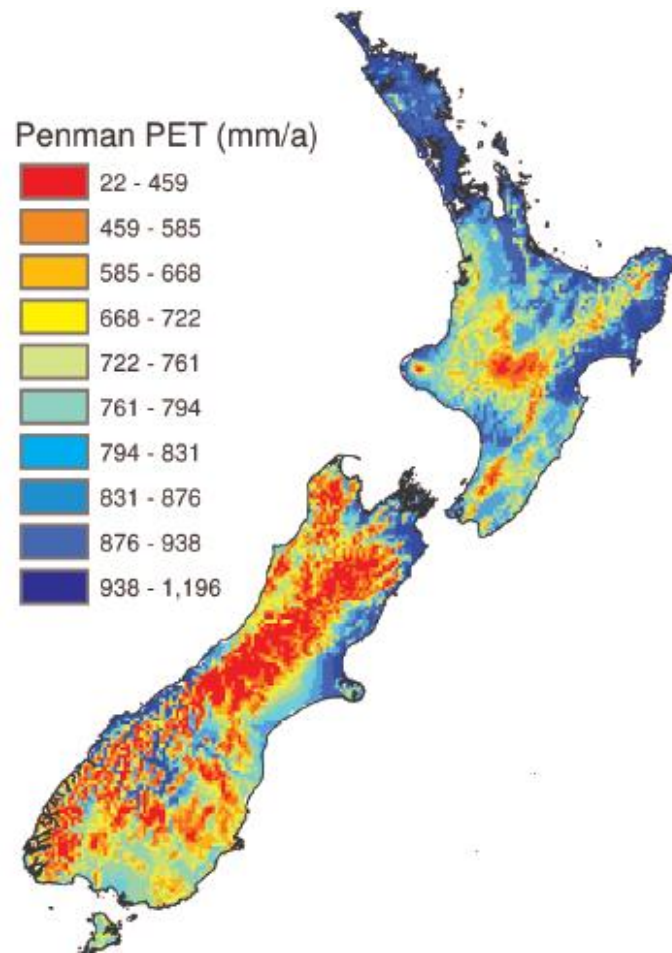


**Figure 3.4** Long-term mean annual Penman potential evapotranspiration over New Zealand during the 1961-2001 period (*from Woods et al., 2006*)

### 3.1.2. Waikato catchment

Waikato catchment is the largest catchment in the North Island of New Zealand. The total area of Waikato catchment is about 14,500 km<sup>2</sup> making up about 12% of the North Island (Figure 3.5). The Waikato River is the longest river in New Zealand with a total length of 425 km. The river originates from Mount Ruapehu, the largest active volcano in New Zealand, at 2,797 m above sea level and drains into Lake Taupo, the largest lake in New Zealand with a surface area of 616 km<sup>2</sup>. The Waikato River flows through the North Island passing eight dams and nine hydroelectric powerhouses northward into the Tasman Sea at Port Waikato from Lake Taupo.

Mean annual precipitation varies between 1,100 mm to 2,000 mm per year in the lower and upper catchment, respectively. Mean annual evapotranspiration is approximately 650 mm per year accounting about half the annual precipitation (Waikato Regional Council, 2008). Evaporation and transpiration are mainly from pasture and forest (Sturman, 2001).

The annual sunshine total ranges between 1,800 hours and 2,100 hours, wind speed is from 2 m/s to 10 m/s depending on the change in topography (Figures 3.6-3.7).

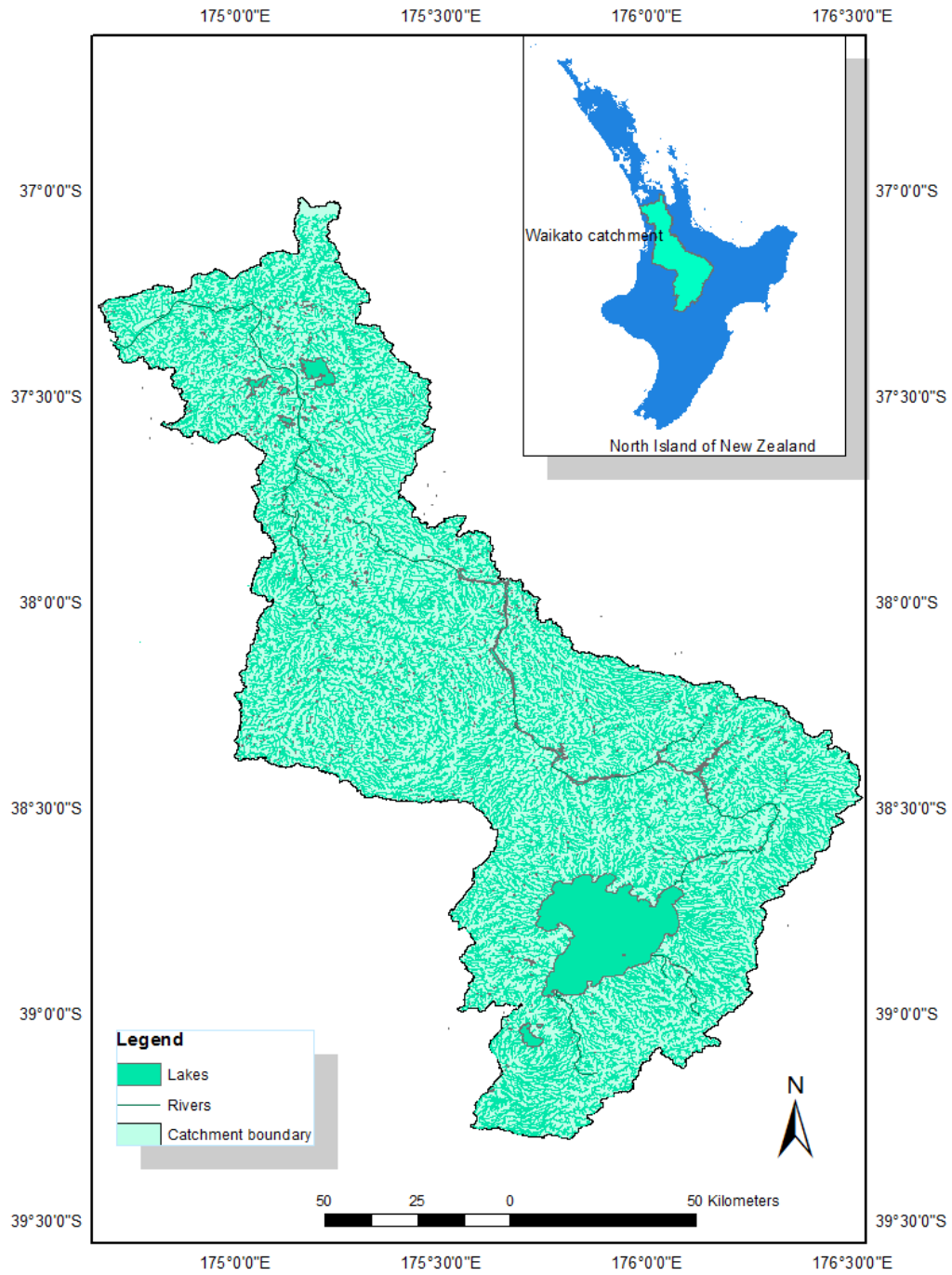


**Figure 3.5** Waikato catchment and its river network

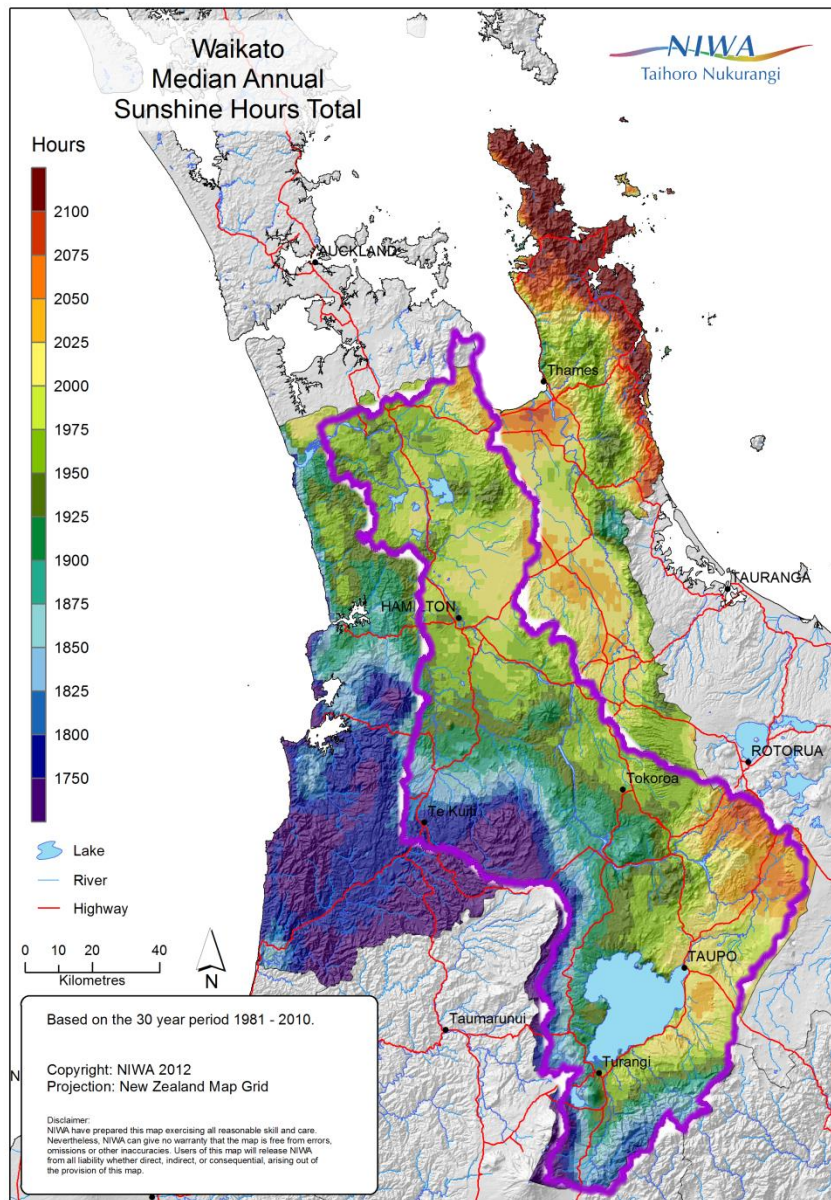


**Figure 3.6** Waikato median annual sunshine hours total based on the 30 year period from 1981 to 2010 (NIWA, 2012)

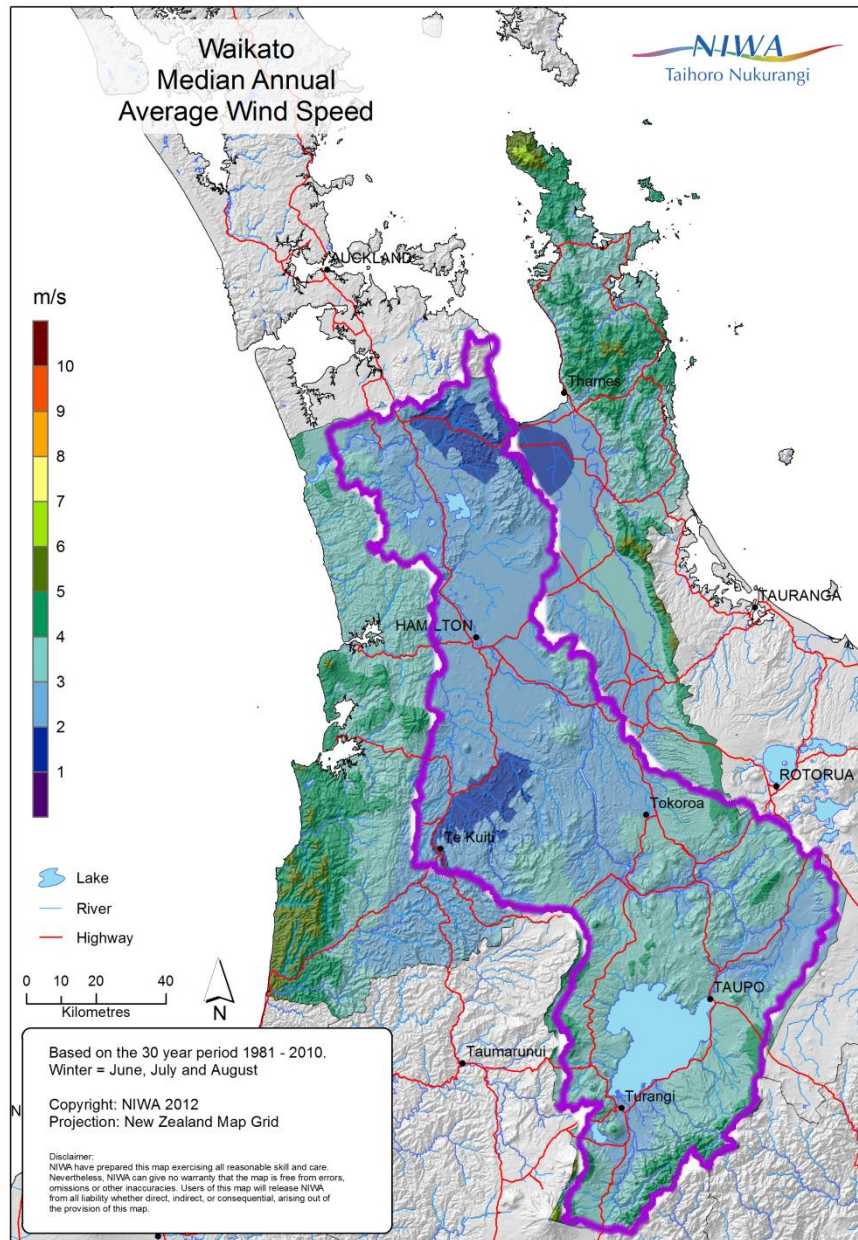


**Figure 3.7** Waikato median annual wind speed based on the 30 year period from 1981 to 2010 (NIWA, 2012)

The Waikato catchment plays an important role in both regional and national development since hydroelectricity and farming are the main activities in the catchment region. For example, the hydroelectric schemes in the Waikato catchment provide approximately 13% of New Zealand's current electricity requirements (Dravitzki, 2009). However, these activities are heavily dependent on precipitation. This may create pressures on the water resource management of the catchment in which the major concern is about evaporative water loss. In addition, soil water deficit also plays an important role in the surface water balance because soils in many areas of New Zealand have highly variable available water capacities (NIWA, 2005). Flooding that is a major consequence of heavy precipitation has become a big problem in the region. Approximately 67% of annual maximum floods occur in the winter-spring period (July-October), and only 14% of annual maximum floods have occurred in the summer months. Although impacts of flood and inundation are mitigated through river control, flood plains are still most vulnerable to flooding. This is because there is rapidly increasing residential and farming activities within the region (Dravitzki, 2009).

### **3.1.3. Representatives of forest and grass sub-catchments**

The Waikato catchment is mainly covered by forest land and grassland accounting for more than 80% of the total catchment area (Figure 3.8). The three representative forest and grass land sub-catchments are selected as pilot case studies which are shown in Figure 3.9 and Figures 3.10-3.12. They are Mangatawhiri, Mangaonua and Whangamarino sub-catchments with a total area of about 182 km<sup>2</sup>, 166 km<sup>2</sup> and 131 km<sup>2</sup>, respectively.

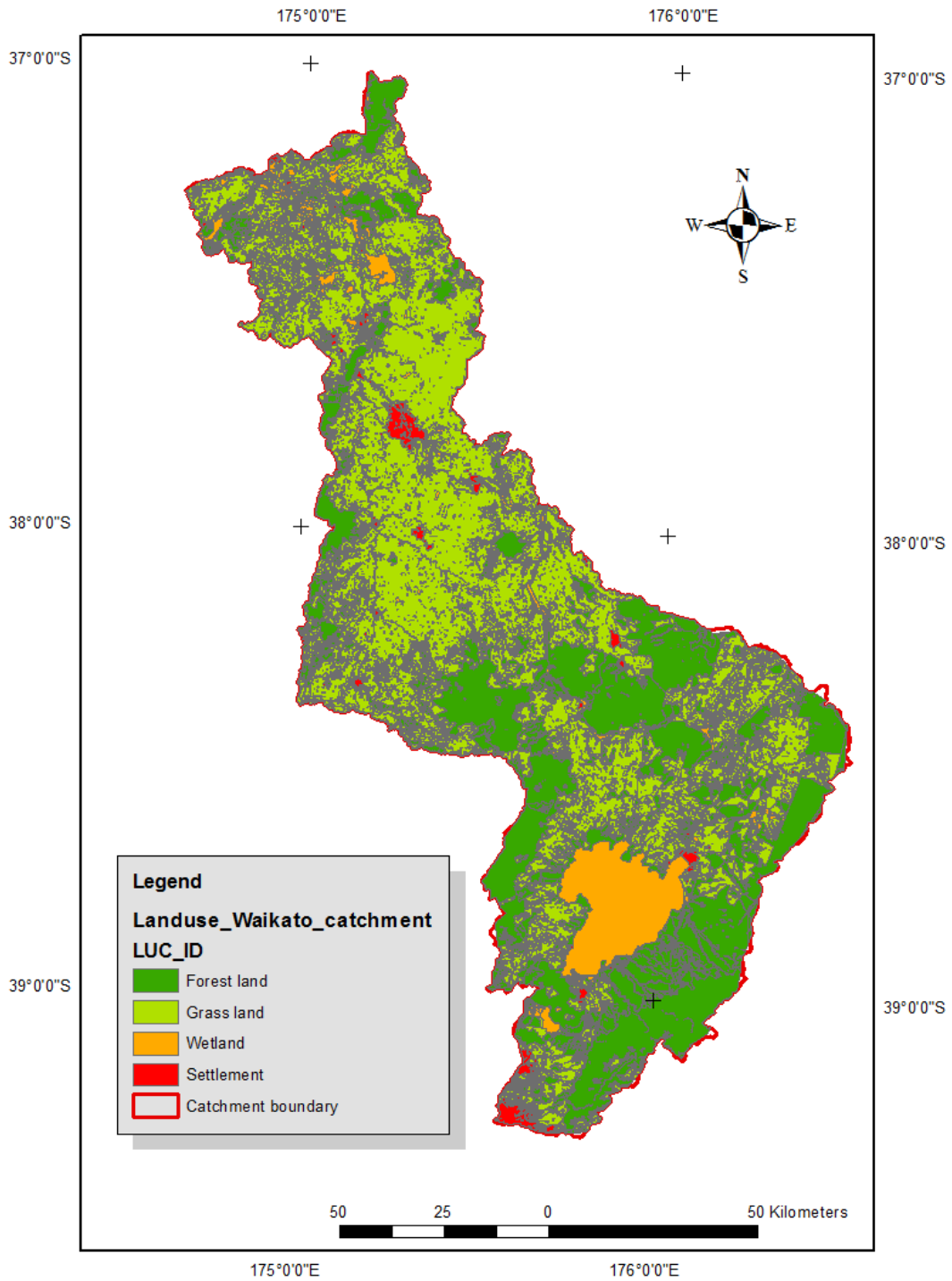
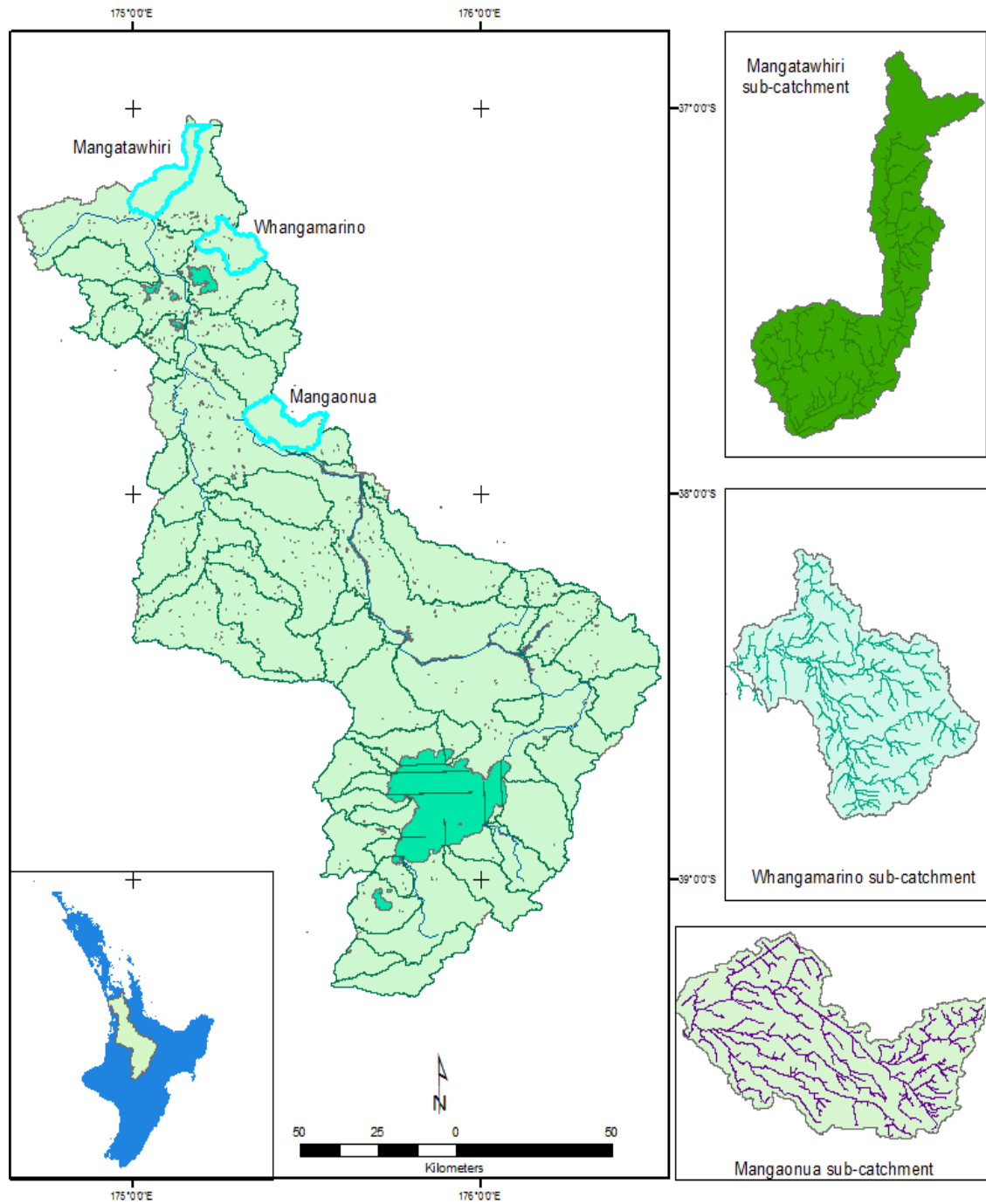
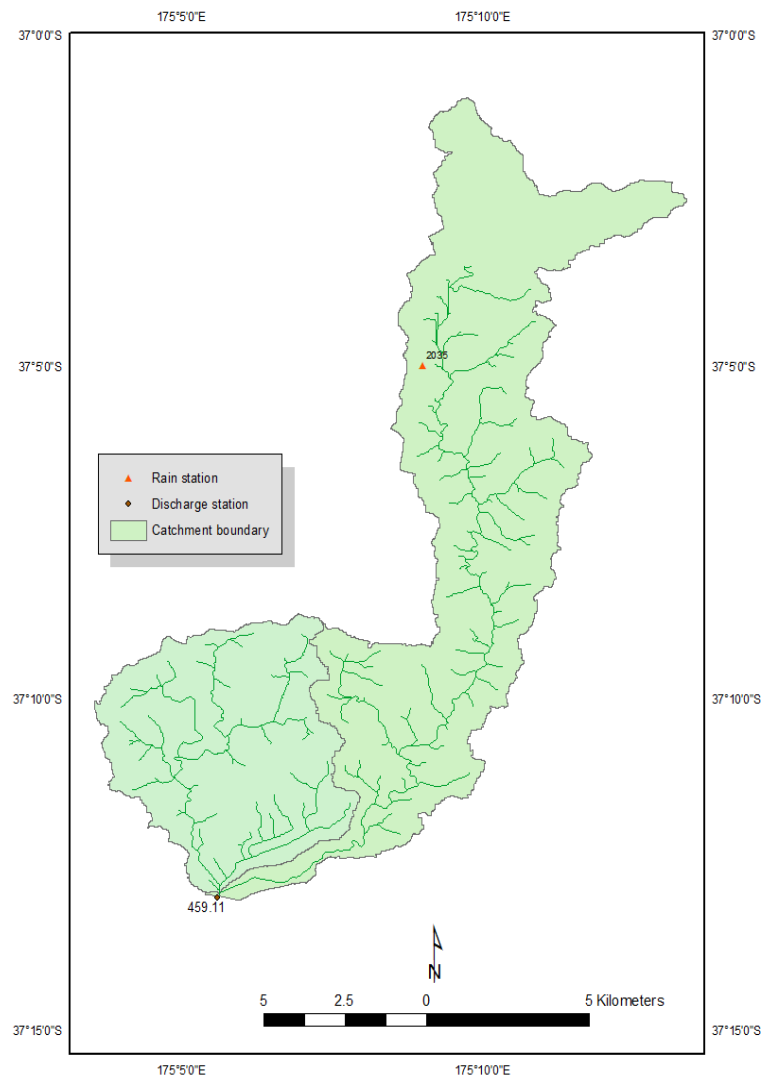


Figure 3.8 Waikato catchment and its landuse



**Figure 3.9** Waikato catchment and its representative sub-catchments



**Figure 3.10** Map of Mangatawhiri sub-catchment and meteo-hydrological stations

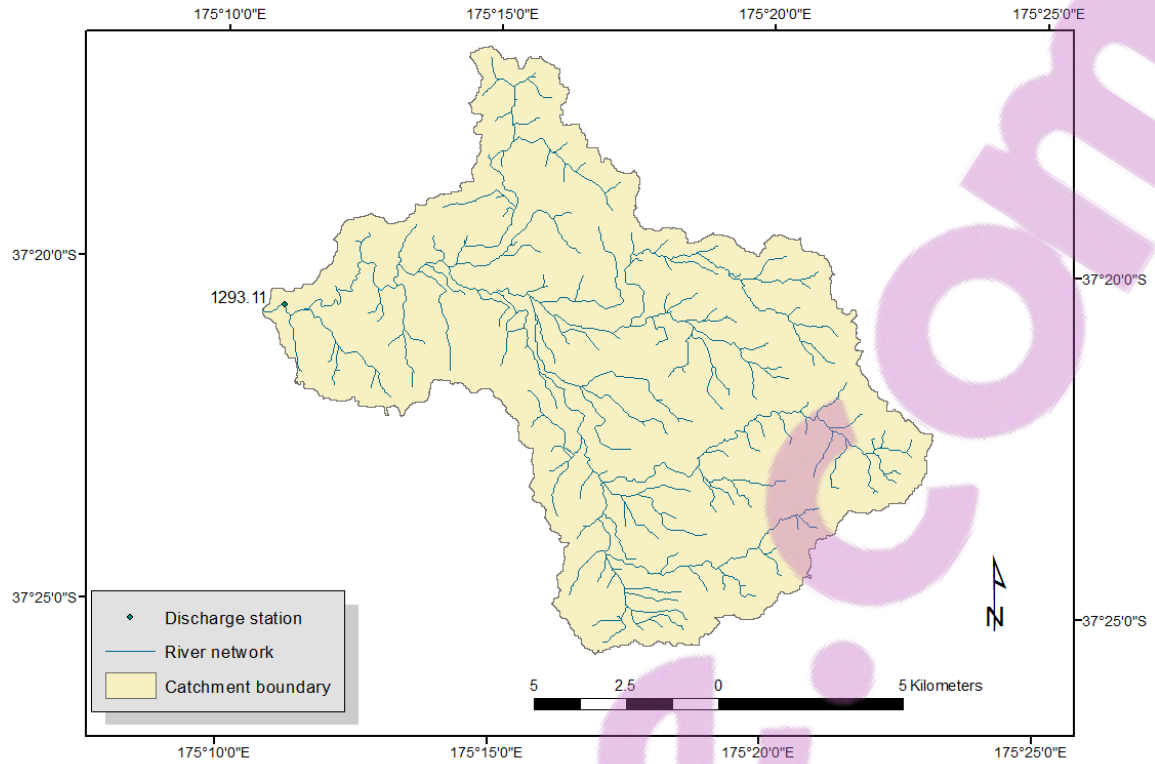


**Figure 3.11** Map of Whangamarino sub-catchment and hydrological stations

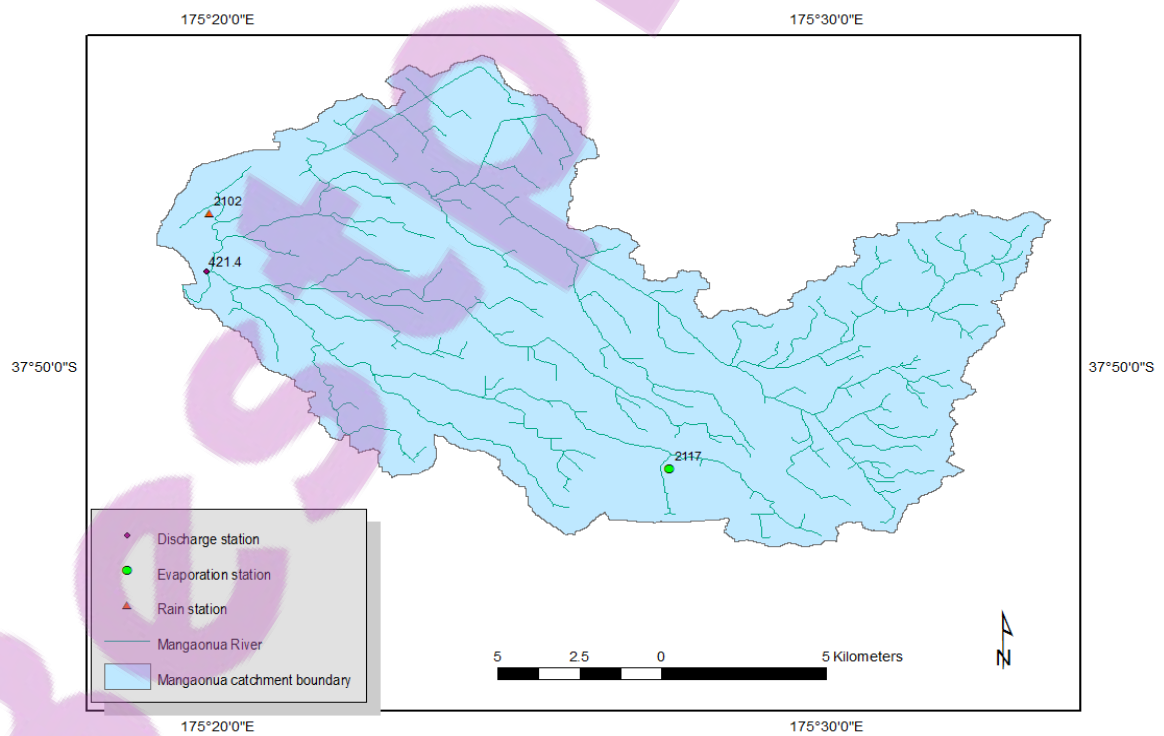


**Figure 3.12** Map of Mangaonua sub-catchment and meteo-hydrological stations

Mean areal annual rainfall in these catchments varies between 1,200 mm and 1,600 mm. Mean annual evaporation varies between 800 mm and 1,100 mm. Recorded mean annual streamflow fluctuates from 540 m<sup>3</sup>/s to 760 m<sup>3</sup>/s. The similar patterns in precipitation, evaporation and flow in these sub-catchments are shown in Figures 3.13 and 3.14. The elevation of these sub-catchments ranges between 40 m and 300 m, stretching from upstream to downstream of the sub-catchments.

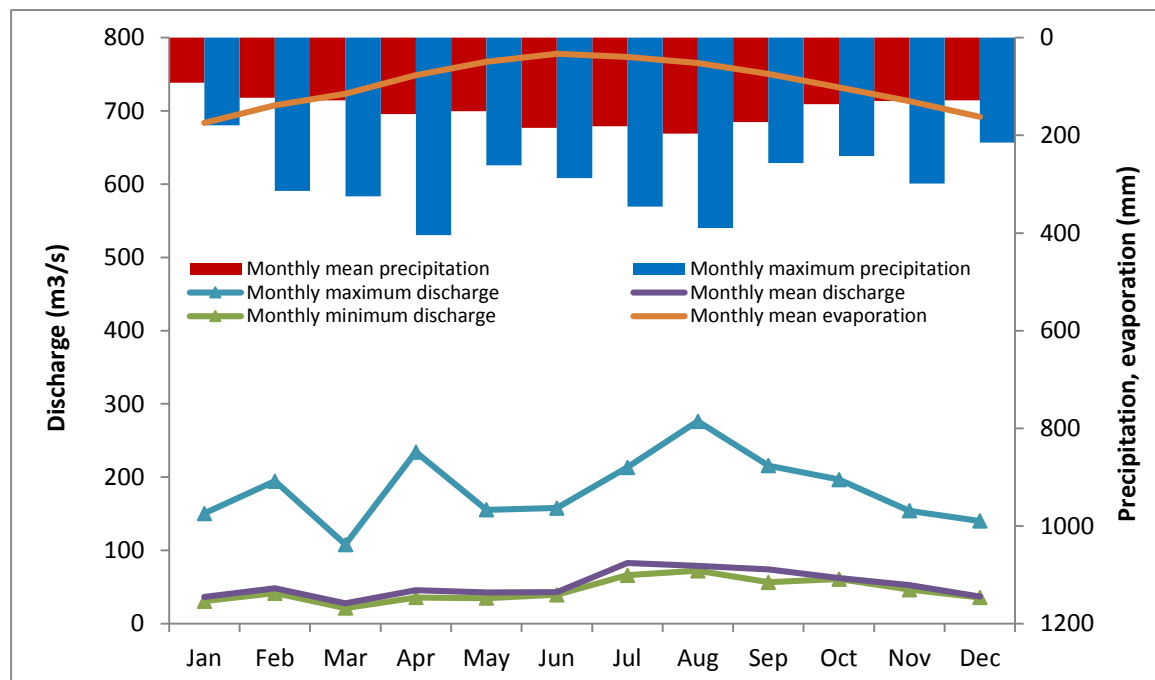


**Figure 3.13** Variation of monthly precipitation, evaporation and discharge at stations in Mangatawhiri sub-catchment

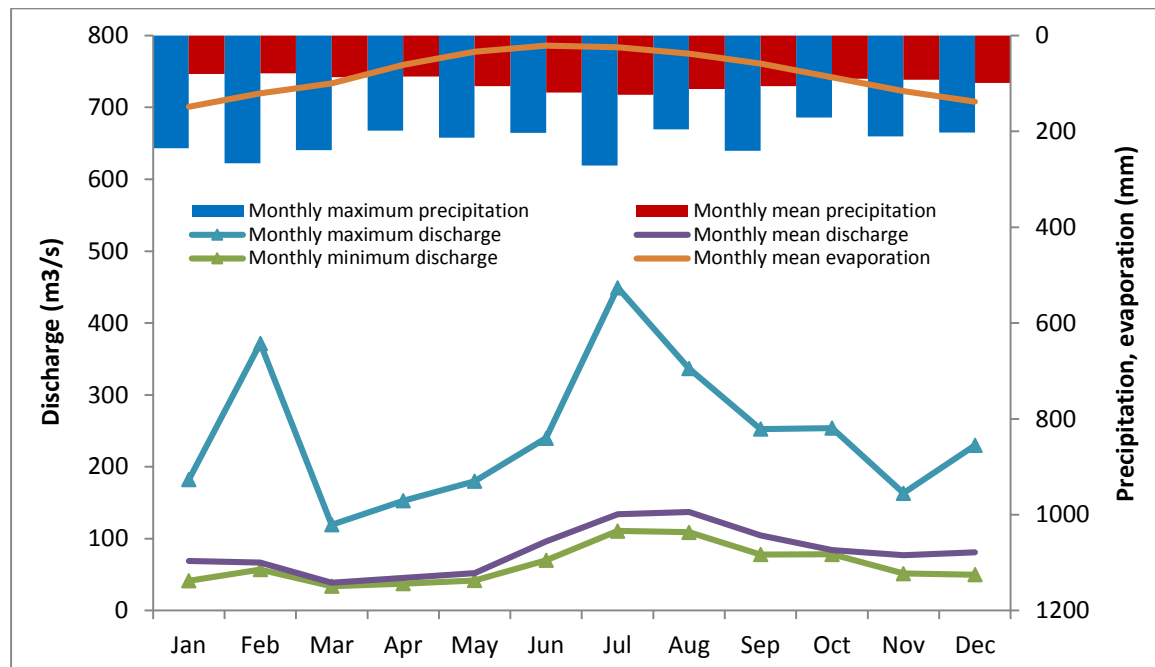


**Figure 3.14** Variation of monthly precipitation, evaporation and discharge at stations in Mangaonua sub-catchment

The evaporation and transpiration processes in these sub-catchments may reflect the impact of vegetation cover on evaporative water loss. Landuse maps are presented in Figures 15-18. Along with this, groundwater and surface runoff could also be controlled by different soil types that differ from sub-catchment to sub-catchment (Figures 3.17-3.19). The dominant soils in the Mangatawhiri and Mangaonua sub-catchment are recent and allophamic soil respectively, while mixed ultic, gley, recent and brown soils are found in the Whangamarino sub-catchment. According to Newsome et al. (2000), recent soils have variable soil texture with high plant-available water capacity. Allophamic soils have low bulk density, little resistance to root growth and their top soils are stable and resist the impact of machinery and grazing animals in wet weather. Gley soils have high ground water table, shallow potential rooting depth and relatively high bulk density. Ultic soils have dispersible surface horizons susceptible to livestock treading damage, and are prone to erosion.

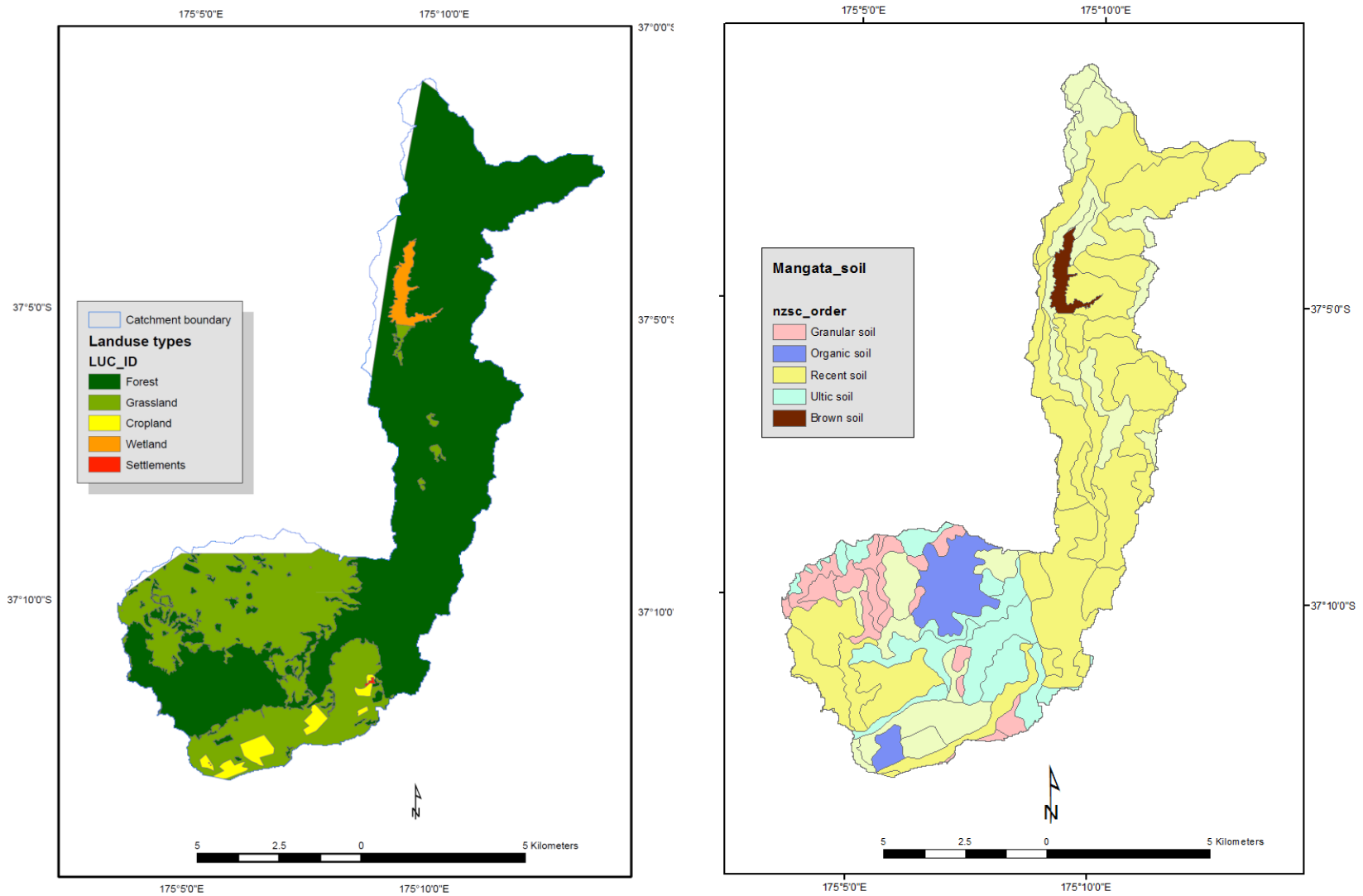
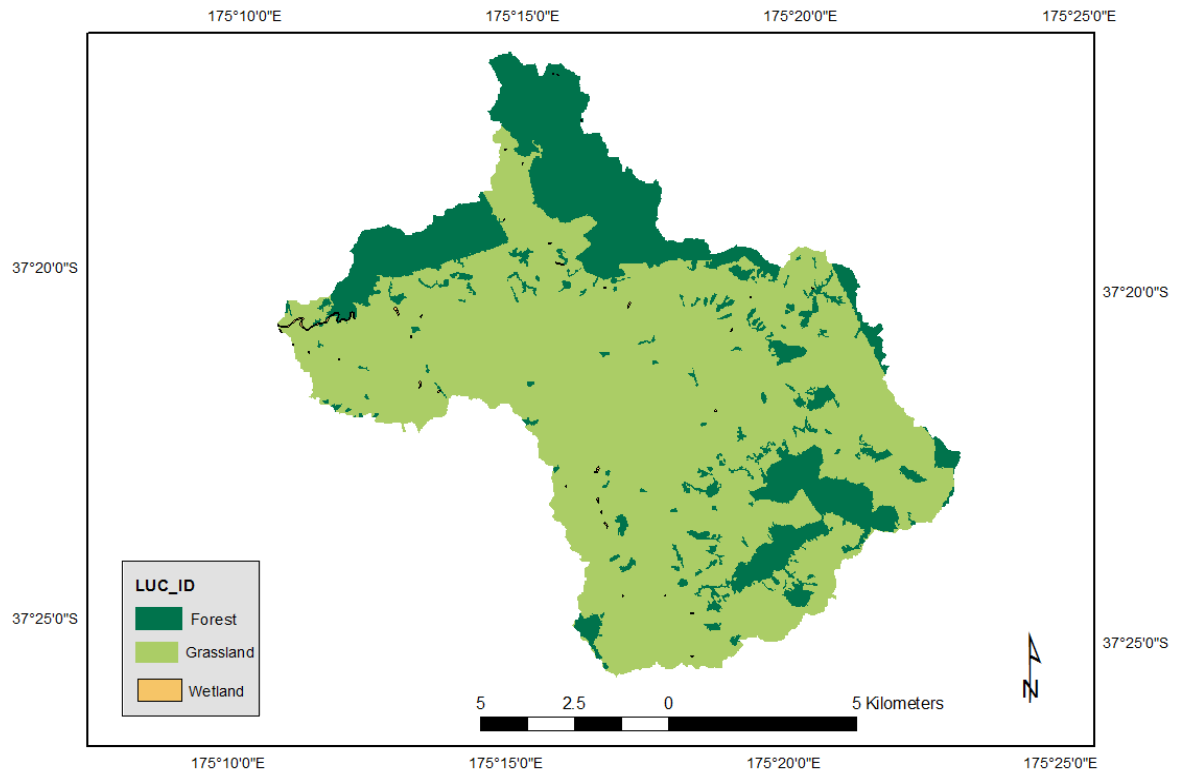
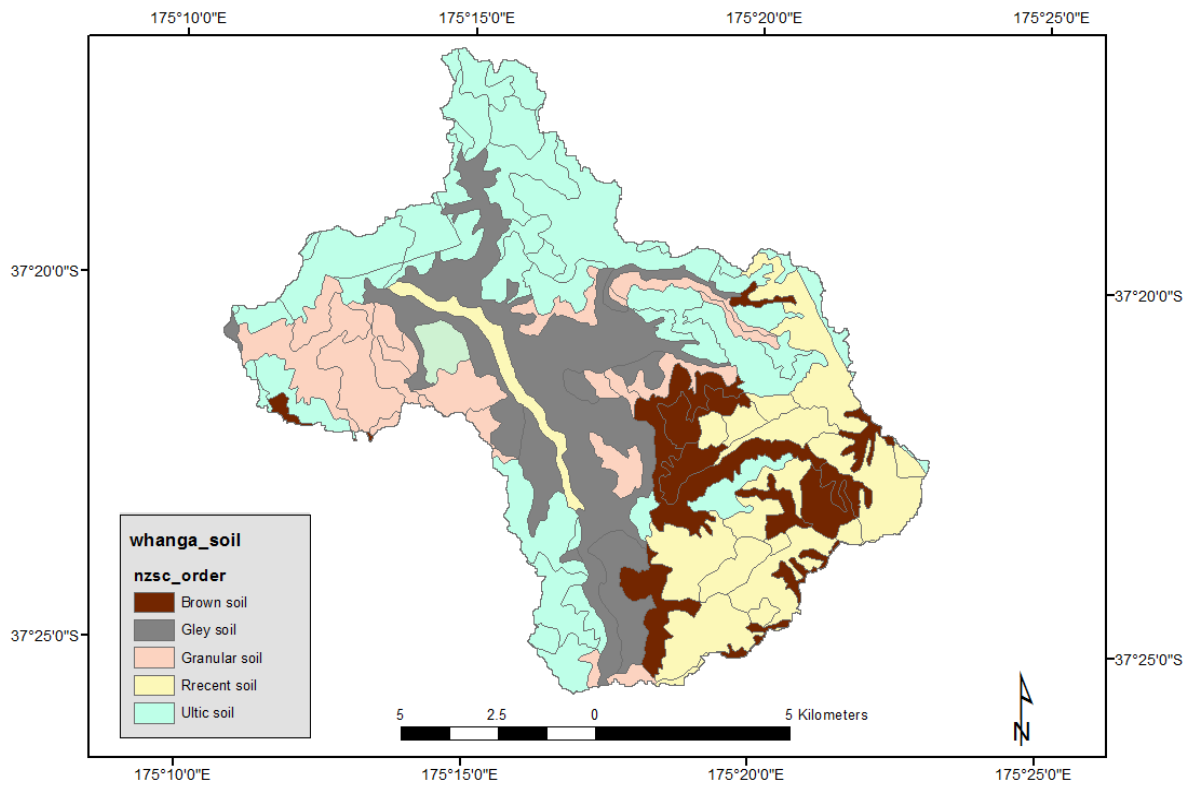


Figure 3.15 Map of Mangatawhiri sub-catchment's landuse and soil types



**Figure 3.16** Map of Whangamarino sub-catchment's landuse



**Figure 3.17** Map of Whangamarino sub-catchment's soil type

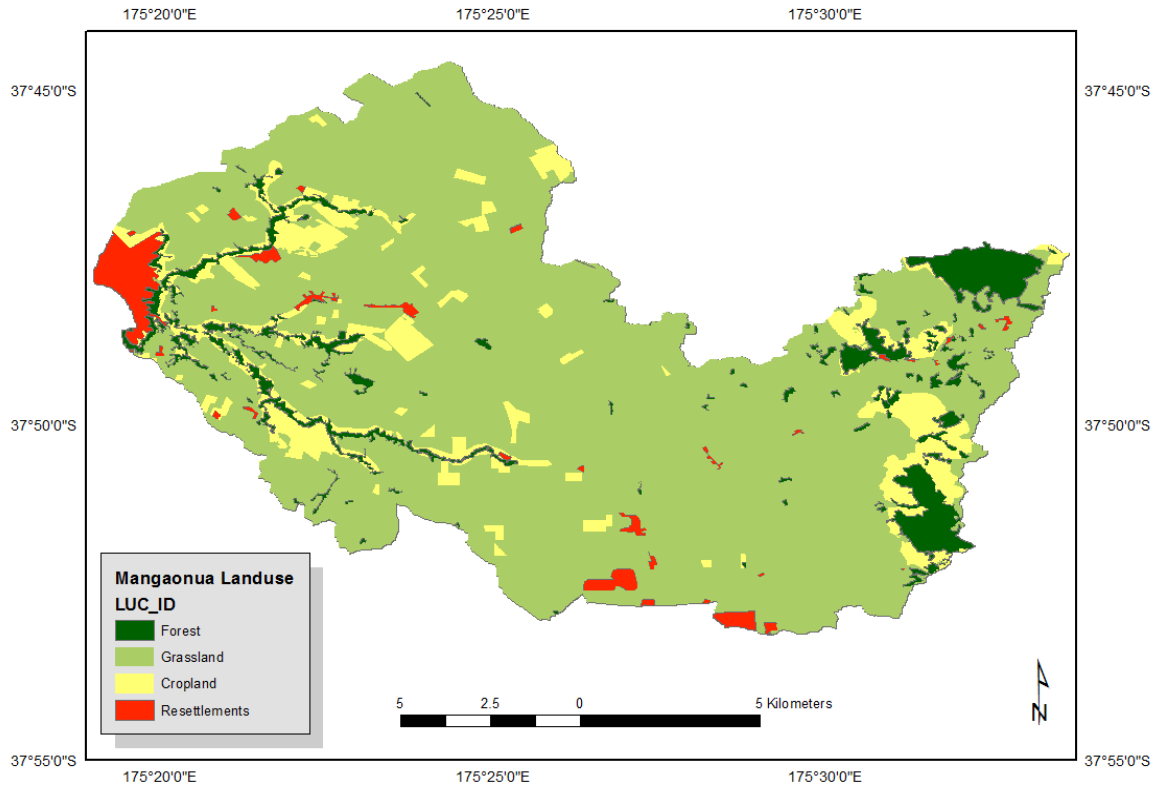


**Figure 3.18** Map of Mangaonua sub-catchment's land use

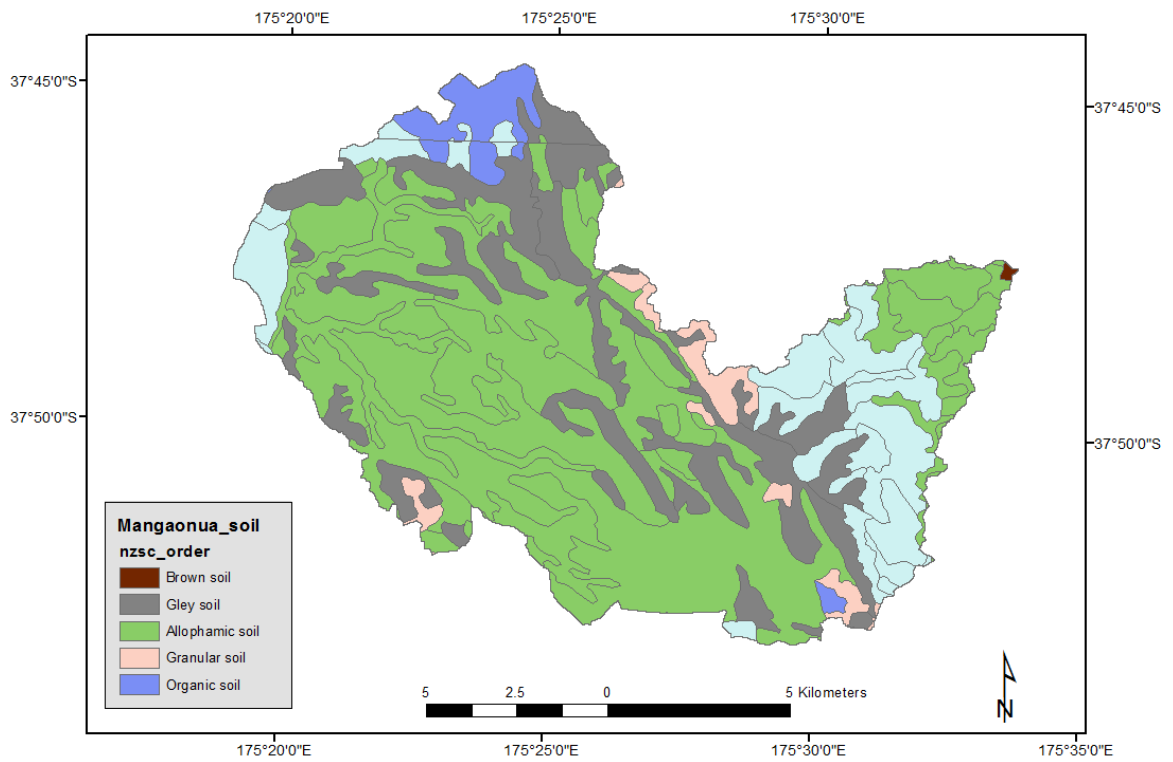


**Figure 3.19** Map of Mangaonua sub-catchment's soil type

## 3.2. Data collection and processing

Data collection and analysis of different data types were implemented. These serve as input for extreme precipitation prediction, potential evapotranspiration estimation and water balance modelling as follows:

- Observed meteo-hydrological data
- Global Climate Model (GCM) and Regional Climate Model (RCM) raw data
- Topographic maps
- Soil and landuse maps

Traditionally, meteo-hydro data is measured at stations. Its daily time scale is appropriate because this properly explains trend in precipitation, potential evapotranspiration and streamflow.

In this research, there are numerous software and programmes were used to process the data. In particular, ArcGIS software version 10 was used to incorporate with spatial data types, such as to build maps, to visualise gridded data and to analyse spatial data.

The HDF View and the Unidat Net CDF packages were used to extract the large-scale data sets from GCMs/RCM at the station locations and for integrating the results over the study period. The two packages were originally developed by National Centre for Supercomputing Application (NCSA) and by North American Regional Climate Change Assessment Program (NARCCAP), respectively.

This research also developed several programmes based on Visual basic and FoxPro languages to deal with time series data pre-processing, including data extraction, combination and analysis.

### 3.2.1. Observed meteo-hydrological data

Meteorological data that is used in this research includes precipitation and evaporation at daily time scale. Observed precipitation data was selected at 36 different stations across the North Island region including Waikato catchment. This selection may accommodate the study on variability of daily precipitation that is apparently very complex in comparison to other climatic variables'. Observed evaporation data from eight stations in the Waikato catchment comprising three representative sub-catchments was assembled to serve the purpose of detecting the trend in evaporation rate from the past to the present, especially over typical forested and grassed surfaces. Data was obtained from the National Institute of Water and Atmospheric Research of New Zealand (NIWA) database website (<http://cliflo.niwa.co.nz/>), which are available to download online. Likewise, daily discharge at three stations in the representative sub-catchments was collected for hydrological model calibrating and validating. This data was obtained from the Environment Waikato Department, New Zealand. In general, the observation period is between 1945 and 2010 for daily precipitation, 1970 and 2006 for daily evaporation. The summary on selected data is presented in Tables 3.1 and 3.2.

**Table 3.1** Information on selected precipitation stations in North Island

No.	Station	Record length	X (°)	Y (°)	Network
1	1022	90	173.532	-34.997	A43951
2	1037	63	173.259	-35.114	A53121
3	1155	62	173.558	-35.653	A53651
4	1200	63	174.091	-35.380	A54301
5	1283	46	174.360	-35.769	A54733
6	1326	31	174.250	-36.100	A64121
7	1330	43	174.370	-36.163	A64132
8	1331	42	174.580	-36.127	A64151
9	1372	40	174.665	-36.402	A64461
10	1410	46	174.624	-36.793	A64761
11	1500	57	174.544	-37.052	A74052
12	1545	63	175.546	-37.300	B75351
13	1564	94	175.654	-37.510	B75561
14	1581	58	175.448	-37.746	B75741
15	1797	91	176.422	-38.314	B86341
16	1874	98	177.287	-38.006	B87023
17	2011	48	174.719	-37.346	C74371
18	2014	53	174.943	-37.337	C74391
19	2312	98	174.506	-39.148	C94151
20	2480	63	175.947	-40.915	D05991
21	2527	63	176.835	-40.150	D06181
22	2563	63	176.543	-40.463	D06451
23	2633	63	175.636	-41.109	D15161
24	2684	63	175.576	-41.481	D15451
25	2791	63	177.719	-38.562	D87571
26	2859	63	178.154	-38.076	D88011
27	2979	63	176.813	-39.413	D96483
28	3037	63	176.478	-39.776	D96741
29	3044	63	176.701	-39.757	D96771
30	3103	105	176.563	-39.983	D96951
31	3120	63	177.321	-39.023	D97031
32	3178	63	175.914	-40.074	E05092
33	3213	105	175.549	-40.222	E05251
34	3384	91	174.752	-41.293	E14271
35	3554	105	174.227	-39.588	E94521
36	3715	74	175.045	-39.938	E95902

*The location and the serial number of these stations are shown in Fig. 4.1.*

**Table 3.2** Information about selected evaporation stations

No.	Station	Record length	X (°)	Y (°)	H (m)	Mean annual $ET_p$ (mm)
1	1841	23	176.072	-38.681	376	1,007
2	2005	19	174.863	-37.208	82	1,122
3	2081	8	175.142	-37.411	32	1,140
4	2101	25	175.313	-37.78	40	897
5	2103	31	175.087	-37.812	104	1,044
6	2128	26	175.498	-37.919	37	865
7	2250	29	175.2598	-38.887	171	740

*$ET_p$  is pan evaporation rate measured at station location.*

**Table 3.3** Information on selected discharge stations

No	Station	Sub-catchment	Area (km <sup>2</sup> )	Record length	X (°)	Y (°)	Specific discharge (m <sup>3</sup> /s/km <sup>2</sup> )
1	459.11	Mangatawhiri	104	29	175.09	-37.341	0.012
2	421.1	Mangaonua	166	15	175.426	-37.829	0.012

### 3.2.2. Global and Regional Climate Model (GCM/RCM) data

Daily large-scale climatic variables including precipitation, air temperature, wind speed, radiation, and relative humidity as the outputs of two GCMs and one RCM are used for this research.

Basically, GCM and RCM data contains daily values of 26 large-scale variables coupled with different scenarios developed by the Intergovernmental Panel on Climate Change (IPCC SRES scenarios). In this research, 26 large-scale variables are obtained from two GCMs, the Canadian Global Climate Model (CCGCM3.1/T47) which is presented in a grid form at 3.75°x3.75° spatial resolution and the United Kingdom Hadley Centre Coupled Model (HadCM3) at 2.5°x2.5° spatial resolution. The corresponding 26 daily

observed large-scale predictor variables are originally from the National Centre of Environmental Prediction (NCEP) re-analysis with spatial resolution of  $2.5^0 \times 2.5^0$ . Both the GCM and NCEP data are obtained from same source in which the NCEP data is regridded to the horizontal grid resolution of the GCM.

The CCGCM3.1/T47 and HadCM3 data were obtained at the Data Access Integration (DAI, see <http://quebec.ccsn.ca/DAI/>) and the Canadian Climate Impacts and Scenarios project (CICS, <http://www.cics.uvic.ca/scenarios/>). Likewise, 26 dynamically downscaled variables from a very high  $0.05^0 \times 0.05^0$  spatial resolution RCM HadCM3 model by the NIWA were used.

These GCM and RCM data sets contain both historical and future data. Data over two different periods, 1961-2000 and 2001-2090 were defined for present and future climates, respectively.

Future data from only one emissions scenario, IPCC SRES A2 scenario, was then used for all simulations. The A2 emissions scenario was selected because it was one of the 'marker' scenarios developed through the IPCC (IPCC, 2000, 2007). Furthermore, the A2 scenario is commonly used by the NIWA to study the climate change effects and impacts assessment for New Zealand local governments (MfE, 2008; Mullan et al, 2001a, b).

CGCM3.1/T47, GCM HadCM3 and RCM HadCM3 data are presented in a grid form with their sizes of 375 km x 375 km, 250 km x 250 km and 5 km x 5km, respectively (Figure 3.20). There are four grid cells in CCGCM3.1/T47 data and six grid cells in GCM HadCM3 data covering the whole North Island including the Waikato catchment. There are 3600 cells in RCM data covering the whole Waikato catchment. RCM data sets are extracted to the points that the selected stations and sub-catchments are located (Table 3.3).

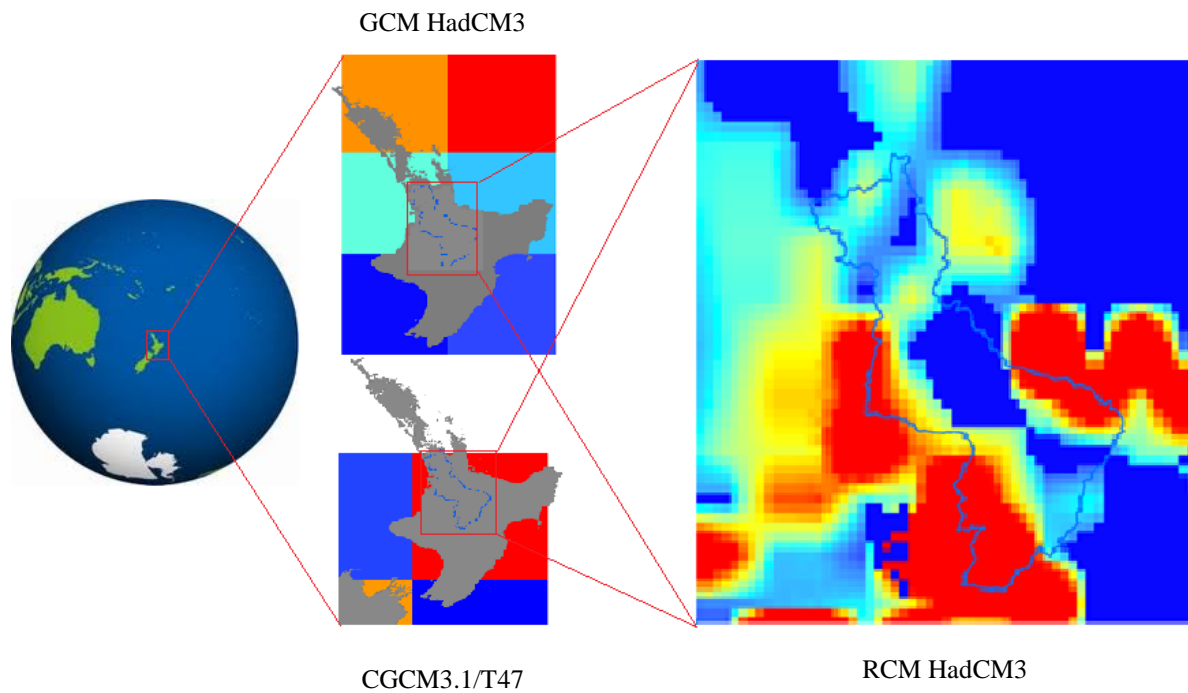


**Figure 3.20** GCMs and RCM data with different spatial resolutions

**Table 3.4** The number of grid cells from RCM HadCM3 found for selected stations and selected sub-catchments

Station/ Catchment	184 1	200 5	208 1	210 1	210 3	212 8	225 0	Whangamarino	Mangatawhiri	Mangaonua
No. of grid cells	1	1	1	1	1	1	1	7	8	10

These data were used for simulating the variation in precipitation and potential evapotranspiration from the past to the future. For the convenience of computation as well as the comprehensive assessment of future projections, the decadal 30-year that was the standard normal period defined by the World Meteorological Organization (WMO) is used.

### 3.2.3. Soil type and landuse maps

For soil-water balance modelling, soil type and landuse maps are required. These data are obtained from the Landcare Research Institute (LRIS), the Waikato Regional Council (WRC).

### 3.3. Summary

This chapter gave a brief overview of the study region and its data availability for the research. The description of the North Island region was first presented, followed by the Waikato catchment and its three sub-catchments. The selection was based on data availability in the study areas and surroundings. Moreover, this research thesis aims to investigate the precipitation variability across the North Island. Evapotranspiration variability is examined over the Waikato catchment while water balance is inspected from its three sub-catchments with different landuse and soils. This chapter also introduced different data types and sources coupled with several software and programs which are effective for both temporal and spatial data ranging from data pre-processing to analysis.

## CHAPTER 4

# Extraction of extreme precipitation

This paper includes partial reproduction of the paper:

Pham, H. X., Shamseldin, A. Y. and Melville, B. W. (2014). Statistical properties of partial duration series. *J. Hydrol. Eng.*, 19, 807-815.

This chapter focuses on abstracting extreme precipitation events from observation time series. A novel peak-over-threshold (POT) method is used to define the most plausible Partial Duration Series (PDS) model for the whole North Island of New Zealand. The first section of the chapter highlights the POT and PDS background and objectives. Following this, the technical and computational details including various statistical tests are explained. Finally, the selection of the most plausible PDS model for the study region is discussed.

## 4.1. Introduction

Partial Duration Series (PDS) model is preferable for hydrological frequency analysis when dealing with values exceeding a certain threshold, and it is capable of capturing more information about extreme events than the rival Annual Maximum Series (AMS) model. However, the use of PDS in hydrological application encounters the difficulty of determining the exceedance threshold due to physical and statistical complexity. There is an inverse relationship between the threshold value and the number of peaks selected above a threshold and a fixed number of average peaks per year is an option to define the threshold value. Along with this, a PDS is generated under an assumption that it is best described by a Generalized Pareto (GP) distribution. To date, the question arisen is how many peaks should be appropriate for modelling the PDS. This research investigates the optimum number of peaks for integer values based on the variability of the GP/PDS parameters with an increase in the value of number of peaks. The research for the first time addresses the question by using a wide range of historical precipitation data from the North Island region of New Zealand.

### 4.1.1. Overview of Partial Duration Series by Peak-Over-Threshold (POT)

#### 4.1.1.1 Characteristics of PDS

PDS is a series of peaks over a threshold (POT) which is characterized by the average number of peaks each year ( $\lambda$ ) or a threshold value ( $u$ ). Given a daily series of observations  $x = \{x_1, x_2, \dots, x_i, \dots, x_n\}$  over  $N$  years,  $n = 365 \cdot N$ , the resulting PDS is the set containing  $M$  values,  $y = \{y_1, y_2, \dots, y_j, \dots, y_M\}$ , which exceed a chosen threshold  $u$ ,  $y_i > u$  with  $u = \text{constant}$ .

In the PDS, the total number of peaks ( $M$ ) is a random quantity which can be chosen from the average number of peaks per year,  $\lambda = M/N$ . The peaks are assumed to be independent random variables described by the GP distribution and the peak arrival following the Poisson distribution (Cunnane, 1973). The special case of the PDS,  $\lambda = 1$ , is the Annual Maximum Series (AMS) where the  $N$  highest peaks within the  $N$  years of data are chosen (Gordon et al., 2004).

The number of elements in the PDS series,  $(\lambda N)$  depends on either the average number of peaks per year or the threshold value. For this reason, the PDS use the information from the original series more efficiently because it includes on average more than one event each year, if they satisfy the conditions established in defining an extreme event.

#### **4.1.1.2 Significance of threshold value**

To date there is no agreement on the selection of the optimum threshold value. Principally, the threshold value ( $u$ ) decreases with the increase in the value of the average numbers of peaks per year ( $\lambda$ ). The threshold value must be set at a high value to ensure only true peaks are selected, with the peak arrival being governed by the Poisson distribution. In contrast, the threshold must be set low enough to ensure that sufficient peaks are selected to enable reliable estimation of the distribution parameters (Ashkar et al., 1983, 1987; Buishand, 1989; Cunnane, 1979, 1985; Langa et al., 1999; Palutikof et al., 1999; Onoz and Bayazit, 2001; Trefry et al., 2005).

## 4.1.2 GP-Poisson distribution and parameter estimators

### 4.1.2.1. The Poisson distribution of peak occurrences

The number of peaks occurring in  $t$  years  $N(t)$  follows a random process which can be described by the Poisson distribution. In the case of the Poisson distribution, the probability density function is given by:

$$f(n, \lambda t) = \frac{e^{-\lambda t} (\lambda t)^n}{n!} \quad (4.1)$$

where  $n$  is the numbers of peaks within time interval  $(0, t)$ , and  $\lambda$  is the mean arrival rate (or the average number of peaks per year) which can be estimated from the sample. One of the properties of the Poisson distribution is that the mean and variance are equal.

### 4.1.2.2. The GP distribution of peak magnitudes

The PDS set contains all mutually independent peaks following the GP distribution. The probability density function of the GP distribution  $f(x)$  for a variable  $x$  is given by:

$$f(x) = \begin{cases} \alpha^{-1} e^{-[(x-\zeta)/\alpha]} & k = 0 \\ \alpha^{-1} [1 - k(x - \zeta)/\alpha]^{1/k-1} & k \neq 0 \end{cases} \quad (4.2)$$

where  $\alpha$ ,  $k$  and  $\zeta$  are the scale, the shape and the location parameters, respectively. These parameters can be estimated by the method of L-moment (L-MOM) according to the following equations given by Hosking and Wallis (1997):

$$k = \frac{1 - 3\tau_3}{1 + 3\tau_3} \quad (4.3)$$

$$\alpha = (1 + k)(2 + k)\lambda_2 \quad (4.4)$$

$$\zeta = \lambda_1 - (2 + k)\lambda_2 \quad (4.5)$$

where  $\tau_3$  is the L-MOM coefficient of skewness while  $\lambda_1$  and  $\lambda_2$  are the first and second order L-MOM.

### 4.1.2.3. Parameter estimators

The use of L-moment measure is very effective for estimating distribution parameters (Greenwood et al., 1979, Hosking, 1986, 1990). Firstly, L-MOM is less influenced by the effects of sampling variability than conventional moments. Also, in some cases it produces more efficient parameter estimates. L-MOM is robust to outliers and virtually unbiased for small samples, making them suitable for regional frequency analysis, including identification of distribution and parameter estimation (Adamowski, 2009).

L-MOM is identified as linear function of PWM:

$$\beta_r = E\{X[F(X)]\} \quad (4.6)$$

where,  $F(x)$  is the cumulative distribution of  $x$

The first four L-MOM expressed as linear combination of PWM are:

$$\begin{aligned} \lambda_1 &= \beta_0 \\ \lambda_2 &= 2\beta_1 - \beta_0 \\ \lambda_3 &= 6\beta_2 - 6\beta_1 + \beta_0 \\ \lambda_4 &= 20\beta_3 - 30\beta_2 + 12\beta_1 - \beta_0 \end{aligned} \quad (4.7)$$

where, L-mean,  $\lambda_1$ , is a measure of central tendency

L-standard deviation,  $\lambda_2$ , is a measure of dispersion

L-coefficient of variation,  $\tau = \lambda_2 / \lambda_1$

L-coefficient of skewness,  $\tau_3 = \lambda_3 / \lambda_2$

L-coefficient of kurtosis,  $\tau_4 = \lambda_4 / \lambda_3$

Physically,  $\tau$  will be smaller if any two values tend to be close together than if they are far apart.  $\tau_3$  will be positive if the lower two values of any subsample of three tend to be closer. Conversely, if the upper two are closer to each other than  $\tau_3$  will be negative. For symmetrical distribution, such as normal distribution,  $\tau_3$  will be close to zero.  $\tau_4$  will be positive if middle values in any subsample of four tend to be closer, or conversely.

## 4.2. Data

Daily rainfall data was assembled from 36 stations (refer to Figure 4.1) where the station record length varied between 31 and 105 years. About 50% of the selected stations have record lengths greater than 60 years (see Figure 4.2).

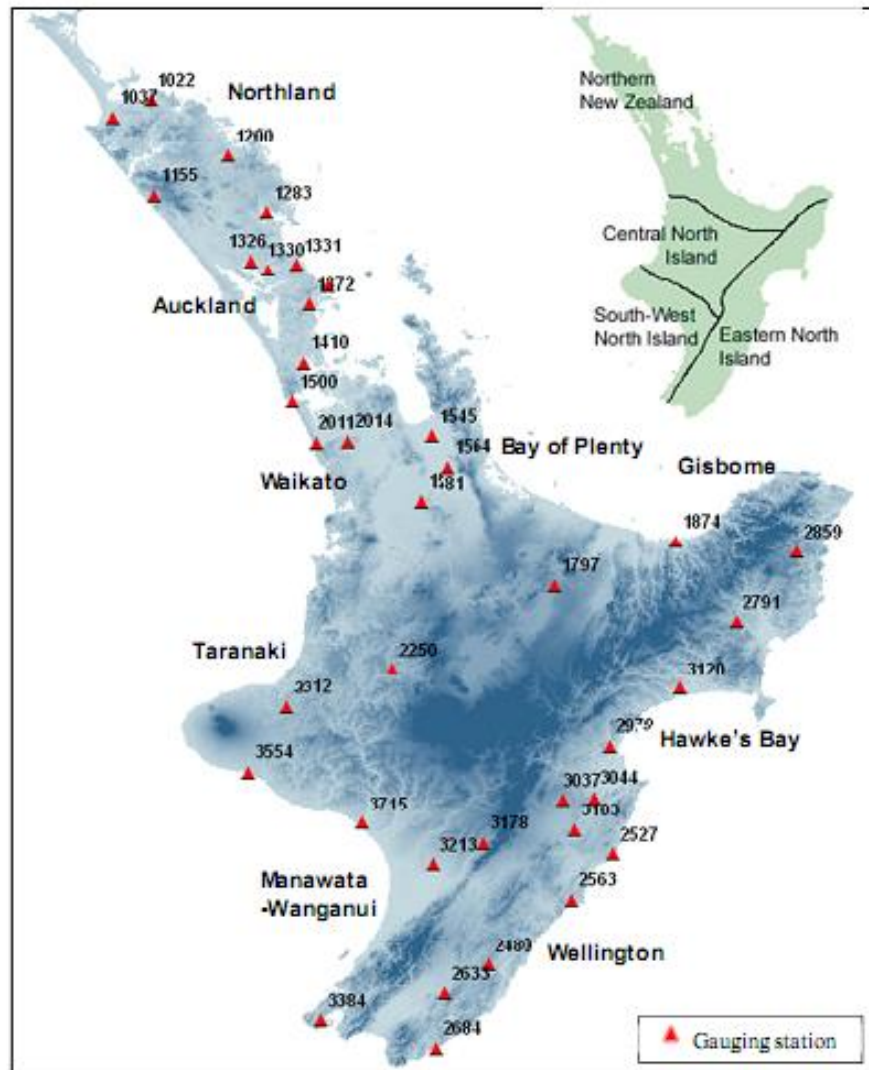


**Figure 4.1** Geographic location of selected stations

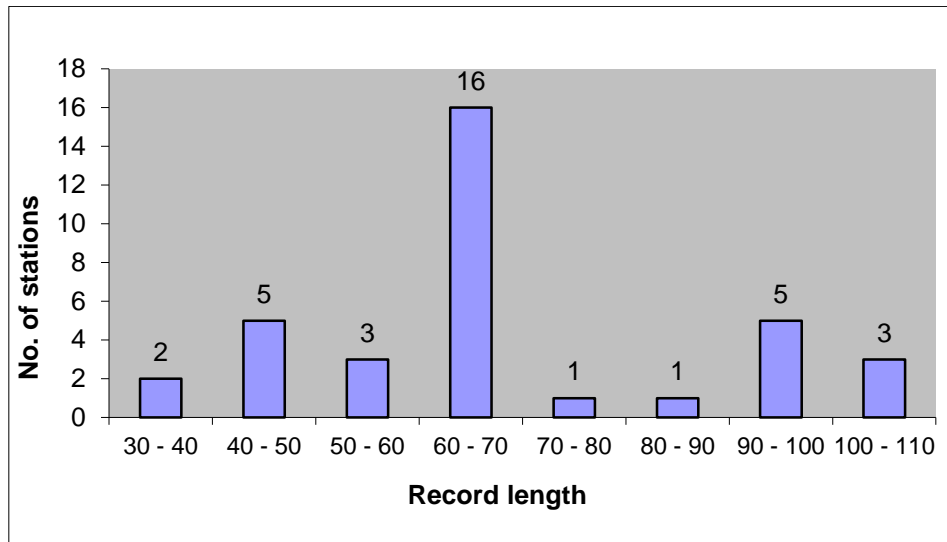


**Figure 4.2** Data record lengths at 36 selected stations

The partial duration series (PDS) set is extracted from the observed daily rainfall data at each station by setting different number of average peaks per year with  $\lambda$  equal to 1, 2, 3, 4 and 5. This is due to the fact that there is no clear predetermined physical threshold in the observed precipitation series available at each station. Although  $\lambda$  can be a real number, this research uses integer values to simplify the analysis. The resulting models henceforth are referred to as PDS1, PDS2, PDS3, PDS4 and PDS5.

### 4.3. Methods

This section deals with the methodology and the techniques used in examining the variability of the GP parameter values with the increase in the value of  $\lambda$ . In particular, this section describes the different statistical tests which are used to test the satisfaction of the assumption made in frequency analysis using the PDS series. This assumption implies that the combined GP-Poisson distribution is considered as best to describe the extreme events above a threshold. These exceedances are mutually independent following a random process.

### 4.3.1. Randomness Test and Trend Test

These tests allow only reasonable PDS series selected from the observed series. This PDS contains all mutually independent peaks following a random process. It is associated with certain  $\lambda$  values.

#### 4.3.1.1. Randomness Detection using Autocorrelation Coefficients

The independence condition of the set of selected peaks is a prerequisite of any statistical frequency analysis. The autocorrelation test is useful for detecting the presence of dependent peaks in the PDS (Langa et al., 1999) which includes the number of peaks chosen regardless of when they occurred (Gordon et al., 2004). Also, this test is adjustable to avoid the problem of autocorrelation by reducing the sample size so that the number of independent samples after adjustment is fewer than the number of observations of the series (Riggs, 1985).

Basically, the autocorrelation coefficients measure the correlation between the PDS peaks separated by  $k$  time intervals. The autocorrelation coefficients measure can be expressed as follows:

$$r_k = \frac{\sum_{i=1}^{M-k} (y_i - \bar{y})(y_{i+k} - \bar{y})}{\sum_{i=1}^M (y_i - \bar{y})^2} \quad (4.8)$$

where  $\bar{y}$  is the average of the  $M$  peak magnitudes in the PDS, an  $r_k$  value of  $(\pm 2/\sqrt{M})$  at significance level  $\alpha = 0.05$  denotes a significant difference from zero and signifies an autocorrelation and  $r_k$  becomes smaller if  $k$  gets larger.

If the peaks are uncorrelated and random, then an autocorrelation coefficient value for non-zero will not be significantly different from zero. Most of the applications use only the first autocorrelation coefficient order in which  $k = 1$ . The reason for this is that any time

persistence in the PDS is likely to be the strongest at lag one. It is worth noting that in some cases the effects of autocorrelation at small lag will influence the estimation of autocorrelation at large lags.

#### 4.3.1.2. Trend Detection using Mann-Kendall Test

Stationarity is another prerequisite to statistical frequency analysis. The Mann-Kendall test is the most commonly used to detect existence of trends in the obtained PDS sets.

This Mann-Kendall statistic trend test is a non-parametric, i.e. distribution free test, that has no constraints on the trend characteristics (Onoz and Bayazit, 2003). It tests Null-hypothesis  $H_0$  (there is no trend in data) against the Alternative hypothesis  $H_A$  (existence of increasing or decreasing trend).

Basically, the existence of a trend is with each pair of observed values  $y_i, y_j$  ( $i > j$ ) of the random variable in order to find out whether  $y_i > y_j$  or  $y_i < y_j$ . If the number of pairs ( $y_i > y_j$ ) is  $P$ , and the number of pairs ( $y_i < y_j$ ) is  $M$ , then  $S$  is defined as following:

$$S = P - M \quad (4.9)$$

It also can be written as:

$$S = \sum_{i=2}^N \sum_{j=1}^{N-1} \text{sign}(y_i - y_j) \quad (4.10)$$

$$\text{sign}(y_i - y_j) = \begin{cases} -1 & \text{for } (y_i - y_j) < 0 \\ 0 & \text{for } (y_i - y_j) = 0 \\ 1 & \text{for } (y_i - y_j) > 0 \end{cases} \quad (4.11)$$

where a positive value of  $S$  indicates that there is an increasing trend and vice versa;  $S$  is asymptotically normally distributed with its expected value (i.e. mean) to be zero ( $S = 0$ ) and has variance as:

$$\sigma = \text{Var}(S) = \frac{N(N-1)(2N+5)}{18} \quad (4.12)$$

For a large sample (its size greater than 10,  $N > 10$ ) and for ties  $y_i = y_j$ , the Z-statistic is used following a normal distribution (Salas, 1993):

$$Z = \frac{|S|}{\sigma^{0.5}} = \begin{cases} \frac{(S-1)}{\sigma^{0.5}} & \text{if } S > 0 \\ 0 & \text{if } S = 0 \\ \frac{(S+1)}{\sigma^{0.5}} & \text{if } S < 0 \end{cases} \quad (4.13)$$

The Null hypothesis  $H_0$  is rejected when the value of Z is greater than  $Z_{\alpha/2}$  value with confidence level  $\alpha = 0.05$ .

### 4.3.2. Validation of the Poisson-GP distribution

This section investigates the optimum  $\lambda$  value based on Dispersion measure and Variance-to-Mean ratio approach. This ensures that the GP-Poisson assumption is valid by selecting an optimum value of  $\lambda$ .

#### 4.3.2.1 Verification of the Poisson distribution using Dispersion measure

The Dispersion measure is widely used for testing the adequacy of the fitted Poisson distribution. This Dispersion measure consists of the Fisher test and the Variance-to-Mean ratio test (Rosbjerg and Madsen, 2004). These will test different PDS series in relation to changes in Poisson arrival rate  $\lambda$ .

As stated in Langa et al. (1999), the Fisher (F) test is based on a dispersion index d. This index is estimated from the variance and the mean of the Poisson distribution. The number of peaks (or peak counts) M is assumed to follow a normal distribution which takes into account that the mean of a Poisson distribution is equal to its variance.

If we assume that the obtained PDS set,  $y = \{y_1, y_2, \dots, y_j \dots, y_M\}$  follows a random process being generated by a Poisson distribution with parameter  $\lambda$ , then the dispersion index is defined as below:

$$d = \sum_{i=1}^N \frac{(m_i - m)^2}{m} \quad (4.14)$$

where  $m$  is sample mean,  $N$  is number of years in PDSs and  $m_i$  is the number of exceedances (peak occurrences) each year.

The difference between the variance and mean obtained from a sample is tested based on a statistic calculated using the  $\chi^2$  distribution, with  $(N-1)$  degrees of freedom, during  $N$  years of record. The probability ( $p$ ) of the hypothesis  $H_0$  that the data follows a Poisson process is accepted when  $0.05 < p < 0.95$  and  $H_0$  is rejected when  $p < 0.05$ .

If the obtained PDS set follows a random process being generated by a Poisson distribution with parameter  $\lambda$ , then the corresponding  $d$  value is equal to 1. Henceforth, a threshold  $u$  is selected so that the dispersion index  $d$  is located in the limits of the confidence interval  $[\alpha = 0.05, \alpha = 0.95]$ .

The Variance-to-Mean ratio test is another approach for evaluating the satisfaction of Poisson assumption with the change in the threshold value. Similar to the above dispersion index test, it also tests the difference between the Poisson distribution variance and mean obtained from a sample. The variance-to-mean ratio is calculated of the successive years and it is subsequently used in the test. The variance-to-mean ratio and dispersion index are expressed in the following formulas, relative to changes in Poisson arrival rate,  $\lambda$ .

$$R = \frac{\sigma^2}{\mu} \quad (4.15)$$

$$d = \frac{M - 1}{R} \quad (4.16)$$

where:  $\sigma^2$  is variance; and  $\mu$  is sample mean

In the Variance-to-Mean ratio diagram, if R values tend to approach or fluctuate around the line  $R = 1$  then the Poisson assumption is accepted. The base line at threshold level  $u$  (named the Poisson admissible truncation level) obtained from the R curves should be chosen high enough above the line  $R = 1$  in order to satisfy the Poisson assumption (Ashkar et al., 1987). This is mainly due to the fact that any truncation level above a Poisson admissible truncation level giving rise to a Poisson process should also be Poisson admissible. This choice of  $u$  is made roughly at the point where R curve starts to stabilize around the line  $R = 1$  by entering a confidence band (upper and lower confidence limits) that is constructed around this horizontal line.

#### **4.3.2.2 Suitability of GP distribution based on L-MOM ratios and sensitivity analysis**

Even though the GP distribution is regarded as the best distribution for the PDS, it is necessary to test the suitability of the GP distribution describing different PDS used in this research as no previous studies have been conducted in the region. Two measures are used in this research to gauge the suitability of GP distribution for frequency analysis of PDS in the study region. The first measure is based on the use of the L-moment ratio diagram which shows the theoretical relationship between L-MOM coefficient of skewness,  $\tau_3$  and the L-MOM coefficient of kurtosis,  $\tau_4$  for different probability distributions. In the L-moment ratio diagram, a two-parameter probability distribution is represented by a point while a three-parameter distribution is represented by a curve. When the  $\tau_3$  and  $\tau_4$  sample estimates are plotted on the L-MOM ratio diagram the clustering of the sample points around the theoretical relationship of a particular distribution can be regarded as a strong

indication for the suitability of the distribution (Hosking and Wallis, 1993). The second measure is based on a systematic evaluation of the change in the GP parameter values with the change in the  $\lambda$  value. The stability of the GP parameter values with the change in  $\lambda$  value is paramount in reducing the corresponding quantile uncertainty by the selection of an optimum  $\lambda$  value (Ashkar et al., 1987; Begueria, 2005; Deidda et al., 2009).

## **4.4. Results and discussions**

### **4.4.1. Random test and trend test**

In the autocorrelation test, the lag-1 autocorrelation coefficients ( $r_1$ ) are computed from the obtained PDS5 and presented in Figure 4.3. Generally, the  $r_1$  values vary around value  $\pm 0.10$  suggesting no significant correlation exists in the PDS. There are only two stations (1326 and 2014) with high  $r_1$  values suggesting the existence of significant correlation between successive peaks. In these two stations the computed  $r_1$  values reach the upper and lower limits of -1.0 and +1.0 as can be seen in Figure 4.3. This may cause errors in data or some local condition which gives rise to the observed correlation. Hence, the selected peaks in the PDS at these stations can be regarded as being significantly correlated and dependent.

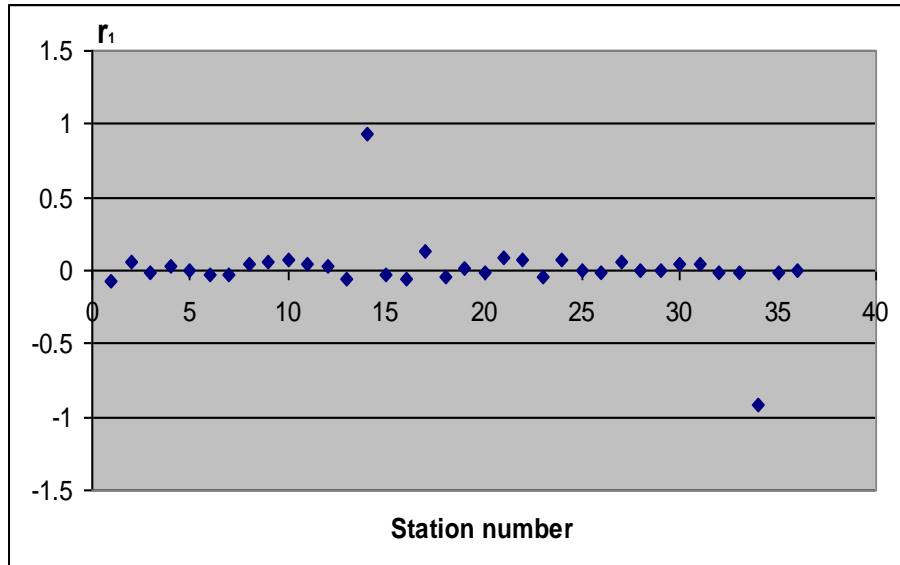


**Figure 4.3** Lag-1 autocorrelation over the selected study stations

In the trend test, the Mann-Kendall probabilities computed from absolute Z values are less than the 95% confidence level at almost all stations. This means that no trend exists in the PDS. Only two stations (1564 and 1797) where the computed probabilities for the PDS5 are about 97% being slightly greater than the confidence level suggest a decreasing or an increasing trend presented in the corresponding PDS5 models.

Therefore, the PDS series at four out of the 36 stations does not satisfy the prerequisite for statistical frequency analysis and are subsequently removed from the study. In summary, the results of the above noted tests confirm that the PDS series at the different stations are random and free from significant trend.

#### **4.4.2. Verification of the Poisson distribution for the changes in peak occurrences**

This section examines whether or not the arrival of random and independent PDS peaks follows the Poisson distribution. In order to conduct these tests, the number of peaks occurring in each year is determined at each station using the five different  $\lambda$  values. Then, the dispersion index  $d$  and the Variance-to-Mean ratio  $R$  are calculated accordingly. These tests are conducted with the 32 stations where the assumptions of randomness and stationarity are satisfied.

##### **4.4.2.1 Fisher test**

The results of the Fisher test are summarized in Table 4.1. The table shows the percentage of stations satisfying the Poisson assumption in each of the climatic zones noted in the section dealing with the study region and data (Section 3.2.1). Inspection of the table shows that the Poisson assumption is satisfied at all stations for PDS1, PDS2 and PDS3. In the case of PDS4 and PDS5, the percentage of stations satisfying the Poisson assumption varies from zone to zone. The table also shows that the Central North Island has the lowest percentage of stations satisfying the Poisson assumption. In general, PDS4 is better than PDS5 in terms of the percentage of stations satisfying the Poisson assumption.

##### **4.4.2.2 Variance-to-Mean ratio test**

The Poisson process is strongly dependent on the variability of the arrival rate ( $\lambda$ ) which is a unique parameter controlling the Poisson frequency distribution. In the Variance-to-Mean ratio diagram, if the  $R$  values tend to approach or fluctuate around the line  $R = 1$  then the Poisson assumption is accepted for the chosen  $\lambda$  value. Table 4.2 shows the percentage of stations satisfying the Poisson assumption.

Inspection of Table 4.2 indicates that the Poisson assumption is not satisfied in the case of PDS1 for all zones. In the case of PDS2, PDS3, PDS4 and PDS5, the percentage of stations satisfying the Poisson assumption varies from zone to zone. Further examination of Table 4.2 reveals that PDS4 and PDS5 have the highest percentages of stations satisfying the Poisson assumption.

**Table 4.1** Summary of acceptance of the Poisson hypothesis based on the Fisher dispersion (F) test (in percentage, %)

Climatic zone	Percentage of stations where the Poisson assumption is satisfied					Stations not satisfying the Poisson assumption <sup>(*)</sup>
	PDS1	PDS2	PDS3	PDS4	PDS5	
Northern North Island	100	100	100	67	58	1155 <sup>λ=5</sup> ; 1200 <sup>λ=4,5</sup> ; 1283 <sup>λ=4,5</sup> ; 1322 <sup>λ=4,5</sup> ; 1330 <sup>λ=4,5</sup>
Central North Island	100	100	100	66.7	33.3	1581 <sup>λ=5</sup> ; 2312 <sup>λ=4,5</sup>
South-West North Island	100	100	100	80	80	3718 <sup>λ=4,5</sup> ; 3384 <sup>λ=4,5</sup>
Eastern North Island	100	100	100	91.7	83.3	2633 <sup>λ=4,5</sup> ; 2859 <sup>λ=5</sup>

<sup>(\*)</sup> Location of the stations can be found in the Fig.4.1

**Table 4.2** Summary of acceptance of the Poisson hypothesis based on the Variance-to-mean ratio (R) test (in percentage, %)

Climatic zone	Percentage of stations where the Poisson assumption is satisfied					Stations not satisfying the Poisson assumption <sup>(*)</sup>
	PDS1	PDS2	PDS3	PDS4	PDS5	
Northern North Island	0	0	40	67	67	1022 <sup>λ=1,2,3</sup> ; 1037 <sup>λ=1,2,3</sup> ; 1155 <sup>λ=1,2,4</sup> ; 1200 <sup>λ=1,2,5</sup> ; 1283 <sup>λ=1,2</sup> ; 1322 <sup>λ=1,2,3</sup> ; 1330 <sup>λ=1,2,3</sup> ; 1410 <sup>λ=1,2,3,4</sup> ; 1500 <sup>λ=1,2,3,4,5</sup> ; 2011 <sup>λ=1,2,3</sup> ; 1545 <sup>λ=1,2,3,5</sup> ; 1874 <sup>λ=1,4</sup>
Central North Island	0	0	0	0	33.3	1581 <sup>λ=1,2,3,4,5</sup> ; 2250 <sup>λ=1,2,3,4</sup> ; 2312 <sup>λ=1,2,3,4,5</sup>
South-West North Island	0	16.7	50	60	60	3178 <sup>λ=1,2,3</sup> ; 3213 <sup>λ=1,2,3</sup> ; 3384 <sup>λ=1,2,4,5</sup> ; 3554 <sup>λ=1,2</sup> ; 3715 <sup>λ=1,2,3,4,5</sup>
Eastern North Island	0	16.7	33.3	66.7	75	2480 <sup>λ=1,2,3</sup> ; 2527 <sup>λ=1,2</sup> ; 2563 <sup>λ=1,2,3</sup> ; 2633 <sup>λ=1,3,4,5</sup> ; 2684 <sup>λ=1,2,4</sup> ; 2797 <sup>λ=1</sup> ; 2859 <sup>λ=1,2,3,4,5</sup> ; 2979 <sup>λ=1,2,3,4,5</sup> ; 3044 <sup>λ=1,2,3</sup> ; 3037 <sup>λ=1,2,3</sup> ; 3103 <sup>λ=1,2,3</sup> ; 3120 <sup>λ=1,2</sup>

<sup>(\*)</sup> Location of the stations can be found in the Fig.4.1.

Figure 4.4 shows a Box-Plot of the R values obtained at the different stations for the five integer  $\lambda$  values. Examination of the figure indicates that the mean R values increase with the increase in the value of  $\lambda$ . In the case of  $\lambda = 1$ , all the R values are less than one. In the case of  $\lambda = 2$ , the majority of R values are less than one. In the case of  $\lambda = 4$  and  $\lambda = 5$ , most of the R values are greater than one. In the case of  $\lambda = 3$ , there is an approximately an even split between R values greater than one and R values less than or equal to one. The figure also suggests that the variability in the R values increases with the increase in the value of  $\lambda$ .

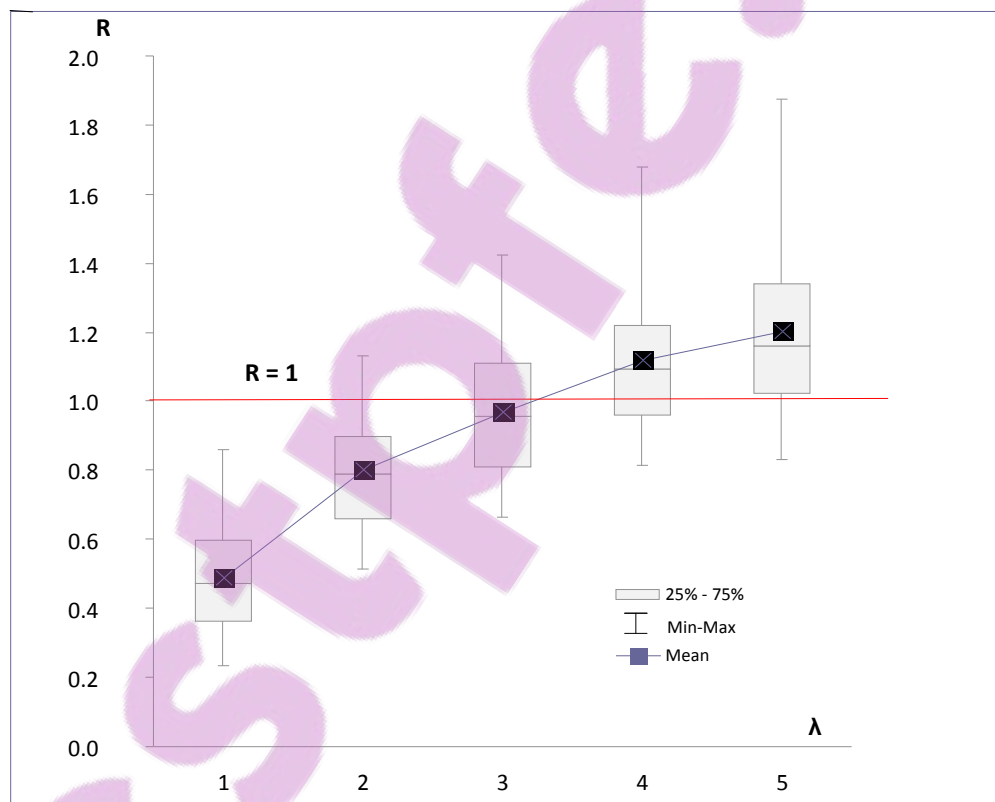


**Figure 4.4** Distribution of R-statistic of the study sites at varying  $\lambda$  values: Upper and lower ranges (lines) are the results from the individual R and averaged regional R (■)

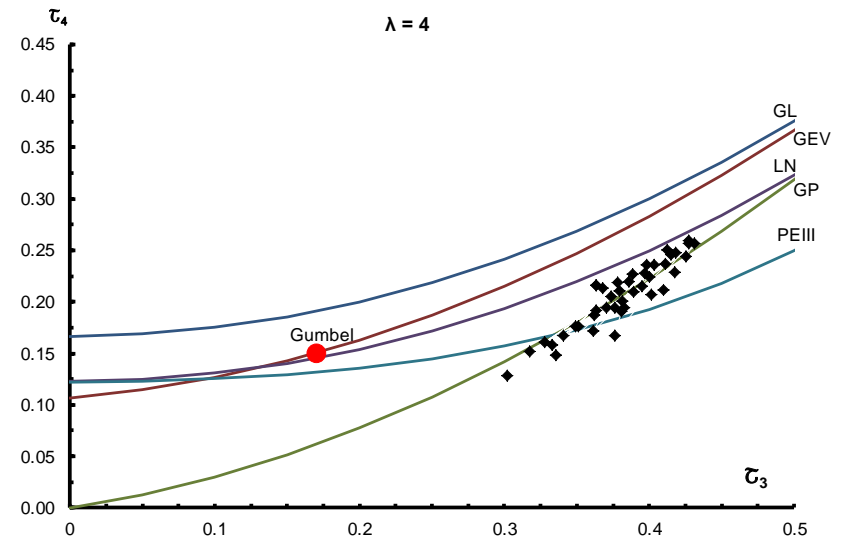
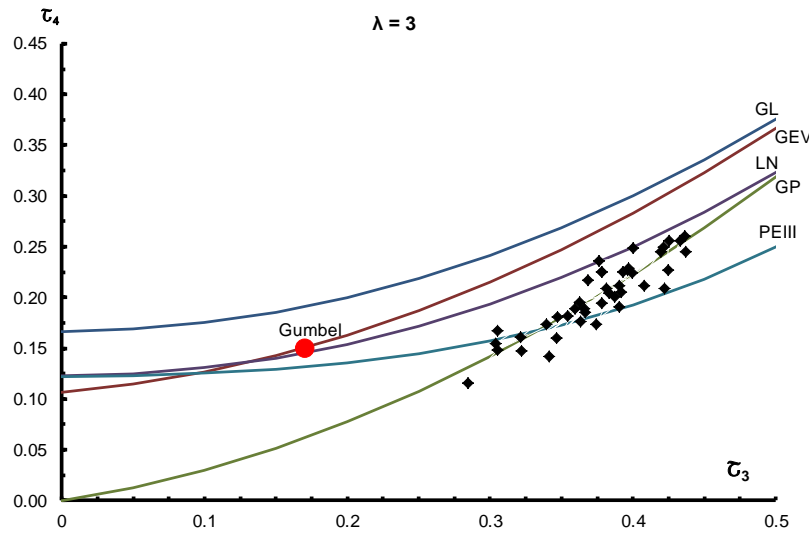
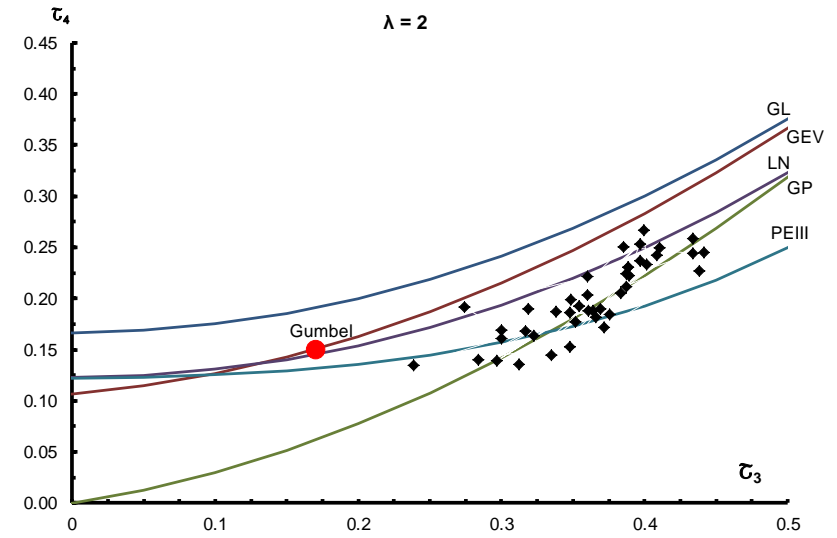
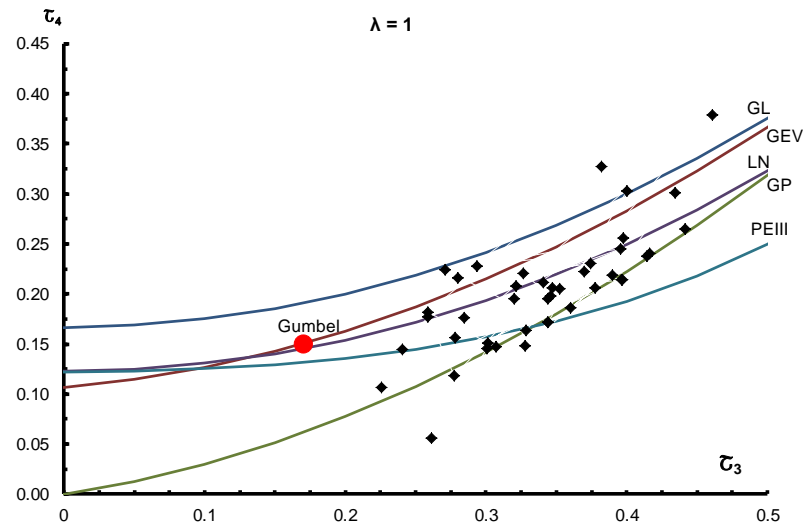
Comparison of the Fisher and the Variance-to-Mean ratio tests shows that these two tests can give conflicting results with regard to the satisfaction of the Poisson assumption. For example in the case of  $\lambda = 1$ , the Fisher test results indicate that the Poisson assumption is satisfied at all stations, while the Variance-to-Mean ratio test results suggest this assumption is not satisfied at any station. This can be explained by the fact that the mean and the variance may be sensitive to the sample size. Therefore, this comparison suggests the simultaneous satisfaction of the Poisson assumption based on these two tests can only be achieved in the majority study region for  $\lambda$  values greater than or equal to four. This conclusion is based on the fact that majority of the stations used in this study satisfies both the Fisher and the Variance-to-Mean ratio tests for a certain value of  $\lambda$ . In other words, if a test is not satisfied at any of regions then the entire study region could be rejected in this regard. It is worth noting that the entire study region is assumed to be statistically homogenous.

#### **4.4.3. Selection of a frequency distribution**

This section investigates which probability distribution is the best in describing the obtained PDS based on visual inspection of the L-MOM ratio diagram. This diagram shows the theoretical relationships between  $\tau_3$  and  $\tau_4$  for different probability distributions. A suitable distribution can be selected based on the closeness of the sample  $\tau_3$  and  $\tau_4$  values to the theoretical relationship of the distribution.

Figure 4.5 shows the theoretical  $\tau_3 \sim \tau_4$  for six probability distributions together with the sample  $\tau_3$  and  $\tau_4$  values obtained at different stations for the five integer  $\lambda$  values. These six probability distributions are the Generalized Logistic (GL), the Generalized Extreme value (GEV), the 3-paramters Log Normal (LN3), the Pearson Type III (PEIII), the Gumbel and the Generalized Pareto (GP) distributions. Examination of the figure shows

that in the case of  $\lambda = 1$  the sample  $\tau_3$  and  $\tau_4$  values scatter over a wide region indicating that there is a variety of distributions which can be used for frequency analysis of the PDS series at each station. However, as the value of  $\lambda$  increases the sample  $\tau_3$  and  $\tau_4$  values tend to cluster around the theoretical  $\tau_3 \sim \tau_4$  curve of the GP distribution with better fit being obtained for  $\lambda = 4$  and  $\lambda = 5$ .



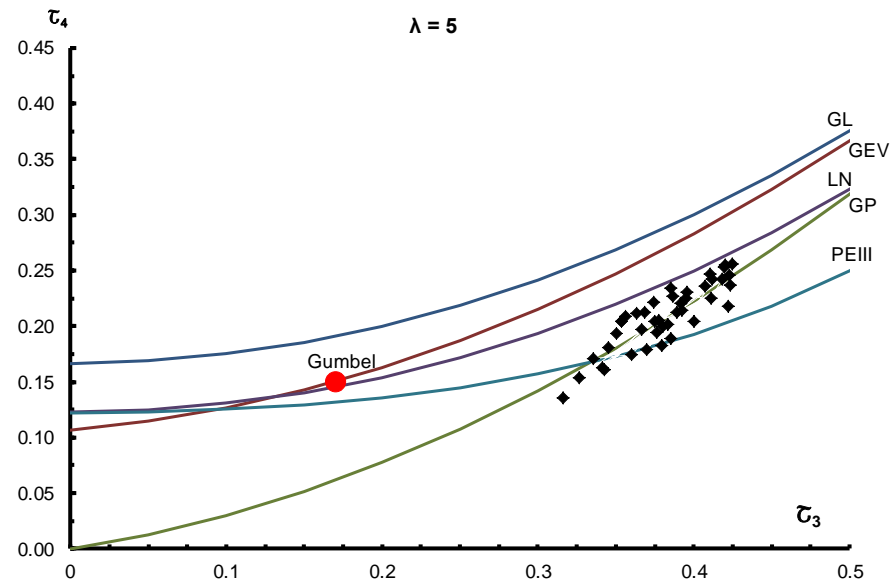


**Figure 4.5** L-MOM diagram, expressing the suitability of PDS with different distribution models

Figure 4.6 shows the variability of the sample  $\tau_3$  and  $\tau_4$  values with the change in the  $\lambda$  values for four stations representing the various regions. These stations are 1037, 1581, 2527, and 3554 representing the Northern, the Central, East Northern and the South-Western regions, respectively. The figure also shows the theoretical  $\tau_3 \sim \tau_4$  curve of the GP distribution. Examination of the figure indicates that the fitting of GP theoretical curve varies from station to station depending on the value of  $\lambda$ . For example, in the case of station 3554, the GP distribution can be regarded as an acceptable description for the PDS series for the five  $\lambda$  values. However, in the case of station 1307 the GP distribution can only be regarded as an acceptable description for the PDS series for  $\lambda = 2$  and  $\lambda = 5$ .

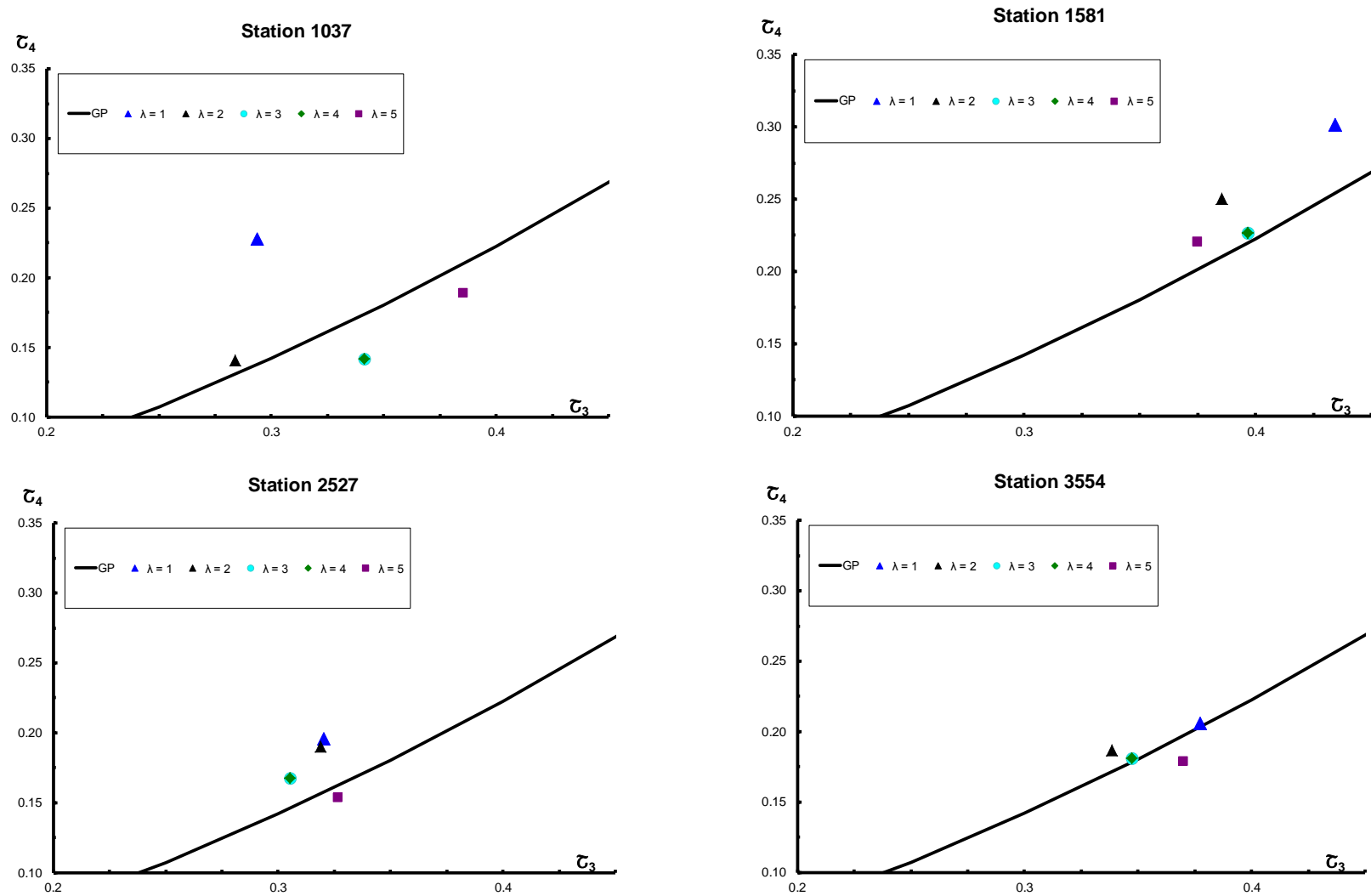


Figure 4.6 L-MOM diagram, expressing the sensitivity of  $C_s$  against  $C_k$  in GP at selected stations

#### 4.4.3.1 Stability of distribution parameters

This part of the study investigates variability in the statistical properties of PDS and the parameter values of the GP distributions with the increase in the value of  $\lambda$  (see Table 4.3). The statistical properties examined in this section are the mean and the Coefficient of variation ( $C_V$ ) of the corresponding PDS. Furthermore, the investigation includes a comparison of location ( $\zeta$ ), scale ( $\alpha$ ) and shape ( $k$ ) parameters in conjunction with L-MOM of the GP distributions for different  $\lambda$  values. The comparison is made accordingly in the Auckland region as an example (Table 4.3). Fundamentally, a GP/PDS model is stabilized if parameter values of  $k$  and  $\alpha$  are approximately constant or have minor variability with the increase in the  $\lambda$  value.

Table 4.3 illustrates that the variability of the GP distribution parameters are strongly dependent on the value of  $\lambda$ . The value of the GP parameters varies along with the change in  $\lambda$  value but tend to be stabilised with the increase in the value of  $\lambda$ . At all stations, there is a significant decrease in the value of the three GP parameters when the  $\lambda$  value increases from one to two. However, there is a gradual decrease in the value of these parameters when the  $\lambda$  value increases beyond two. In particular, the variability of the GP location parameters ( $\zeta$ ) is the most sensitive with the increase in the value of  $\lambda$ , compared to the GP scale ( $\alpha$ ) and shape ( $k$ ) parameters but become constant at  $\lambda = 5$ .

**Table 4.3** The PDS mean and  $C_v$  values as well as GP distribution parameters estimated for different  $\lambda$  values for selected stations in the Northern North Island

St. No.	$\lambda$	1	2	3	4	5
1283	$X_o$ (mm)	115.12	95.95	85.55	78.18	72.43
	$C_v$	0.31	0.33	0.35	0.37	0.39
	$\xi$	86.85	68.13	59.92	52.70	46.84
	$\alpha$	24.21	26.19	22.96	23.53	24.29
	$k$	-0.14	-0.06	-0.10	-0.08	-0.05
1322	$X_o$ (mm)	98.95	81.74	72.60	66.44	61.66
	$C_v$	0.24	0.30	0.33	0.35	0.37
	$\xi$	71.38	56.87	50.06	44.93	40.49
	$\alpha$	32.48	24.78	20.52	19.26	19.12
	$k$	0.18	0.00	-0.09	-0.10	-0.10
1330	$X_o$ (mm)	103.73	86.80	77.15	70.30	64.95
	$C_v$	0.27	0.30	0.33	0.35	0.38
	$\xi$	74.35	62.38	53.53	46.69	41.22
	$\alpha$	28.68	21.51	21.31	22.04	22.68
	$k$	-0.02	-0.12	-0.10	-0.07	-0.04
1410	$X_o$ (mm)	92.83	75.72	66.43	60.51	56.13
	$C_v$	0.35	0.38	0.41	0.42	0.44
	$\xi$	68.68	52.03	44.06	40.00	36.69
	$\alpha$	17.81	20.46	19.33	16.84	15.75
	$k$	-0.26	-0.14	-0.14	-0.18	-0.19
1500	$X_o$ (mm)	77.99	65.32	58.14	53.14	49.24
	$C_v$	0.23	0.28	0.31	0.33	0.36
	$\xi$	58.03	46.59	40.15	35.64	31.77
	$\alpha$	22.54	19.19	17.73	16.88	16.99
	$k$	0.13	0.02	-0.01	-0.04	-0.03

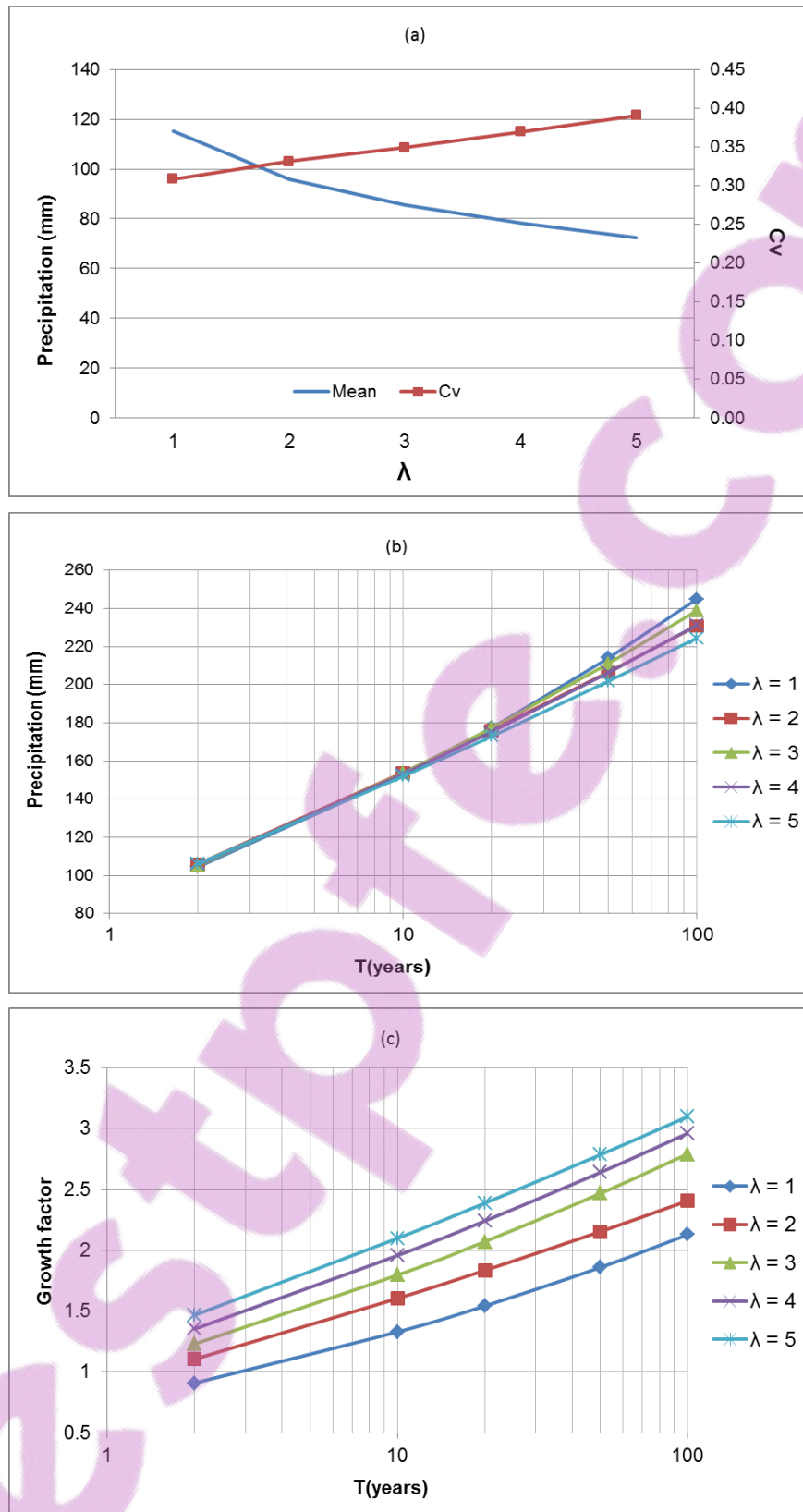
(Note:  $X_o$  – mean daily precipitation,  $C_v$  – variation coefficient,  $\xi$  – location parameter,  $\alpha$  – scale parameter, and  $k$  – shape parameter)

Figure 4.7 shows how the PDS mean and  $C_V$  values vary with the increase in the value of  $\lambda$  for station 1283 as an example. Examination of Figure 4.7a indicates that the increase in the value of  $\lambda$  will result in a decrease in the mean value and hence a decrease in the value of the location parameter as can be seen from Table 4.3 in the case of the other stations.

Further examination of the figure shows that the  $C_V$  value increases with the increase in the value of  $\lambda$  as a direct consequence of the increased variability in the corresponding PDS. The effects of the increase in the  $C_V$  value with  $\lambda$  can be seen in a plot of dimensionless frequency curves for different values of  $\lambda$  (see Figure 4.7c). The dimensionless frequency curves shown in Figure 4.7b are obtained by normalizing the original frequency curve by the corresponding mean value (growth factor),  $x_T = \frac{X_T}{\bar{X}}$ .

Inspection of Figure 4.7b reveals that the higher the  $C_V$  value, the steeper is the dimensionless frequency curves implying higher quantile estimates. In this case, the dimensionless frequency curve for  $\lambda = 5$  will be steeper than those obtained for the other values of  $\lambda$ .

Although, the PDS mean decreases and the dimensionless frequency becomes steeper with the increase in the value of  $\lambda$  their effects may cancel each other. Figure 4.7b shows that the frequency curves for different values of  $\lambda$  yield similar results for the return period less than or equal to 10 years. The difference in frequency curves will become more noticeable for high return periods. Further examination of Figure 4.7b shows that the frequency curves of  $\lambda = 1$  gives upper bound while  $\lambda = 5$  gives the lower bound. The observed behaviour seen in Figure 4.7c is the result of the compensation effects between the mean and the  $C_V$  as the value of  $\lambda$  increases.



**Figure 4.7** Plot of variation of the PDS mean and  $C_v$  (a); frequency curve (b); and dimensionless frequency curve (c) for different values of  $\lambda$

## 4.5. Summary

This chapter gave detailed information on how to extract the most reliable extreme precipitation from observation data. Firstly, the autocorrelation and the Man-Kendall tests were used to detect the existence of dependence and trend in PDS series obtained from observation. This ensures that a certain threshold level or a number of peaks per year  $\lambda$  generates the corresponding stationary PDS series. Secondly, the Fisher (F) and Variance-to-Mean ratio (R) tests were also used to test whether or not the selected peaks from the PDS series are random and independent. Finally, the L-moment ratio diagram was used to test the suitability of the Generalized Pareto (GP) distribution for frequency analysis of the PDS series. In a line, the sensitivity of the parameters of the GP distribution was also examined with changes in the value of  $\lambda$ .

In this research, the daily partial duration series of precipitation (PDS) for 36 stations located in the North Island of New Zealand were examined. The examination involved the use of five different PDS series obtained by setting the average number of peaks  $\lambda$  equal to 1, 2, 3, 4 and 5. The results of F and R tests showed that these two tests can give conflicting results with regard to satisfaction of the Poisson assumption and that a higher value  $\lambda$  is required for simultaneous satisfaction of the Poisson assumption based on these two tests. The L-moment ratio diagram demonstrated that for small  $\lambda$  values it was found that a variety of distributions can be used for frequency analysis of the PDS at each station. However, the GP distribution is the most suitable distribution for frequency analysis of the PDS when  $\lambda$  is equal to or greater than 4. The sensitivity test of the parameters of the GP distribution to changes in the value of  $\lambda$  also confirmed that the parameter values vary with the change in the value of  $\lambda$  can reach constant values with the increase in the value of  $\lambda$ . Therefore, in the application of PDS in the North Island of New Zealand, a value of  $\lambda$

greater than or equal to 4 is preferable. This value could satisfy the assumption made in the Poisson and the GP models.

## CHAPTER 5

# Regional extreme precipitation analysis

This chapter includes partial reproduction of the paper:

Pham, H. X., Shamseldin, A. Y. and Melville, B. W. (2013). Statistical properties of partial duration series and its implication in frequency analysis. *J. Hydrol. Eng.* 19(7): 1471-1480.

This chapter introduces the new implication of a regional frequency analysis (RFA) that is used to validate the extracted PDS model. The initial section of the chapter presents the rationale of the use of the RFA. Its basic requirements are explained in the next section including different statistical and computational tests. The final section discusses the results of those tests and then an optimum PDS is confirmed for the study region.

## 5.1. Introduction

Even though the use of Partial Duration Series (PDS) is considered plausible for the North Island of New Zealand with the number of average peaks per year ( $\lambda$ ) being greater than or equal to 4, this investigation is carried out at single stations. However, there are only limited studies which address this difficulty when the PDS is used in the context of regional frequency analysis (RFA). An optimum regional value of  $\lambda$  for the North Island of New Zealand is determined by examining the performance of the PDS when used in a regional frequency analysis. In particular, this study develops a regional frequency function of PDS defined by a regional unique-optimum value of  $\lambda^R$ . The suitability of a number of frequency distributions to be used in the regional frequency is examined. The Generalized Pareto (GP) best described the PDS. The  $\lambda^R$  value is optimized from both at-site and regional PDS series, which is expected to yield the most reliable quantiles for both small and large return periods. A D/E procedure that employs the distribution D and an estimation method of E, is used for the PDS4 and PDS5 series extracted from 32 relevant stations across the North Island region of New Zealand. The details of data used are described in Chapter 4.

## 5.2. Methods and techniques

This section presents the methods used to examine the validity of the PDS/GP model for modelling PDS4 and PDS5. Even though these are confirmed to be appropriate models at individual sites, it is very important to test their performance in a regional frequency analysis, which ensures the parent distribution is valid for the whole region and for different return periods (Cunnane, 1988).

A regionalization D/E procedure is widely used in regional frequency analysis (Hosking and Wallis, 1993; Fowler and Kilsby, 2003; Trefry et al., 2005; Norbiato et al., 2007; Saf, 2009). The D/E procedure includes several steps: firstly, observed data is screened for gross errors, inconsistencies, shifts and trends at-sites. Secondly, statistically homogeneous regions are defined from given sites. In this step, at-site data is pooled in a group. Thirdly, all L-moment ratios are regionalised from sites in a homogenous region. Fourthly, a robust regional frequency distribution is selected. Finally, the validity of the regional distribution is assessed based on at-site and regional quantiles.

As one prerequisite of the regional frequency analysis, the first step of D/E procedure is very important to ensure that input data is accurate and adequate for analysis. It has been tested using Lag-1 autocorrelation and Mann-Kendal trend tests dealing with randomness and stationarity of successive peaks selected in PDS5 (refer to Chapter 4, Section 4.3).

### **5.2.1. Identification of homogeneous regions**

This section describes several statistical tests commonly used to identify a homogenous region from at-site data. This is comprised of discordancy ( $D_i$ ) and heterogeneity (H) measures using the sample L-Moment (L-MOM) ratios (Das and Cunnane, 2010; Saf, 2010; Yang et al., 2010).

#### **5.2.1.1. Discordancy Measure ( $D_i$ )**

The discordancy measure is based on the difference between the L-MOM ratios of a site and the average L-MOM ratios of a group of similar sites. This can be used not only to identify erroneous data, but also to aid in defining homogeneous regions. However, it is recognized that a site's L-MOM may differ from other similar sites by chance alone (Adamowski, 2000; Trefry et al., 2005).

The discordancy measure is based on a discordancy index ( $D_i$ ) that is defined for site  $i$  within  $N$  sites in a region. Its general form is given by:  $D_i = D[N, \tau^{(i)}, \tau_3^{(i)}, \tau_4^{(i)}]$ , with  $\tau$ ,  $\tau_3$ ,  $\tau_4$  being the L-MOM coefficients of variation, skewness and kurtosis, respectively.

Generally, any site with  $D_i > 3$  can be regarded as region discordant, and then it could be moved to another region. However, this may be caused by only a few unusual rainfall events (Hosking and Wallis, 1997; Fowler and Kilsby, 2003; Yang et al., 2010).

### 5.2.1.2. Heterogeneity Measure (H)

Once the accordant sites are defined, stations can be grouped to form one region. However, this is usually done subjectively by using a number of selected site characteristics (i.e., latitude, longitude, elevation, and mean annual precipitation) (Trefry et al., 2005). ‘A heterogeneity measure based on the H-statistic is then used to compare the between site variation in sample L-MOM for a group of sites with what would be expected for a homogeneous region’ (Hosking and Wallis, 1997).

The H-statistic for  $N$  sites is given by:

$$H_j = \frac{V_j - \mu_v}{\sigma_v} \quad (5.1)$$

where  $\mu_v$ , and  $\sigma_v$  are mean and standard deviation of the computed inter-site variation; and  $V_j$  is the standard deviation of each generated region. In particular,  $V_1$ ,  $V_2$  and  $V_3$  are standard deviation of variation, the L-MOM coefficients of variation, skewness and kurtosis, respectively.

$V$  is calculated from the region data based on a corresponding V-statistics bellows:

$$V_1 = \frac{\sum_{i=1}^N n_i (\tau_{v,i} - \bar{\tau}_v)^2}{\sum_{i=1}^N n_i} \quad (5.2)$$

$$V_2 = \frac{\sum_{i=1}^N \left[ n_i \sqrt{(\tau_{v,i} - \bar{\tau}_v)^2 + (\tau_{3,i} - \bar{\tau}_3)^2} \right]}{\sum_{i=1}^N n_i} \quad (5.3)$$

$$V_3 = \frac{\sum_{i=1}^N \left[ n_i \sqrt{(\tau_{3,i} - \bar{\tau}_3)^2 + (\tau_{4,i} - \bar{\tau}_4)^2} \right]}{\sum_{i=1}^N n_i} \quad (5.4)$$

The value of H less than 1.0 indicates that the region is acceptably homogeneous. The value of H between 1.0 and 2.0 indicates possibly homogeneous region. If H value is greater than 2.0, the region may be regarded as heterogeneous.

In practical applications, the value of  $H_1$  is usually greater than  $H_2$ , and  $H_2$  is greater than  $H_3$ . This is due to the existence of sample mean variability that has already been reflected in natural sample variability at single sites (Hosking and Wallis, 1993; Trefry et al., 2005). Therefore, the combined use of the  $H_1$ ,  $H_2$  and  $H_3$  is a better option in testing of homogeneity. In order to reduce uncertainty due to in-site variability when the tests take place at individual sites, 500 repeated Monte-Carlo simulations are performed. This basically simulates a homogeneous region with sites having record lengths equal to those of the observed data (Adamowski, 2000).

### 5.2.2. Regional frequency distribution

This part of the study deals with choosing and verifying the most appropriate frequency distribution from at-site data as well as making it valid for a statistically homogenous region. Goodness-of-Fit and Robustness tests are the two measures to help in the selection of appropriate regional frequency. Regional L-MOM ratios need to be computed beforehand.

### 5.2.2.1. Regionalization

This step aims at determining regional weighted average L-MOM ratios according to record length used to identify a regional frequency distribution apart from at-site data (Trefry et al., 2005; Yang et al., 2010).

If there are  $N$  sites in a region with sample size  $n_1, n_2, \dots, n_N$ , respectively and the sample L-MOM ratios at site  $i$  are denoted as  $t_r^i$  with the  $r$ -order of L-MOM ratios then the regional weighted average L-MOM ratios are defined:

$$t_r^R = \frac{\sum_{i=1}^N n_i t_r^i}{\sum_{i=1}^N n_i} \quad (5.2)$$

### 5.2.2.2. Goodness-of-Fit test using L-MOM ratio diagram and Z-statistic

In the context of regional frequency analysis, the goodness-of-fit test is used to measure whether or not the data of a particular site are consistent with the fitted probability distribution to that site. This measure is also useful to reduce inter-sampling variability (Hosking and Wallis, 1993).

In this section, a regional distribution is defined from candidate distributions at-site as well as from theoretical distributions. This will be examined based on the Z-statistic and the L-MOM ratio diagram with five candidate distribution models, namely, Log Normal (LN), Generalised Extreme Value (GEV), Generalised Pareto (GP), Pearson Type III (P3), and Generalised Logistic (GL) which are arguably alternatives for fitting PDS series (Jaiswal et al., 2003). Goodness-of-fit measures with 500 Monte-Carlo simulations will be estimated not only to minimise model errors, but also to maximise model fitness (ShinYie and Ismail, 2012).

The Z-statistic determines how well the L-MOM ratios of the candidate (theoretical) distribution match with the regionally averaged L-MOM ratios. Theoretically, best regional distribution is defined if its Z value is the smallest being close to zero.

The Z-statistic is defined for a particular distribution:

$$Z_4^{dist} = \frac{\bar{\tau}_4^R - \tau_4^{dist} + B_4}{\sigma_4} \quad (5.3)$$

where  $\tau_4^{dist}$  is the theoretical L-Kurtosis of the fitted distribution,  $t_4^R$  is the regional weighted average L-Kurtosis,  $B_4$  is a bias correction factor obtained by fitting a GP distribution to the regional average L-moments and repeated Monte Carlo simulation experiments similar to the heterogeneity test and  $\sigma_4$  is the standard deviation of the  $t_4^R$  obtained from the Monte Carlo simulation experiments.

The distribution giving the minimum  $|Z^{dist}|$  but also less than 1.64 is considered the best-fit-distribution at the 90% of confidence level (Trefry et al., 2005). Furthermore, it is concluded that a distribution with more parameters, e.g., 3 parameter-GP distribution, would be less biased and provides more accurate quantile estimation.

Alternatively, the L-MOM ratio diagram based on  $\tau_3$  and  $\tau_4$  coefficients has been widely used as a direct measure for selecting the best-fit-distribution (Cunnane, 1983). This gives a visual identification of appropriate regional distribution by examining the closeness of observed data towards a presumed distribution. The diagram also allows the selection of a better PDS model to be used in conjunction with the regional distribution.

### 5.2.2.3. Robustness Test

The purpose of this test is to estimate errors due to the distribution assumption. It means that best fitted distribution defined for the whole region is assessed again with the observed at-site data.

Robustness of the candidate distribution is measured by comparing the bias, the standard error of estimate (SE) and the root mean square error (RMSE) of the estimated extreme quantiles when the distribution is correctly specified, and when the distribution is misspecified (Birikundavyi and Rousselle, 1997; Madsen et al., 1994). The bias, B, SE and RMSE are given by:

$$B = E(X_{test} - X_T) = X_{test} - X_T \quad (5.4)$$

$$SE = \sqrt{E(X_{test} - X_T)^2} = \sqrt{\frac{\sum (X_{test} - X_T)^2}{N-1}} \quad (5.5)$$

$$RMSE = \sqrt{E(X_{test} - X_T)^2} = \sqrt{\frac{(X_{test} - X_T)^2}{N}} \quad (5.6)$$

where  $X_{test}$  and  $X_T$  are the regionally estimated and at-site observed quantiles of extreme precipitation, respectively, using the same candidate distribution.

### 5.2.3. Monte-Carlo simulation/repetition

Monte-Carlo method relies on repeated random sampling to obtain numerical results. Typically, one runs simulations many times over in order to obtain the distribution of unknown probabilistic entity. The simulation procedure for each of the above cases was organized in the following steps:

- Specify the region in terms of the number of sites and record lengths at each site same as those in corresponding real world region

- Calculate the at-site parameters of the underlying frequency distribution based on the sample L-moment ratios
- Calculate the at-site quantiles of known exceedence probabilities based on the at-site frequency distributions and store them for calculation of the accuracy measures.

For each of the 500 times

- Using the underlying distribution, generate random sample data of the same lengths as those of the sites in real world region
- Calculate at-site L-moment ratios and regional average L-moment ratios at all the sites in the simulated region
- Fit the candidate distribution
- Calculate estimates of the regional growth curve and at-site quantiles
- Calculate the relative bias and RMSE of the estimated quantiles at each site and accumulate them for the purpose of calculating their average over all the simulated regions
- Calculate the regional average relative bias, regional average absolute relative bias and regional average RMSE of the estimated quantiles over all the sites in the region.
- The distribution that produces the least biased estimates is the most robust.

#### 5.2.4. Regional quantile estimation

Estimation is done on a basis of computed regional distribution frequency by GPA as being examined in at-site scale.

$$X_T^r = \zeta^r + \frac{\alpha^r}{k^r} \left[ 1 - \left( \frac{1}{T} \right)^{k^r} \right] \quad (5.7)$$

Regional GPA shape parameter is given by:

$$k^r = \frac{1 - 3\tau^r_3}{1 + 3\tau^r_3} \quad (5.8)$$

Regional GPA scale parameter is given by:

$$\alpha^r = (1 + k^r)(2 + k^r)\lambda^r_2 \quad (5.9)$$

Regional GPA location parameter is estimated as:

$$\xi^r = \lambda^r_1 - (2 + k^r)\lambda^r_2 \quad (5.10)$$

Together with quantile estimations, growth factors are another common indicator in a frequency analysis. In practice, the growth factor should be used at site for which PDS are available in conjunction with the at-site estimate of mean annual precipitation ( $\bar{X}$ ).

Ungauged catchment precipitation estimation should also use regional growth factor ( $x_T$ ) along with  $\bar{X}$  estimated from a regionally validated relation between  $\bar{X}$  and catchment characteristics. Where records are short or non-existent the uncertainty associated with the  $\bar{X}$  estimate overwhelms that associated with the  $x_T$ .

Both the regional and at-site growth factors are as follows:

$$x_T = \frac{X_T}{\bar{X}} \quad (5.11)$$

where:  $x_T$  is a growth factor for T year return period (mm),  $X_T$  is a precipitation estimate for T year return period (mm) and  $\bar{X}$  is a mean annual precipitation (mm)

## 5.3. Results and discussions

### 5.3.1. Overview on partial duration series (PDS) and its frequency distribution

The PDS4 and the PDS5 series from 32 stations were extracted using the Peak-Over-Threshold (POT) method (Cunnane, 1983). In particular, this was performed by fixing the number of average peaks per year (i.e. for  $\lambda = 4$  and  $\lambda = 5$ ). PDS5 at station 1155 is shown in Figure 5.1 as an example. All peaks above the threshold level ( $u$ ) were selected to generate the corresponding PDS series. These peaks were confirmed to be independent and stationary from previous chapter. The result of this study also reveals that a GP distribution best describes PDS4 and PDS5 at almost stations using L-MOM ratio diagram approach coupled with the GP distribution parameters' sensitivity. The results shown in Figure 5.2 and Table 5.1 indicate that the performance of PDS5 is better than that of PDS4. This is also clearly explained in next section.

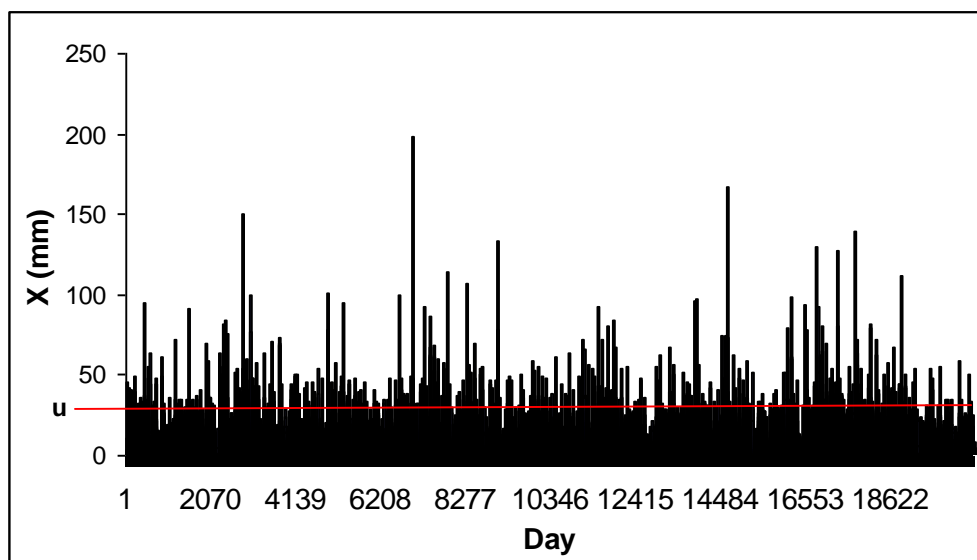


**Figure 5.1** PDS5 extracted from daily hyetograph at station 1155 with the threshold value  $u = 36.878$  mm

**Table 5.1** L-MOM ratios of PDS4 and PDS5 for 32 stations

Site	Station	PDS4					PDS5				
		N	$\lambda_1$	$\tau$	$\tau_3$	$\tau_4$	N	$\lambda_1$	$\tau$	$\tau_3$	$\tau_4$
1	1022	360	66.84	0.16	0.38	0.19	449	62.51	0.16	0.39	0.20
2	1037	252	63.33	0.16	0.38	0.16	315	59.10	0.17	0.39	0.19
3	1155	247	56.20	0.17	0.43	0.25	310	52.33	0.18	0.42	0.25
4	1200	251	70.46	0.16	0.38	0.21	315	65.62	0.17	0.36	0.21
5	1283	176	73.80	0.19	0.36	0.21	220	72.43	0.18	0.36	0.20
6	1330	172	65.57	0.19	0.37	0.21	215	64.95	0.19	0.36	0.20
7	1331	168	57.69	0.17	0.42	0.25	210	56.99	0.17	0.41	0.25
8	1372	160	72.10	0.19	0.39	0.19	200	66.72	0.20	0.40	0.20
9	1410	184	56.54	0.19	0.40	0.21	230	56.13	0.19	0.43	0.23
10	1500	228	49.11	0.18	0.36	0.19	285	49.24	0.18	0.35	0.18
11	1545	253	46.96	0.20	0.40	0.24	315	46.41	0.19	0.38	0.22
12	1581	174	52.08	0.15	0.40	0.22	289	44.71	0.17	0.39	0.22
13	1874	392	58.23	0.18	0.43	0.26	490	58.11	0.18	0.42	0.25
14	2011	192	49.25	0.18	0.38	0.20	240	49.21	0.18	0.39	0.21
15	2312	391	76.58	0.14	0.43	0.25	490	72.20	0.15	0.43	0.25
16	2480	252	53.87	0.18	0.40	0.21	315	49.87	0.19	0.39	0.22
17	2527	252	56.70	0.17	0.32	0.15	315	52.43	0.18	0.33	0.15
18	2563	252	62.54	0.19	0.38	0.19	315	57.63	0.20	0.38	0.20
19	2633	252	44.14	0.18	0.41	0.21	315	40.91	0.19	0.41	0.22
20	2684	252	49.54	0.18	0.42	0.25	315	45.98	0.19	0.42	0.24
21	2791	252	59.21	0.19	0.41	0.23	315	54.63	0.20	0.41	0.23
22	2859	252	101.63	0.18	0.38	0.20	315	93.77	0.20	0.38	0.20
23	2979	252	63.19	0.18	0.36	0.18	315	58.20	0.19	0.35	0.19
24	3037	252	59.18	0.16	0.30	0.12	315	54.87	0.18	0.32	0.13
25	3044	251	44.92	0.18	0.34	0.15	315	41.56	0.19	0.34	0.16
26	3103	418	46.83	0.17	0.37	0.19	525	43.26	0.19	0.37	0.20
27	3120	252	83.95	0.18	0.36	0.17	315	77.71	0.19	0.38	0.18
28	3178	251	50.12	0.18	0.43	0.24	315	46.41	0.19	0.42	0.24
29	3213	420	38.34	0.15	0.39	0.21	525	35.93	0.16	0.39	0.21
30	3384	252	60.72	0.14	0.39	0.22	455	51.63	0.15	0.40	0.22
31	3554	420	37.25	0.19	0.36	0.17	525	36.60	0.19	0.37	0.18
32	3715	276	34.89	0.16	0.37	0.21	370	34.94	0.17	0.39	0.23

### 5.3.2. Identification of homogenous region

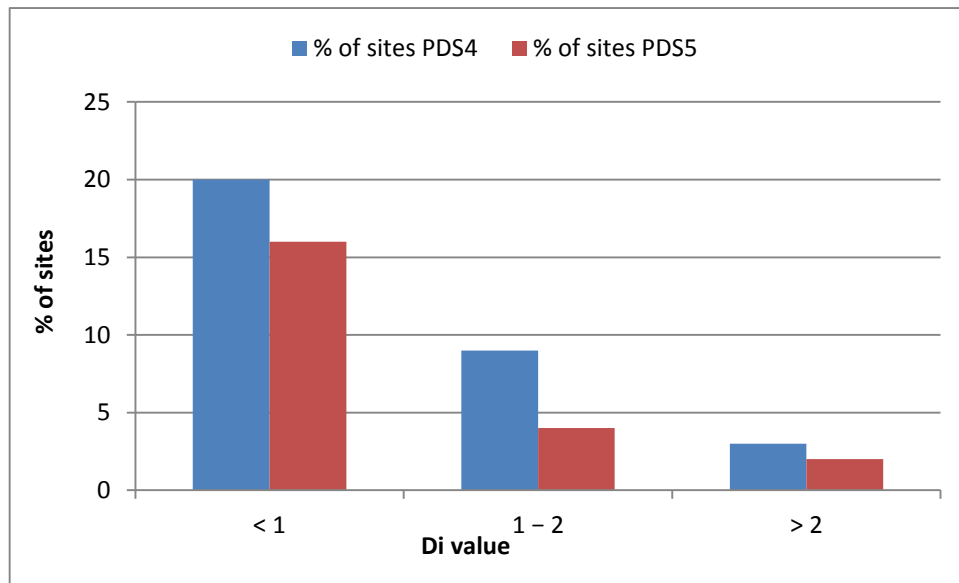
It is assumed that the 32 selected stations form a statistically homogenous region and resulting PDS series at these stations are adequate for regionalization process. The D and H statistics will be used to test this hypothesis. Results computed for both PDS4 and PDS5 are summarized in Tables 5.2 and 5.3.

Table 5.2 presents the results of the D-statistic for assessing the homogeneity of data in a group of different sites. The value of  $D_i$  varies from station to station for both PDS4 and PDS5. In the case of PDS4, there are three stations (1037, 2312 and 3037) having the value of  $D_i$  values greater than two. This suggests that the PDS4 at these stations are discordant. In the case of PDS5, the majority of the computed  $D_i$  values are less than two suggesting that these stations are accordant and thereby satisfying the assumption of regional homogeneity. There are two stations (2312 and 3037) with  $D_i$  values slightly greater than two indicating a rather less appropriate series in comparison with other stations. These sites are discordant, perhaps due to the presence of errors in data or some local condition. In general, PDS5 is considered appropriate with a minor exception in term of the value of  $D_i$ . This can be clearly seen in Figure 5.2.

**Table 5.2** Discordance ratio ( $D_i$ ) computed for PDS4 and PDS5 at station with 500 Monte-Carlo simulations

Site	Name	PDS4				PDS5			
		$\tau$	$\tau_3$	$\tau_4$	$D_i^*$	$\tau$	$\tau_3$	$\tau_4$	$D_i^*$
1	1022	0.1565	0.3824	0.1873	0.85	0.15	0.36	0.18	1.76
2	1037	0.1634	0.3786	0.1618	<b>2.41</b>	0.17	0.39	0.19	1.49
3	1155	0.1713	0.4298	0.2525	0.75	0.18	0.42	0.25	0.71
4	1200	0.1564	0.381	0.2055	0.6	0.17	0.36	0.21	1.1
5	1283	0.1874	0.3599	0.2095	1.83	0.18	0.36	0.20	1.21
6	1330	0.1931	0.367	0.2062	1.15	0.19	0.36	0.20	1.26
7	1331	0.17	0.4216	0.2497	0.65	0.17	0.41	0.25	0.72
8	1372	0.1895	0.3855	0.1889	0.83	0.20	0.40	0.20	1.51
9	1410	0.1887	0.404	0.2102	0.77	0.19	0.43	0.23	1.1
10	1500	0.1788	0.3623	0.189	0.26	0.18	0.35	0.18	0.6
11	1545	0.1976	0.3956	0.2415	1.86	0.19	0.38	0.22	1.16
12	1581	0.1538	0.4035	0.2183	0.82	0.15	0.40	0.22	1.33
13	1874	0.1835	0.434	0.2633	1.13	0.18	0.42	0.25	0.83
14	2011	0.1803	0.3834	0.2025	0.05	0.18	0.39	0.21	0.12
15	2312	0.1427	0.4337	0.2544	<b>2.43</b>	0.15	0.43	0.25	<b>2.31</b>
16	2480	0.1802	0.3974	0.2123	0.14	0.19	0.39	0.22	0.21
17	2527	0.1694	0.3187	0.1466	1.69	0.18	0.33	0.15	1.32
18	2563	0.189	0.3778	0.1911	0.41	0.20	0.38	0.20	0.65
19	2633	0.1832	0.4122	0.2082	1.35	0.19	0.41	0.22	0.71
20	2684	0.182	0.415	0.2481	0.7	0.19	0.42	0.24	0.63
21	2791	0.191	0.4133	0.2343	0.69	0.20	0.41	0.23	1.03
22	2859	0.1844	0.3758	0.2017	0.21	0.20	0.38	0.20	0.42
23	2979	0.1793	0.364	0.1834	0.18	0.19	0.35	0.19	1.2
24	3037	0.1626	0.3027	0.1223	<b>2.63</b>	0.18	0.32	0.13	<b>2.35</b>
25	3044	0.1756	0.339	0.1463	1.03	0.19	0.34	0.16	1.01
26	3103	0.174	0.3719	0.1919	0.06	0.19	0.37	0.20	0.2
27	3120	0.1828	0.3633	0.1674	0.71	0.19	0.38	0.18	1.28
28	3178	0.1836	0.4278	0.241	0.84	0.19	0.42	0.24	0.83
29	3213	0.152	0.3905	0.2074	0.82	0.16	0.39	0.21	0.79
30	3384	0.1432	0.3929	0.2239	1.87	0.15	0.40	0.22	0.98
31	3554	0.1942	0.3624	0.1724	0.95	0.19	0.37	0.18	0.71
32	3715	0.1615	0.3658	0.2082	1.33	0.17	0.39	0.23	0.49

*$D_i$  values in bold indicate inappropriate data*



**Figure 5.2**  $D_i$  statistic results for different PDS4, 5

Table 5.3 shows the H- statistic results obtained based on the 500 Monte-Carlo simulations. The values of  $H_1$  and  $H_2$  are much higher than the value of  $H_3$  for both PDS4 and PDS5. In particular, the values of  $H_1$  and  $H_2$  computed for PDS5 are higher than those for PDS4. Whereas, the values of  $H_3$  computed for PDS5 are much lower than those for PDS4. Even though the  $H_1$  statistical measure is more important compared to the  $H_2$  and the  $H_3$  measures, the combined use of  $H_1$ ,  $H_2$  and  $H_3$  statistics could be a comprehensive solution for defining statistical homogenous groupings. Therefore, the group of 32 stations can be accepted as not far from a homogenous region for both PDS 4 and PDS5.

**Table 5.3** Heterogeneity measures, H, for a homogenous region with 500 Monte-Carlo simulations

Regional parameters/index	Symbol	PDS4	PDS5	Note
Observed S.D. of pooled $\tau$	$V_1$	0.0154	0.0154	
Simulated Mean of S.D. of pooled $\tau$	$\mu$	0.0109	0.0102	
Simulated S.D. of S.D. of pooled $\tau$	$\sigma$	0.0014	0.0014	
Standardized test value H(1)	$H_1^*$	3.1000	3.7300	> 1.00
Observed average of $\tau/\tau_3$ distance	$V_2$	0.0305	0.0298	
Simulated Mean of averaged $\tau/\tau_3$ distance	$\mu$	0.0287	0.0264	
Simulated S.D. of averaged $\tau/\tau_3$ distance	$\sigma$	0.0034	0.0034	
Standardized test value H(2)	$H_2^*$	0.5200	1.0000	
Observed average of $\tau_3/\tau_4$ distance	$V_2$	0.0376	0.0356	
Simulated Mean of averaged $\tau_3/\tau_4$ distance	$\mu$	0.0392	0.0360	
Simulated S.D. of averaged $\tau_3/\tau_4$ distance	$\sigma$	0.0047	0.0048	
Standardized test value H(3)	$H_3^*$	-0.3400	-0.0800	

(Value > 1.00) indicate heterogeneous groupings

### 5.3.3. Identification of a regional frequency distribution

This part of the study deals with modelling a regional frequency analysis which best describes observed data from stations located within a statistically homogenous region. This also confirms which PDS series (between PDS4 and PDS5) is most reliable in this regard.

As a prerequisite of regionalization process, the regional L-MOM coefficients are firstly computed using equation (5.2), as shown in Table 5.4. The table indicates that there is a very slight difference among the three regional L-MOM coefficients computed for PDS4 and PDS5.

**Table 5.4** Regional L-MOM estimator for PDS4 and PDS5 (for  $\lambda = 4$  and 5) for the homogenous North Island region

Weighted average L-MOM ratios	$\tau$	$\tau_3$	$\tau_4$
PDS4	0.1739	0.3855	0.2049
PDS5	0.1790	0.3854	0.2085

#### 5.3.3.1. Goodness-of-fit test

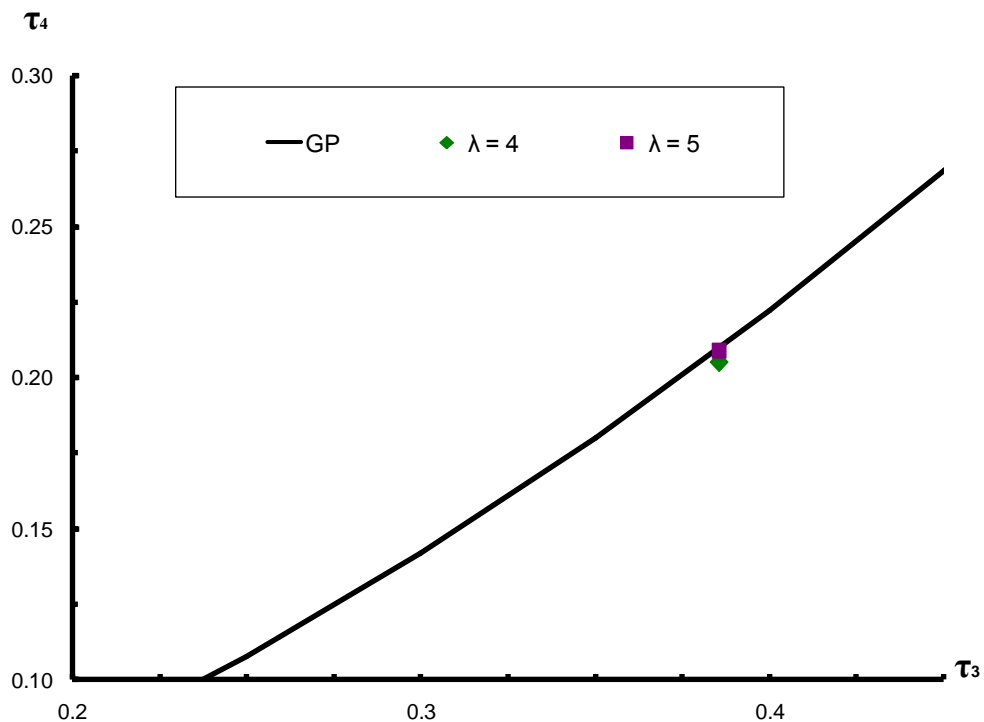
As demonstrated in the previous chapter, the GP frequency distribution is confirmed as best describing PDS4 and PDS5 for at-site analysis. In general, the PDS5/GP model relatively outperforms the PDS4/GP model. In order to investigate whether the GP would be a preferred distribution for the whole region, it is tested against other four competing distributions, namely, Generalised Logistic (GL), Generalised Normal (LN), Generalised Extreme Value (GEV), and Pearson Type III (P3). L-MOM ratio diagram and Z-statistic are performed in this context.

Table 5.5 presents the results of Z-test with 500 Monte-Carlo simulations. The table shows that for PDS4 and PDS5, the value of Z is very high in the case of the GL and the GEV distributions. For the case of LN and P3 distributions, there is a significant decrease in the value of Z. In the case of the GP distribution, the Z value is the lowest confirming its the most suitable regional distribution. This result is in line with the theoretical background in which the GP distribution best describes the PDS.

**Table 5.5** Goodness-of-fit measures with 500 Monte-Carlo simulations for different 3-parameter distributions tested with PDS4 and PDS5

Candidate distribution model	Symbol	Z-value	
		PDS4	PDS5
GEN. Logistic	GL	13.54	14.33
GEN. Extreme value	GEV	10.55	11.03
GEN. Normal	LN	5.49	5.44
Pearson Type III	P3	-3.13	-4.09
GEN. Pareto	GP	0.60	0.02

Figure 5.2 shows the regional L-MOM coefficient values for  $\tau_3$  and  $\tau_4$  computed for PDS4 and PDS5, together with a theoretical  $\tau_3$ - $\tau_4$  for the GP distribution. The figure confirms the results of the Z-statistic test, which supports the GP as an appropriate distribution to be used in conjunction with PDS4 and PDS5. Inspection of the figure shows that in the case of PDS5 the sample  $\tau_3$  and  $\tau_4$  value lies approximately on the theoretical  $\tau_3$ - $\tau_4$  curve of the GP distribution indicating that the GP distribution can be used for frequency analysis of the PDS5 series. For the case of PDS4, the sample  $\tau_3$  and  $\tau_4$  value lies slightly off the theoretical  $\tau_3$ - $\tau_4$  curve of the GP distribution. Therefore, the GP distribution is confirmed as the regional distribution having best fit in the case of PDS4 and PDS5.



**Figure 5.3** Regional L-MOM ratio diagram for PDS4 and PDS5

### 5.3.3.2. Regional quantile estimation

With the regional GP distribution, its parameters are estimated using equations (4.3) to (4.7). Also, regional quantiles with different return periods are computed using equation (4.2). The results are presented in Table 5.6 and 5.7.

Table 5.6 shows the results of the three GP parameters computed for PDS4 and PDS5. In general, there is a very small difference in these parameter values between PDS4 and PDS5.

**Table 5.6** Estimates of the GP distribution parameters for PDS 4 and PDS5

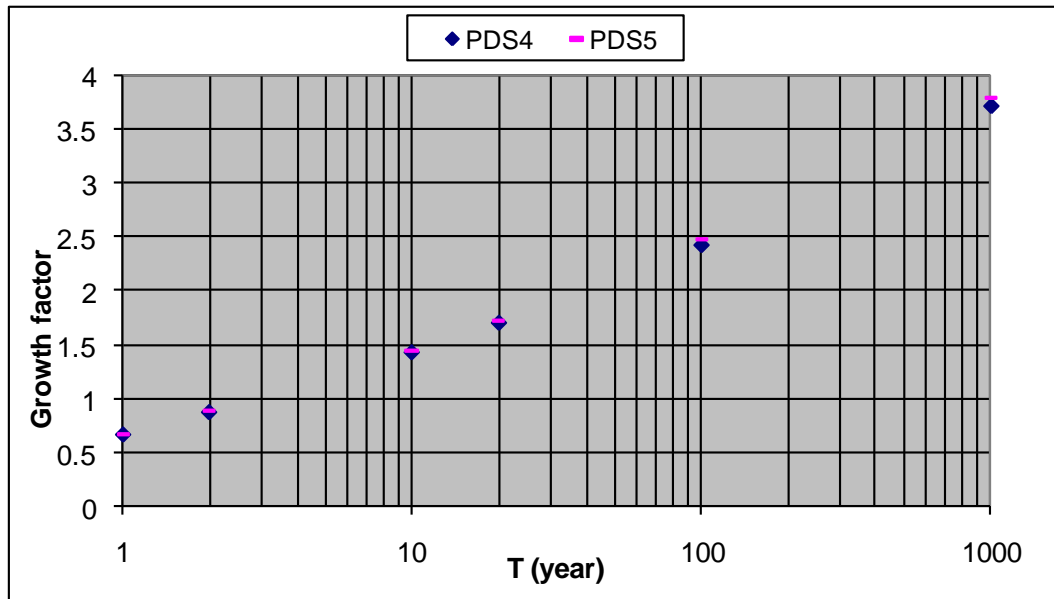
Regional weighted GP parameters	$\zeta$	$\alpha$	k
PDS 4	0.672	0.291	-0.113
PDS 5	0.662	0.3	-0.113

Table 5.7 compares the value of quantiles and T-year extreme events computed for PDS4 and PDS5. Inspection of the table shows a small difference between these values for low return periods ( $T \leq 2$  years). In particular, the percentage of difference of precipitation magnitudes for PDS4 and PDS5 is about 2.5%. The percentage of difference of precipitation magnitudes increases gradually for  $2 \text{ years} < T \leq 100$  years, varying from 2.7% to 3.8%. The most significant increase in the percentage of difference of precipitation magnitudes is around 6.3% for  $T \geq 1000$  years.

**Table 5.7** T-year quantile estimation from the regional GP distribution for PDS 4 and PDS5 accepted at the 90% confidence level

Non-exceedance probability (%)	Return period (years)	Quantiles for different return period		Quantile difference (%)
		$X_T$ (mm) PDS4	$X_T$ (mm) PDS5	
		0.68	0.67	2.5
0.02	1.60	0.68	0.67	2.5
0.05	1.63	0.69	0.68	2.5
0.1	1.68	0.70	0.69	2.5
0.2	1.82	0.74	0.73	2.6
0.5	2.5	0.88	0.88	2.7
0.9	10.5	1.44	1.45	3.4
0.95	20.5	1.71	1.73	3.8
0.99	100.5	2.43	2.47	4.6
0.999	1000.5	3.72	3.80	6.3

Figure 5.3 gives comparison on quantile values computed for PDS4 and PDS5 for different return periods. There is a very small difference in quantile values when computed for PDS4 and PDS5 for lower return periods ( $T \leq 100$  years). The difference in these values is little higher for  $T \geq 1000$  years. The best match among the quantile values is found for the case of  $T \leq 2$  years.

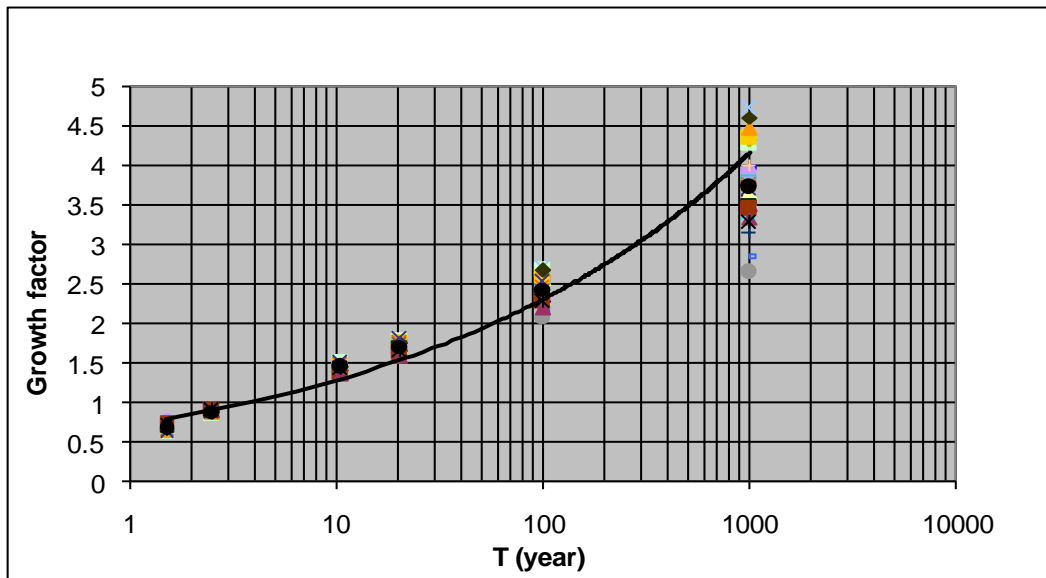


**Figure 5.4** Comparison of regional quantile estimates for PDS4 and PDS5 for different return periods, T

### 5.3.3.3. Robustness test

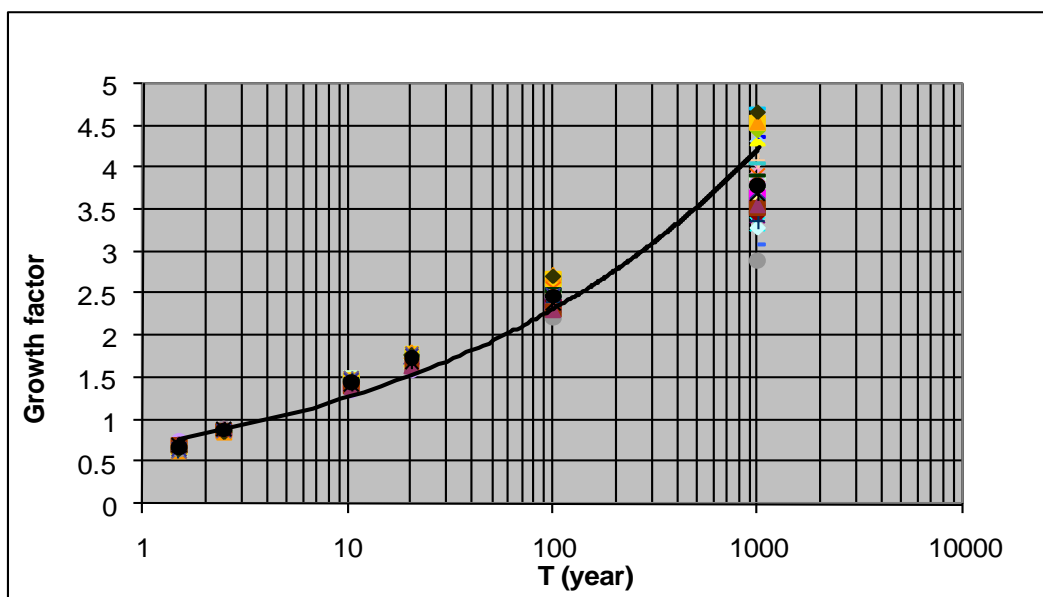
Even though the GP distribution is confirmed as a best description for regional frequency analysis of PDS4 and the PDS5 series, for more accurate estimation of the obtained regional GP distribution its probability function still needs to be verified with at-site observation series. The robustness test is used herein to compare the quantiles values for different return periods using the at-site and the regional probability function of the GP distributions. The results are presented in Figs. 5.4 and 5.5. The value of quantiles computed at-site are presented as points, while the curve represents computed regional quantiles.

Figure 5.4 shows a comparison between estimated quantiles for different return periods (1, 2, 10, 20, 100 and 1000 years) using at-site and regional GP for PDS4. In general, there is a close match between regional and at-site precipitation estimates for  $T$  less than or equal to 100 years. For the case of  $T = 1000$  years, quantile values vary from station to station and they differ slightly from the regional quantile values.



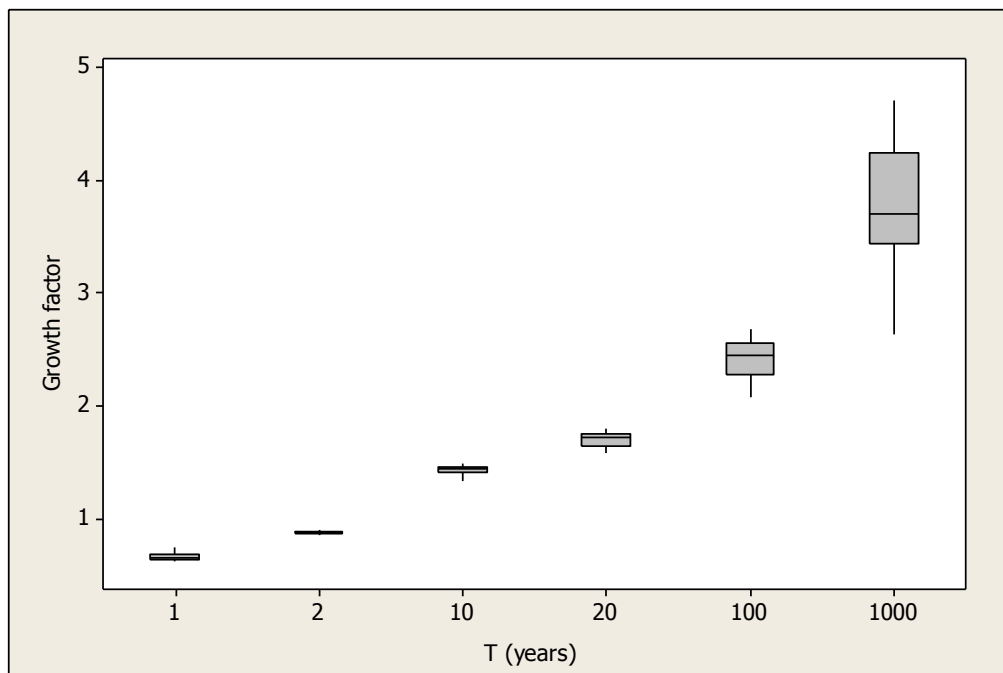
**Figure 5.5** Comparison of estimated quantile using at-site (point) and regional (line) GP model for PDS4

Figure 5.5 shows the difference between quantile values for PDS5 when they are computed by at-site and regional GP. Similar to PDS4 case, overall the value of regional quantiles best matches with at-site quantiles for T value less than or equal to 100 years. There is a significant difference among at-site quantile values for T = 1000 years. This may lead to an underestimation over overestimation of 1000-year quantiles at some stations when a regional distribution is used.



**Figure 5.6** Comparison of estimated quantile using at-site (point) and regional (line) GP model for PDS5

Figures 5.6 and 5.7 present the percentage difference between at-site and regional quantiles computed for different return periods across 32 stations based on PDS4 and PDS5, respectively. It can be seen that regional frequency analysis was best performed for both PDS4 and PDS5 cases with much lower biases ranging between 0.3% and 5% for T from 1 to 20 years, respectively, and with bias varying around 25% for T equal to 100 years. However, in both cases the regional frequency analysis performs less satisfactorily with high biases of approximately 50%. The variation of quantile values at T = 1000 may be affected by the sample size. The smaller the sample size, the larger degree of variation of quantiles. This may be due to the fact that the length of the observed data used in this study is usually restricted to 100 years or less.



**Figure 5.7** Box plot of growth factor computed for different return periods for PDS4 across 32 stations

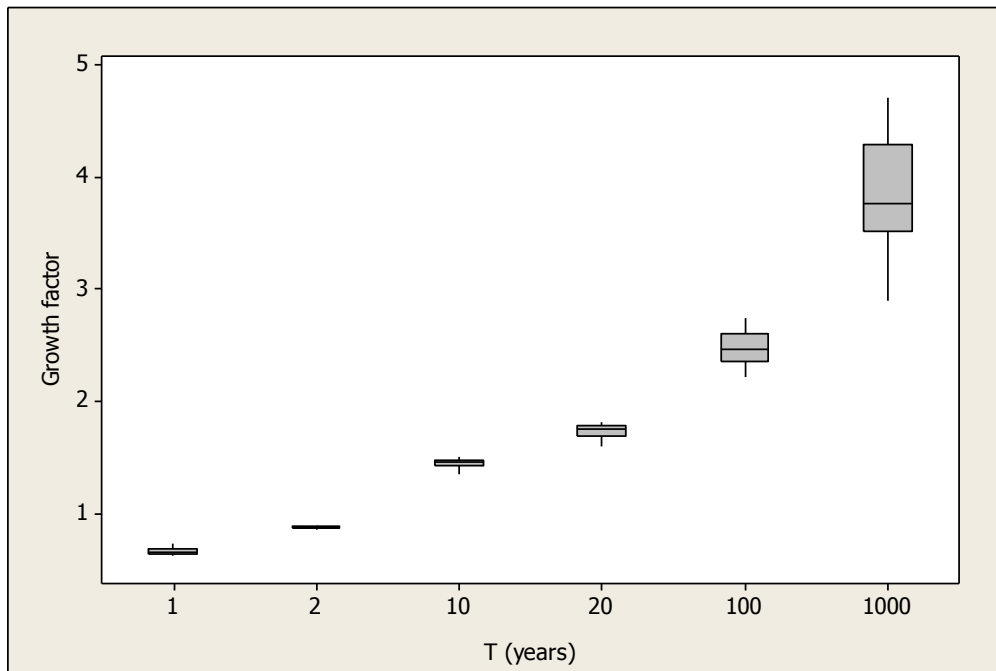


**Figure 5.8** Box plot of growth factor computed for different return periods for PDS5 across 32 stations

#### 5.3.4. Comparison of PDS4/GP and PDS5/GP results

The research reveals that the GP distribution is valid for representing the PDS series not only at single station, but also at every station within the North Island region. Also, the PDS5 outperforms the PDS4 model as shown by a number of statistical measures. The results are summarized in Table 5.8 below. In general, there is a significant difference between quantiles estimated for PDS4 and PDS5 if the return period is very large ( $T > 1000$  years).

**Table 5.8** Results of discordance, heterogeneity, goodness-of-fit and robustness tests for PDS4 and PDS5 (for  $\lambda = 4$  and  $\lambda = 5$ )

Model	Discordancy measure ( $D_i$ )			Heterogeneity measure			$ Z  \leq 1.64$	Best fit	RMSE (%) for 100-yr quantiles
	Min	Max	Percentage of stations with accordant data	$H_1$	$H_2$	$H_3$			
PDS4	0.18	2.63	90.63	3.10	0.52	-0.34	0.60	GP	16
PDS5	0.12	2.35	93.75	3.73	1.00	-0.08	0.02	GP	15

## 5.4. Summary

This chapter presented the alternatives of regional frequency analysis (RFA) to validate the partial duration series (PDS) model in the study of extreme precipitation variability. The key tests are homogeneity, goodness-of-fit and robustness. By using these tests, the selected PDS series were assured to be valid for the whole region. This is useful for data extraction and interpolation within the region.

The homogeneity test indicated that the entire North Island region was considered as a statistically homogenous region. The regionalization test also revealed that PDS5 (with five peaks in average year,  $\lambda = 5$ ) had a slightly better performance than PDS4 ( $\lambda = 4$ ) for regional extreme rainfall estimation. In addition, PDSs ( $\lambda > 5$ ) had a high variability as well as contained dependent peaks. Hence,  $\lambda = 5$  can be regarded as the optimum regional value for the average number of peaks per year for the North Island of New Zealand. There was a small difference between estimated quantiles using the at-site and regional GP distribution. The quantile values were more reliable when estimating for return periods less than or equal to 100 years ( $T \leq 100$  years).

## CHAPTER 6

# Statistical downscaling of daily precipitation

This chapter includes partial reproduction of the paper:

Pham, H. X, Shamseldin, A. Y. (2013). Statistical downscaling of daily precipitation using UKSDSM model, *6<sup>th</sup> Thailand-Japan International Academic Conference*, Osaka, Japan: 9-11 November.

This chapter presents the application of the statistical downscaling model (SDSM) to downscale the local daily precipitation at station location from large-scale climatic variables. The first section of the chapter gives a brief introduction on the rationale and objectives of using SDSM, followed by the study region and data description. The next section of the chapter introduces the details of the statistical downscaling model theory as well as its technical requirements. The final section of the chapter discusses the modeled results.

## 6.1 Introduction

A Statistical Downscaling Model (SDSM) is commonly used for studying the assessment of climate change impacts at the catchment-scale. Despite the model performance capacity, its applicability is still limited when it downscales daily precipitation to the station location. This is due to the complex characteristics of daily events. Unlike other climate variables, the simulation of daily precipitation is very complicated due to the non-normal distribution of daily precipitation as well as the mixed distribution of wet and dry days in daily precipitation series (Grimm, 2010; Pattanaika et al., 2010; Zhang, 2010). As a result, underestimation and/or overestimation of future precipitation are envisaged to occur. There are few studies in New Zealand dealing with statistical downscaling of daily precipitation, and none in the North Island region. This study for the first time investigates the use of SDSM model for downscaling daily precipitation over Waikato catchment in the North Island of New Zealand from different large-scale climatic variables obtained from Global Climate Model (GCM) output.

## 6.2 Study region and data

The Waikato catchment in the North Island region of New Zealand is selected for this study. The daily precipitation data is obtained from 14 stations over 30 year period (i.e., from 1960 to 1990) across the study region and its surrounding areas (see Figure 6.1).

Also, 26 large-scale variables obtained from the Canadian Global Climate Model (CCGCM3.1/T47) and from the United Kingdom Hadley Centre Coupled Model (HadCM3) coupled with IPCC SRES A2 scenario are used. The corresponding 26 daily observed large-scale predictor variables are also obtained from the National Centre of

Environmental Prediction (NCEP) re-analysis (refer to Chapter 3). The information about the large-scale variables is presented in Table 6.2.

These GCMs and NCEP data sets for the current climate (1961-2000) and future climate (2001-2100) for the study area are extracted from the closest grid box ( $Y = 35$ ;  $X = 48$ ) from the Australia and New Zealand window (Figure 6.2).

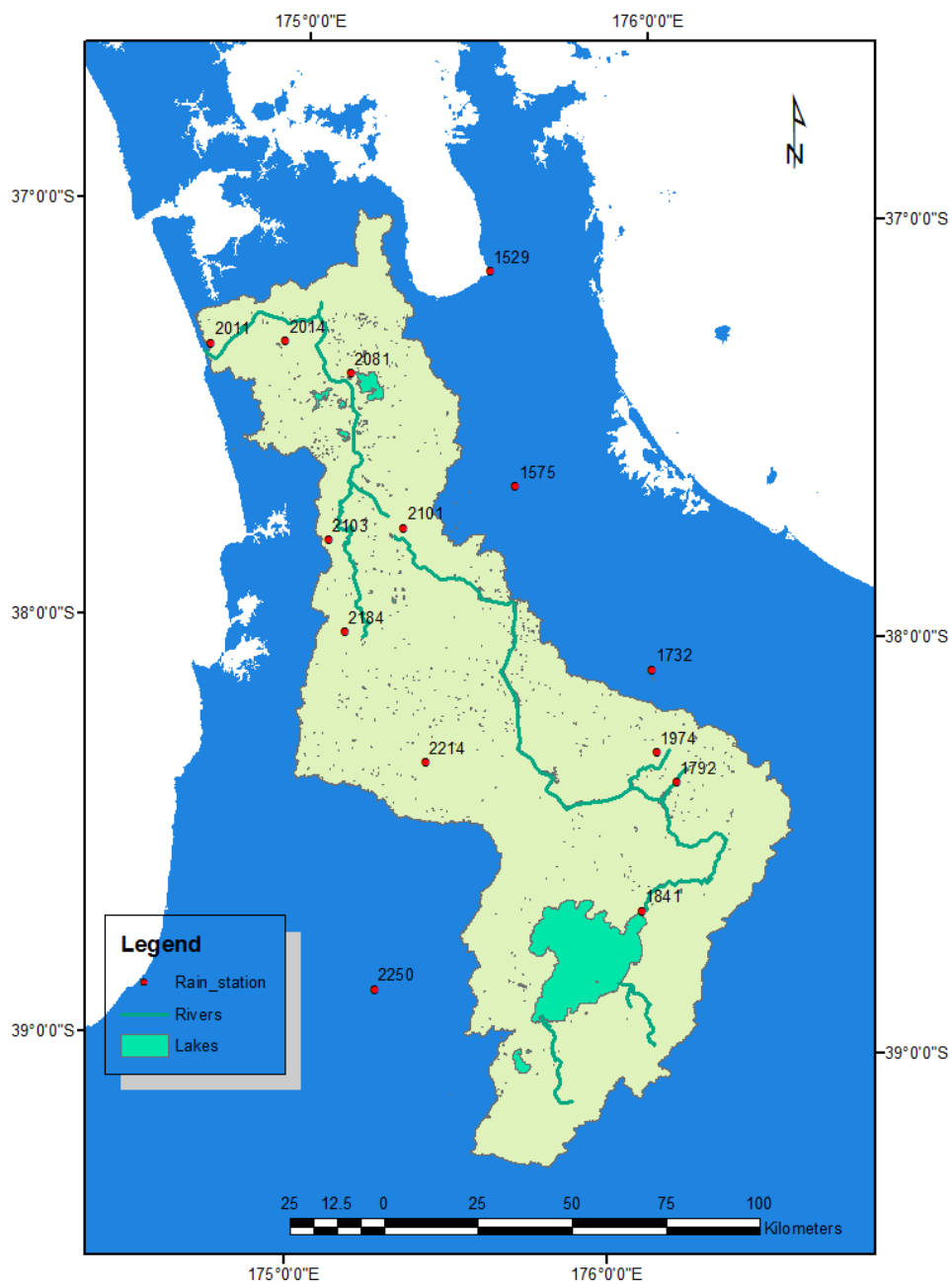


**Figure 6.1** Geographical locations of the study region and selected stations

**Table 6.1** Information about meteorological station in the study region

No	Station	X ( $^{\circ}$ )	Y ( $^{\circ}$ )	H (m)	Mean annual precipitation (mm)
1	1529	175.14	-37.21	3	1268
2	1575	175.64	-37.67	55	1213
3	1732	175.5	-37.92	570	2075
4	1792	176.16	-38.37	305	1263
5	1841	174.94	-37.34	376	1149
6	1974	175.79	-38.56	119	1362
7	2011	174.71	-37.34	52	1361
8	2014	176.91	-39.5	46	1403
9	2081	174.86	-37.21	32	1144
10	2101	174.67	-37.26	40	1199
11	2103	175.09	-37.81	104	1593
12	2184	176.07	-38.68	170	2281
13	2214	175.39	-38.34	320	1847
14	2250	175.31	-37.78	171	1451

**Table 6. 2** 26 large-scale GCM and NCEP predictor variables and their description

No	Predictor	Description	No	Predictor	Description
1	prcpgl	Accumulated precipitation	14	p5zhgl	500hPa Divergence
2	p_zhgl	1000hPa Divergence	15	p5thgl	500hPa Wind direction
3	p_thgl	1000hPa Wind direction	16	p5_zgl	500hPa Vorticity
4	p_zgl	1000hPa Vorticity	17	p5_vgl	500hPa Meridional velocity
5	p_vgl	1000hPa Meridional velocity	18	p5_ugl	500hPa Zonal velocity
6	p_ugl	1000hPa Zonal velocity	19	p5_fgl	500hPa Wind speed
7	p_fgl	1000hPa Wind speed	20	tempgl	Screen air temperature (2m)
8	p8zhgl	850hPa Divergence	21	shumgl	1000hPa Specific humidity
9	p8thgl	850hPa Wind direction	22	s850gl	850hPa Specific humidity
10	p8_zgl	850hPa Vorticity	23	p500gl	500hPa Geopotential
11	p8_vgl	850hPa Meridional velocity	24	msslpgl	Mean sea level pressure
12	p8_ugl	850hPa Zonal velocity	25	p850gl	850hPa Geopotential
13	p8_fgl	850hPa Wind speed	26	s500gl	500hPa Specific humidity

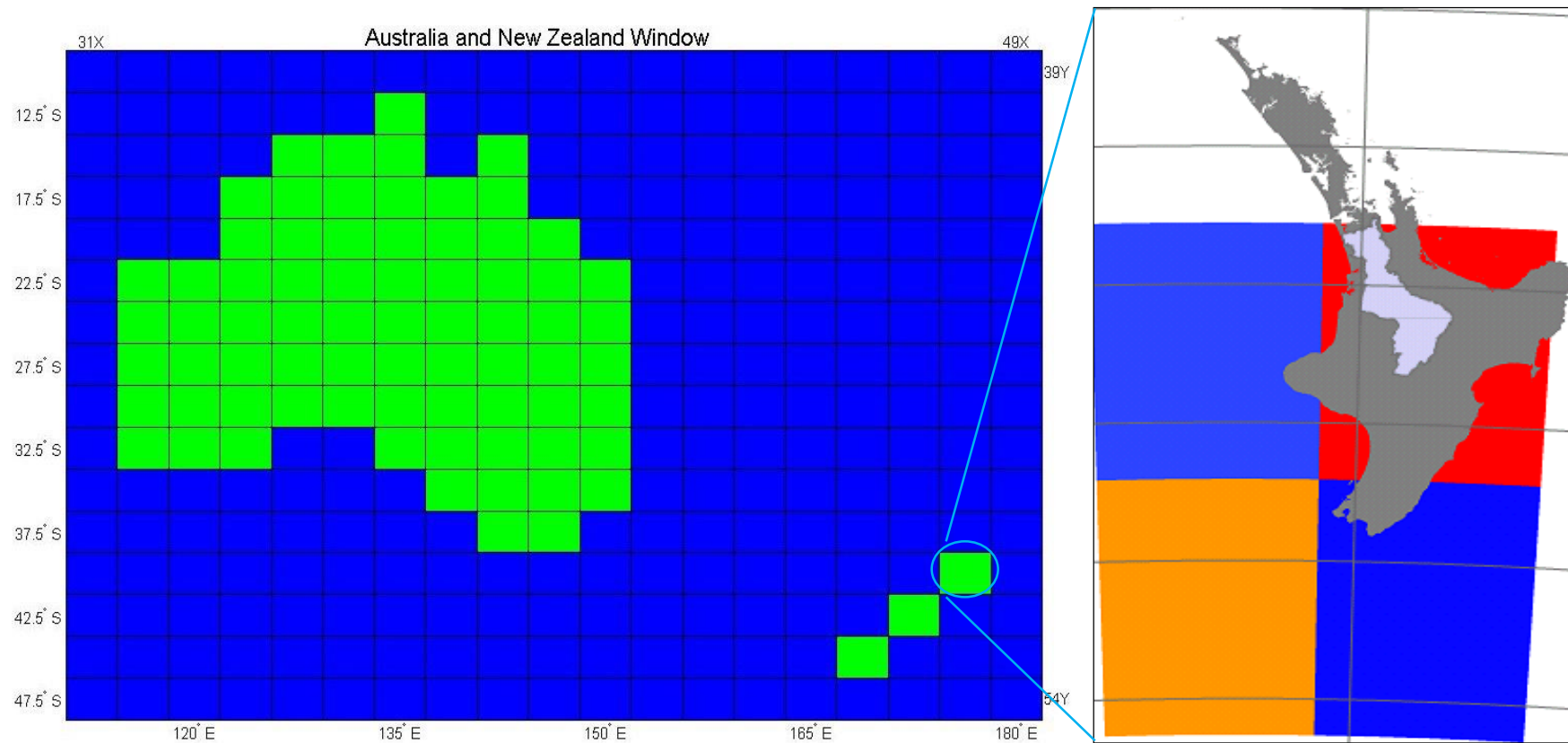


**Figure 6.2** The closest grid box to the Waikato catchment (in red) extracted from Australia and New Zealand Window

## 6.3 Methods and Techniques

A statistical downscaling model developed in the United Kingdom (SDSM) by Wilby et al. (2002) is a hybrid of a stochastic weather generator and regression methods. This hybrid method is able to reduce uncertainty as well as to maximise the downscaling performance, especially for future projections (Wang et al., 2012).

In this research, SDSM model is applied to downscale daily precipitation to 14 station locations across the Waikato catchment. The monthly sub-model was employed in this study with unconditional processes for the modeling of precipitation occurrence and conditional processes for the modeling of precipitation amounts.

### 6.3.1 Statistical downscaling methods

A statistical downscaling approach is based on a statistical relationship between large-scale atmospheric variables and local-scale variables (Chu et al., 2010 and Wang et al., 2012).

This statistical relationship is defined by Chu et al. (2010) and Wang et al. (2012) as:

$$Y = F(X) \quad (6.1)$$

$$Y = \beta_0 + \beta_1 X_1 + \beta_2 X_2 + \dots + \beta_n X_n + \varepsilon \quad (6.2)$$

where Y is the predictand (a local climate variable); F is a the statistical function;  $X_{i=1,2, \dots, n}$  are n large-scale atmospheric predictors;  $\beta_i$  are constant and  $\varepsilon$  is the error term.

In SDSM, precipitation occurrence and amount are simulated from large-scale atmospheric variables on wet days following the formulas below:

$$w_t = \alpha_0 + \sum_{j=1}^n \alpha_j u_t^j + \alpha_{t-1} w_{t-1} \quad (6.3)$$

where t is the specific day;  $w_t$ ,  $w_{t-1}$  are the probability of precipitation occurrence on day t and day t-1, respectively;  $u_t^j$  is the normalized predictor;  $\alpha_j$ ,  $\alpha_{j-1}$  are the regression

parameter and lag-1 day regression parameter, respectively. Depending on study areas and predictand,  $w_{t-1}$  and  $\alpha_{j-1}$  are optional for usage. The assumption made is that rain would happen if  $w_t \leq r_t$  with  $r_t$  is a uniformly distributed random number and  $0 \leq r_t \leq 1$ .

On a wet day, precipitation can be described by a z-score as:

$$Z_t = \beta_0 + \sum_{j=1}^n \beta_j u_t^j + \beta_{t-1} Z_{t-1} + \varepsilon \quad (6.4)$$

where  $Z_t$ ,  $Z_{t-1}$  are the z-score on day t and day t-1, respectively,  $\beta_j$ ,  $\beta_{t-1}$  are the regression parameters. As mentioned earlier in this section,  $\beta_{t-1}$  and  $Z_{t-1}$  are optional, and  $\varepsilon$  is a random error that can be simulated by a normal distribution  $N(0, \sigma_z^2)$ . The amount of precipitation  $y_t$  on day t can be simulated as:

$$y_t = \frac{\phi(Z_t)}{F} \quad (6.5)$$

where  $\Phi$  is the normal cumulative distribution function and F is the empirical distribution function of  $y_t$ .

By substituting the parameters from Eq. (6.4) into Eq.(6.5) the resulting equation is:

$$y_t = \text{Exp}(Z_t) = \text{Exp}\left(\beta_0 + \sum_{j=1}^n \beta_j u_t^j + \beta_{t-1} Z_{t-1} + \varepsilon\right) \quad (6.6)$$

The expected value is given by the following equation:

$$E(y_t) = \varphi \cdot B_c \cdot \text{Exp}\left(\beta_0 + \sum_{j=1}^n \beta_j u_t^j + \beta_{t-1} Z_{t-1} + \varepsilon\right) \quad (6.7)$$

where  $B_c$ ,  $\varphi$  are empirical correction ratio and variance inflation factor to correct the bias in the estimation of the precipitation amount  $y_t$  and the variance of the precipitation amount, respectively (Hashmi, 2012).

### 6.3.2 Selection of large-scale predictor variables

The success of the model performance is strongly dependent on the selection of large-scale predictor variables (Chen, Brissette and Leconte, 2011; Chu, et al., 2010) because they directly control the local predictand (IPCC, 2007).

In principle, candidate predictor variables should be physically and conceptually sensible with respect to the predictand and realistically modeled by GCMs (Wibly and Dawson, 2007; Jeong et al., 2012; Liu, 2008; Hashmi, 2012 and Wang et al., 2012). Ideally, the combination of predictors is preferred because they include circulation variables, temperature-related variables and moisture-related variables (Jeong et al., 2012). Also, multi-grid predictors surrounding and closest to an underlying location could give best information on single-grid predictors for each station (Liu, 2008).

In this research, a combination of predictors is used for both individual precipitation at station and areal precipitation. Correlation and cross-correlation tests are used to define the predictor variables relevant to the predictand. The former is used to investigate the association between predictors and predictand, and then the most relevant predictors to the predictand are confirmed. The latter is used to find the time lag(s) at which the predictor and predictand series showed the strongest correlation (Wilby et al., 2002).

Even though cross-correlation analysis is widely used in finding the most related predictors, it is recommended that this analysis should be used with caution. Basically, maximum cross-correlations among variables are confirmed when the value of correlation coefficients reaches -1 and/or +1 with a confidence level  $\alpha = 0.01$ . However, strong correlations may not be very useful for prediction if there is a weak link between long term mean values of predictor and predictand. In addition, the standard cross-correlation assumes observations were independent. Moreover, the cross-correlation was not sensitive

to small change in predictor variables because this was calculated as the average over all months (Huang et al., 2011).

In some cases where the transformation function does not effectively work, predictands at station can be replaced by regional predictands (i.e., spatial average predictands computed from single predictands at sites) (Hashmi, 2012; Wang et al., 2012). Areal average precipitation was computed using the Thiessen polygon method. Regional precipitation series is calculated using the following equation:

$$\bar{y}_{(j)} = w_{1(j)} \cdot y_{1(j)} + \dots + w_{n(j)} \cdot y_{n(j)} \quad (6.8)$$

where  $\bar{y}$  is the spatial average precipitation on day  $j$ ;  $n$  is the number of stations;  $w_{i=1-n}$  is the weight factor of each station;  $y_{i=1-n}$  is the value of precipitation at station  $i$  on day  $j$ .

### 6.3.3 Model Calibration and Validation

The observed precipitation data was split into two periods 1961-1980 and 1981-1990 for calibration and validation, respectively. Model calibration and validation were implemented on station-by-station basis. This was then integrated to produce mean areal precipitation over the region. The precipitation was synthesized from 20 ensembles. We also tested the sensitivity of using numbers of ensemble of 100 but found no significant changes in the results. With predictors established for predictand variables defined for each station, statistical regression equations were developed and then used for the A2 scenario downscaling experiment. The simulation was forced by bias correction ( $B_c$ ) and variance inflation factors ( $\phi$ ) (Wang et al., 2012). The optimization sets of  $B_c$  and  $\phi$  were obtained using trial-and-error procedure. The SDSM calibration was executed with different sets of predictors. For model validation, the model parameters were also tested by season or months together (Hu et al., 2013).

### 6.3.4 Evaluation for model performance

In the process of calibration and validation, an optimum model parameter set is obtained by examining the model performance with sets of predictors and predictand over the calibration and validation periods.

Model performance was evaluated based on three different coefficients, namely coefficient of determination ( $R^2$ ); root-mean-square error (RMSE) and percent bias (PBIAS). The first measures the statistical relationship between observed and simulated variables, the second measures the differences between predicted values by a model and the observed values, while the last measures the average trend of the simulated data to determine if it is larger or smaller than the observed data (Krause et al., 2005; Gupta et al., 1998). Also, the percentage difference (SE) is used to determine the agreement between seasonal observed and simulated precipitations.

The values of  $R^2$ , RMSE and PBIAS are defined as:

$$R^2 = \frac{\sum_{i=1}^n (X_{obs,i} - \bar{X}_{obs})(\bar{X}_{sim,i} - \bar{X}_{sim})}{\sqrt{\sum_{i=1}^n (X_{obs,i} - \bar{X}_{obs})^2 \sum_{i=1}^n (X_{sim,i} - \bar{X}_{sim})^2}} \quad (6.9)$$

$$RMSE = \sqrt{\frac{\sum_{i=1}^n (X_{sim,i} - X_{obs,i})^2}{n}} \quad (6.10)$$

$$PBIAS = \frac{\sum_{i=1}^n (X_{obs,i} - X_{sim,i})}{\sum_{i=1}^n X_{obs,i}} * 100\% \quad (6.11)$$

$$SE = \left| \frac{X_{obs,i} - X_{sim,i}}{(X_{obs,i} + X_{sim,i})/2} \right| * 100\% \quad (6.12)$$

where  $n$  is the number of time-steps;  $X_{obs,i}$ ;  $X_{sim,i}$  are the observed and simulated values at time step  $i$ .

## 6.4 Results and Discussions

### 6.4.1 Selection of large-scale predictor variables

Different sets of predictors were selected for different stations (see Table 6.3). As can be seen from the table, the number of predictors varies from station to station. For the CGCM3/T47 model, the most common predictors were geopotential height at 500 hPa and 850 hPa, mean sea level pressure, vorticity at 500 hPa, 850 hPa and 1000 hPa, wind speed at 850 hPa, and meridional velocity at 500 hPa. Whist, vorticity at 500 hPa, specific humidity at 1000 hPa, geopotential height at 500 hPa and 850 hPa and mean sea level pressure are the most common predictors of the GCM HadCM3 model. The common predictors were later used for computing mean areal precipitation.

The off-line correlation analysis also reveals that five out of 14 stations, namely 1841, 2011, 2014, 2101 and 2103, give the strongest correlation between predictand and predictor variables generated from the CGCM3/T47 model (Appendix C). The predictor and predictand variables were less correlated in the remaining stations. For the GCM HadCM3 model, the predictand - predictor correlation is only found at stations 1841, 2014, 2101 and 2103. In contrast, the predictors are not correlated to the predictand variables in the remaining stations.

In general, the local predictand at station was least correlated to large-scale predictor variables. This may be due to the coarse spatial resolution of the grid covering the entire Waikato catchment used in this study. Therefore, it is suspected that spatial average precipitation, i.e. regional predictand, could improve the correlation of predictor-predictand pairs.

**Table 6.3** Predictor variables selected for different stations

No	Predictor	Description	CGCM3*	HadCM3*	No	Predictor	Description	CGCM3*	HadCM3*
1	prcpgl	Accumulated precipitation			14	p5zhgl	500hPa Divergence	3	
2	p_zhgl	1000hPa Divergence			15	p5thgl	500hPa Wind direction	1	
3	p_thgl	1000hPa Wind direction	1		16	p5_zgl	500hPa Vorticity	<b>6</b>	<b>3</b>
4	p_zgl	1000hPa Vorticity	<b>4</b>		17	p5_vgl	500hPa Meridional velocity	1	
5	p_vgl	1000hPa Meridional velocity			18	p5_ugl	500hPa Zonal velocity	3	
6	p_ugl	1000hPa Zonal velocity			19	p5_fgl	500hPa Wind speed	2	
7	p_fgl	1000hPa Wind speed			20	tempgl	Screen air temperature (2m)	1	
8	p8zhgl	850hPa Divergence	2		21	shumgl	1000hPa Specific humidity	1	<b>3</b>
9	p8thgl	850hPa Wind direction			22	s850gl	850hPa Specific humidity	2	
10	p8_zgl	850hPa Vorticity	<b>7</b>		23	p500gl	500hPa Geopotential	<b>8</b>	<b>3</b>
11	p8_vgl	850hPa Meridional velocity	2		24	mslpgl	Mean sea level pressure	<b>9</b>	<b>4</b>
12	p8_ugl	850hPa Zonal velocity	1		25	p850gl	850hPa Geopotential	<b>11</b>	<b>4</b>
13	p8_fgl	850hPa Wind speed	<b>6</b>		26	s500gl	500hPa Specific humidity	1	

*\*The selection was made for individual stations*

Mean areal precipitation is computed using the Thiessen method (see Figure 6.3). Inspection of the Figure 6.3 indicates that precipitations at four stations (i.e., 1841, 2081, 2101, and 2214) make a contribution to regional precipitation. In addition, off-line correlation analysis results demonstrated that lag-1 is applicable for only two predictor variables, namely ncepp5\_vgl and ncepp8-fgl, are lagged by one day, while all other predictor variables have no lag time. Information about candidate predictor variables as well as results of cross-correlation analysis are presented in Table 6.4.

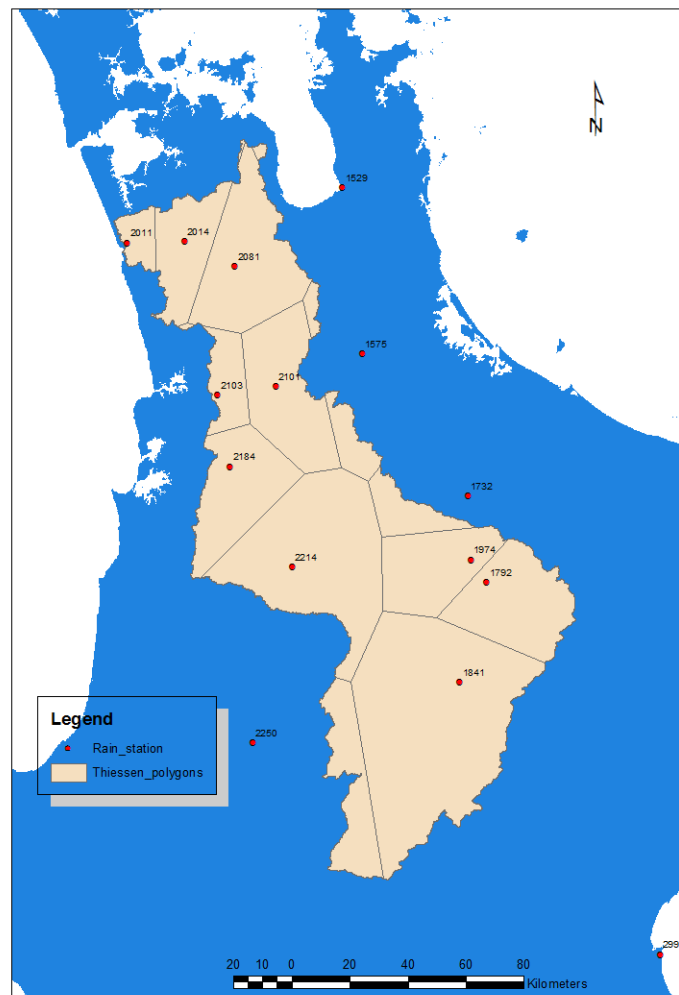


**Figure 6.3** Estimation of regional precipitation using spatial interpolation Thiessen

**Table 6.4** List of 8 large-scale predictors and results of cross-correlation analysis for both GCMs

No	Predictor variable	Predictor description	Optimal lag
1	nceppmslgl.dat	Mean sea level pressure	
2	ncepp_zgl.dat	1000hPa Vorticity	
3	ncepp5_vgl.DAT	500hPa Meridional velocity	-1
4	ncepp5_zgl.dat	500hPa Vorticity	
5	ncepp500gl.dat	500hPa Geopotential	
6	ncepp8-fgl.DAT	850hPa wind speed	-1
7	ncepp8_zgl.dat	850hPa Vorticity	
8	ncepp850gl.dat	850hPa Geopotential	

## 6.4.2 Model Calibration and validation

A model calibration and validation were performed using precipitation data at all individual stations in line with regional precipitation. A comparison of the individual and regional simulations was made where appropriate. Large-scale predictor variables confirmed from previous tests were used together with surface-observed precipitation predictand. In this study, model calibration and validation process were done over the period of 1961 – 1980 and 1981-1990, respectively.

### 6.4.2.1 Model Calibration

The model calibration was undertaken with a combination of variance inflation factor ( $\psi$ ) and bias correction ( $B_c$ ) parameters on station basic. The results of model calibration are presented in Tables 6.5 and 6.6 for GCM3/T47 and GCM HadCM3 model, respectively.

Table 6.5 shows that corresponding values of  $R^2$ , RMSE and PBIAS computed for observed and calibrated precipitation series also vary from station to station. The  $R^2$  value

differs from 0.004 to 0.188 suggesting a weak statistical relationship between the observed and simulated time series of precipitation. Likewise, RMSE value computed at almost all stations fluctuates around 8.0 indicating a difference between the observation and the simulation of daily precipitation. In addition, most of the values of PBIAS are in positive indicating that there is underestimation of precipitation in these stations.

**Table 6.5** Model assessment for daily and seasonal precipitation simulations from CGCM3/T47 model

No	Station	Calibration			Validation					
		R <sup>2</sup>	RMSE (mm)	PBIAS (%)	RMSE (mm)	PBIAS (%)	SE (%)			
							Winter	Spring	Summer	Autumn
1	1259	0.052	8.73	5.37	8.15	1.68	7.58	8.44	8.90	6.10
2	1575	0.008	6.11	2.09	8.03	-13.39	8.02	5.96	6.20	5.59
3	1732	0.005	10.24	14.20	10.11	-54.68	10.74	13.28	11.88	11.17
4	1792	0.035	8.73	10.26	8.37	2.15	8.47	8.42	7.22	6.48
5	<b>1841</b>	<b>0.152</b>	7.42	-21.10	6.99	-29.83	11.27	9.17	8.16	8.38
6	1974	0.013	8.85	-42.39	8.89	13.36	10.20	8.98	8.19	9.84
7	<b>2011</b>	<b>0.124</b>	8.08	12.60	7.71	-34.84	11.09	10.04	8.76	8.55
8	<b>2014</b>	<b>0.152</b>	8.06	8.03	0.28	-17.72	10.62	9.89	8.93	9.09
9	2081	0.031	8.69	29.08	8.53	-2.99	9.35	8.92	7.67	7.54
10	<b>2101</b>	<b>0.176</b>	7.27	-18.87	6.78	-26.72	10.11	9.07	8.09	8.00
11	<b>2103</b>	<b>0.188</b>	8.55	12.30	8.63	-15.33	11.44	10.76	9.86	9.78
12	2184	0.039	14.11	4.96	14.01	-24.85	17.8	15.39	15.52	16.26
13	2214	0.004	11.54	-19.74	12.20	-13.39	13.22	12.43	11.70	13.10
14	2250	0.032	8.75	6.56	8.65	-28.90	11.85	11.8	10.24	8.78

Unlike the results from CGCM3/T47, the daily precipitation from the GCM HadCM3 is only successfully downscaled to four stations, namely 1841, 2011, 2014, 2101 and 2103. The resulting coefficients are presented in Table 6.6. Overall, the SDSM model likely performs at three stations with the values of  $R^2$  varies between 0.127 and 0.145, RMSE values fluctuate around 4.51 to 5.99 and the values of PBIAS range from 2.61 to 8.71 (except for station 2014). At these station, the values of  $R^2$ , RMSE and PBIAS are 0.014, 17.76 and -0.19, respectively. This means that there is a very weak correlation between predictors and predictand, and simulated precipitation underestimates the observation.

**Table 6.6** Model assessment for daily and seasonal precipitation simulations from GCM

HadCM3 model

No	Station	Calibration			Validation					
		$R^2$	RMSE (mm)	PBIAS (%)	RMSE (mm)	PBIAS (%)	SE (%)			
							Winter	Spring	Summer	Autumn
1	1841	0.140	4.51	2.61	6.927	-7.47	5.70	5.71	8.30	6.00
2	2014	0.014	17.76	-0.19	42.25	76.84	3.1	12.73	34.32	27.9
3	2101	0.127	4.69	8.71	6.949	-0.21	6.3	5.33	7.53	7.27
4	2103	0.145	5.99	8.06	8.77	5.63	8.12	8.31	8.53	8.67

The assessment of statistical modelling performance of mean areal precipitation is shown in Table 6.7. Inspection of the table reveals that the SDSM model is likely to perform well for the large-scale variables from both GCM models with the same value of RMSE of 5.18. However, the relatively higher correlation between predictors and predictand is found for the CGCM3 output. The  $R^2$  values are 0.020 and 0.012 for the CGCM3 and HadCM3, respectively. Notably, the negative and positive PBIAS coefficient values are computed for these models, respectively. This conflicting result implies a significant difference between simulations between these two model outputs against the observation. The CGCM3 simulation overestimates, while the HadCM3 underestimates the mean areal daily precipitation.

**Table 6.7** Assessment of the model performance for daily mean areal precipitation using the Thiessen polygon method

No	Model	Calibration			Validation					
		$R^2$	RMS E (mm)	PBIAS S (%)	RMS E (mm)	PBIAS S (%)	SE (%)			
							Winter	Spring	Summer	Autumn
1	CGCM3	0.02	5.18	-9.49	3.80	-14.00	4.26	4.49	4.80	4.25
2	HadCM3	0.01	5.18	15.73	4.03	-19.61	4.48	4.60	4.85	4.48

Figure 6.4 gives information on the model performance from two GCM outputs at station 2101 as an example. Overall, the model performs relatively well with  $R^2$  is equal to 0.1767 and 0.1271 for the CGCM3 and HadCM3, respectively. This means that parts of observed and simulated precipitation series were statistically agreed. However, precipitation was not well modeled for high values that were probably extreme events recorded in the

observation. This is a limitation of the SDSM model as it is unable to capture all large-scale variables to local scale.

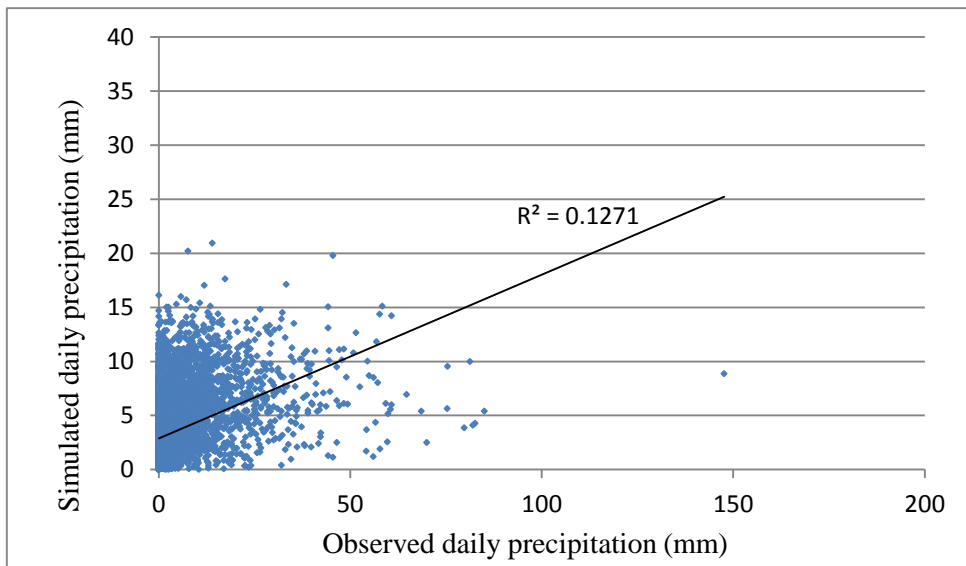
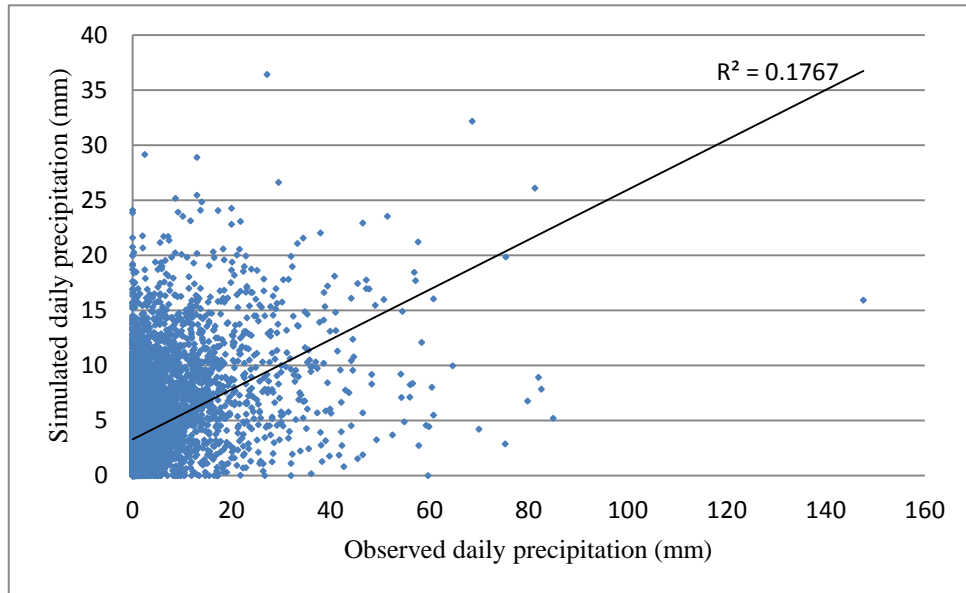


**Figure 6.4** Model calibration: Observed and simulated daily precipitation at station 2101 from CGCM3/T47 (upper) and GCM HadCM3 (lower) over 1961-1980

Bestpofe.com

### 6.4.2.2 Model Validation

Parameters determined during the calibration process that explain the statistical agreement between observed and simulated data were then used for model validation. The 10 year data (1981-1990) were used to validate the performance of the model. The evaluation of model performance was undertaken for mean areal daily precipitation and seasonal precipitation.

As the calibrated simulation of daily precipitation, the model did not perform well for extreme events for both GCM outputs. For station 2101, precipitation with a magnitude greater than 60 mm/day was weakly validated (see the Figure 6.5). The best simulation was found for precipitation observed at 40 mm/day or less. This may be due to the model assumption in which statistical relationship between large-scale predictor and local predictand variables is unchanged from current to future climate.

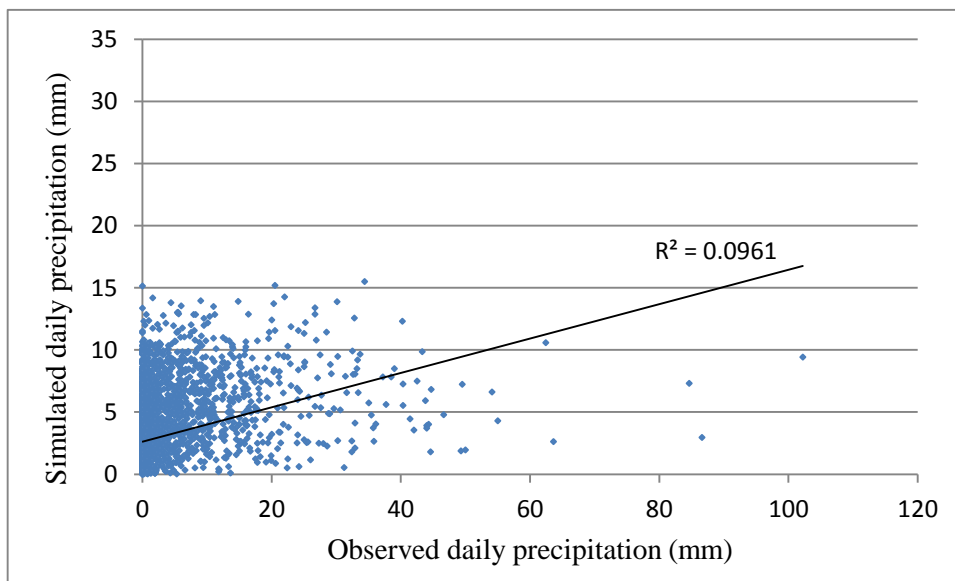
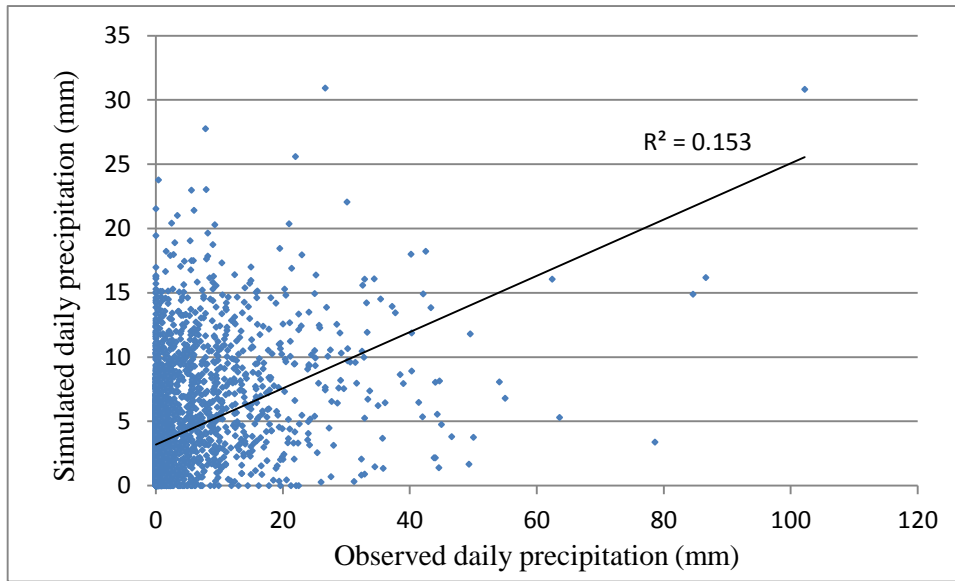


**Figure 6.5** Model validation: Observed and the simulated daily precipitation at station 2101 from CGCM3/T47 (upper) and GCM HadCM3 (lower) over 1981-1990

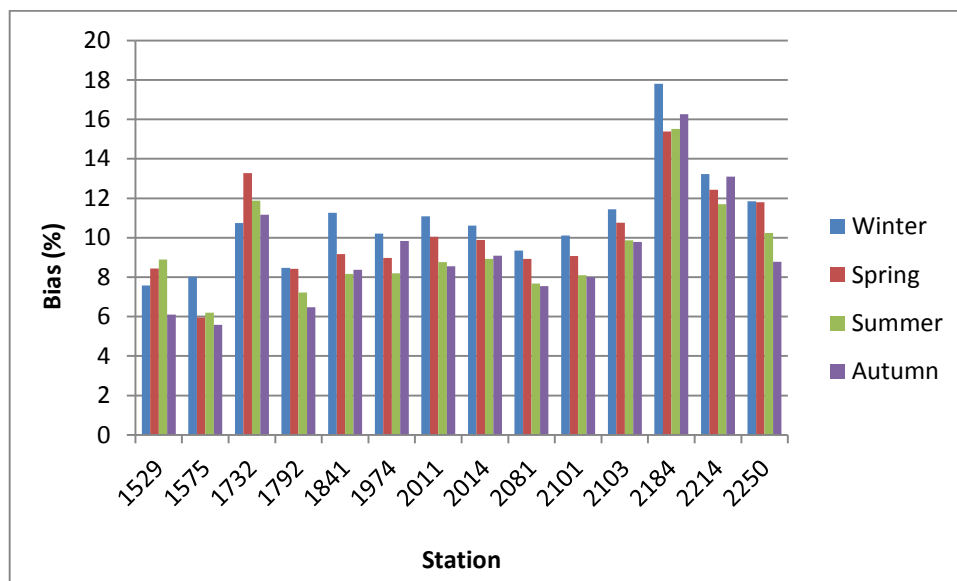
As can also be seen in Table 6.5 for the case of CGCM3/T47, the model steadily performs for all stations with the value of RMSE slightly differing from that produced in the calibration process. However, there is a significant change in the value of PBIAS. The model overestimates precipitation at almost all station since 11 out of 14 stations having negative PBIAS value. This uncertainty may originate from model feature itself as it lies mainly on the unchanged regression relationship among variables.

Examination of Table 6.6 for the case of GCM HadCM3 indicates that like the calibrated results, the SDSM performs poorly at station 2014 with high values of RMSE and PBIAS. However, the model apparently performs well for other stations. Nevertheless, the model overestimates at two stations (1841 and 2101) and underestimates at two other stations (2014 and 2103). This implies a significant difference of modelled results from calibration to validation periods.

Table 6.7 also shows that the SDSM model is likely to simulate mean areal daily precipitation determined from both CGCM3/T47 and GCM HadCM3 outputs. The model overestimates for both cases with negative values of PBIAS. The values of RMSE range from 3.80 to 4.03 for CGCM3/T47 and GCM HadCM3 outputs, respectively.

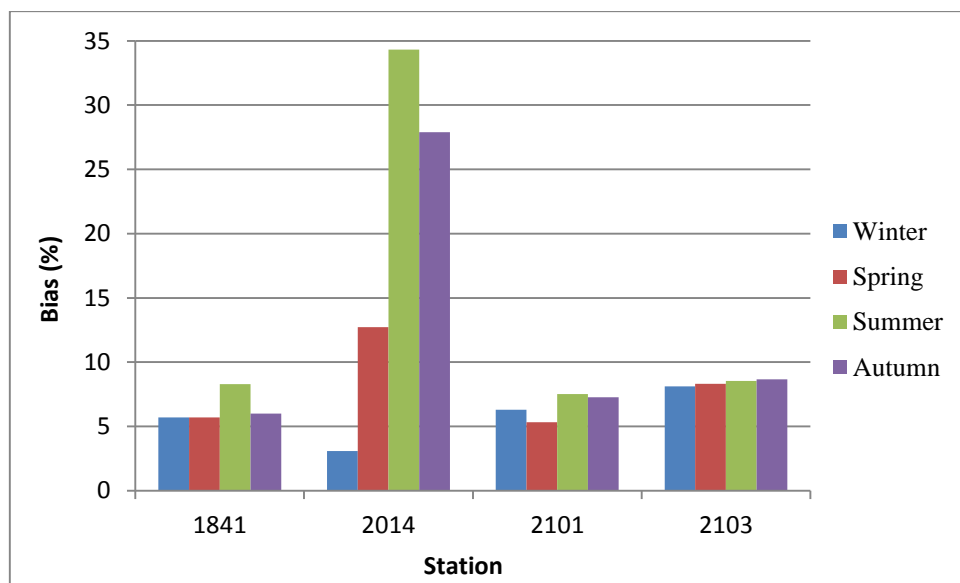
Figures 6.6 to 6.8 present the bias between the observed and the simulated seasonal precipitation from different GCMs for both cases, at single stations and over the region.

Figure 6.6 shows the bias between observations and simulations from CGCM3/T47 across 14 stations. Inspection of the figure indicates that at almost all stations the bias value is very high during the winter compared to other seasons of the year. This suggests that the model performance is less effective in the winter. The highest bias values of winter precipitation at station 1529 and 1732 were found in the summer and spring, respectively. In general, the common trend found in all stations was that the model performs best during autumn.



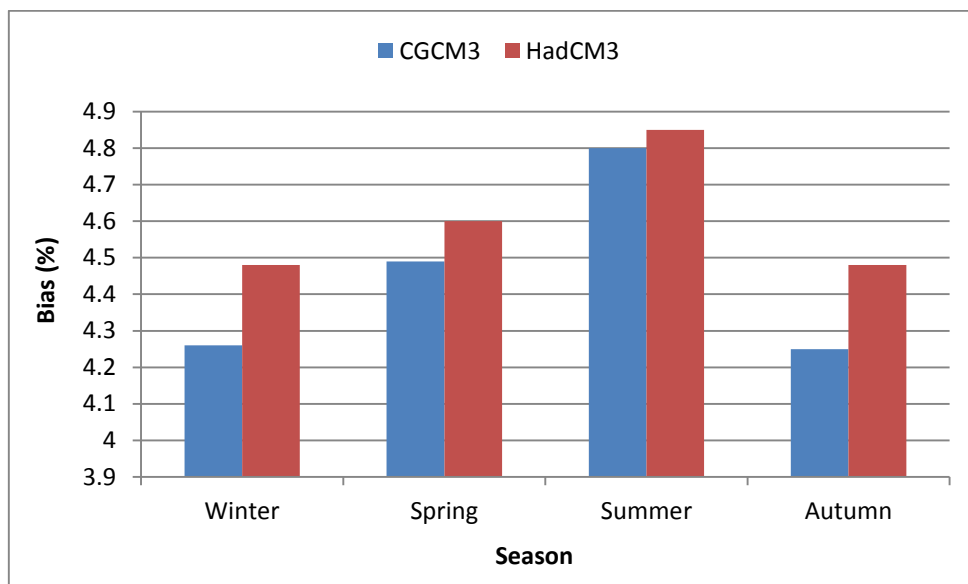
**Figure 6.6** Model validation: Bias (percentage difference between observed and simulated monthly precipitation) from CGCM3/T47 over period 1981-1990.

Fig. 6.7 exhibits the difference between the observed and simulated seasonal precipitation from GCM HadCM3 at 4 stations. For a special case of station 2014, the bias values are high in the summer, following by the autumn values. However, the difference in bias values among season is low. Most considerably, the bias values computed in four seasons are very high at station 2 (2101) in comparison to the rest. This may be due to errors inherited in observed series including repeated data.



**Figure 6.7** Model validation: Bias (percentage difference between observed and simulated monthly precipitation) from GCM HadCM3 over period 1981-1990.

Figure 6.8 gives information about the percentage difference between the observation and the simulation of mean areal seasonal precipitation from CGCM3/T47 and GCM HadCM3. In general, the bias values computed from GCM HadCM3 are higher than that from CGCM3/T47 for four seasons, of which the highest bias values are found in the summer following by the spring. The values of bias are the same for both autumn and winter months. Therefore, CGCM3/T47 and GCM HadCM3 are likely to simulate mean areal precipitation accurately.



**Fig. 6.8** Model validation: Bias (percentage difference between observed and simulated mean areal monthly precipitation) from CGCM3/T47 and GCM HadCM3 over period 1981-1990.

## 6.5 Summary

This chapter presented information on the downscaling of daily precipitation from two different Global Circulation Models (GCMs) outputs using the UKSDSM model. This was carried out at-site as well as regional scales over the Waikato catchment. Comparison of model performance for different GCM variables, for at-site and mean areal precipitation were also made.

In general, the SDSM model performs better for mean areal precipitation rather than for at-site precipitation. For both cases, the model performance is dependent on time-variant precipitation.

At station location, the GCM HadCM3 variables are more sensitive to observed precipitation than the CGCM3/T47 variables. The large-scale variables (predictors) from the GCM HadCM3 model and local precipitation observed at four stations (predictand) are correlated. For the case of the CGCM3/T47 model, correlations between predictors and predictand are found at all 14 stations. Daily precipitation was overestimated at some stations and was underestimated at others. For both GCM data, the extreme precipitation events are not properly simulated.

The most common predictors were used to simulate mean areal precipitation over the Waikato catchment. The results obtained from CGCM3 were rather better than that from GCM HadCM3. However, the simulation of extreme precipitation was unable to be assessed.

For both at-site and regional scales, the SDSM best performed in autumn season. The bias between observation and simulation of precipitation from the GCM HadCM3 is higher than that from the CGCM3/T47 variables.

## CHAPTER 7

# Future projections on extreme precipitation

This chapter includes partial reproduction of the paper:

Pham, H., Shamseldin, A. and Melville, B. (2014). Downscaling of daily precipitation and projection of future extreme precipitation. *J. Hydrol. Eng.* (ASCE) (in-press).

Based on the findings of statistically downscaled precipitation using different global circulation models (GCMs) in the previous chapters in which the coarse spatial resolution GCMs significantly affect the accuracy of the downscaled precipitation including extreme precipitation, this chapter introduces the comparative use of statistical and dynamic downscaling techniques. They are examined with daily precipitation for both at-site and catchment scales. Moreover, the regional frequency curve of the North Island region that is developed and explained in Chapter 5 is employed to test the reliability of downscaled precipitation from statistical and dynamic downscaling models. The performance of the partial duration series (PDS) over the annual maximum series (AMS) model is also examined with regard to future extreme precipitation projection.

## 7.1 Introduction

Regional Circulation Models (RCMs), a result of dynamical downscaling of Global Circulation Models (GCMs) to an area of interest, recently became competitors of the GCM statistical downscaling. There are several studies comparing the statistical and dynamic downscaling of daily precipitation from different GCMs in order to best downscale large-scale variables to local precipitation (Drost et al., 2007; Misra et al., 2013; Randall, et al., 2007; Rummukainen, 2010). The performance of these two techniques may differ from one another for daily precipitation projections when applied in the same region. However, these studies did not deal with extreme precipitation projections, especially partial duration series (PDS) of daily precipitation projections (Cavazos, 1998; Furcolo et al., 1995; Lambert et al., 1994; Zhang et al., 2010).

This research for the first time examines the use of the frequency analysis of partial duration series of daily precipitation (FA/PDS) to evaluate the accuracy of downscaled daily precipitation series. These series generated from different models, namely CGCM3/T47, GCM HadCM3 and RCM HadCM3 developed by Canadian and British scientists. The novel FA/PDS5 model defined in the previous chapters is used. This is also compared to the conventional frequency analysis of annual maximum series of daily precipitation (FA/AMS). In addition, the downscaled precipitation time series from two GCMs and a RCM are compared with observations.

## 7.2 Data sets and methods

This section presents the detail of the different data types as well as the techniques used to localize the global climate to the catchment precipitation. A method of predicting extreme precipitation events is also described in detail.

## 7.2.1. Data sets

### 7.2.1.1 Precipitation station data

Daily precipitation data observed at 14 stations over 30 year period, from 1961 to 1990, was selected (refer to Chapter 6).

### 7.2.1.2 Downscaled precipitation data

The statistically downscaled precipitation data from both CGCM3 and CGM HadCM3 is used. The details of these data sets are explained in Chapter 6. The comparison of the performance of these models to the RCM HadCM3 is made through at the study as appropriate.

### 7.2.1.3 Gridded precipitation data

Precipitation data generated from RCM HadCM3 (as RCM hereinafter) at  $0.05^0 \times 0.05^0$  spatial resolution is used. This bias-corrected data is obtained from the National Institute of Water and Atmospheric Research (NIWA). An example of RCM precipitation on 31<sup>st</sup> December 1971 is presented in Figure 7.1.

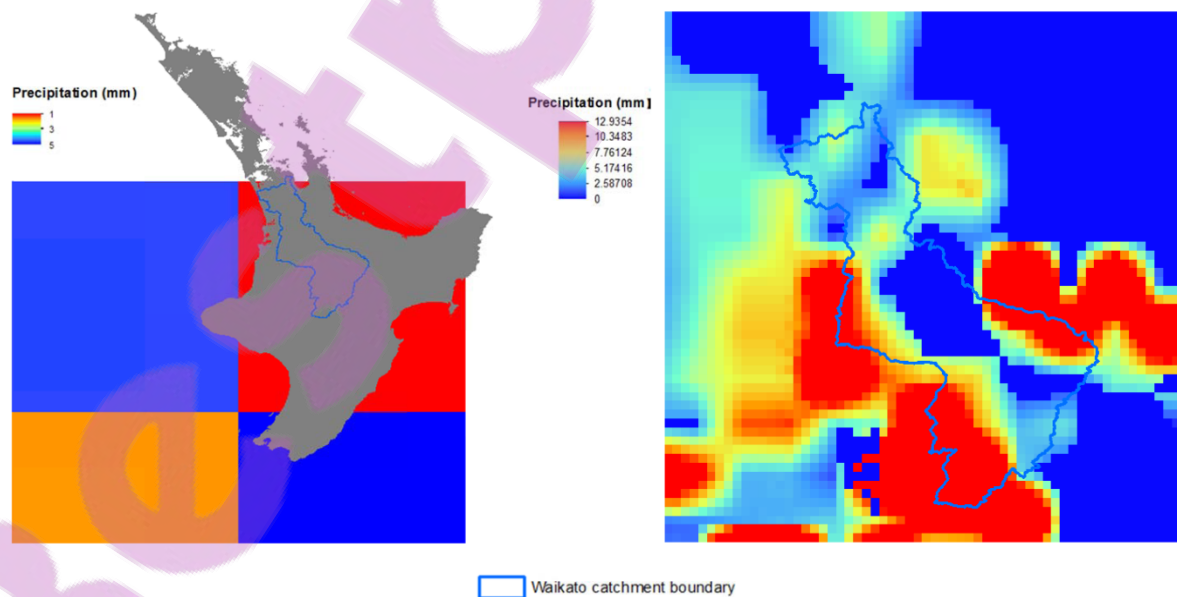


**Figure 7.1** Gridded precipitation data from GCM and RCM models: CGCM3/T47 (left) and RCM HadCM3 (right) over the Waikato catchment

## 7.2.2. Methods

This section presents the step-by-step procedure which is used in this research to obtain the projection of extreme precipitation. Firstly, the precipitation time series from GCMs and RCM are generated for both present and future time slices. Then, these precipitation time series are compared to the observed precipitation. The third and the important step is to validate the precipitation time series generated from GCMs and RCM using a frequency analysis of partial duration series. Finally, the projection of daily and extreme precipitation is performed to predict their future changes, including a comparative frequency curve of PDS and AMS for future extreme precipitation predictions.

### 7.2.2.1. Downscaling and extracting daily precipitation time series

In this step, data generated from GCMs and RCM are extracted and then used to develop precipitation time series at the station level and for the whole study area. The definition of present and future climate is made consistent for all GCMs and RCM.

As explained in Chapter 6, the 30 year-time series of precipitation is extracted from the RCM. The precipitation time series during the period 1971-1990 and 2011-2070 represent the present and the future climate, respectively. The HDF View and the Unidat Net CDF packages are used to extract the precipitation at the station locations and for integrating the results over the study period.

The comparison of downscaled precipitation time series for the present and future climate gives rise to changes in precipitation over decades. The comparison is carried out for the precipitation time series at the site level as well as for the mean areal precipitation time series across the study catchment.

### 7.2.2.2. Evaluation of point and areal precipitation data

The grid cell precipitation time series from RCM is assumed to be a good representation of the precipitation at the gauging site when it is located within a single grid cell. In case where the gauging site is located along the boundary of two or more grid cells, the site precipitation time series is obtained as the average of the precipitation time series of these grid cells. The precipitation is averaged out over 360 grid cells that cover the Waikato catchment in order to obtain the mean areal precipitation (Fig. 1). The RCM precipitation is directly compared to the observed time series at the gauging station. The assumption made here is that the observation at the rainfall gauging stations is considered as ground truth for a 5kmx5km pixel area corresponding to  $0.05^0 \times 0.05^0$  spatial resolution of the RCM.

For simplicity in evaluating the GCM and RCM model simulations together with observed data availability, the 20-year GCM and the RCM downscaled precipitation time series from 1971 to 1990 are compared. Both probabilistic and deterministic performance of GCMs/RCM is evaluated. For deterministic performance evaluation, two statistical coefficients namely, the root-mean-square-root (RMSE) and the percent bias (PBIAS) of the daily time series are calculated for assessing the similarity between the observed and simulated outputs (refer to equations 6.10 and 6.11). Furthermore, an Upscaling (UP) method is also used to verify the probabilistic performance of the GCM and RCM model simulations. This method is based on the Equitable Threat Score (ETS) which discriminate between an event and a non-event (Ebert, 2008 and JWGV, 2009). The ETS can be expressed as follows:

$$ETS = \frac{a - a_r}{(a + b + c - a_r)} \quad (7.1)$$

$$a_r = \frac{(a + b) * (a + c)}{(a + b + c + d)} \quad (7.2)$$

where: a is number of correct simulations of occurrences; b is the number of incorrect simulations of occurrences; c is the number of incorrect simulations of non-occurrences; and d is the number of correct simulations of non-occurrences. The ETS ranges between 1/3 to 1. The closer the ETS value to 1, the better is the model performance.

More importantly, quantiles are computed for different return periods in accordance with GCM and RCM generated precipitation series. The corresponding growth curves are compared to the regional growth curve developed for the whole North Island of New Zealand as detailed in Chapter 5.

### **7.2.2.3. Simulation and projection of future extreme precipitation**

As explained in the previous chapters, a frequency analysis of partial duration series (PDS) could improve the quality of extreme simulations from observations. The use of PDS requires the specification of the average number of peaks per year which is used to define an extreme event. This is because the determination of occurrence and magnitude of extreme precipitation events is more reliable when using a certain threshold value of precipitation or an average number of peaks per year.

It has been shown that an average of five peaks per year from the original daily precipitation series can generate the most reliable series (PDS5) for predicting extreme precipitation over the North Island region of New Zealand, including the Waikato catchment (Pham et al., 2014). In addition, PDS5 series was also confirmed to be valid for regional frequency analysis of precipitation over the catchment (Pham et al., 2013).

In this chapter, the PDS5 series is extracted from the downscaled time series for both present and future climate. From the precipitation time series for the present climate, the PDS data is generated and then used in the frequency analysis. Likewise, the PDS5 series extracted from downscaled precipitation time series for the 2070s is used for future analysis. It is worth noting that off-line statistics confirmed the 14 selected stations located within the catchment to be statistically homogenous.

Extreme precipitation magnitude at a certain period is computed using the Generalised Pareto (GP) frequency distribution (Hosking and Wallis, 1997) for the PDS5 series which is compared to that estimated by the Generalised Extreme Value (GEV) distribution for AMS.

## **7.3 Results and Discussions**

As explained in the method section, any comparison among GCM and RCM precipitation simulation is based on a 20 year time series basis from 1971 to 1990. More detail on the RCM precipitation simulation is presented in this section in which the simulated precipitation time series is compared to the observed time series.

### **7.3.1. Daily precipitation time series generated from GCMs/RCM**

A comparison is made between the RCM generated precipitation and the observed precipitation measured at the station level. The results of validation of both deterministic and probabilistic performance of the RCM are shown in table 7.1 which shows the RMSE, PBIAS and ETS values. Examination of the table shows that the RMSE and PBIAS values computed from RCM generated precipitation series. Examination of the table shows that the RMSE values range between 9.88 and 14.14 suggesting that the simulation is not fitting the observation very well. The most significant difference in the value of RMSE is found

at station 1732 having a RMSE value of 17.31. For the PBIAS coefficient, the negative values are obtained at the majority of stations. This suggests an overestimation from observation. The model underestimation can be found at stations 1732, 2103, 2184, 2214 and 2250 with positive values of PBIAS. Further inspection of the table also shows that the value of ETS computed for all stations is negative, which varies between -0.157 and -0.035 indicating a likely poor simulation of precipitation occurrences.

**Table 7.1** Criteria for assessing the RCM precipitation simulation against observed precipitation between 1971 and 1990

No	Station	Mean daily precipitation (mm)	RMSE (mm)	PBIAS (%)	ETS
1	1529	3.39	12.10	-24.93	-0.035
2	1575	3.45	12.36	-40.10	-0.040
3	1732	5.83	17.31	7.20	-0.066
4	1792	3.63	12.24	-23.35	-0.057
5	1841	3.25	10.45	-24.91	-0.105
6	1974	4.85	13.03	-26.94	-0.084
7	2011	3.91	11.79	-4.96	-0.075
8	2014	3.98	10.13	-4.36	-0.038
9	2018	2.02	9.8	-34.04	-0.055
10	2101	3.35	9.88	-15.46	-0.093
11	2103	4.54	10.09	21.20	-0.086
12	2184	6.62	14.14	45.80	-0.108
13	2214	5.35	13.12	34.25	-0.108
14	2250	3.66	11.48	7.08	-0.157

The mean areal precipitation simulation differs in accuracy from model to model. Table 7.2 presents the information on how the model fits the observation. This has been tested for the three different models used in this study. Inspection of the table reveals that all models overestimate the mean areal precipitation with negative values of PBIAS. This may be caused by bias or errors inherited in the large grid size of the CGCM3 output compared to the smaller grid size of the HadCM3 output. The RMSE values also indicate a close fit of the precipitation from GCM HadCM3 to observation with the lowest RMSE value being 2.89 mm. The weakest fit is found for the CGCM3. There is a moderate fit between observed and simulated precipitation for the RCM HadCM3. For the simulation of precipitation occurrences, both GCM HadCM3 and RCM HadCM3 models give the higher values of ETS. The value of ETS computed for these two models varies between 0.171 and 0.442, respectively. For the CGCM3 model, the ETS value is 0.006, close to 0, which means that the model has difficulty to simulate the occurrence of daily precipitation.

**Table 7.2** Assessment of the downscaling performance for areal daily precipitation over the 1971–1990 period

No	Model	RMSE (mm)	PBIAS (%)	ETS
1	GCM CGCM3	4.17	-12.49	0.006
2	GCM HadCM3	2.89	-2.16	0.171
3	RCM HadCM3	8.72	-4.01	0.442

The accuracy of mean areal precipitation simulation is also evaluated (see Figure 7.2 and Table 7.3). Examination of the figure demonstrates that the extreme precipitation events are not captured when using SDSM. For both GCMs, the maximum value is 15 mm while, the RCM captures the maximum of 130 mm. Investigation of Table 7.3 also reveals that the extreme precipitation occurring at station is quite high in magnitude. For example, an extreme event recorded at station 2214 on 15<sup>th</sup> November 1978 was 220.8 mm.

**Table 7.3** Extreme precipitation events recorded at stations from 1971 to 1990

No	Station	Extreme magnitude (mm)	Date of occurrence
1	1529	149.4	1/1/1971
2	1575	138.2	21/3/1987
3	1732	163.3	5/1/1986
4	1792	99.4	26/4/1973
5	1841	110.2	31/12/1988
6	1974	166.2	17/2/1985
7	2011	168.3	17/2/1985
8	2014	149.9	17/2/1985
9	2018	136.7	17/2/1985
10	2101	102.2	17/2/1985
11	2103	109.3	17/2/1985
12	2184	187.1	9/3/72
13	2214	220.8	15/11/78
14	2250	99.4	21/4/73

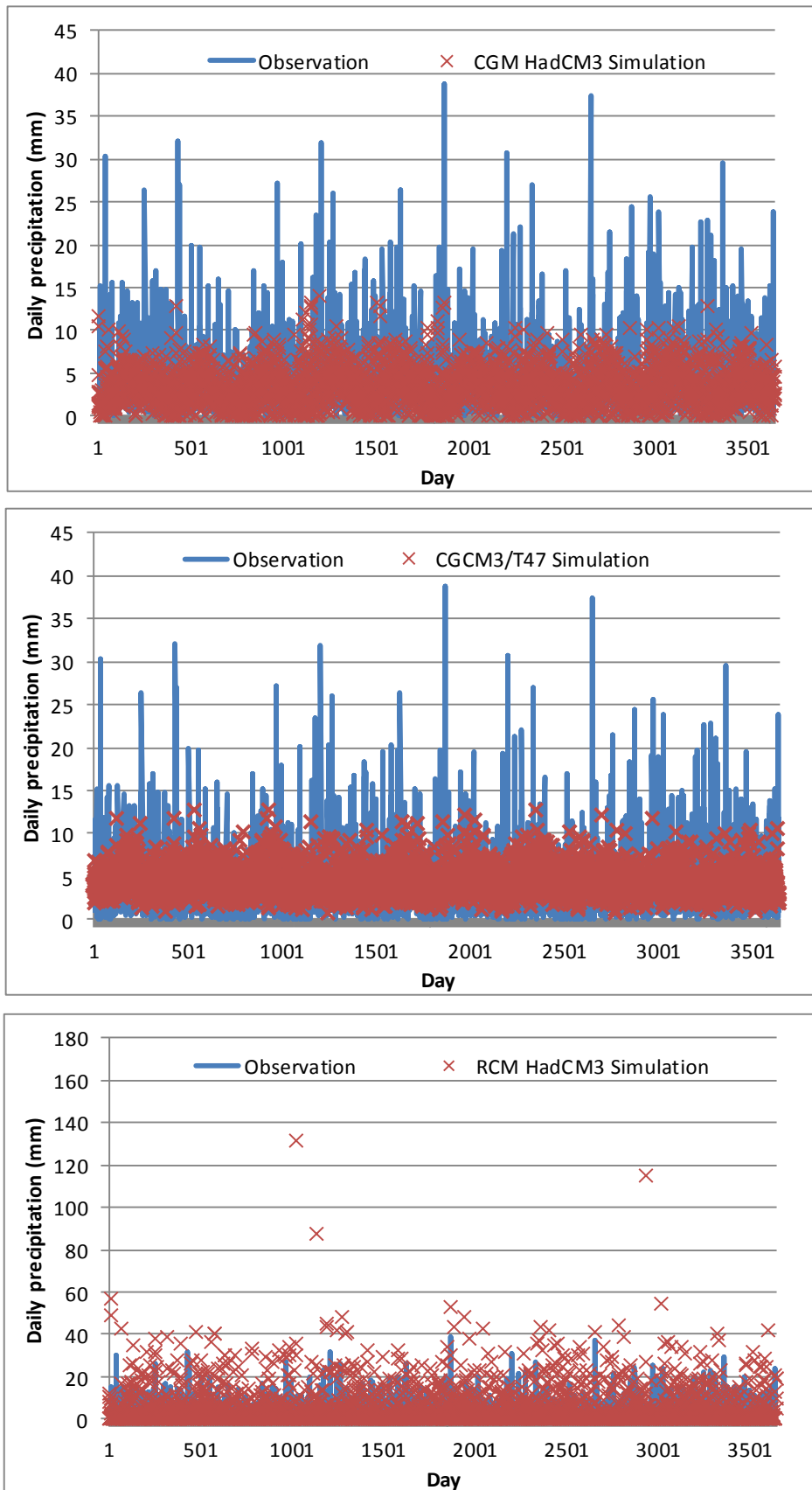


**Figure 7.2** Graphs of areal precipitation simulation from different models against observation over the 1971-1980 period

### 7.3.2. Extreme precipitation estimation

The regional frequency curve of North New Zealand daily precipitation was used as a standard one for assessing the accuracy of extreme precipitation from GCMs and RCM. PDS5 series corresponding to GCMs and RCM mean areal precipitation time series is generated. The precipitation quantiles ( $X_T$ ) were computed according to different return periods ( $T$ ) for the three GCMs and RCM. Also, the regional growth curve obtained from observation (refer to Chapter 5) is shown. The results are presented in Table 7.4 and Figure 7.3.

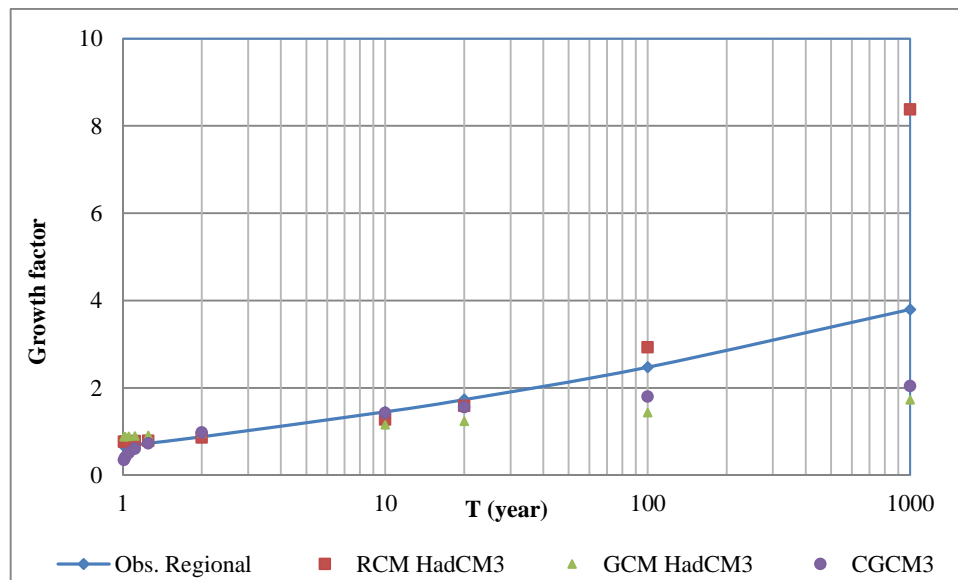


**Figure 7.3** Frequency curves developed for regional observation and model simulation over the period 1971-1990

**Table 7.4** Quantile estimated for regional observed and RCM precipitation

Model	1 – P (%)	0.01	0.02	0.05	0.1	0.2	0.5	0.9	0.95	0.99	0.999
	T (year)	1.010	1.020	1.053	1.111	1.25	2	10	20	100	1000
Regional		0.665	0.668	0.678	0.694	0.730	0.878	1.45	1.73	2.47	3.79
RCM HadCM3	$X_T$ (mm)	0.764	0.765	0.769	0.776	0.790	0.859	1.27	1.58	2.93	8.37
GCM HadCM3		0.884	0.885	0.889	0.895	0.909	0.963	1.15	1.23	1.43	1.72
CGCM3/T47		0.344	0.408	0.509	0.603	0.725	0.981	1.42	1.55	1.80	2.04

Examination of the Table 7.4 and the Figure 7.3 reveals that all three curves are close to the regional curve for T less than or equal to 100 years. However, the quantile values computed for the two GCMs are lower than those of the regional curve, while the RCM quantile values are higher than those of the regional curve. For T equal to 1000 years, the quantile value from the CGCM3 is insignificant although from that of GCM HadCM3 but much lower than regional quantiles. However, the value of RCM quantile is about two times higher than the regional quantile. This may be due to the fact that the 20 year-observations used to develop frequency curves are too short and there may be localized effects caused by topography.

### **7.3.3. Projection of future extreme precipitation**

The mean areal daily precipitation from RCM HadCM3 was selected for studying the variability of extreme precipitation for the future. This runs for emission scenarios A2 over the period 2011-2070 based on 30 year time slice.

Off-line statistics of daily precipitation time series for observation and future projections indicate a rise of annual mean daily precipitation by 1.174% and 2.059% for the 2011-40 and 2041-70 periods, respectively. The statistics also reveal that there is a high variability of daily precipitation in the past with the coefficient of variation ( $C_v$ ) of 0.208. Meanwhile, the values of  $C_v$  computed for 2011-40 and 2041-70 periods are 0.147 and 0.148 respectively, suggesting no substantial change in the variability of future daily precipitation.

Furthermore, the 30 year-daily precipitation projections for the 2011-40 and 2041-70 periods are comparable based on the frequency analysis of extreme precipitation. The results are presented in Figure 7.4. As can be seen from Figure 7.4, there is an agreement

on future extreme event magnitudes for the two scenarios for return periods less than or equal 100 years.

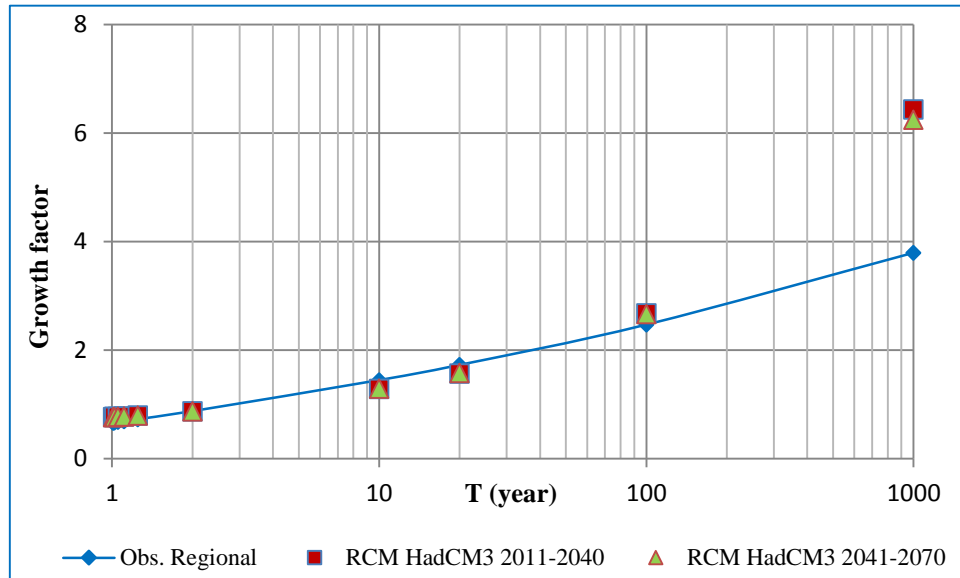


**Figure 7.4** Frequency curves developed for regional observation and model simulation corresponding to the 2011-40 and 2041-70 future scenarios

#### 7.3.4. Future projection of extreme precipitation from AMS and PDS

Even though literature demonstrates that PDS outperforms AMS, the advantage of PDS (also known as PDS5), that is confirmed to be plausible for the study region over AMS, is never examined with future data. The comparison of PDS5 and AMS performance using future data over the Waikato catchment is made hereinafter.

Figure 7.5 shows the frequency curves developed for regional PDS5 and AMS. This is computed for the 2011-44 and 2041-70 periods. In general, a perfect agreement is found between PDS5 and AMS for  $T$  is less than 20 years. For  $T$  is greater than 20 years, the value of growth factor computed for AMS is relatively higher than that computed for PDS5. However, for the case of AMS there is a significant difference in quantiles for  $T$  is greater than 100 years, especially for  $T$  is equal to 1000 years.

Overall, PDS and AMS are likely to well simulate future extreme precipitation for T less than 10 years. However, the AMS overestimates PDS for higher T values, especially when it is greater than 100 years.

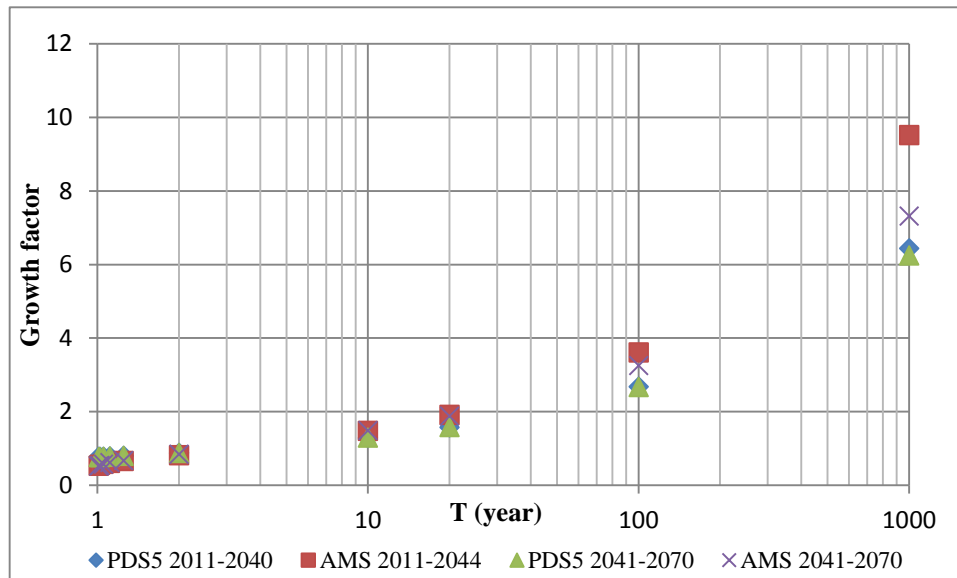


**Figure 7.5** Frequency curves developed for AMS and PDS5 corresponding to 2041-70 and 2041-70 future periods

## 7.4 Summary

This chapter provided more information about obtaining the most reliable future daily precipitation from appropriate GCMs and RCM. They should provide adequate large-scale variables for modelling local daily precipitation including extreme daily precipitation. Firstly, the simulation of historical and present daily precipitation was compared to observation depending on data availability. Both at-site and mean areal daily precipitation were used. The partial duration series (PDS) of daily precipitation was validated using the regional frequency analysis (RFA) which was tested with a wide range of data and over the larger region. Secondly, the simulation of future extreme daily precipitation was evaluated using the RFA/PDS against the annual maximum series (AMS) of daily precipitation (RFA/AMS).

The results showed that the mean areal precipitation from GCMs and RCM are significantly different. However, the RCM mean areal precipitation time series from RCM contains more extreme events than that obtained from GCMs. The research found that extreme precipitation events from GCMs and RCM are very close in magnitude to those obtained from observation for return periods less than or equal to 100 years. There was a significant difference in the magnitude of extreme events for high periods. Therefore, RCM HadCM3 is used for further computation in this research.

## CHAPTER 8

# Future projections on potential evapotranspiration

This chapter includes partial reproduction of the paper:

Pham, H., Shamseldin, A. and Melville, B. (2014). Projection of potential evapotranspiration under climate change over forest and grass catchments, *19<sup>th</sup> Congress of the Asia and Pacific Division of the International Association for Hydro-Environment Engineering and Research (ADP-IAHR)*, Hanoi, Vietnam: 21 – 25 Sept.

This chapter introduces the most advance methods of predicting potential evapotranspiration (PET). The first section of this chapter gives a brief introduction about the combined method as well as its rationale and objectives. The following sections present the data types as well as theories and technical requirements to accommodate the proposed methods. The last section discusses the results computed for both present and future scenarios.

## 8.1. Introduction

The accuracy of PET estimation in the context of climate change studies is dependent on both the methods used to compute potential evapotranspiration as well as the input data from Global and Regional Circulation Models (GCMs/RCMs) (Milly and Dunne, 2011). Different methods and GCMs/RCMs could have different uncertainties/errors depending on their own features (Brazel et al., 1993; Kay and Davies, 2008), causing the inadequate estimation of spatial and temporal evapotranspiration variability (Andersen, 2008). Recently, the use of Regional Circulation Models (RCMs) output data has become preferable for the future projections of PET, especially when it is coupled with the use of the PET method developed by the Food and Agriculture Organization (FAO) (IIASA, 1994; Zotarelli et al., 2010). This combined use could improve the accuracy of PET estimation including very small regions. However, the RCMs perform differently for different regions. There are few studies dealing with PET estimation using the RCM output data. These studies indicate that the higher spatial resolution the RCM, the better is the estimation of PET. However, the RCMs in these studies produce output data up to 25 km as the finest spatial resolution. For this reason, this research aims to examine the use of the FAO-56 method coupled with the daily outputs from the 5 km spatial resolution RCM to predict evapotranspiration rate up to the year 2090. The observation against the simulations is carried out at observation stations as well as being examined in three typical forest and grass sub-catchments within the Waikato catchment.

## 8.2. Data sets and methods

This section presents detailed information on input data requirements, pre-processing and PET computation process. These data sets and methods are also described in the following sub-sections.

### 8.2.1. Data sets

For this research, the data required consisted of the following:

- (1) Daily observed evaporation from the gauging stations (Table 8.1) to be used as the dependent variables. The observation period is from 1970 to 1990; and
- (2) Large-scale data sets as an output of the Hadley Centre Coupled Model, version 3 (HadCM3) are used as independent variables during the period 1971-2090. These data sets were provided by the National Institute of Water and Atmospheric Research (NIWA). In particular, daily values of five major daily large-scale predictor variables in a grid cell of 5km x 5km spatial resolution were used for the SRES A2 scenario (refer to Chapter 3 for more details). The large-scale climatic variables are max and min air temperature  $T_{\max, \min}$  ( $^{\circ}\text{F}$ ), mean relative humidity  $\text{RH}_{\text{mean}}$  (%), solar radiation  $R_s$  (W/d) and wind speed at 5 m over the surface  $U_5$  (m/d).

Three representative forest and grass land sub-catchments of the Waikato catchment are selected as pilot case studies, as shown in Fig. 3.7 (Chapter 3). They are Mangatawhiri, Mangaonua and Whangamarino catchments with total area of about 182 km<sup>2</sup>, 166 km<sup>2</sup> and 131 km<sup>2</sup>, respectively. The evaporation and transpiration processes in these sub-catchments may reflect the impact of vegetation cover on evaporative water loss.

### 8.2.2. Mann-Kendall trend test

The study of the change in evapotranspiration rate from the past to the future requires long-term data sets for both historical and future time slices. Mann-Kendall test is used in this study to investigate the existence of any increasing/decreasing trends in data time series. This is useful to confirm whether or not evaporation paradox occurs in the study region.

The details of this as a non-parametric test are explained in Chapter 4.

For the study region, it may be difficult to determine the trend in evapotranspiration at a certain station. This is due to constrain in data availability and continuity. Therefore, only five out of seven stations with their record length greater than 13 years are selected for the trend test.

### 8.2.3. A combined FAO-RCM approach and EToCal model

Literature demonstrates that the FAO-56 method is expected to be very adequate with the involvement of as many sensitive climatic variables as possible (Bell et al., 2011; Roderick et al., 2009; Shen et al., 2010; Teuling et al., 2009; Abteu et al., 2011). The most controlling variables are air temperature T, relative humidity RH, radiation  $R_s$  and wind speed  $U_s$ . These variables generated from RCM HadCM3 model are used as the input data of the FAO-56 based EToCal model.

#### 8.2.3.1. FAO-56 method

The FAO-56 method estimates evaporative water from a reference grass surface. It is a large uniform grass field that completely covers the soil which is “*kept short, well watered and is actively growing under optimum agronomic conditions*” (Zotarelli et al., 2010). The FAO-56 method is based on the Penman-Monteith equation and can be expressed by the following equation (Zotarelli et al., 2010):

$$ET_0 = \frac{0.408\Delta(R_n - G) + \gamma \frac{900}{T + 273} U_2 (e_s - e_a)}{\Delta + \gamma(1 + 0.34U_2)} \quad (8.1)$$

where  $ET_0$  is the reference evapotranspiration (mm/day);  $R_n$  is the net radiation at crop surface ( $\text{MJ}/\text{m}^2\text{day}$ );  $G$  is the soil heat flux ( $\text{MJ}/\text{m}^2\text{day}$ );  $T$  is the average air temperature ( $^{\circ}\text{C}$ ) recorded at 2.0 m height;  $U_2$  is the wind speed measured at 2.0 m height (m/s);  $e_s$  is the saturation vapour pressure and  $e_a$  is the actual vapour pressure (kPa);  $\Delta$  is the slope

vapour pressure curve ( $\text{kPa}/^{\circ}\text{C}$ );  $\gamma$  is the psychrometric constant ( $\text{kPa}/^{\circ}\text{C}$ ); and 900 is the conversion factor for daily time step and  $\text{ET}_0$  in  $\text{mm}/\text{day}$ .

In this research, a likely actual environment generated from RCM replaces a reference landscape. This is owing to the fact that the global atmospheric circulation and internal surface interactions in GCMs stem to RCMs are then extracted to the interest point or area. In this case, the Penman-Monteith equation still remains the same with its parameters obtained indirectly from the  $T_{\max}$ ,  $T_{\min}$ ,  $\text{RH}_{\text{mean}}$ ,  $R_s$  and  $U_5$  which are optimized at certain height where they dramatically fluctuate. In particular, the optimized height is 3 meters while the FAO reference grass height is 2 meters. The FAO-56 method is utilized in this study for estimation of PET at point (station location) and over an interest area (representative sub-catchment).

### **8.2.3.2. EToCal model**

The PET rate is computed by using EToCal model version 3.2 which was developed by Dirk (2012). This model allows users to compute PET at any location on the globe at different time scales varying from daily, 10-day to monthly. This model also offers different options to represent the data and results in the form of graphs, report and time series.

In practice, the input data preparation is very important in running this model. The first step is to input data into the model. Two different types of input files are station characteristics and meteorological data. The former involves information on station location (attitude, longitude, latitude, coastal, territorial, etc.) and local climate features (arid, semi-arid, humid, semi-humid climate, etc.). The latter includes temperature, humidity, wind speed, and radiation data time series at different time scales depending on

the study purposes. In this step, the time series data is assessed to ensure that they are of good quality and in proper format.

The second step is to assign periods for model calibration as well as climatic parameters. In this step, climatic variables are given upper and lower limits to suit their local climate characteristics. This is adjustable and exchangeable. Also, different units of climate variables are convertible to accommodate these variables in the model domain if they are generated from different RCMs. In the next step, the resulting PET is computed and saved in desired formats.

This process is carried out based on 30-year basis for RCM-generated variables. The resulting 30-year time series of PET is then used to study the change in PET from the present to the future.

### **8.2.3.3. Evaluation of catchment PET simulation**

Observed evaporation data at stations is used for evaluating and validating the FAO-56 based EToCal performance and its simulation in order to avoid errors in future prediction. Thus, future projections of PET in three typical forest and grass sub-catchments are computed which promises to be accurate.

In this research, both daily and monthly PET simulations are evaluated against observed evapotranspiration. The comparison between daily pan evaporation and simulated PET is made among stations. In fact, the observation network is scarce and the observed data is limited. Hence, observed data at station was used with its full record to maximize the overlapping period among stations. Therefore, a 30 year-period from 1971 to 2000 was used for the model evaluation.

In addition, the resulting PET is compared to that computed using Tait-Wood's formula. It is the only comprehensive method and is used nationwide in New Zealand. The Tai-

Wood's formula is based on the relationship between the pan evaporation and PET estimated by the Penman equation. This empirical relationship was tested with all observation stations over the whole New Zealand. The Tait-Wood's formula is as below (Tait and Wood, 2007):

$$PET_p = 0.77 ET_p \quad (8.2)$$

where  $PET_p$  is daily potential evapotranspiration rate that is estimated from Penman equation; and  $ET_p$  is daily pan evaporation rate.

Different statistical coefficients are used for this evaluation consisting of mean, coefficient of variation ( $C_v$ ), quantiles ( $ET_{25\%, 50\%, 75\%}$ ), root-mean-square-error (RMSE) and Nash-Sutcliffe. This is carried for both daily and monthly PET at 7 stations and over three sub-catchments.

The  $C_v$ , quantiles and RMSE are calculated using equations (4.2-4.7 and 5.6). The Nash-Sutcliffe is given as following:

$$E = 1 - \frac{\sum_{i=1}^N (X_{obs,i} - X_{sim,i})^2}{\sum_{i=1}^N (X_{obs,i} - \bar{X}_{obs})^2} \quad (8.3)$$

Where:  $X_{obs,i}$ ,  $X_{sim,i}$ , are the observation and the simulation of evapotranspiration on day  $i$  (mm),  $\bar{X}_{obs}$  is mean daily evapotranspiration measured over  $N$  years (mm).

Monthly pan evaporation and monthly PET plots were used to examine if there was any shift of evaporation pattern from observed to simulated evaporation.

#### 8.2.4. Future projection of PET

With variables generated from RCM, daily PET rate is simulated for three different future time slices namely, 2001-2030, 2031-2060, and 2061-2090. This is calculated for the three sub-catchments (Figure 3.9). The difference in PET between these sub-catchments is

useful for investigating the PET process from different surfaces, particularly forest and grass.

## 8.3. Results and Discussions

### 8.3.1. Long-term daily pan evaporation data sets

As stated earlier, the observation period varies from station to station. In general, the record length of data sets at selected stations ranges between 6 and 31 years. The statistical analysis shows that even though there is a significant difference in data length, the time series among stations have the same level of variability (see Table 8.1). In almost all stations, the value of coefficient of variation ( $C_v$ ) varies from 0.61 to 0.71 (except station 2103). At station 2103, the  $C_v$  value is 1.30 suggesting a high variability in the observed time series. However, the value of daily mean and quantiles ( $ET_{25\%}$ ,  $ET_{50\%}$ ,  $ET_{75\%}$ ) among stations are in good agreement. The difference in these values accounts for about 5% as the maximum.

**Table 8.1** Statistical characteristics of daily evaporation observed at stations

No	Station	Record length (N, years)	Statistical parameters				
			Mean (mm)	$C_v$	$ET_{25\%}$ (mm)	$ET_{50\%}$ (mm)	$ET_{75\%}$ (mm)
1	1841	23	2.26	0.69	0.9	1.9	3.4
2	2005	16	2.30	0.61	1.0	2.2	3.3
3	2081	8	2.25	0.65	0.9	2.0	3.4
4	2101	25	2.30	0.65	1.0	2.0	3.6
5	2103	31	2.73	1.30	1.1	2.0	3.2
6	2128	6	2.35	0.72	1.0	2.0	3.5
7	2250	29	2.00	0.71	0.7	1.7	3.1

*The station location is shown in Fig.3.7, Chapter 3*

### 8.3.2. Trends in daily pan evaporation data

The Mann-Kendall test was carried out for five stations with long record length (Table 8.2). It can be seen from the table that there is no common trend in the pan evaporation for the five selected stations. In particular, the decreasing trend was found in time of two stations namely, 1841 and 2250. However, there is an increasing trend in time series of station 2101. For stations 2005 and 2103, no trend in series was found. Therefore, it is impossible to conclude whether or not there is an increasing or decreasing trend in observed evaporation over the study region. For this reason, the change in pan evaporation over the past decades was not validated in the context of this research.

**Table 8.2** Mann-Kendall test results for different locations

No	Station	Z	P (%)	Trend
1	1841	-1.19	11.7	Decreasing
2	2005	-3.26	0.6	No trend
3	2101	0.88	81.6	Increasing
4	2103	-4.38	0.0	No trend
5	2250	-1.39	8.23	Decreasing

*The test was done at the 5% significance level*

### 8.3.3. Potential evapotranspiration estimation and FAO-RCM model validation

Daily PET was computed using  $ET_0$ Cal model with RCM-generated  $T_{max, min}$ ,  $RH_{mean}$ ,  $R_s$  and  $U_5$  being used as input data. This is carried out at seven station locations and over the three selected sub-catchments over the 1971-2000 period. The statistical analysis result of daily PET simulation is presented in Table 8.3. Examination of the table indicates that similar to statistical characteristics of observed data time series, there is good agreement on mean,  $C_v$  and quantile values for almost all stations. However, the values of mean,  $C_v$  and quantiles computed for station 2250 are much smaller than the rest. This may be due to the effect of topography, vegetation cover or land use. In general, the results presented in the table indicate that there is a good agreement between the simulation and the observation of PET values in terms of mean,  $C_v$  and quantiles.

**Table 8. 3** Statistical characteristics of daily PET simulation for the 1971-2000 periods

No.	Station	Sub-catchment	Statistical parameters				
			Mean (mm)	$C_v$	ET <sub>25%</sub> (mm)	ET <sub>50%</sub> (mm)	ET <sub>75%</sub> (mm)
1	1841		2.68	0.57	1.4	2.4	3.7
2	2005		2.89	0.43	2.0	2.7	3.7
3	2081		2.85	0.47	1.8	2.7	3.8
4	2101		2.84	0.51	1.7	2.6	3.8
5	2103		2.78	0.49	1.7	2.6	3.7
6	2128		2.78	0.58	1.6	2.5	3.8
7	2250		2.33	0.53	1.2	2.0	3.2
8		Whangamarino	2.81	0.48	1.7	2.6	3.7
9		Mangatawhiri	2.85	0.45	1.9	2.7	3.7
10		Mangaonui	2.76	0.51	1.6	2.5	3.7

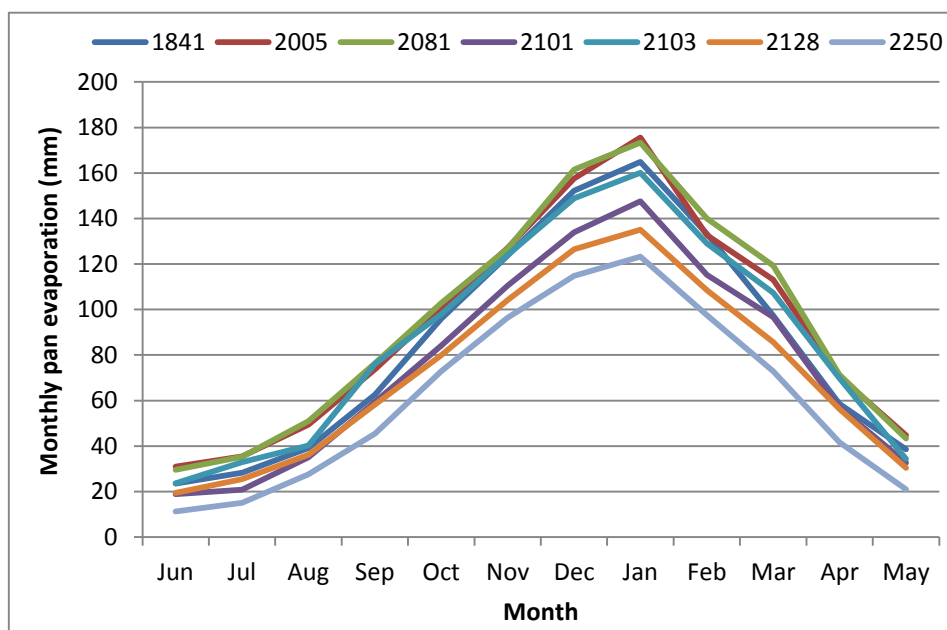
Further statistical analysis also confirms the similarity in results between observation and simulation (i.e., observed evaporation and PET modeled by FAO-56 method) as well as between the Tait-Wood and FAO-56 simulation. This is examined for seven stations (Table 8.4). In general, the RMSE values computed for the Tait-Wood and FAO-56 simulations are higher than that from the observation and FAO-56 simulation. However, the difference of RMSE values is very small being between 0.02 mm to 0.07 mm for almost all station. This suggests that both the Tait-Wood and FAO-56 methods give similar results of PET rates. The largest different value of RMSE of 0.12 mm is found at station 2101 the estimations of PET by using the FAO and the Tait-Wood methods are slightly different. Similarly, the Nash- Sutcliffe coefficient (E) values range between 0.62 and 0.95 indicating a good agreement on daily PET rate estimated from these two methods.

**Table 8.4** Assessment of daily PET simulation against observation, and for different methods

No.	Station	RMSE (mm)		Difference (%)	Nash-Sutcliffe (E)
		Observation vs. FAO56	Tait-Wood's <sup>(*)</sup> vs. FAO56		
1	1841	2.00	2.02	0.02	0.69
2	2005	2.10	2.13	0.03	0.62
3	2081	2.22	2.25	0.03	0.95
4	2101	1.51	1.63	0.12	0.83
5	2103	2.41	2.43	0.02	0.95
6	2128	2.32	2.39	0.07	0.95
7	2250	1.83	1.89	0.06	0.85

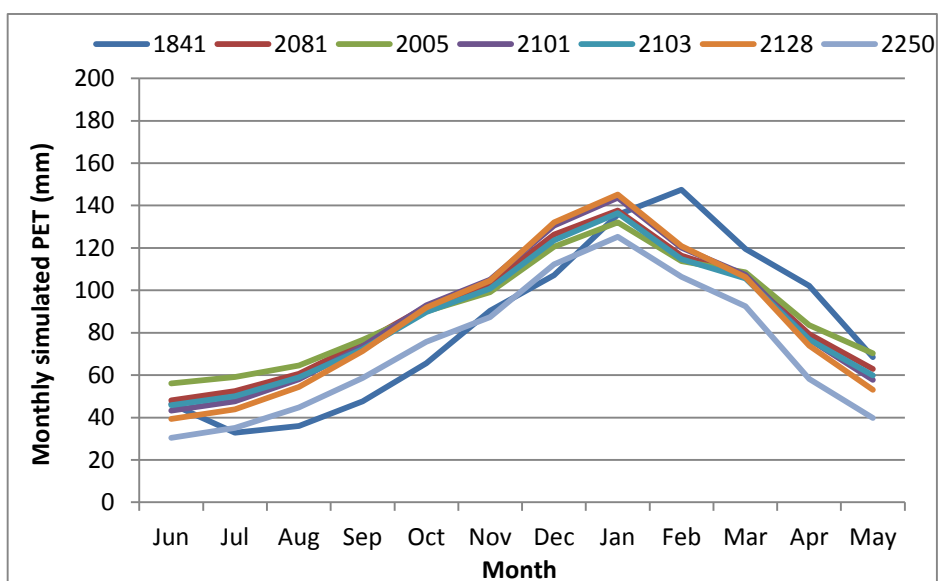
<sup>(\*)</sup>Refer to formula (8.2) developed by Tait and Woods (2007)

In order to investigate the pattern of PET against that of pan evaporation, the monthly time series of observation and simulation is used. Fig. 8.1 presents the monthly pattern of pan evaporation for different stations. As can be seen from the figure, at all stations the record length does not have any significant effects on their evaporation distributions because they follow strictly one common pattern. In a typical year, the maximum evaporation is recorded in January when the amount of evaporative water reaches up to 170 mm/month for station 2005, as the highest peak. Other stations also experience a monthly peak in evaporation but at smaller magnitude, such as evaporation at station 2128 of about 130 mm/m. The lowest evaporation rate occurs in June at 20 mm/m for station 2101. Similar rates are also found in other stations during this month.



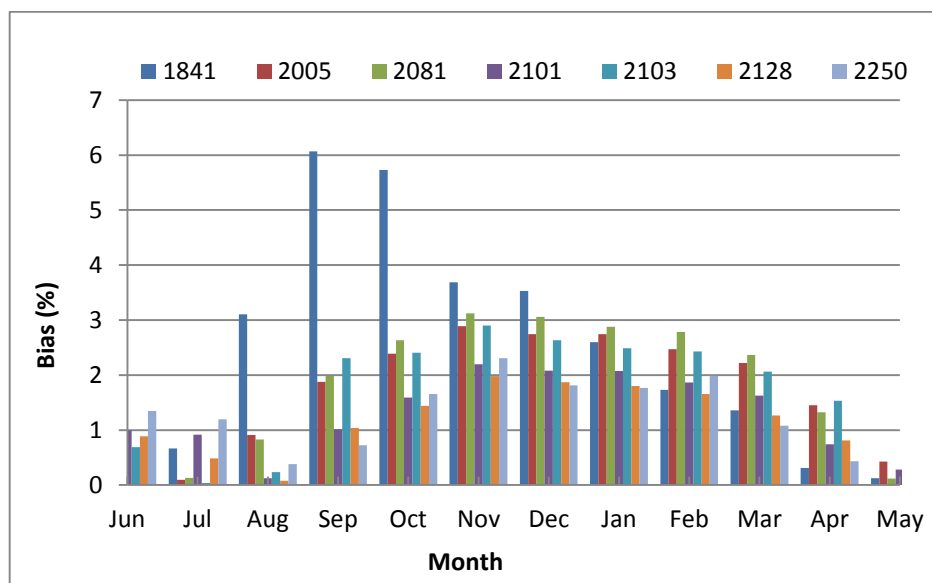
**Figure 8.1** Monthly pan evaporation distributions for different stations

Fig. 8.2 shows a pattern of monthly PET computed from RCM-generated variables using the  $ET_0$ Cal model. In general, the monthly PET simulation follows a pattern found in every station with peaks occurring in January. However, a shift in peak by one month is found at station 1841 even though its PET rate is the highest. There is a small difference of peak magnitude among stations which ranges between 125 mm/m to 145 mm/m. The minimum value of PET is computed at 30 mm/m at station 2250 in June.



**Figure 8.2** Monthly simulated PET distribution for different stations

Fig. 8.3 gives information on the difference between observed and simulated monthly evapotranspiration. Examination of the figure indicates that at almost all stations there is a significant difference in evapotranspiration rate in spring and summer months (from Sept to Mar). Exception of station 1841, the estimation and observation of evapotranspiration are greatly different in Aug, Sep and Oct. This may be due to the errors in measurement and data interpretation at this station.



**Figure 8.3** Bias (percentage difference between observed and simulated monthly evapotranspiration) at different stations

### 8.3.4. Future projections of daily potential evapotranspiration of different sub-catchments

The 30 year time series of daily PET is projected for three future time periods, namely 2001-2030, 2031-2060 and 2061-2090. The results are presented in Table 8.5. Inspection of the table indicates the common tendency found in the three selected sub-catchments. In general, there is an increase in the daily PET mean,  $C_v$  as well as in the annual mean PET

towards the future time. However, the degree of increase of these parameters in Whangamarino sub-catchment is higher than that found in the Mangatawhiri and the Mangaonua sub-catchments. The change in  $C_v$  differs from catchment to catchment, and from time to time.

Further examination of the table also shows that, there is an increase in the mean daily PET with time. For the 2001-30 period, the mean daily PET rate is 2.89 mm, 2.93 mm and 2.87 mm for Mangatawhiri, Whangamarino and Mangaonua sub-catchments, respectively. After 30 years, the mean daily PET is projected to be 2.95 mm, 3.02 mm and 2.92 mm for the 2031-60 period resulting in an increase in annual evapotranspiration of 1.8%, 2.8% and 4% for the three sub-catchments, respectively. This increasing trend maintains for the 2061-90 period over all three sub-catchments varying from +1.6% to +4% relative to the 2001-30 period.

**Table 8.5** Summary on characteristics of future PET projections for different sub-catchments

No.	Catchment	Cover type	Future time slide	Mean daily PET (mm)	$C_v$	Annual PET (mm)	% change
1	Whangamarino	Grass-land	2001-30	2.93	0.44	1,056	+2.9
			2031-60	3.02	0.45	1,086	+2.8
			2061-90	3.14	0.44	1,130	+4.0
2	Mangatawhiri	Natural forest	2001-30	2.89	0.44	1,041	0.0
			2031-60	2.95	0.45	1,060	+1.8
			2061-90	3.07	0.44	1,105	+8.5
3	Mangaonua	Grass-land	2001-30	2.87	0.44	994	-1.4
			2031-60	2.91	0.46	1,034	+4.0
			2061-90	3.02	0.46	1,050	+1.6

Overall, the mean daily PET increases with time in three sub-catchments. This can also be clearly seen in Figure 8.4. Changes in future PET remain at relatively same rate from sub-scenario to sub-scenario, thus more water loss is projected from both forested and grassed surfaces. The evapotranspiration rate is found higher from grassed surface rather than from forested surface. This can be explained by the effect of surface type.

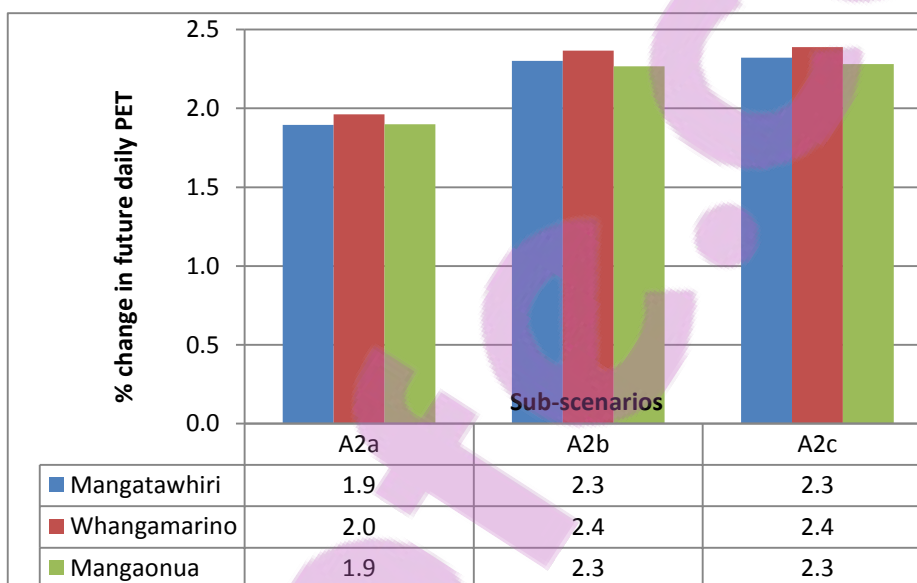


**Figure 8.4** Future change in mean daily PET for different sub-catchments

Figure 8.5 shows the variation of projected daily PET series over three climate scenarios using a dimensionless coefficient of variation ( $C_v$ ). This is examined for all three sub-catchments. The figure indicates increasing  $C_v$  values revealing a rising variability in daily PET series. The same trends in  $C_v$  are found for both the Whangamarino and Mangatawhiri sub-catchments. The  $C_v$  values increase by 1% from 2031 to 2060 and then decrease by the same rate during the 2061-90 period. For the Mangaonua sub-catchment, the value of  $C_v$  projected for the 2031-60 and 2031-60 periods varies more than that for the 2001-30 period. A rise of  $C_v$  value suggests a high variability in the daily PET series. This occurs in all but with different degree of changes by scenarios among sub-catchments. The daily PET projections in both Mangatawhiri and Whangamarino sub-catchments have the same level of variability. The value of  $C_v$  increases by approximately 2.2 % from the 2001-30 period to the 2031-60 period. Higher variation of daily PET projections is found in Mangaonua sub-catchment. The value of  $C_v$  is 0.44 for the 2001-30 period and then increases by about 4.4% up to 0.46 for both the 2001-30 and 2031-60 periods.

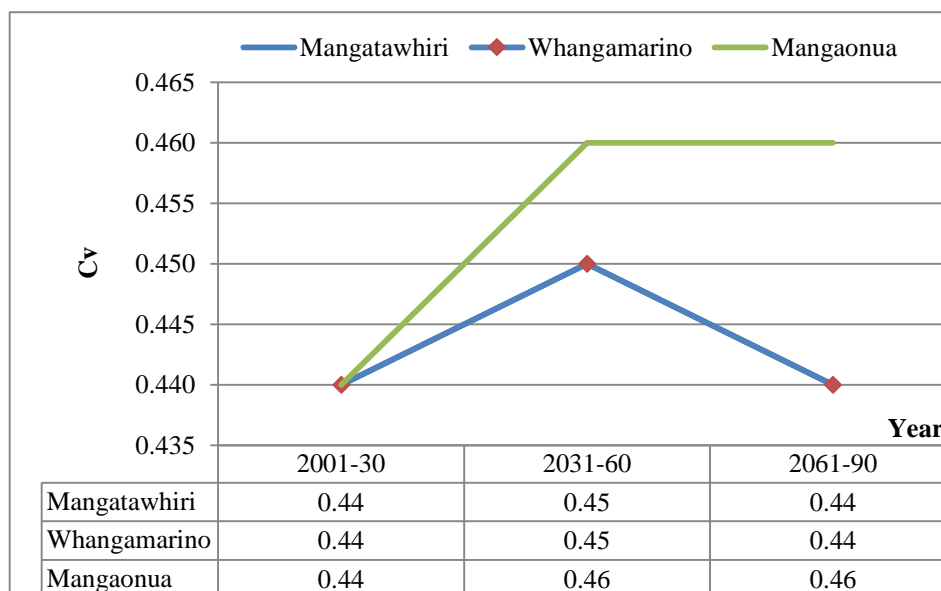


**Figure 8.5** Variation coefficient of mean daily PET projections for different sub-catchments

## 8.4. Summary

This chapter gave the details of predicting future PET from very high RCM spatial resolution. Different statistical tests were used to evaluate the PET simulations against the observation from stations. Consequently, the water loss due to evaporation and transpiration processes from different surfaces was also projected for three different future periods, such as 2001-30, 2031-60 and 2061-90.

The trend test showed an increasing trend in the daily observed evaporation in one station, a decreasing trend in two stations and no change in daily evaporation series in two other stations. This may be due to the effects of data length and topography as well as surface type.

Evaluation of daily potential evapotranspiration (PET) simulation revealed that the  $ET_0$ Cal model is an effective tool for computing PET from  $T_{\max, \min}$ ,  $RH_{\text{mean}}$ ,  $R_s$  and  $U_5$  variables. These climatic variables were generated from RCM-HadCM3 model at 5km x 5km resolution and effective for this research. Overall, the model performed very well at all stations with acceptable RMSE and E values. In addition, there was a good agreement between daily PET simulation from  $ET_0$ Cal model and that from the Tait-Wood formula. The former relatively overestimated the later. However, the difference in daily PET from these two methods accounts for only about 2%.

The monthly PET simulation also showed a good fit to the observation. In general, the monthly simulated PET distribution was found to be similar to the observed one with the peaks appearing in January. However, the monthly PET simulation was underestimated with their peak magnitudes at 150 mm in comparison to 170 mm in monthly evaporation observation.

The results also showed a good agreement between observation and simulation at all stations, including the three sub-catchments in terms of statistical coefficients. However, there was a slight different in monthly pattern between observation and simulation over the past years. Future projections of potential evapotranspiration (PET) of three sub-catchments indicated an increasing tendency for daily and annual PET rate from grassed surface to be higher than that obtained from forested surface. An increase in daily PET is projected up to 2% by 2030, 2.4 % by 2090 relative to 1971-2000, which amplifies the future changes in annual PET up to +2.9% and 8.5% by 2030 and 2090, respectively.

## CHAPTER 9

# Assessment of climate change impacts on catchment water balance

This chapter includes partial reproduction of the paper:

Pham, H., Shamseldin, A. and Melville, B. (2014). The assessment of climate change impact on water balance of forested and farmed catchments. *J. Hydrol. Eng. (ASCE)* (in-press).

This chapter integrates the results of precipitation and potential evapotranspiration from the previous chapters into the combined modelling of catchment water balance. The rationale and objectives are introduced in the early sections of the chapter. A brief overview of data and methods used together with computational aids are presented in the following parts. The final section of the chapter discusses the modelled results in detail as well as the uncertainty sources that may affect the results.

## 9.1. Introduction

Water balance modelling is commonly used to quantify the impacts of climate change on water availability of a region or a catchment. Under climate change, significant variability in precipitation and evapotranspiration would dramatically affect the catchment water balance. Changes in soil and vegetation also have large impacts on water resources. However, current water balance modelling is mainly dependent on precipitation while evapotranspiration is a fixed proportion of precipitation. Also, the interaction of the various phases of rainfall- runoff transformation within the soil is not fully computed. This research for the first time investigates the combined effects of precipitation and evapotranspiration on the water balance of three typical grass and forest sub-catchments of the Waikato catchment. The conceptual lumped water-soil MIKE-11 NAM model was employed to simulate the land phase of the hydrological cycle including soil moisture and ground water recharge from rainfall, evapotranspiration at catchment scale for both historical and future time slices. The change in catchment water balance from past to future times was investigated.

## 9.2. Data and methods

### 9.2.1. Data

Data on daily precipitation and potential evapotranspiration (PET) are employed as the key inputs of daily water balance models. Daily observed precipitation, evaporation ( $ET_p$ ) and observed discharge were obtained from gauging stations and used as a baseline which is represented for present climate. Data from at least one station located within the catchment or in vicinity was used. This is due to the limitation of data observation.

Mean areal precipitation and potential evapotranspiration generated from a regional climate model developed by the Hadley Centre in the United Kingdom version 3 (HadCM3) were used. These gridded data were adopted from the previous chapters which were assessed to be reliable for studying climate change. Data over two different periods, 1961-2000 and 2001-2090 were used for present and future climate modelling, respectively. The summary of data selected for the study is presented in Table 9.1.

**Table 9.1** Summary of historical data used in the study

No	Catchment	Gridded precipitation	Gridded PET	Observed precipitation	Observed ET	Observed discharge
1	Mangatawhiri	1961-2090	1961-2090	1973 - 1983	1973 - 1983	1971 – 2000
2	Whangamarino	1961-2090	1961-2090	1982 - 1990	1982 - 1990	n/a
3	Mangaonua	1961-2090	1961-2090	1981 - 1996	1981 - 1996	1981 - 2000

The description of three representative sub-catchments namely Mangatawhiri, Mangaonua and Whangamarino is presented in Chapter 8. Their soil and land use maps are presented in Chapter 3 (Figures 3.15 – 3.19). The three catchments had similar patterns of precipitation, evaporation and flow as shown in Figures. 3.13 and 3.14.

## 9.2.2. Materials and Methods

This section presents information on data analysis of the daily potential evapotranspiration and daily water balance model as well as its performance in simulating and predicting the water balance for both historical and future climates. Following on from this the change in water balance in three catchments with different characteristics was investigated.

### 9.2.2.1. Bias-corrected potential evapotranspiration

The daily precipitation is directly extracted from the HadCM3 model, while the PET is computed from different climatic variables (i.e., temperature, relative humidity, radiation and wind speed) which are extracted from the same HadCM3 model (refer to Chapters 5 to 8). The results reveals that daily precipitation time series generated from the HadCM3 model are suitable for future prediction using a frequency analysis of partial duration series of daily precipitation. The PET series computed from HadCM3 variables ( $PET_{RCM}$ ) is underestimated in winter months and overestimated in summer months when it is compared to evaporation observed at station. Therefore, a bias-correction method was employed to correct  $PET_{RCM}$  in this study in order to give more accurate runoff production and streamflow.

The bias-correction method is expressed mathematically as follows (Habte, 2013):

$$PET_{bias-corrected}(i) = PET_{RCM}(i) \cdot \frac{\overline{PET_{obs}}}{\overline{PET_{RCM}}} \quad (9.1)$$

where  $PET_{bias-corrected}(i)$  is the corrected RCM evapotranspiration on day  $i$  (mm);  $PET_{RCM}(i)$  is the raw RCM precipitation on day  $i$  (mm);  $\overline{PET_{obs}}$  is the mean monthly evaporation obtained from observations for a given month (mm), and  $\overline{PET_{RCM}}$  is the mean monthly potential evapotranspiration from RCM HadCM3 variables for a given month (mm).

In this research, the areal mean PET from RCM is corrected to the observation at stations which is located within the catchment or vicinity.

### 9.2.2.2. Lumped and conceptual model

This research employs a lumped, conceptual rainfall-runoff model, namely Nedbør-Afstrømnings-Model (NAM) for simulating precipitation-evapotranspiration-runoff process over three selected sub-catchments. This model was originally developed by the Department of Hydrodynamics and Water Resources at the Technical University of Denmark (DHI, 2009). It accounts for the spatial and temporal variability of hydrologic processes, especially when the catchment size is small ranging from 104 km<sup>2</sup> to 166 km<sup>2</sup>.. In this case, small catchments are considered to be homogenous in term of hydro-meteorology for the best simulation of catchment water balance. The NAM model is applicable for a number of catchments with different hydrological regimes and climatic conditions (DHI, 2009; Brauer, 2007; Hafezparast et al, 2013; Nayaka et al, 2013; Vaitiekuniene, 2005).

The NAM model represents various components of the rainfall-runoff process by continuously accounting for the water content in four different and mutually interrelated storages. Each of these represents different physical elements of the catchment (DHI, 2004). This model can be applied to individual catchments although regional uniformity does not exist, and then is able to transpose to ungauged catchment (Vaitiekuniene, 2005). In addition, the NAM model allows users to take man-made interventions in the hydrological cycle such as irrigation and groundwater abstraction into account. However, NAM model also exhibits some errors in simulated runoff which is too dependent on human interference, like reservoir operation (Brauer, 2007).

The model simulates river flow from overland flow, interflow and baseflow as a function of the water storage in the four storages. The structure of the NAM model is shown in Figure 9.1. The basic input requirements for the NAM consist of model parameters, initial

conditions, meteorological data including precipitation, potential evapotranspiration, and runoff data for model calibration and validation.

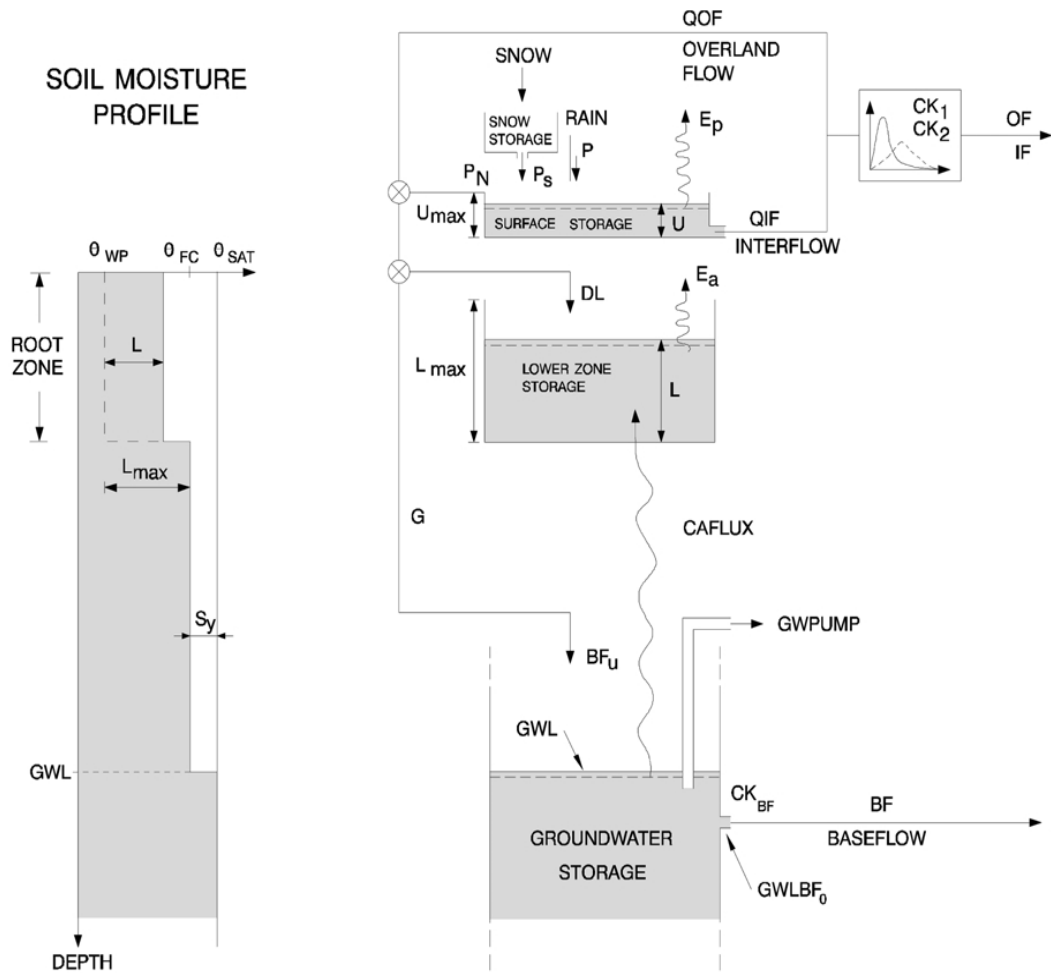


Figure 9.1 NAM model structure (from Madsen et al., 2002)

### 9.2.2.2.1. Model calibration and validation

Due to the discontinuity of observed data series, the calibration and validation periods for two catchments are different. Table 9.2 gives more details about the calibration and validation periods. Both trial-and-error and auto-optimization procedure were applied to determine the optimized model parameter sets which give the most reliable results for both calibration and validation processes. The most physically sensitive parameters to the catchment characteristics are presented in Table 9.3.

**Table 9.2** Model calibration and validation periods for different catchments

No	Catchment (Gauge ID)	Calibration period	Validation period
1	Mangatawhiri (459.11)	2/1/1973 – 31/12/1981	1/1/1982 – 31/12/1983
2	Mangaonua (421.1)	1/1/1981 – 31/12/1993	1/1/1994 – 31/12/1996

*Model calibration and validation is not applied for the ungauged Whangamarino catchment*

**Table 9.3** Summary of NAM model parameters

No.	Parameter	Unit	Description	Effect	Range
1	$U_{\max}$	mm	Upper zone storage capacity (mm)		1 - 100
2	$L_{\max}$	mm	Lower zone storage capacity (mm)		20 - 500
3	CQOF		Overland flow runoff coefficient		0 - 1
4	TOF, TIF, TG		Overland flow, interflow and Recharge threshold coefficients, respectively		0 - 0.95
5	$CK_{1,2}$	h	Time constant for overland flow and interflow routing.		3 - 48
6	$CK_{IF}$	h	Time constant for interflow from the surface storage		500 - 1000
7	$CK_{BF}$	h	Baseflow time constant for baseflow from the groundwater storage		500 - 5000

*(From Madsen et al., 2002)*

### 9.2.2.2.2. Model performance evaluation

In order to assess the reliability of model used in this study, different statistical coefficients are used consisting of Coefficient-of-Efficiency, CE by Nash Sutcliffe (1970) and Kling-Gupta-Efficiency coefficient, KGE by Gupta et al. (2009). These coefficients are commonly used to test agreement between observation and simulation. CE and KGE are sensitive to time to peak, however the application of KGE shows its advantages over the CE criteria. In particular, the use of CE underestimates the variability and mean of flows but introduces largest errors in peak runoff. In contrast, the KGE presents variability, mean of flow and linear correlation well (Pechlivanidis et al., 2010). Also, root-mean-square-error RMSE and water balance error WBL coefficients are used. The four coefficients are expressed as below which are used for both calibration and validation stages.

$$CE = 1 - \frac{\sum_{i=1}^n (S_i - O_i)^2}{\sum_{i=1}^n (O_i - \bar{O})^2} \quad (9.2)$$

$$KGE = 1 - ED \quad (9.3)$$

$$\text{with } \alpha = \frac{\sigma_{S_i}}{\sigma_{O_i}}, \beta = \frac{\bar{S}}{\bar{O}} \quad (9.4)$$

$$\text{and } ED = \sqrt{(r-1)^2 + (\alpha-1)^2 + (\beta-1)^2} \quad (9.5)$$

r = linear correlation coefficient

$$WBL = \left| \frac{\sum_{i=1}^n (S_i - O_i)}{n} \right| \quad (9.6)$$

where  $O_i$  is the observed streamflow on day  $i$  ( $\text{m}^3/\text{s}$ );  $S_i$  is the simulated streamflow on day  $i$  ( $\text{m}^3/\text{s}$ );  $\bar{O}$  is the mean of the observed streamflow data, and  $\bar{S}$  is the mean of the simulated streamflow data.

### **9.2.2.3. Modelling of future runoff production and assessment of catchment water balance**

After the most plausible sets of NAM model parameters were obtained, they are then used to predict future runoff from future precipitation and potential evapotranspiration data. 30 year-based time series was generated for this purpose.

The parameter sets optimised for the Mangaonua catchment are adapted to simulate streamflow in the Whangamarino catchment which has the same characteristics. This is because no data on discharge was available for the Whangamarino catchment.

Future catchment runoff volume is predicted from future precipitation and PET data for the 2001-2030, 2031-2060 and 2061-2090 periods. The change in runoff volume is assessed among future scenarios and against observation periods between year 1973 and 1996 depending on catchments.

## **9.3. Results and Discussions**

### **9.3.1. The MIKE-NAM calibration and validation**

The optimized parameter sets for two Mangatawhiri and Mangaonua catchments are presented in Table 9.4 below. Inspection of the table shows that the most significant difference is found for  $U_{\max}$  and corresponding  $L_{\max}$ ,  $CK_{1,2}$ , TOF, TIF and TG parameter values. These are known as the most sensitive parameters to the catchment characteristics. These parameters are strongly related to soil permeability and surface interception capacity which directly influences the stream flow generation from groundwater and interflow within the soil profile (DHI, 2004; Sun and Liu, 2010).

**Table 9.4** NAM parameters for different catchments

Parameter	Unit	Lower bound	Upper bound	Final value	
				Mangatawhiri (forested)	Mangaonua (grass)
$U_{\max}$	mm	5	35	<b>6</b>	<b>20</b>
$L_{\max}$	mm	50	350	<b>70</b>	<b>201</b>
CQOF		0	1	0.45	0.35
CKIF	h	500	1000	762	773
$CK_{1,2}$	h	3	35	<b>14.14</b>	<b>26.68</b>
TOF		0	0.7	<b>0.44</b>	<b>0.395</b>
TIF		0	1	<b>0.293</b>	<b>0.909</b>
TG		0	0.7	<b>0.058</b>	<b>0.482</b>
CKBF	h	500	4000	2698	2981

Further examination of Table 9.4 reveals that the values of  $U_{\max}$ ,  $L_{\max}$ ,  $CK_{1,2}$ , TOF, TIF and TG computed for the Mangaonua catchment are higher than that for the Mangatawhiri catchment. This suggests a resistance of permeable soil and grassed surface which requires a long time to generate ground-and-inter flows in the Mangaonua catchment. In contrast, a well-developed porosity of soil texture in the forested Mangatawhiri catchment requires less time but high threshold values allowing rain water infiltrate and travel through soil layers to river. This result is consistent with the main properties of recent soils.

Table 9.5 presents information about model performance evaluation using five different coefficients which are explained in the previous section. In general, the model performs well for the Mangaonua catchment with higher values of  $r$ , CE and KGE and lower values of RMSE and WBL in comparison to its performance for the Mangatawhiri catchment. These results are likely for both model calibration and validation processes. A relatively poor agreement between observation and simulation is found in the Mangatawhiri catchment. This may be due to the fact that the water balance input data consisting of the selected precipitation and evaporation do not fully represent the catchment conditions (Boughton, 2005). In particular, precipitation and evaporation data in the Mangaonua catchment are obtained from the stations located within the catchment, while the data used for the Mangatawhiri catchment runoff modelling are from one station in the catchment and one station in the vicinity. The distribution of these data can be seen in Figures 3.13 and 3.14 (Chapter 3).

**Table 9.5** Model evaluation for different catchments

Catchment	Calibration period					Validation period				
	r	RMSE	CE	KEG	WBL	r	RMSE	CE	KEG	WBL
Mangatawhiri	0.42	3.98	0.42	0.48	3.0%	0.40	7.80	0.40	0.49	35.40%
Mangaonua	0.60	1.31	0.59	0.72	4.1%	0.56	2.15	0.55	0.66	0.7%
Whangamarino	n/a	n/a	n/a	n/a	n/a	n/a	n/a	n/a	n/a	n/a

*NAM parameters for the Whangamarino catchment are adapted from Mangaonua-NAM parameters*

*Whangamarino simulated discharge and volume are compared to Mangaonua observation*

Figures 9.2 to 9.5 introduce the visualization of model calibration and validation for the Mangatawhiri and Mangaonua catchments. However, for the overall testing consisting of both calibration and validation periods the model performance is likely to be acceptable with  $r$  of 0.43 and 0.53 for the Mangatawhiri and Mangaonua catchment, respectively. For both cases, the WBL value is 0% indicating a perfect simulation regarding the runoff volume accuracy.

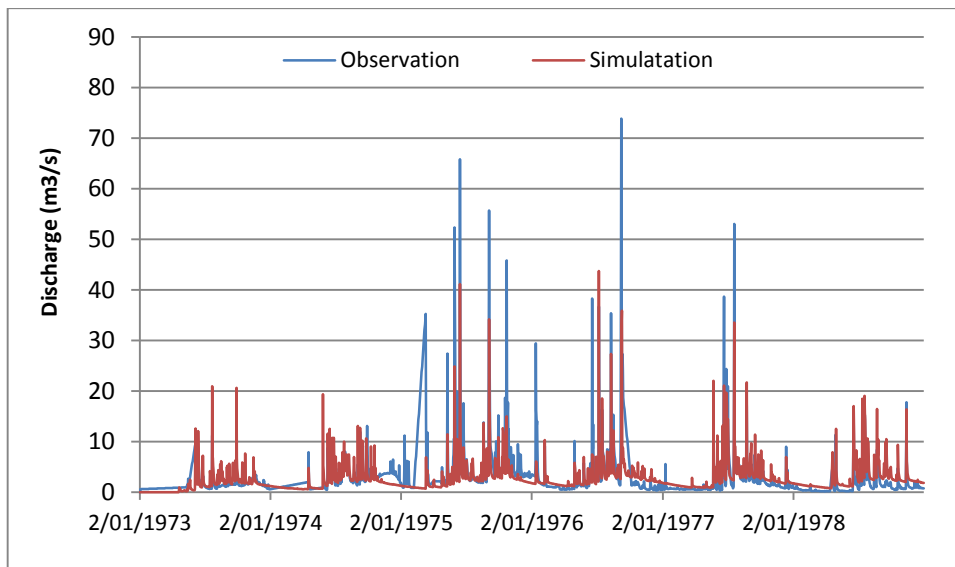


**Figure 9.2** Calibrated hydrograph for Mangatawhiri catchment over the 1973-78 period

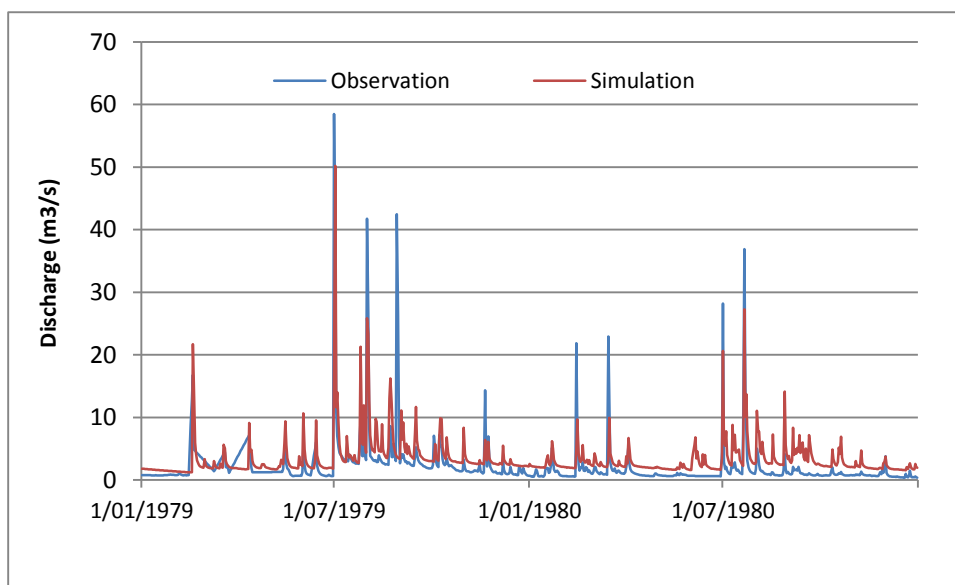


**Figure 9.3** Validated hydrograph for Mangatawhiri catchment during the 1979-80 period

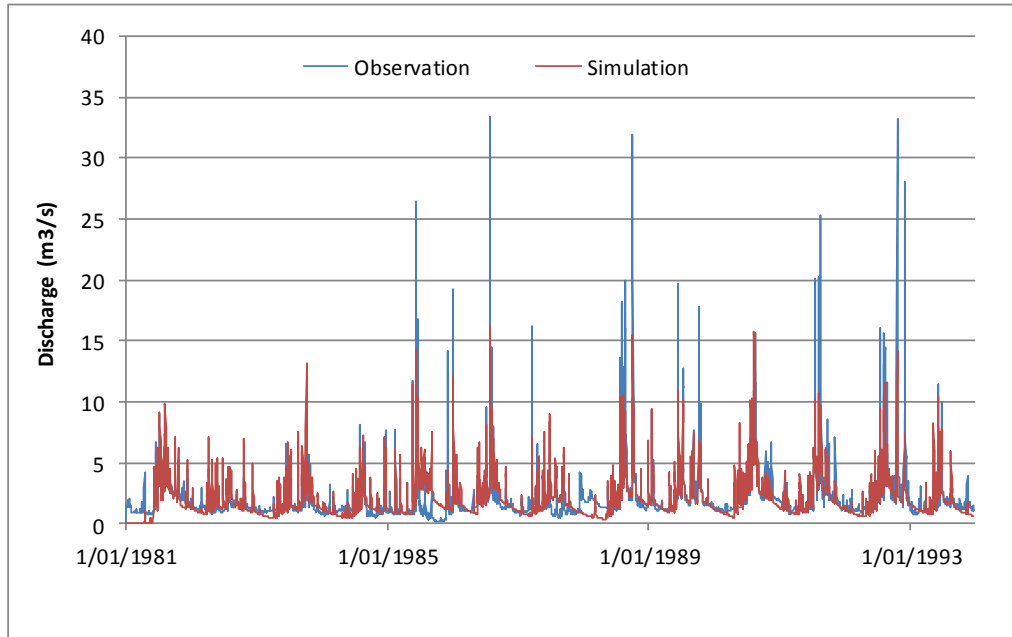


**Figure 9.4** Calibrated hydrograph for Mangaonua catchment during the 1981-93 period

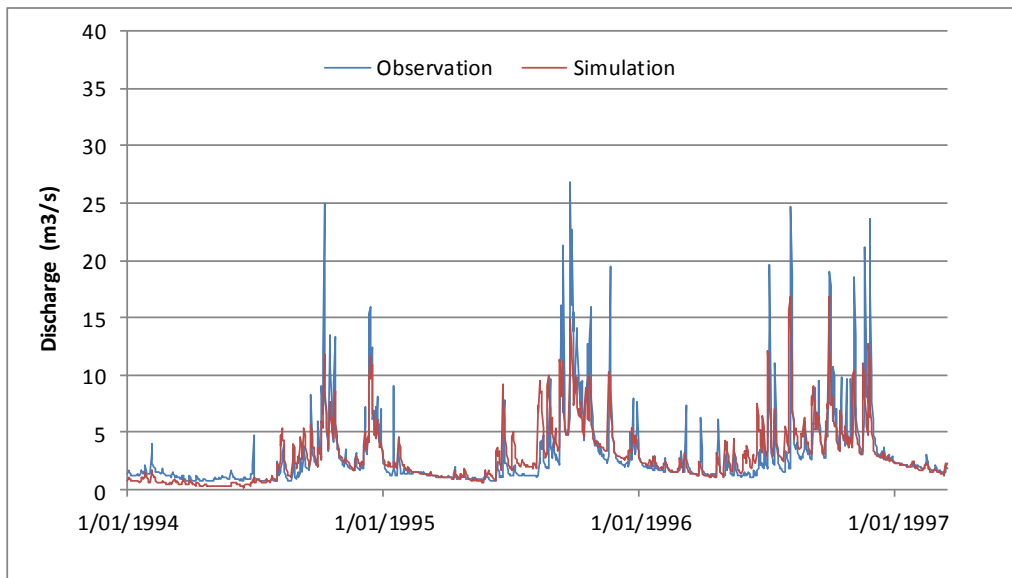


**Figure 9.5** Validated hydrograph for Mangaonua catchment during the 1994-96 period

The Whangamarino catchment with dominant ultic, gley and recent soil types which are relatively permeably characterized may constrain the flow generation. This characteristic is relatively similar to the dominant soil type in the Mangaonua catchment. Moreover, these two catchments are dominantly covered with grasses. Therefore, the adapted NAM model parameter of the Mangaonua catchment is considered to be valid for the Whangamarino catchment.

### **9.3.2. Projected changes in future water balance**

The validated parameter sets for each catchment are used to project the future stream flows. 30 year-time flow series are projected for the 2001-30, 2031-60 and 2061-90 periods. A comparison between future projections of streamflow computed from unbiased corrected PET and bias-corrected PET is made, accordingly.

Figures 9.6 to 9.8 show the changes in runoff volume among future sub-scenarios. In general, a decrease in runoff volume is found with time. Particularly, water yields for the 2031-60 period are less than that for the 2001-30 period, but higher than for the 2061-90 period. However, the degree of changes differs from catchment to catchment. Examination of these figures reveals that the most dramatic reduction in runoff volume occurs in both grassed catchments, Whangamarino and Mangaonua. This decreasing trend in water volume is consistent with an increasing PET and decreasing precipitation that occurs in the study catchments.

The overall change in runoff volume for all the three catchments also appears in Table 9.6.

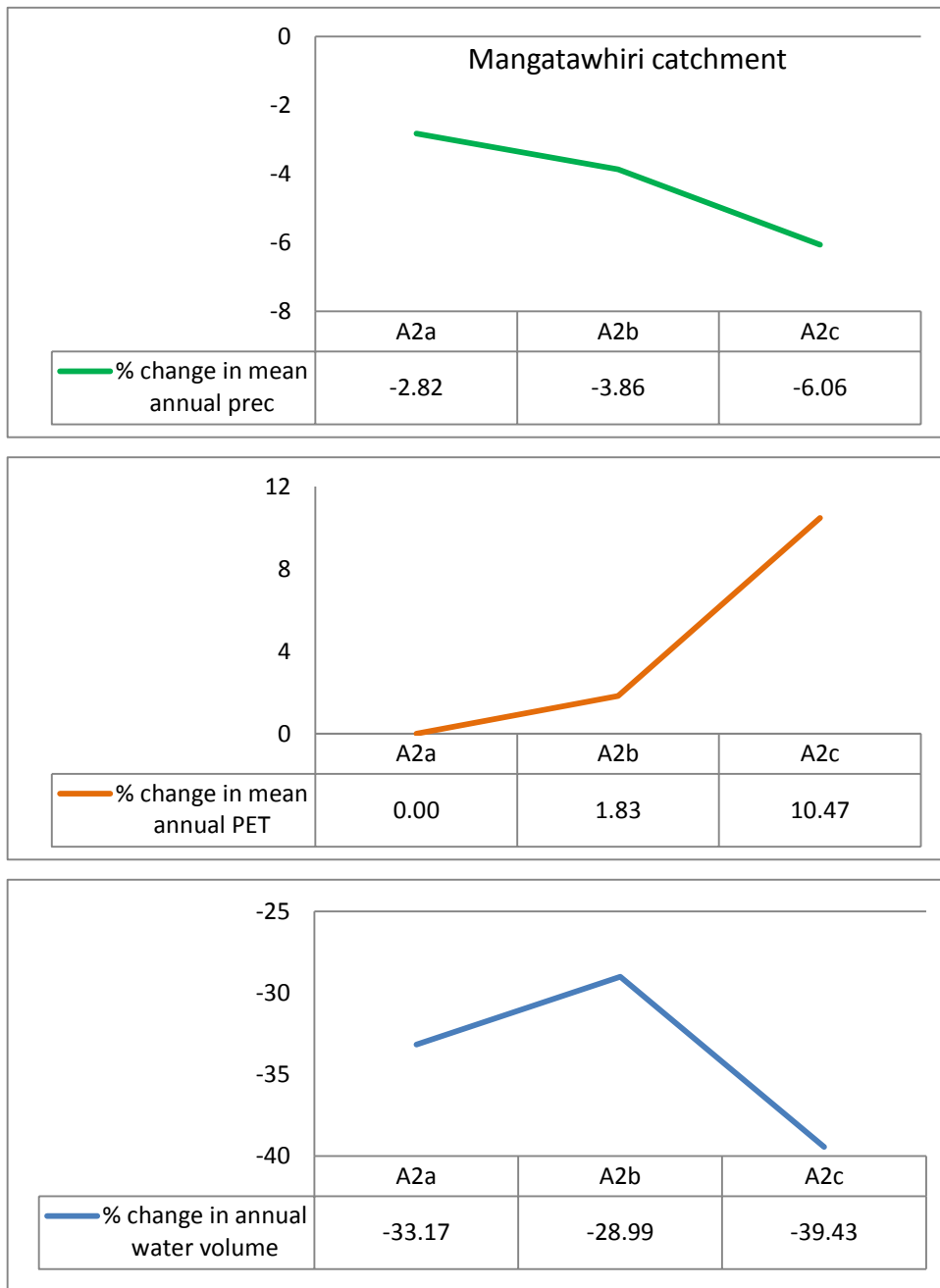


**Figure 9.6** Future changes in annual precipitation, PET and runoff volumes for the periods 2001-30, 2031-60 and 2061-90 relative to the observation period - the Mangatawhiri catchment

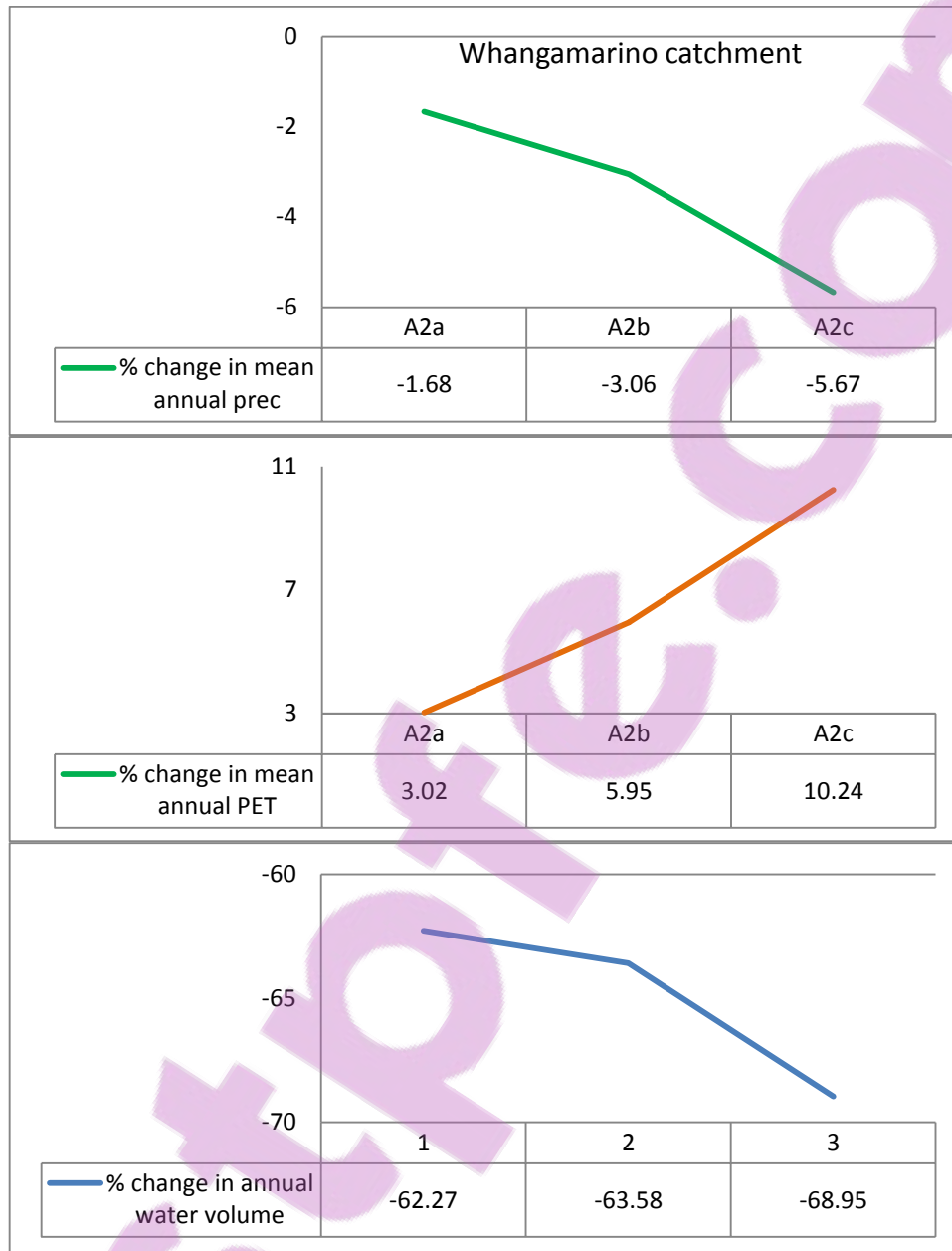


**Figure 9.7** Future changes in annual precipitation, PET and runoff volumes for the periods 2001-30, 2031-60 and 2061-90 relative to the observation period - the Whangamarino catchment

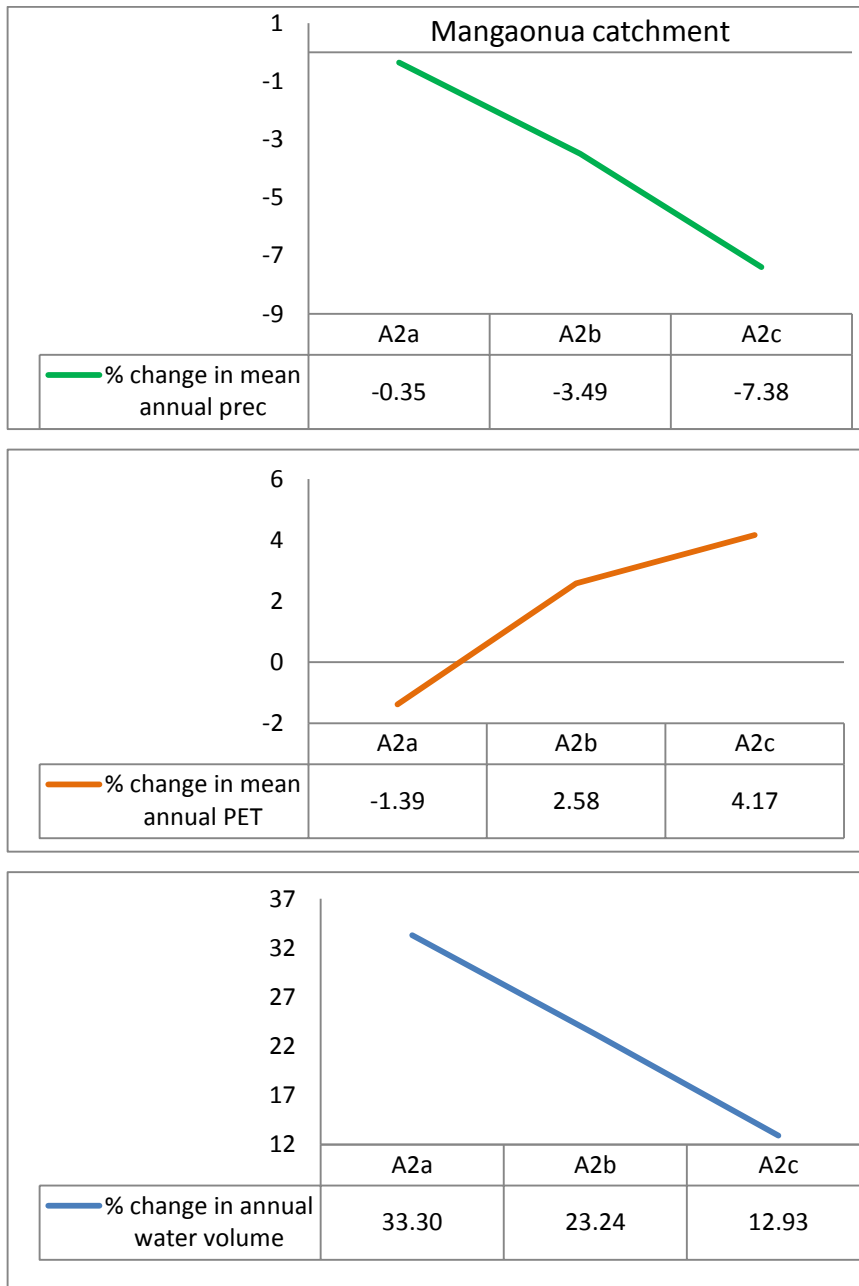


**Figure 9.8** Future changes in annual precipitation, PET and runoff volumes for the periods 2001-30, 2031-60 and 2061-90 relative to the observations - the Mangaonua catchment

**Table 9.6** Future projections of catchment water balance

Catchment	Future projection		
	(Change in runoff volume, %)		
	2001 – 2030	2031 – 2060	2061 – 2090
Mangatawhiri	-33.0	+6.25	-15.0
Whangamarino	-6.0	-3.0	-15.0
Mangaonua	+3.3	-8.0	-8.0

*The change in runoff volume for the 2001-30 period is relative to the observed volume, and that for the 2031-60 and 2061-90 periods are compared to the change in runoff volume for the 2001-30 period.*

*(-), (+) indicate a decrease/increase in runoff volume, respectively*

For the Mangatawhiri catchment as an example, runoff volume decreases by approximately 33% as a result of decreasing precipitation by 2.8% by 2030 relative to the 1973-83 period. For the 2031-60 period, a combined effect of changing precipitation and evapotranspiration by -3.86% and +1.83 respectively could terrify a decrease in runoff volume. However, a small increase in volume by about 6.25% is projected after 30 years. This could be caused by a variation of RCM data series.

The dependence of future river flow on changing evapotranspiration is also shown in Figures 9.9 to 9.11. This is tested with the three catchments over three sub-scenarios by comparing discharge from non-bias-corrected and bias-corrected PET. An adjustment is made between individual months. PET rate increases by about 1.0 to 1.2 times during the summer months (Nov – Mar) and decreases by around 0.7 to 0.8 times in the winter months. As can be seen from these figures, monthly flow experiences a significant change in volume with time in all three catchments which is consistent with changing PET. For the Mangatawhiri catchment, a change in monthly flow is projected between -10% and +15% in Feb and Jun, accordingly. A projected change in the Whangamarino catchment flow is up to -22% and +20% in the same months. This tendency is proved in all three sub-scenarios, A2a, A2b and A2c. In the Mangaonua catchment, a dramatic change in monthly flow is projected by -60% and +40% in Feb and Jun months for A2b and A2c scenarios. However, river flow is projected to increase whole year and its maximum change is up to 35% in Jun month for A2a scenario. This may be compensated by increasing precipitation.

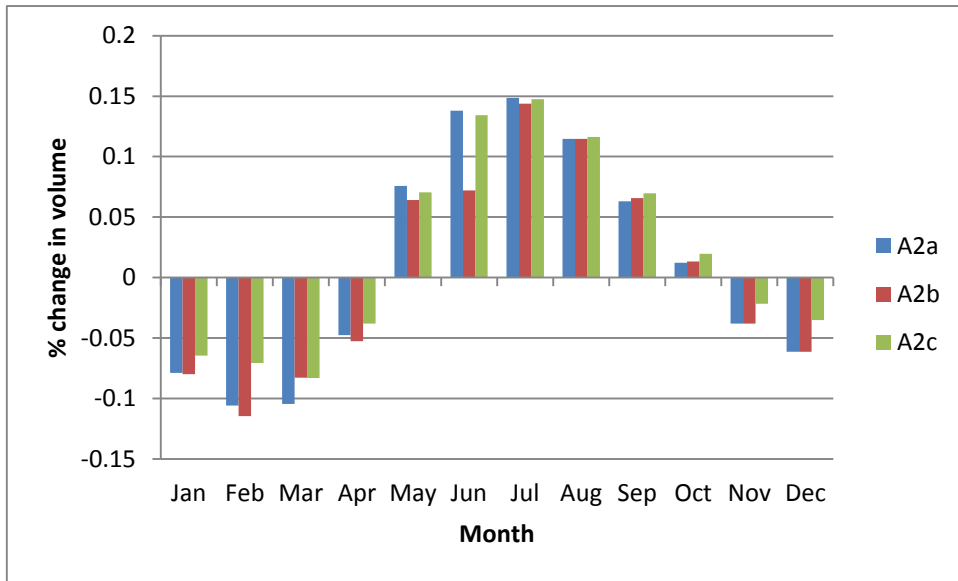


**Figure 9.9** Change in river flow computed from bias-corrected PET relative to what computed from unbias-corrected PET for the 2001-30, 2031-60 and 2061-90 periods - the Mangatawhiri catchment

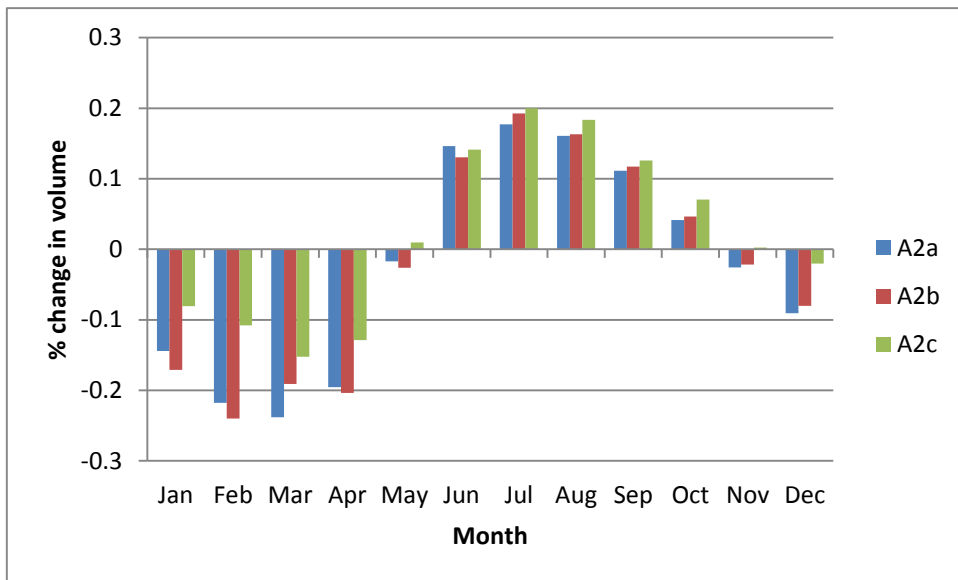


**Figure 9.10** Change in river flow computed from bias-corrected PET relative to what computed from bias-corrected PET during the 2001-30, 2031-60 and 2061-90 periods - the Whangamarino catchment

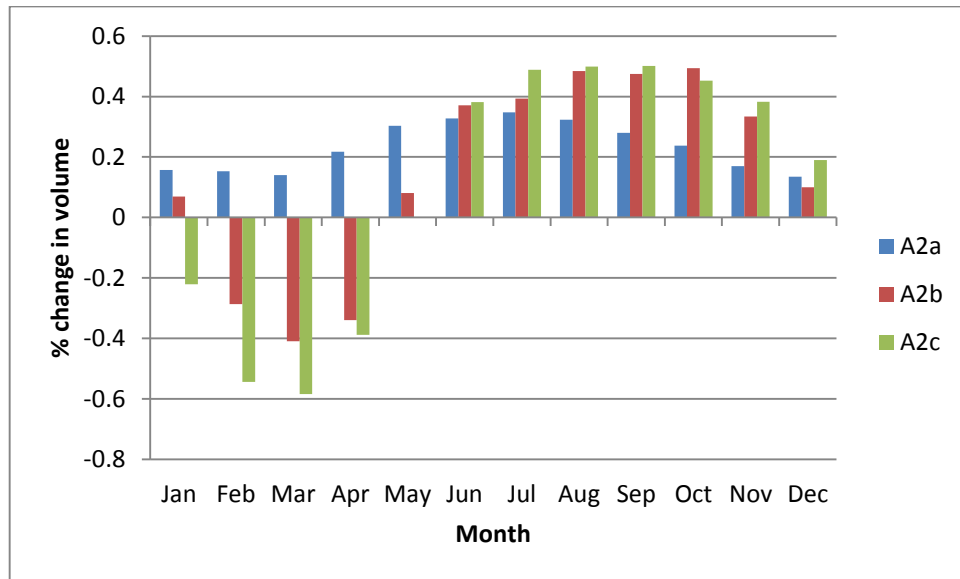


**Figure 9.11** Change in river flow computed from bias-corrected PET relative to what computed from unbiass-corrected PET for the Mangaonua catchment for the 2001-30, 2031-60 and 2061-90 periods

Further examination of Figures 9.9 to 9.11 also indicates that, the correction of daily RCM-generated PET to observed evaporation at station has a dramatic effect on the catchment runoff. Overall, the reduction of PET in the winter months raises the mean daily runoff in the same months up to 50%. The same rate is also found in the decrease of mean daily runoff in the summer months with increasing PET. The distribution of corrected runoff seems to be more reliable than that of uncorrected one because it suits the local weather in which more evaporation but less precipitation occur in the summer and versa in the winter. Therefore, the use of bias-correction method is necessary to model monthly and seasonal runoffs in the study catchments.

### 9.3.3. Errors in a combined modelling of future streamflow

This section presents major errors that may affect the accuracy of streamflow simulations and projections. This is because the study utilises various data sources as well as models/programmes. Moreover, in order to simplify and make use of certain techniques applied with scarce data availability, some assumptions were also made in this study. These persistent errors in the modelling of catchment water balance may originate from the following sources.

#### 9.3.3.1. Uncertainty embedded in regional climate model

Literature has indicated that both technical and scientific limitations are inherited in any GCMs and RCMs (Chun, 2010; Dubrovsky, 2009; Im et al., 2010; Mujumdar and Ghosh, 2008; Jeong et al., 2012; Pielke, 2012; Wilby et al., 1999). These limitations include parameterization, resolutions, initial and boundary conditions, inter-model variability, and validation/verification issues (Foley, 2010; Pielke, 2012; Rummukainen, 2010). Many errors in the GCMs stem from the RCMs because “*the dynamics and physics of the RCM are the same as in the GCM except for certain parameterization constants that had to be set differently to account for the higher resolution of the RCM*” (Drost et al., 2007). Also, initial and boundary conditions are used differently to model a nested region (Randall et al., 2007). In this case, the structure of these RCMs becomes more complex resulting in inter-model variability (Chen et al., 2012; Dubrovsky, 2009; Mpelasoka, 2000; Mujumdar and Ghosh, 2008). As a result, RCM-generated variables are biased, and not all of them are bias-corrected with the observed data during the validation/verification processes (Pelt et al, 2009; Sunyer et al., 2012) (Drost et al., 2007).

### **9.3.3.2. Uncertainty from future scenarios**

The IPCC SRES scenarios are used as the standard one dealing with the study on the impact of future changes which is developed based on historically decadal trends in climate and human activities (Bakker et al, 2011; Esqueda et al., 2011; IPCC, 2000). All regional climate change scenarios are driven by the GCM scenarios that are rather limited for climate and hydrological extremes (Bronsterst et al, 2007; Qian et al, 2010; Wang et al., 2012). This is a major consequence of scenario uncertainty on the climate change signal (Baguis et al, 2010). Like the driving GCM scenarios, high resolution RCM scenarios developed from regional climate model experiments also contain inherent uncertainty during modelling (Mearns et al., 2003; Schmidli et al., 2007).

### **9.3.3.3. Uncertainty caused by observation and usage**

For the study catchments, observation network and data are limited or discontinuous. Observed data from nearby stations was used because climate variables between target and study stations are correlated. However, the surrounding environment of the selected stations is not exactly the same. In fact, the measured climate variables are strongly dependent on local environment such as, topography, attitude, vegetation cover, land use, etc. (Craig, 2006; Roderick and Farquhar, 2002).

### **9.3.3.4. Uncertainty created by hydrological models and other programs**

This study uses various programs and models ranging from input data extraction and correction to hydrological simulation. For the data extraction programs, gridded data is extracted from RCM output by the latitude and longitude position on the surface of the study catchments. The accuracy of extracted data for that catchment may be  $\pm 1$  grid cell when the catchment boundary lies within 2 or more grid cells. This error may be minor for

a catchment with large area, but it could come to be major for small catchments in this study. In fact, the size of each grid cell of HadCM3 output used is 5km x 5km. The area of study catchments varies from 104 km<sup>2</sup> to 166 km<sup>2</sup> covering about 5 to 10 grid cells at 5km resolution. The EToCal program is used to compute PET from climate variables which are also based on some certain assumptions of local climate. This can create errors in the resulting PET. For the hydrological NAM model, it is important to relate model parameters to catchment properties that directly drive the streamflow generation as well as runoff production. Furthermore, simulation of runoff in the ungauged catchments is challenging because the correlation between the calibrated parameters and catchment characteristics is not accounted for the current models (Boughton, 2005). However, as demonstrated in many studies, the modelled results are strongly dependent on the input data rather than the effects of the characteristics of a catchment and its hydrological responses (Boughton, 2005a, b, c; Boughton, 2006; Droogers and Allen, 2002).

### **9.3.3.5. Uncertainty caused by study assumptions**

Due to the existing circumstance of study catchments and their data, this study has made some assumptions that are listed below.

- Model parameter are adapted for a ungauged catchment
- Model parameters are unchanged under climate change
- Only one IPCC SRES A2 scenario is considered
- Data on precipitation and evapotranspiration computed from RCM over the 1961-200 period are used as historically observed precipitation during the model calibration stage.

These typical underlying assumptions may affect the accuracy of modelled results. In particular, errors persistent in model parameters could still stem from a gauged catchment

to an ungauged catchment. Furthermore, the valid model parameters may not be adequate for future projection where climate change takes place. This is another error in modelling future runoffs. In addition, the use of only one SRES A2 scenario may not provide a comprehensive assessment of catchment response to climate change. In this regard, more SRES scenarios could give a better assessment. Finally, the data over the 1961-2000 period may not fully present the climate state of the past century. This could result in a difficulty in investigating the change in catchment runoffs from the past to the future times.

## 9.4. Summary

To summarise, this chapter provided detail on the modelling of catchment water balance from the changing precipitation and potential evapotranspiration towards future times. The importance of these two key components of a catchment water balance was also addressed.

A simulation of historical streamflow from observed precipitation and evaporation was considered to be in good agreement with the observed flow. The values of KGE coefficient ranged between 0.5 and 0.7 for the Mangatawhiri and Mangaonua catchments, respectively. The results also revealed that the model performance can much improve if the observed data on precipitation and evaporation are representative of those catchments.

For the three catchments used in this study, the selected precipitation stations are located in the downstream or even near the catchment outlet where the elevation is just about one third or one fourth of what in the upstream of the catchment. However, if any systematic errors tolerated in the historical simulations may not have significant impacts on the future projections. The validated model parameters, therefore, are accepted for future projections of streamflow of those catchments as well as of ungauged catchments.

The research also found that changes in precipitation and especially potential evapotranspiration have a large impact on streamflow even though they do not much affect runoff volume. By comparing the patterns of monthly streamflow conducted from unbiased and bias-corrected evapotranspiration, the results also demonstrate that if the evapotranspiration rate increases or decreases by 1.0 times, the mean daily streamflow consequently decreases or increase by the same rate at up to 50%.

Streamflow is projected to dramatically decrease in 2030, 2060 and 2090 in the grassed catchments while an inconsiderable reduction is found in the forested catchment.

## CHAPTER 10

# Conclusions and recommendations

In this chapter, conclusions which have been reached based on the results of this research are provided together with the contributions to knowledge in this research field. Recommendations for possible further research are also presented.

## 10.1. Conducting remarks

### 10.1.1. Future projection of extreme precipitation

Precipitation, the most important component of the catchment water balance, is one of the primary issues addressed in this thesis. Daily precipitation was projected for selected sub-catchments, namely Whangatawhiri, Whangamarino and Mangaonua within the Waikato catchment in North Island of New Zealand. The projected precipitation proves to be reliable for the research, based on the estimation of extreme events and with different Global Climate Models (GCMs) and Regional Climate Model (RCM) data. The guidelines developed by this research are:

- The projected precipitation time series would produce reliable extreme events if it is valid for both present and future climate;
- Multi-use of GCMs/RCMs would provide robust future projections; and
- For the present climate, the simulated precipitation time series should also be statistically correlated to the observed series.

#### 10.1.1.1. Extreme precipitation definition

The daily partial duration series of precipitation (PDS) for 36 stations across the North Island of New Zealand are examined. These stations were selected randomly across the research region, which was assumed to be statistically homogenous. The analyses involved the use of five different PDS series obtained by setting the average number of peaks  $\lambda$  equal to 1, 2, 3, 4 and 5. Different statistical tests were used in order to obtain the most reliable PDS (or  $\lambda$  value) that should be valid for both cases, at station location (at-site) and over the study region (areal). To account for the variability of daily precipitation, which is very complex and changes with time and space.

For at-site precipitation analysis:

- Autocorrelation and the Man-Kendall tests were used to test the existence of dependence and trend in PDS obtained at different stations. The results of these tests indicate that the PDS is random and stationary at most of the stations.
- In addition, the Fisher (F) and the Variance-to-Mean ratio (R) tests were also used to test whether or not the arrival of random and independent peaks follows the Poisson distribution that is assumed to best describe the number of peaks from the PDS. The results of these two tests show that these two tests can give conflicting results with regard to the satisfaction of the Poisson assumption and that a higher value  $\lambda$  is required.
- Moreover, the Generalized Pareto (GP) distribution was confirmed to be the most suitable for frequency analysis of the PDS series using the L-moment ratio diagram and GP parameter sensitivity test. This test is valid for  $\lambda$  is equal to or greater than four.

For areal precipitation analysis:

- The homogeneity test indicates that even though the North Island of New Zealand comprises different climatic zones, it is still considered as a statistically homogenous region in terms of partial duration series (PDS). PDS5 (with five peaks in average year,  $\lambda = 5$ ) was found in this research to have the best performance.
- The regional frequency analysis was successfully carried out in this research to reduce uncertainty occurring in PDS (i.e., both single-site and inter-site sampling variability). There is a small difference between estimated quantiles using the at-site and regional distribution. The quantile values are more reliable when estimating for return periods less than or equal to 100 years ( $T \leq 100$  years).

### **10.1.1.2. Validity of statistically downscaled daily precipitation for present climate**

The research used two global climate models, CGCM3.1/T47 and GCM HadCM3 with spatial resolution of  $3.75^{\circ} \times 3.75^{\circ}$  and  $2.5^{\circ} \times 2.5^{\circ}$ , respectively. The most commonly used statistical downscaling model (SDSM), was used to generate local daily precipitation series from GCMs. This research evaluated the SDSM model performance for both at-site and areal daily and monthly precipitation for the period 1971 to 1990 for Waikato catchment.

In general, the SDSM model performs well for mean areal precipitation rather than for at-site daily precipitation. This may be due to the effects of topography. Large-scale variables from the GCM HadCM3 are more sensitive to the observed precipitation than that from the CGCM3/T47 model. This may be owing to the efficiency of fine spatial resolution of the GCM HadCM3 model that provides more detailed information on a single grid cell.

At-site monthly precipitation simulations from the CGCM3/T47 and the GCM HadCM3 exhibit conflicting results. Precipitation is adequately simulated in autumn and winter months. Mean areal monthly precipitation simulations from the two GCMs show the same trends. More biases in the summer and autumn, while equality of simulation is found in spring and winter months.

### **10.1.1.3. Validity of downscaled extreme precipitation for future climate**

Although the SDSM successfully downscales the daily precipitation from the CGCM3.1/T47 and GCM HadCM3 models, the results do not, however, satisfy the model evaluation criteria in term of the adequacy of daily precipitation simulations. In this regard, the regional climate model RCM HadCM3 data at  $0.05^{\circ}$  spatial resolution is used. Thus, extreme precipitation is projected for future climate from CGCM3.1/T47, GCM HadCM3 and RCM HadCM3. To account for the estimation of extreme precipitation, the PDS5

found to be suitable for the entire North Island region and its Waikato catchment that is located in the middle of the North Island.

Overall, at-site daily precipitation from CGCM3.1/T47, GCM HadCM3 and RCM HadCM3 is relatively well simulated. However, the mean areal precipitation from GCMs and RCM are significantly different. The mean areal precipitation time series from RCM HadCM3 contains more extreme events than that obtained from GCMs. This difference between the two time series may be caused by the use of Thiessen spatial interpolation to obtain the GCMs mean areal precipitation.

The results of this research showed that extreme precipitation events from GCMs and RCM are very close in magnitude to those obtained from observation for return periods less than or equal to 100 years. There is a significant difference in the magnitude of extreme events for high periods. This is performed using the regional frequency analysis of partial duration series of daily precipitation (RFA/PDS).

This research also reveals an outperformance of the RFA/PDS over the RFA/AMS for projecting future extreme precipitation from global data. A significant difference in extreme magnitude is identified for return periods equal to or greater than 100 years. The magnitude of extreme precipitation simulated from AMS is always higher than that from PDS.

### **10.1.2. Future projections of potential evapotranspiration**

Local daily potential evapotranspiration (PET) was statistically downscaled from large-scale variables from both CGCM3.1/T47 and GCM HadCM3. For both cases, the downscaled PET was not statistically correlated to the observed evaporation. Thus, RCM HadCM3 with very high spatial resolution was used. PET was directly simulated from HadCM3, including maximum and minimum air temperature, mean relative humidity,

radiation and wind speed variables. Consequently, future PET is projected for the 2001-2030, 2031-60 and 2061-90 periods. Future projected PET was compared to the observation from 1971 to 2000 to determine the change in PET from the present to the future.

The trend test was used in this research to investigate whether or not the evaporation paradox exists in the research region. The results show an increasing trend in the daily observed evaporation in one station, a decreasing trend in two stations while no change in daily evaporation series in two other stations. This may be due to the effects of data length and topography as well as surface type.

The research also showed a good agreement between the daily PET simulation from RCM HadCM3 and the observation. The methods used to simulate PET are the FAO-56 and the Tait-Woods' formula. The monthly PET simulation was also well matched with the observation with the peaks appearing in January. However, the monthly peak magnitudes were underestimated by 2% of the observed peaks.

For a better understanding of evapotranspiration process, the daily PET was also simulated for three sub-catchments, namely Whangawhiri, Whangamarino and Mangaonua with similar area but different vegetation. The first one is mainly dominated by forests while the two latter are covered by grasses. The future PET was projected over three typical forest and grass sub-catchments from year 2001 to 2090. Increasing daily and annual PET rates were projected for all three sub-catchments by on average 1.6% to 1.2% per 30-years. Evapotranspiration rate from grassed surface was higher than that from forested surface.

### **10.1.3. Combined effects of changing precipitation and PET on catchment surface water**

Changes in precipitation and PET from the past to the future are believed to dramatically affect the catchment streamflow and runoff volume. A water-soil lumped model (NAM) was used to model the streamflow from precipitation and PET together with sub-flows between soil layers. Three selected sub-catchments were of the research interest.

The results show that variability of daily precipitation and potential evapotranspiration is likely to have large impacts on catchment streamflow.

- For the present climate, there is a good agreement between modelled and observed streamflow in the Mangatawhiri and Mangaonua sub-catchments. In fact, only few observation stations located within the catchments and the surrounding areas are used due to the sparse observation network and limited data. Thus, streamflow in the ungauged grassed Whangamarino sub-catchment was modelled from the grassed Mangaonua sub-catchment.
- For the future climate, mean annual runoff are expected to decrease by 15% and increase by 6.25% from 2001 to 2030 depending on the catchment. During the 2031-60 period, runoff in three sub-catchments would decrease by 3% to 8% relative to the 2001-30 period. An exception of the Mangatawhiri, water volume would increase by 6.25% as a result of RCM data variability. Water volume is projected to decrease by maximum 15% from 2061 to 2090 in both Mangatawhiri and Whangamarino sub-catchment. Furthermore, the results also indicate a significant dependence of streamflow on PET. The results demonstrate that if the evapotranspiration rate increases or decreases by 1.0 times, the mean daily streamflow consequently decreases or increase by the same rate at 25%, respectively.

## 10.2. Contributions to knowledge

The results of this research thesis indicate that the combined changing precipitation and potential evapotranspiration (PET) are likely to significantly affect the catchment streamflow and runoff volume. Particularly, the change in PET would considerably impact the streamflow in forest and grass sub-catchments when climate change takes place.

The use of FA-56 method coupled with a very high spatial resolution RCM are effective for future projection of daily PET. However, the bias-correction is required to obtain the adequate PET in terms of its magnitude and pattern.

New criteria developed for quantifying the downscaled daily precipitation from GCMs/RCMs in this research thesis would improve the quality of future projection of precipitation. This emphasizes the importance of extreme events contained in the downscaled series. The partial duration series (PDS) that is tested with a wide range of individual observed data at stations and then is regionalized for the entire study area is an efficient model for modelling the extreme events for both present and future climate. This regional PDS corresponding to a certain threshold value would be applicable for extreme modelling in ungauged catchments with similar characteristics.

## 10.3. Possibilities for further research

This research utilizes various data sources and programs that may incur different errors affecting the accuracy of the results. For the catchments with limited observed data, the improvement of global/regional climate model outputs is essential. Likewise, the data processing programs and hydrological models are also required to be verified in different regions. Uncertainty analysis could be useful to give upper and lower bounds of modeled results.

For all simulations in this research thesis, only one SRES A2 scenario is used. For better understandings of the impacts of climate change, SRES A1B, B1 and A1F1 scenarios should be considered in future research work. Furthermore, landuse in the selected sub-catchments is assumed to be unchanged from the present to the end of 21<sup>st</sup> century. Thus, the effect of landuse change is necessary for further research.

These improvements would provide more reliable future projections for daily precipitation, potential evapotranspiration and resulting streamflow.

**APPENDIX A**

Long term mean daily precipitation for the 1960-90  
period for 36 stations

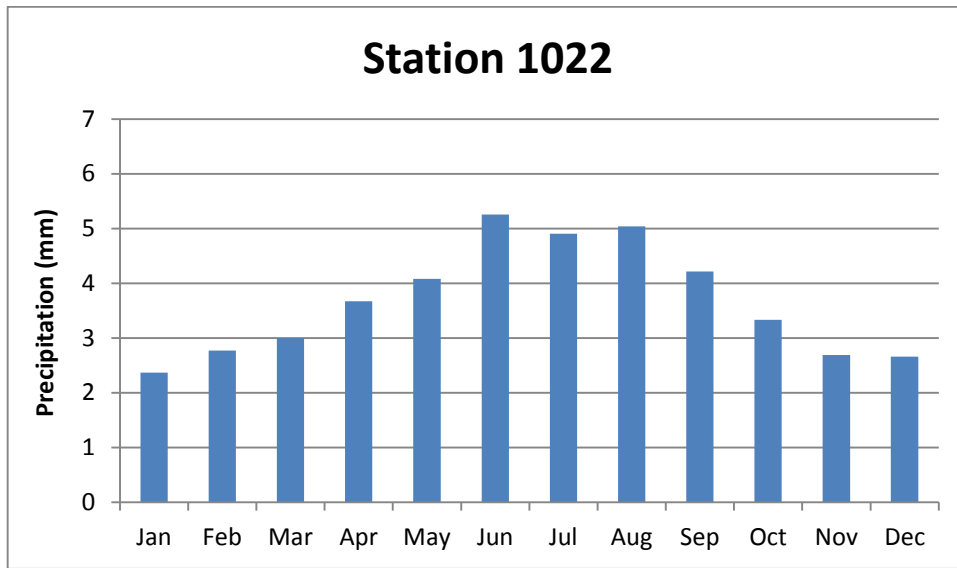


Figure A -1

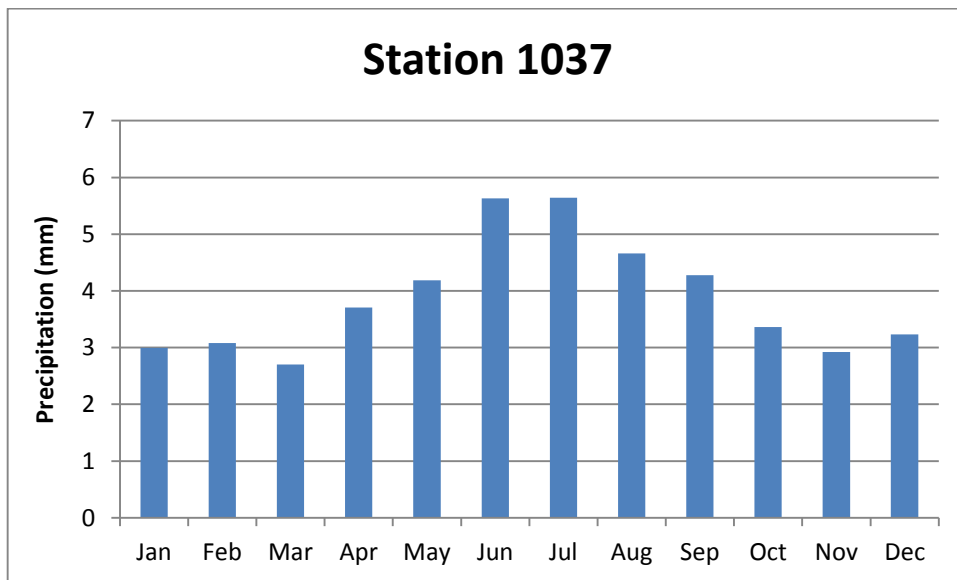


Figure A -2

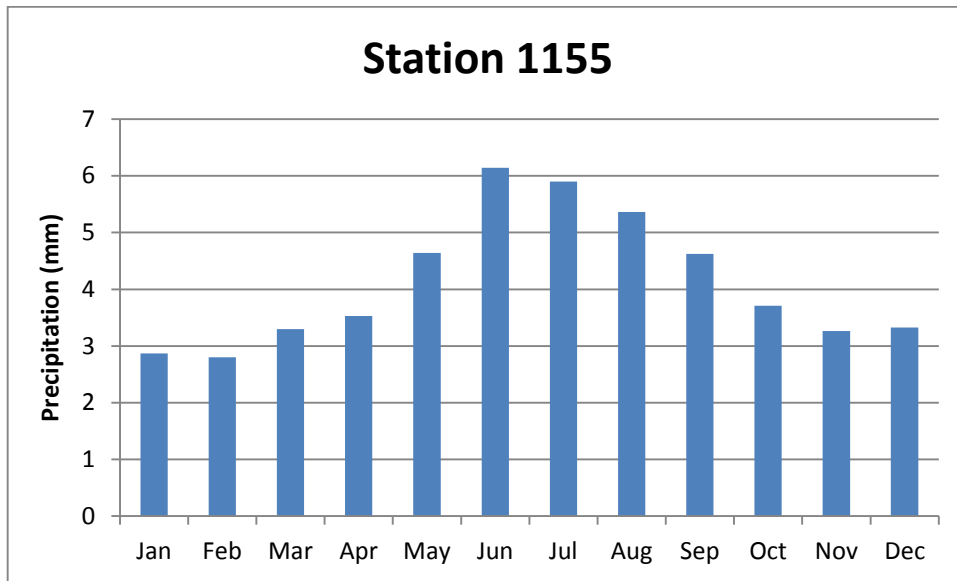


Figure A -3

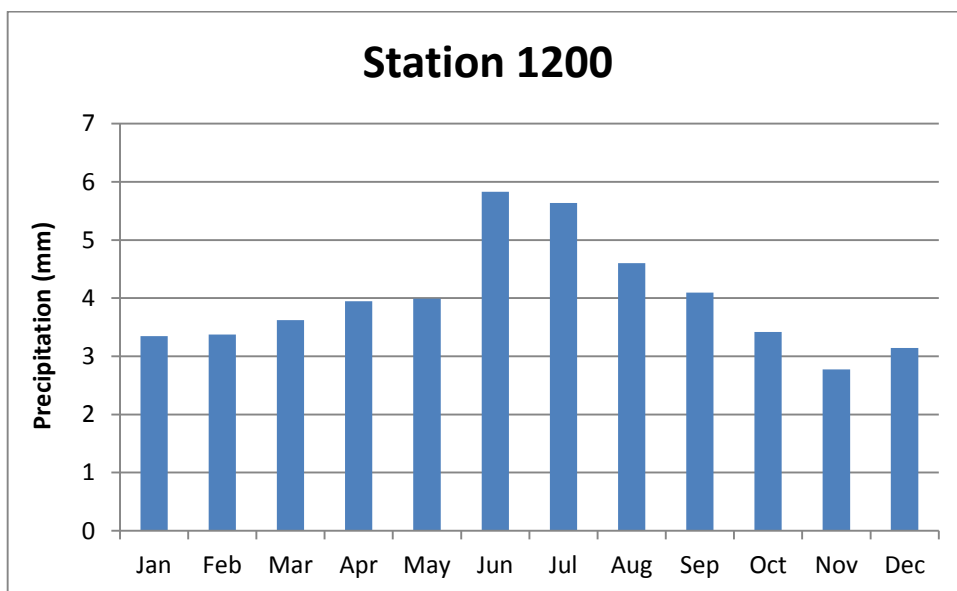


Figure A -4

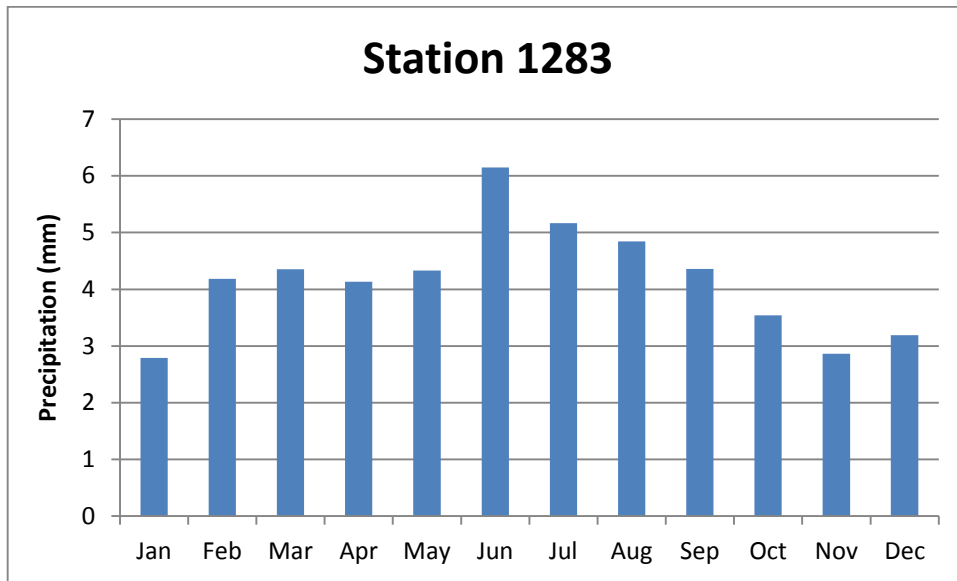


Figure A -5

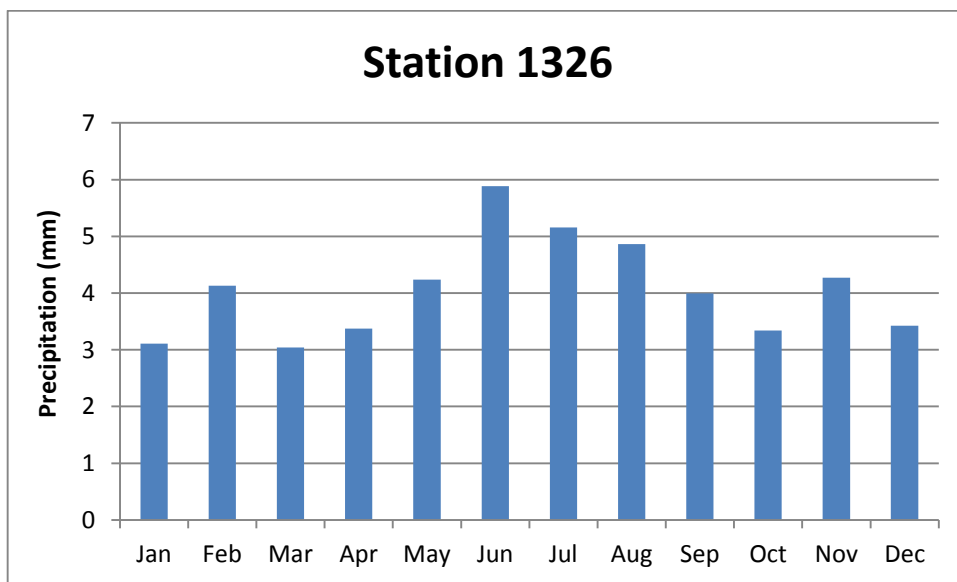


Figure A -6

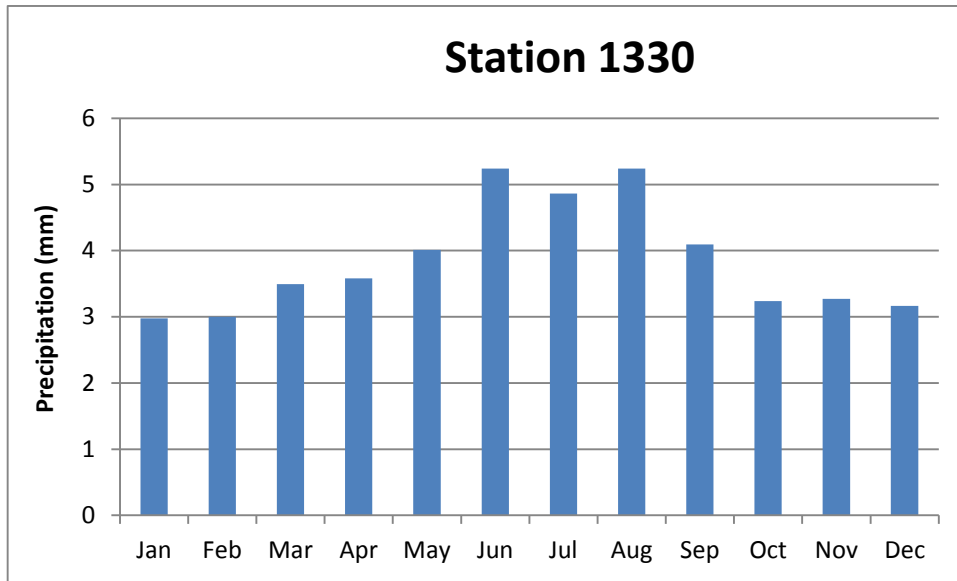


Figure A -7

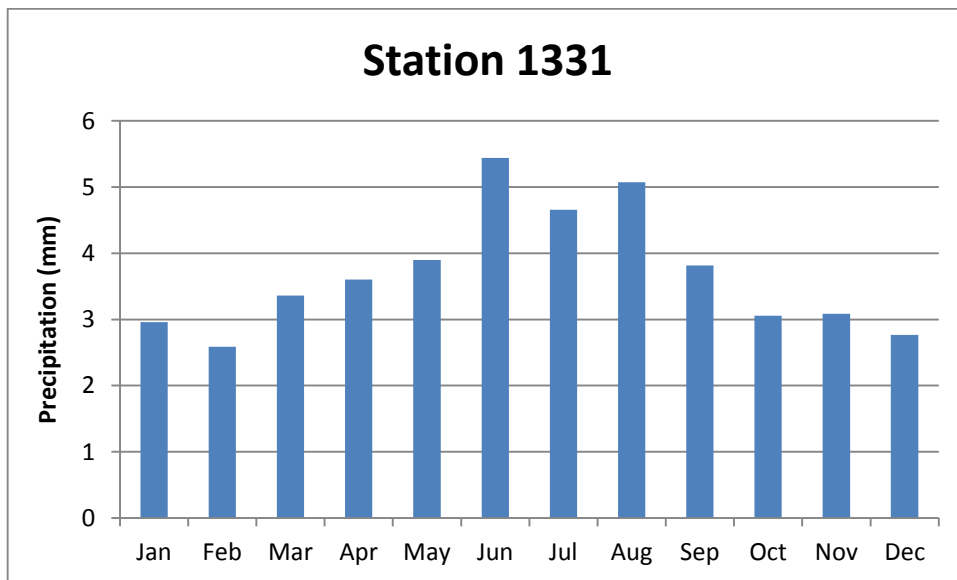


Figure A -8

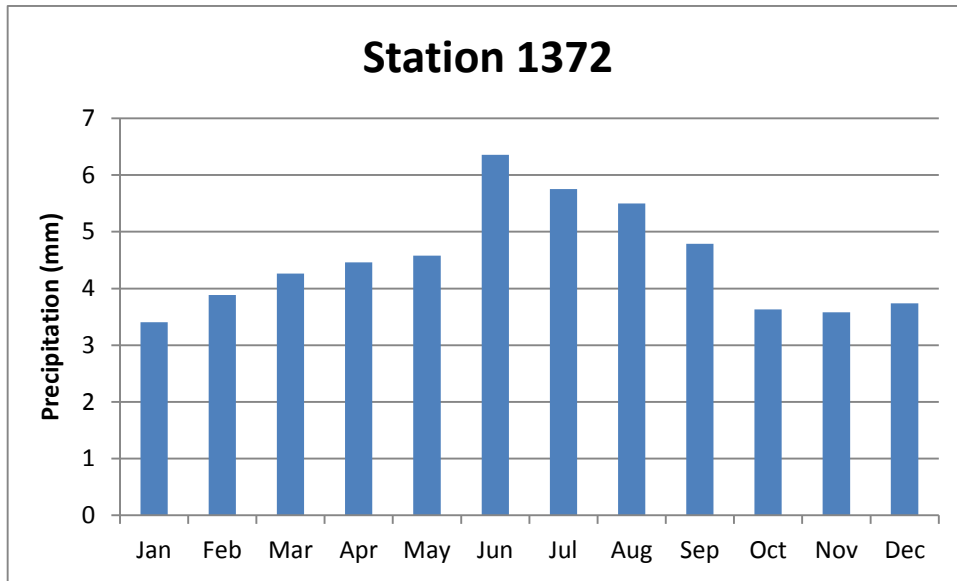


Figure A -9

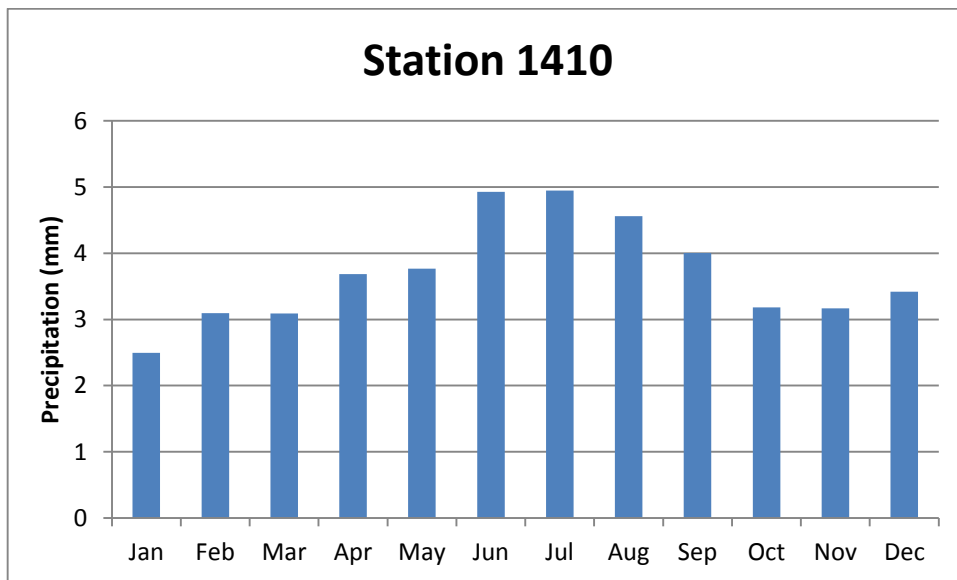


Figure A -10

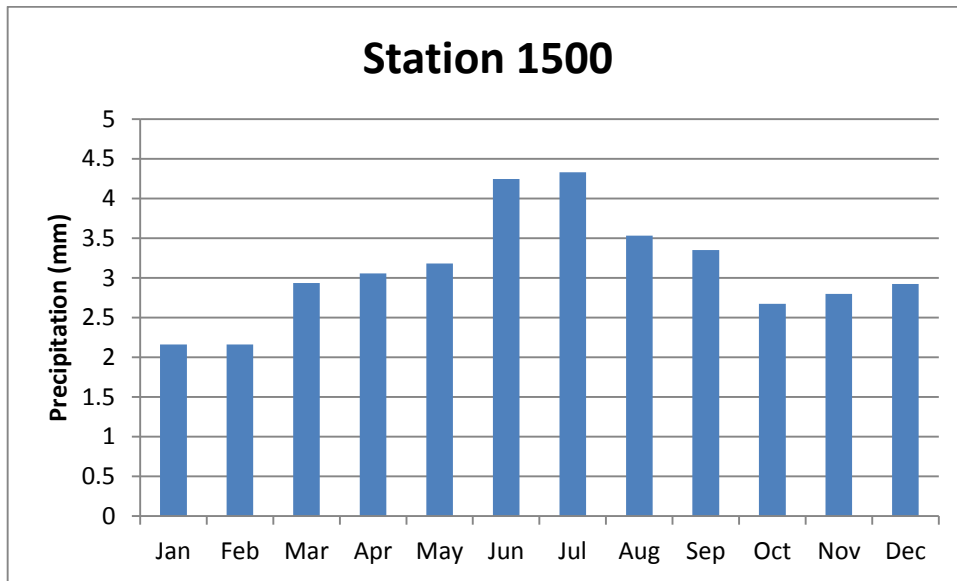


Figure A -11

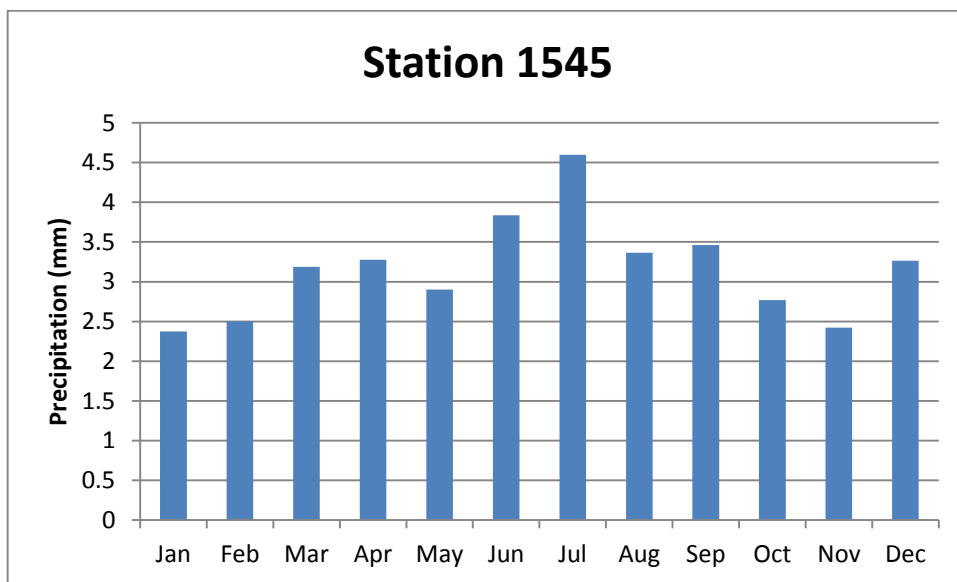


Figure A -12

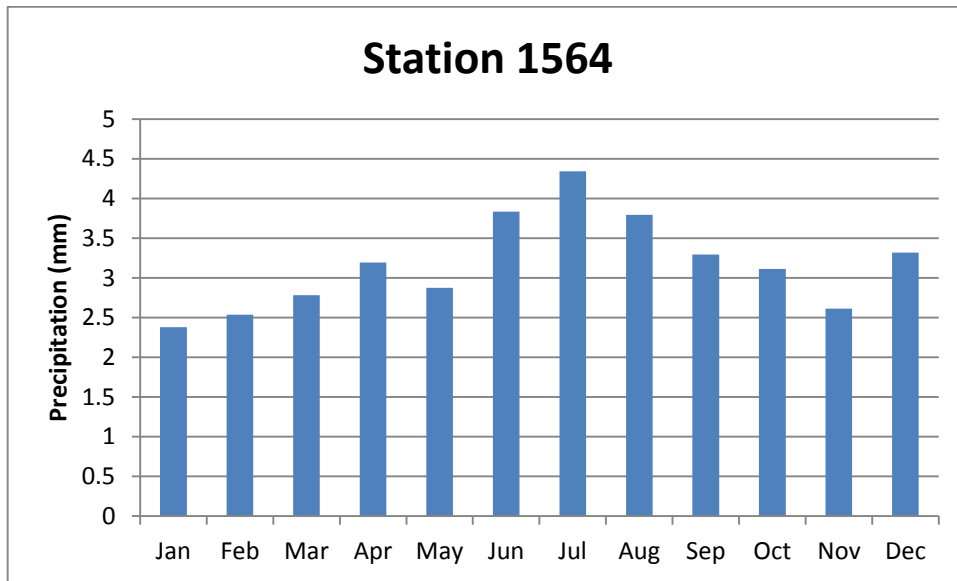


Figure A -13

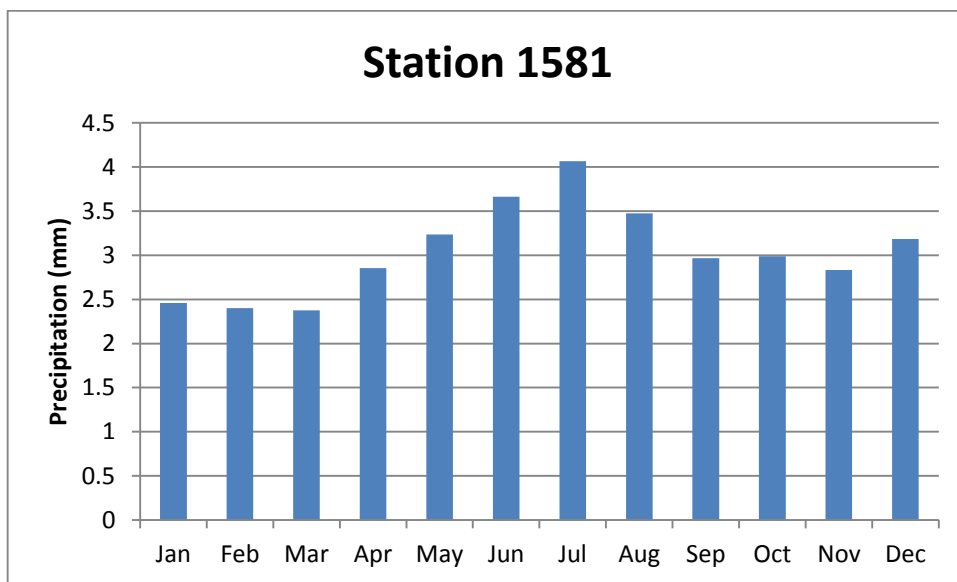


Figure A -14

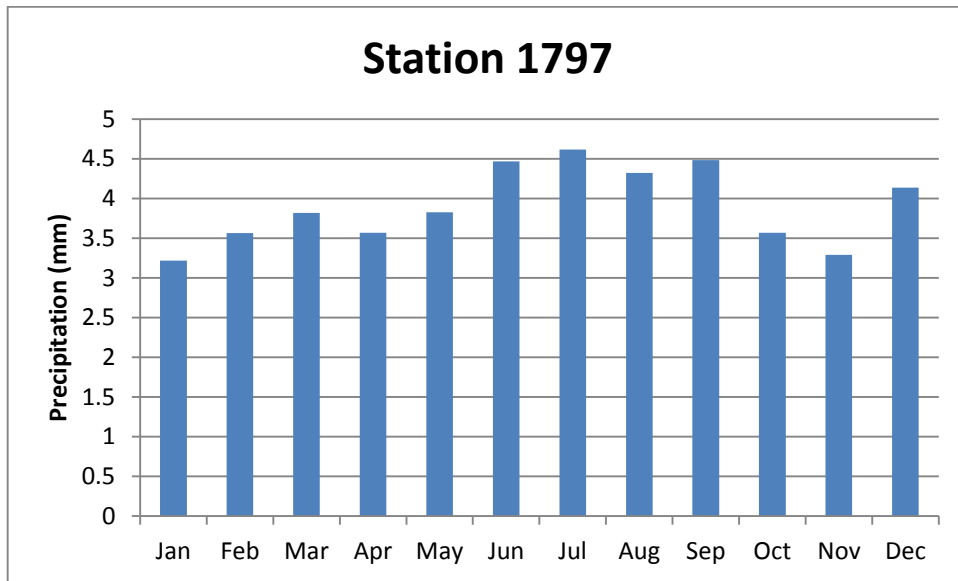


Figure A -15

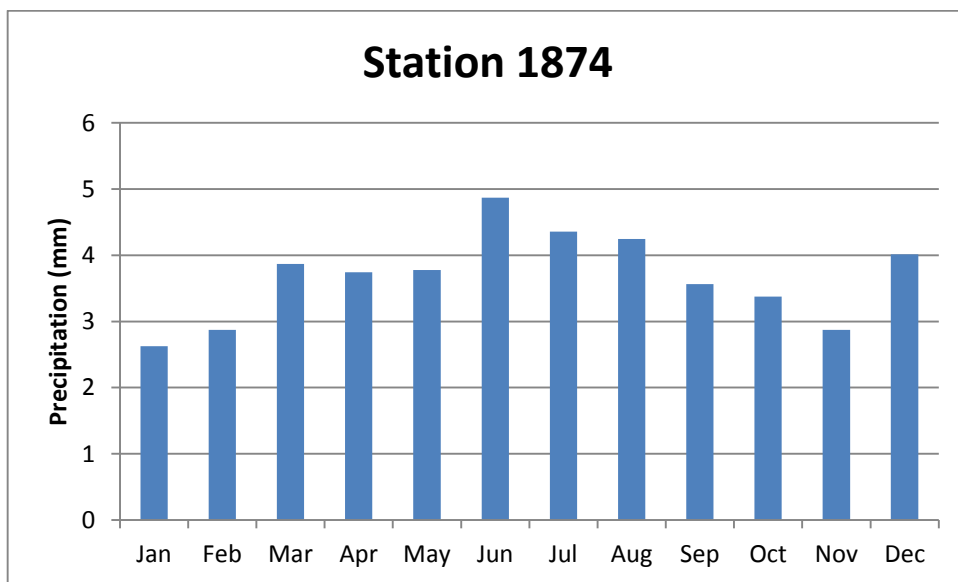


Figure A -16

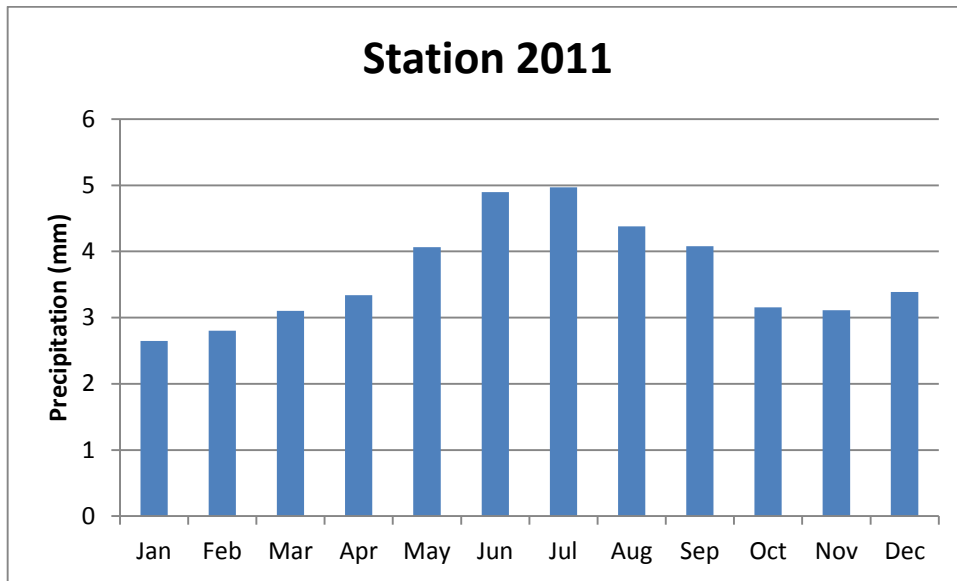


Figure A -17

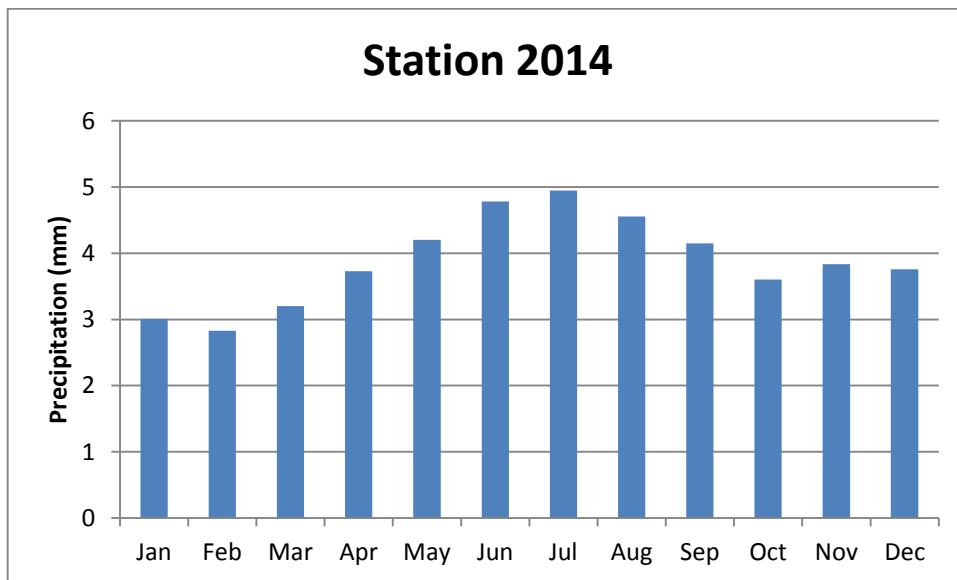


Figure A -18

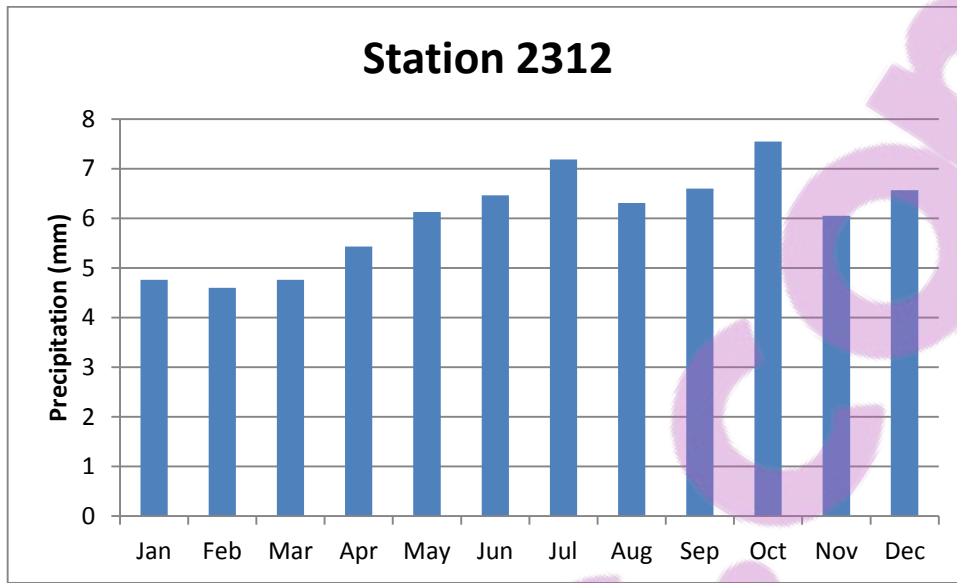


Figure A -19

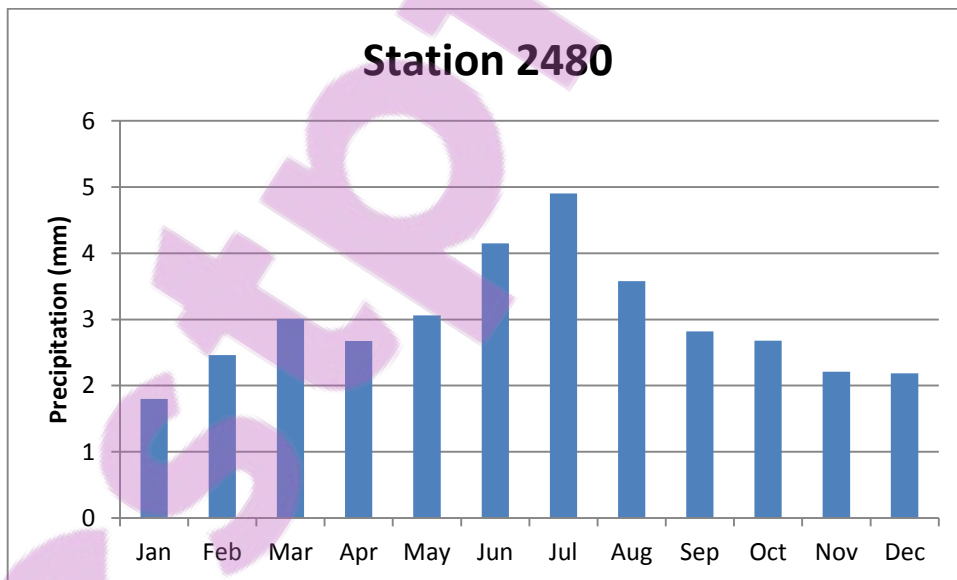


Figure A - 20

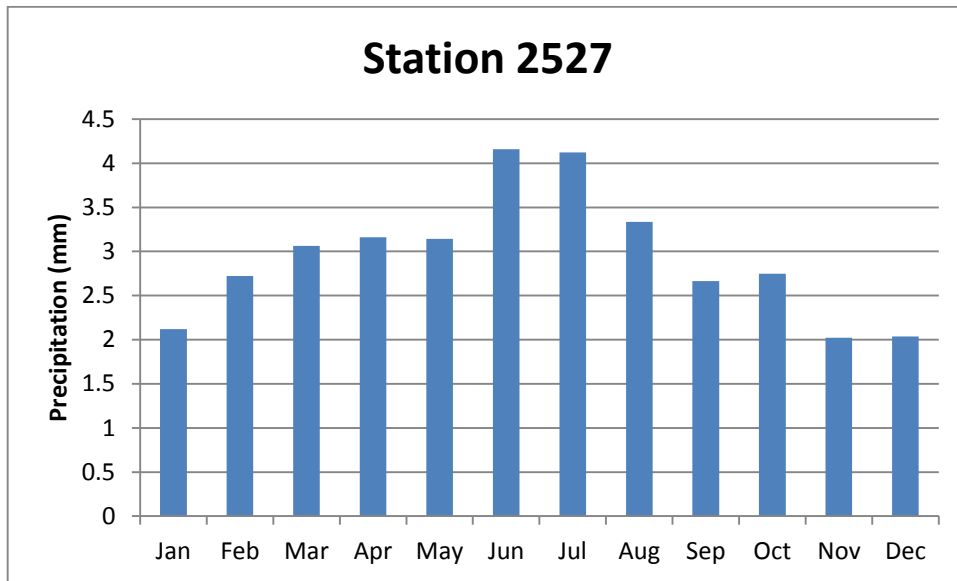


Figure A - 21

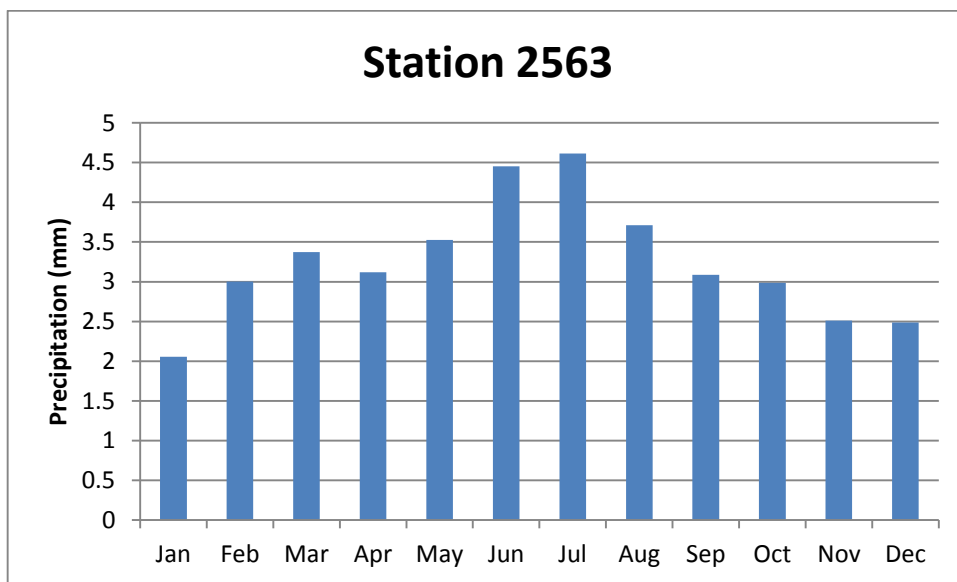


Figure A - 22

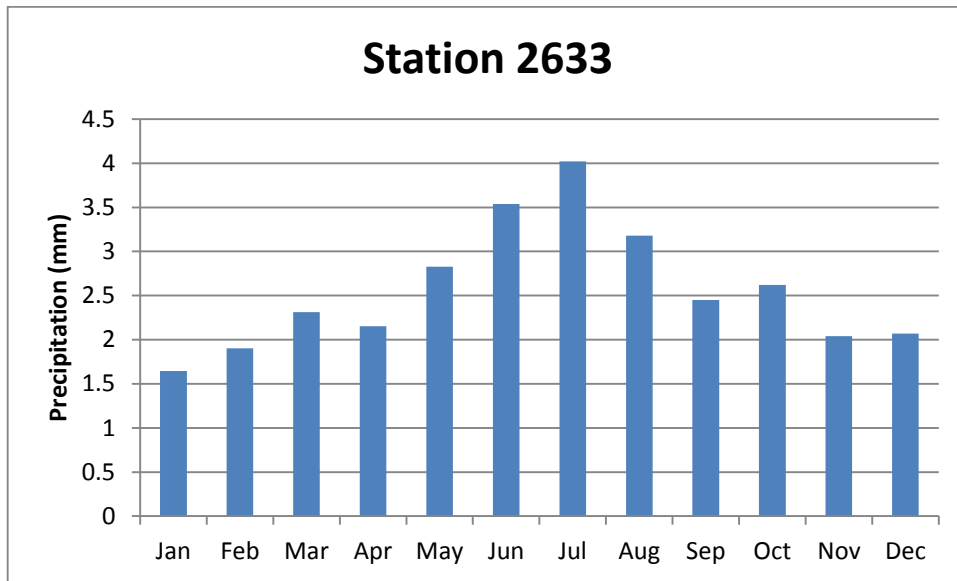


Figure A - 23

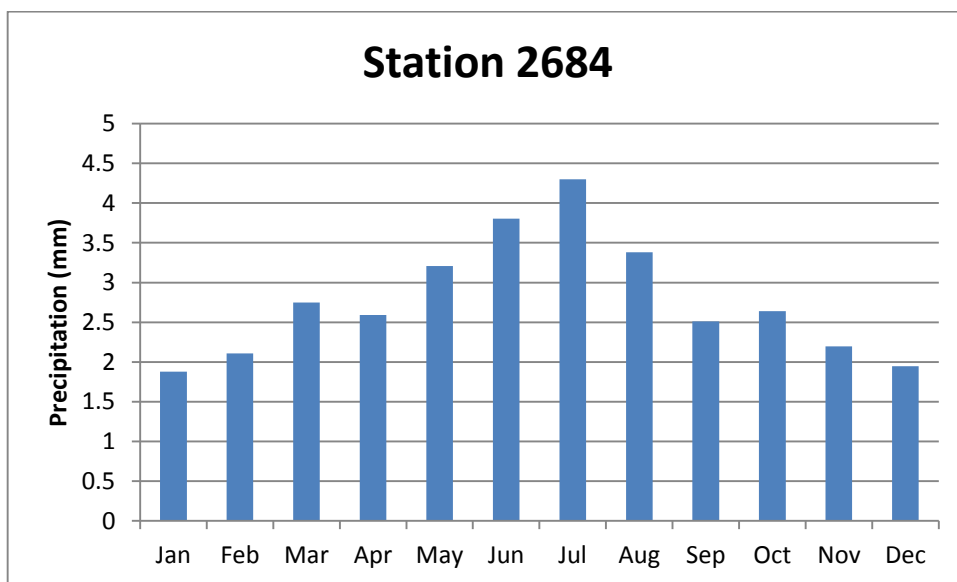


Figure A - 24

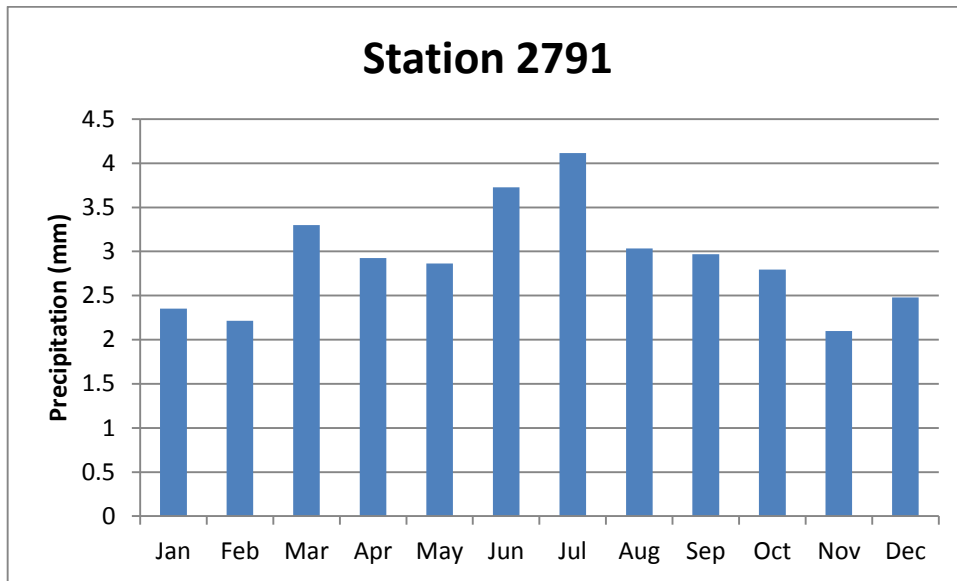


Figure A – 25

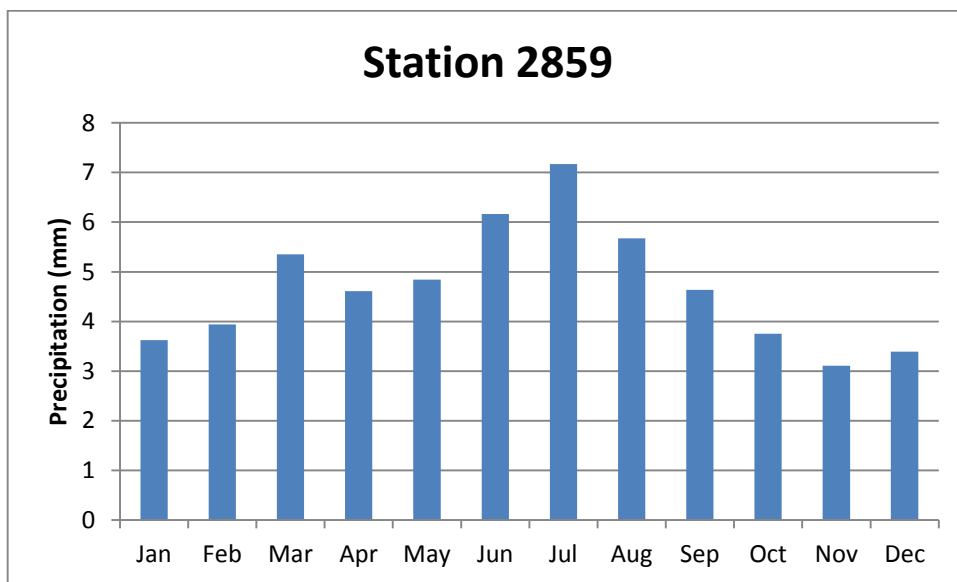


Figure A - 26

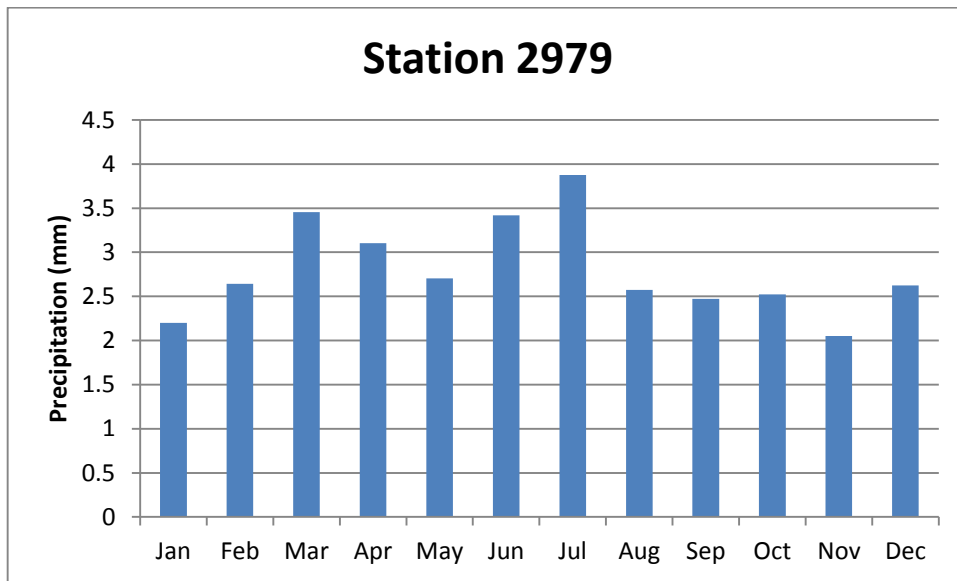


Figure A - 27

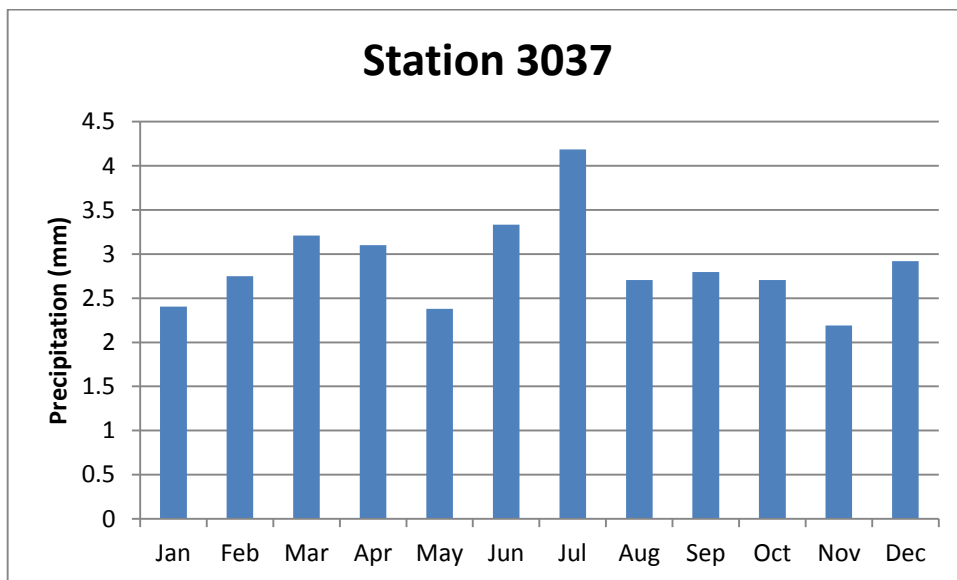


Figure A - 28

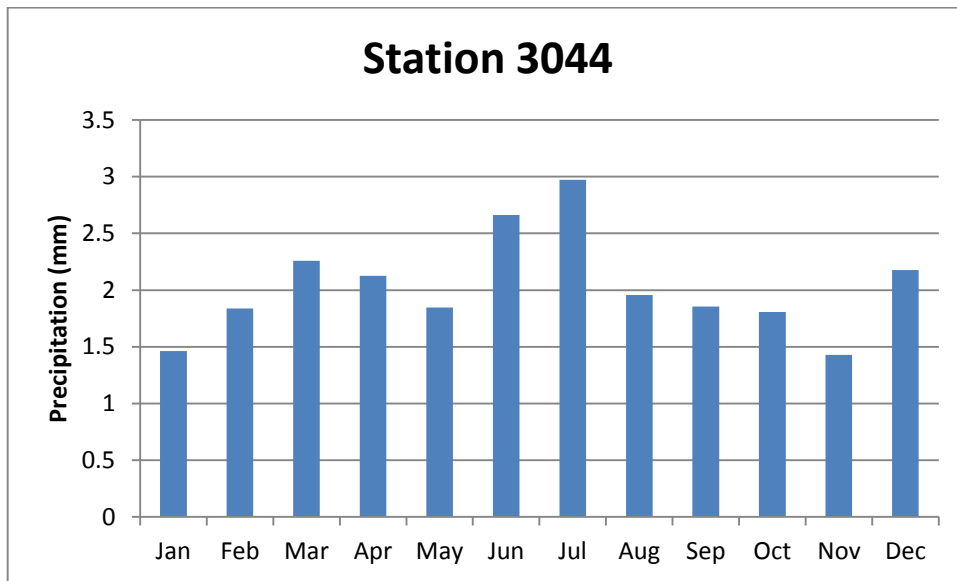


Figure A - 29

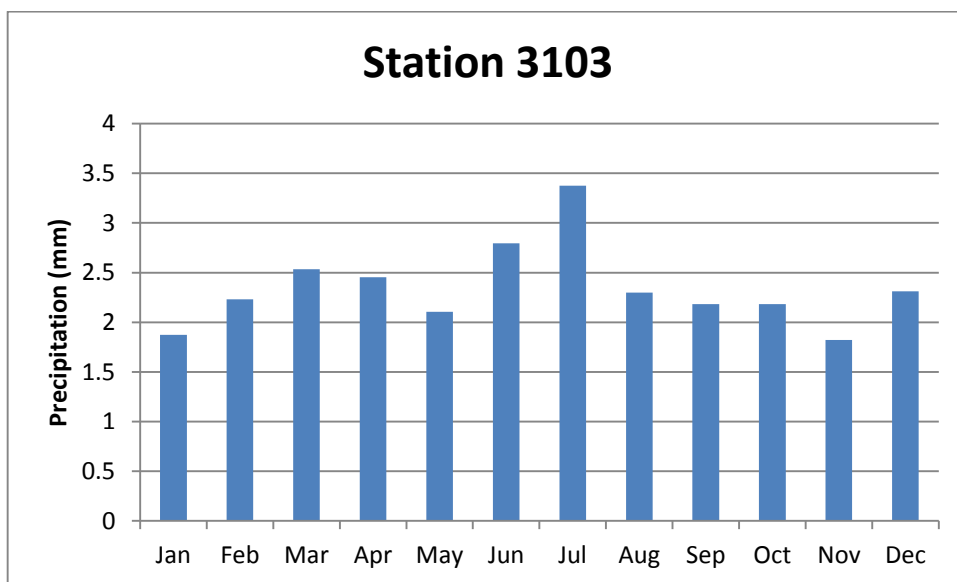


Figure A - 30

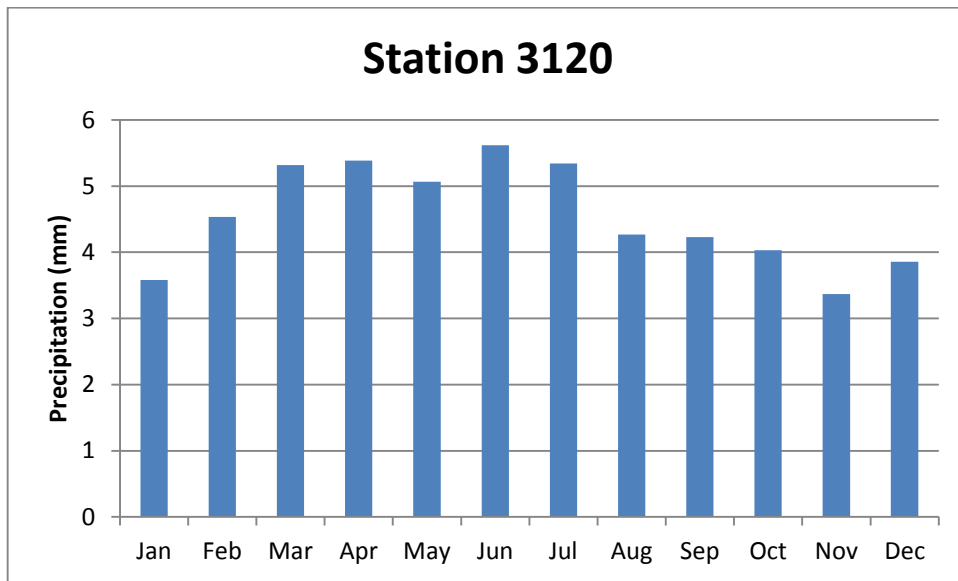


Figure A - 31

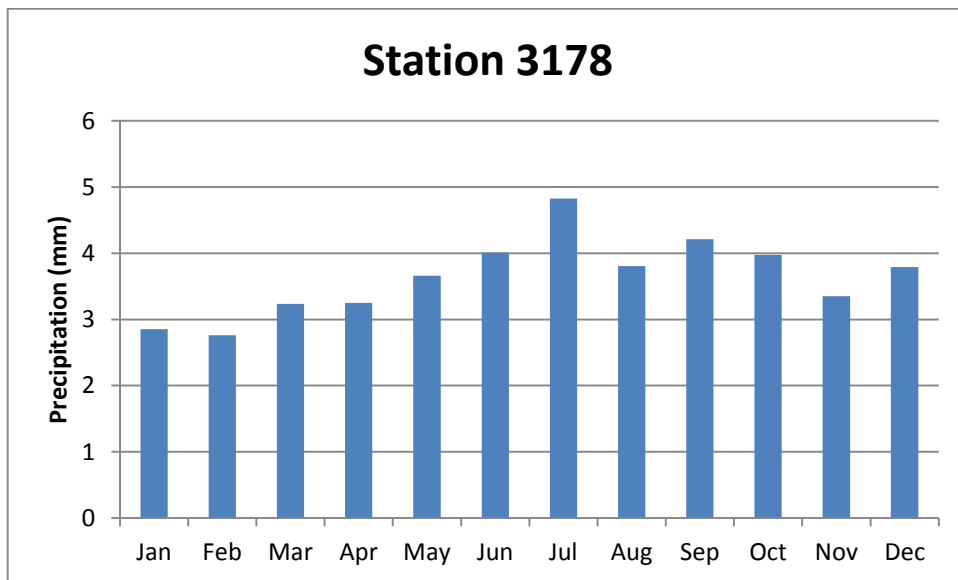


Figure A - 32

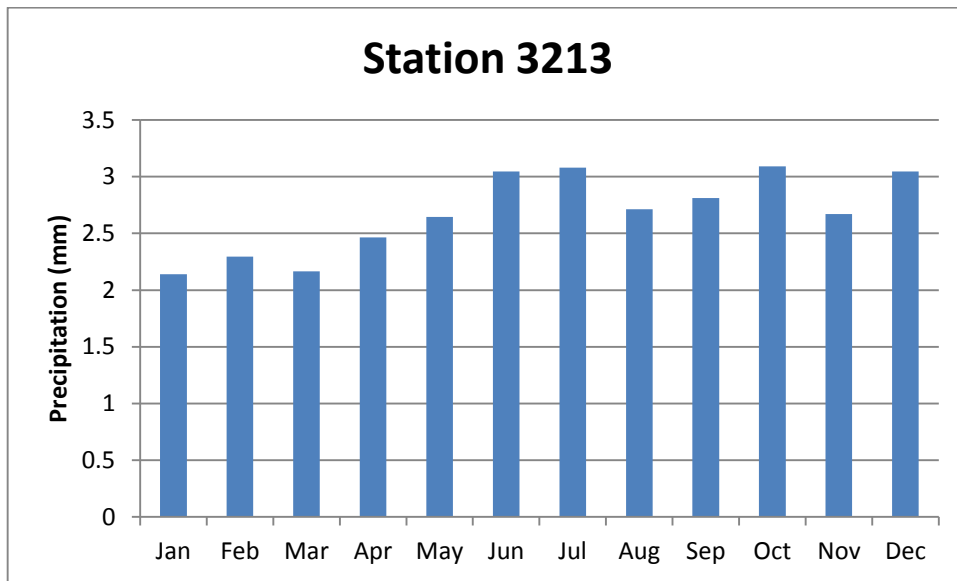


Figure A – 33

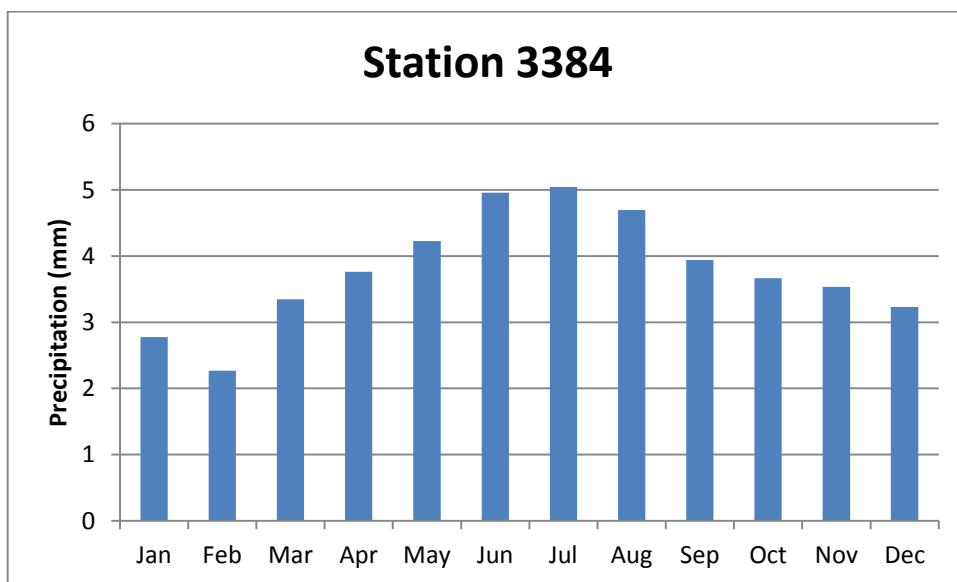


Figure A - 34

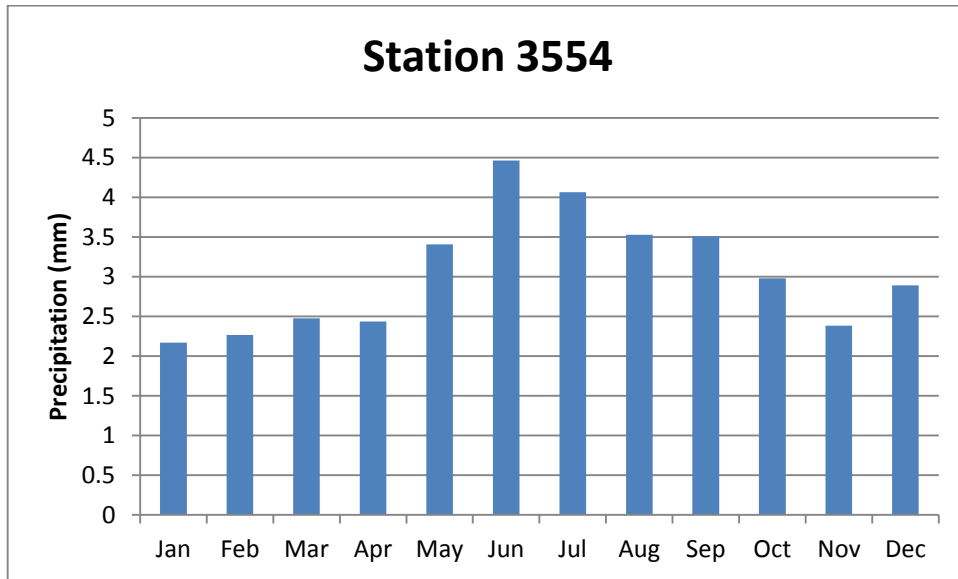


Figure A - 35

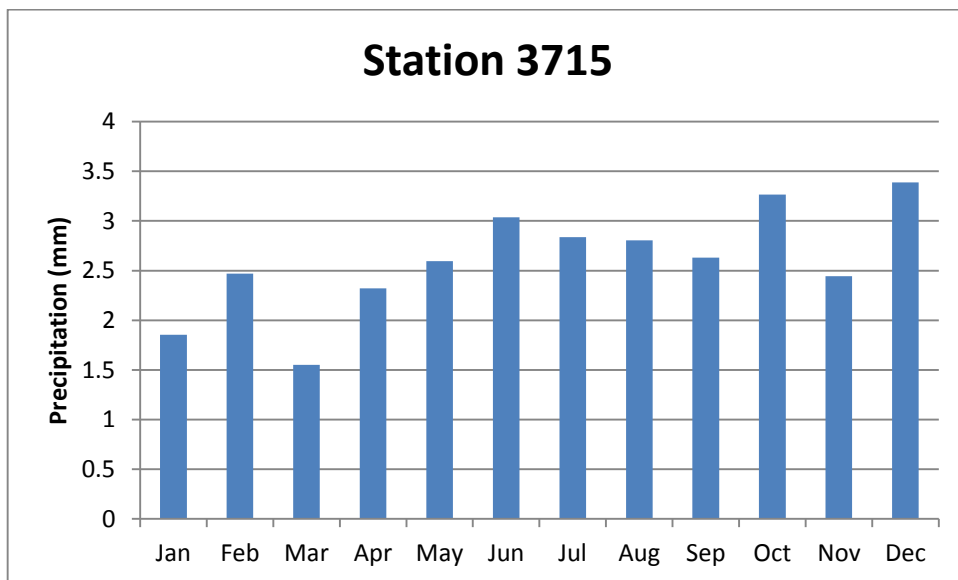


Figure A - 36

## APPENDIX **B**

Long term mean daily evaporation for the 1961-90  
period for 7 stations

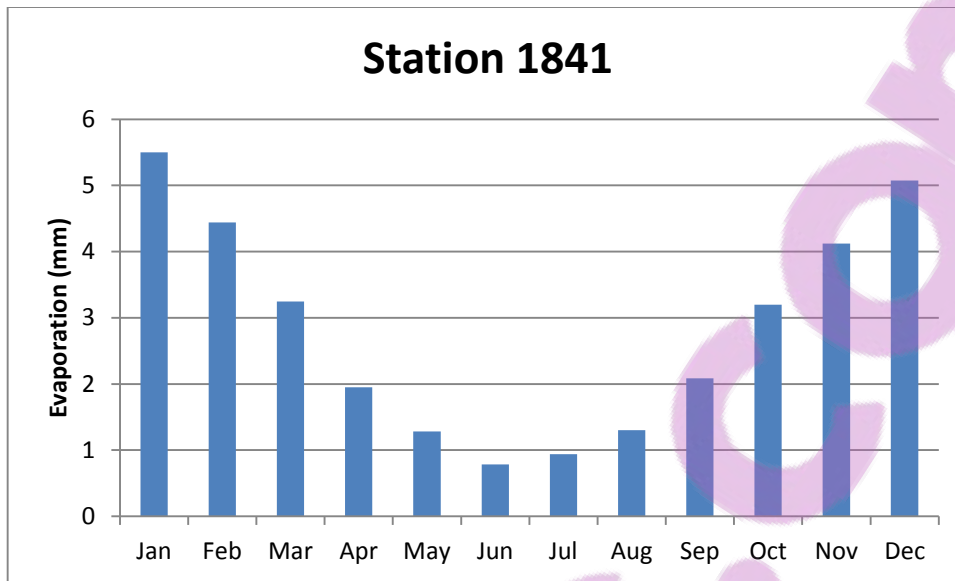


Figure B-1

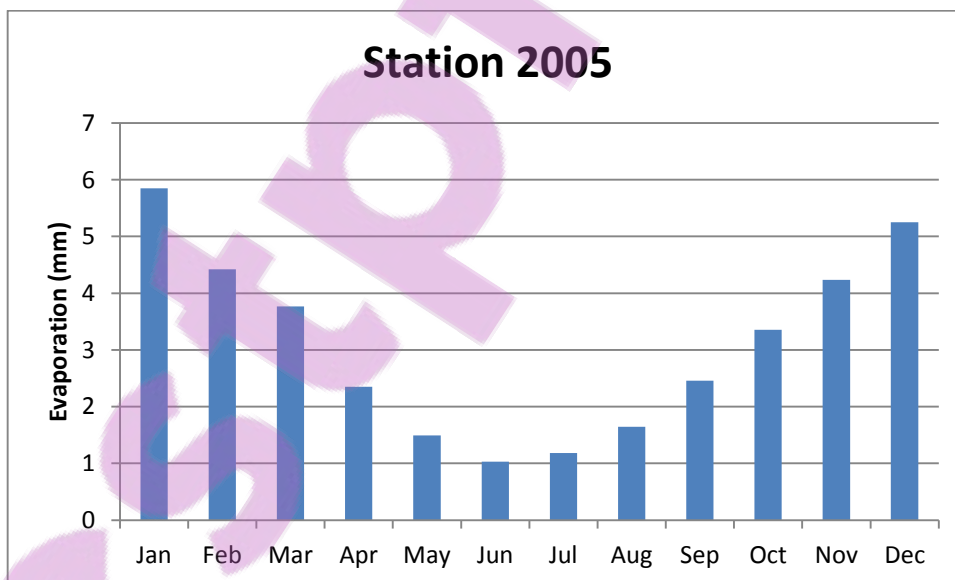


Figure B-2

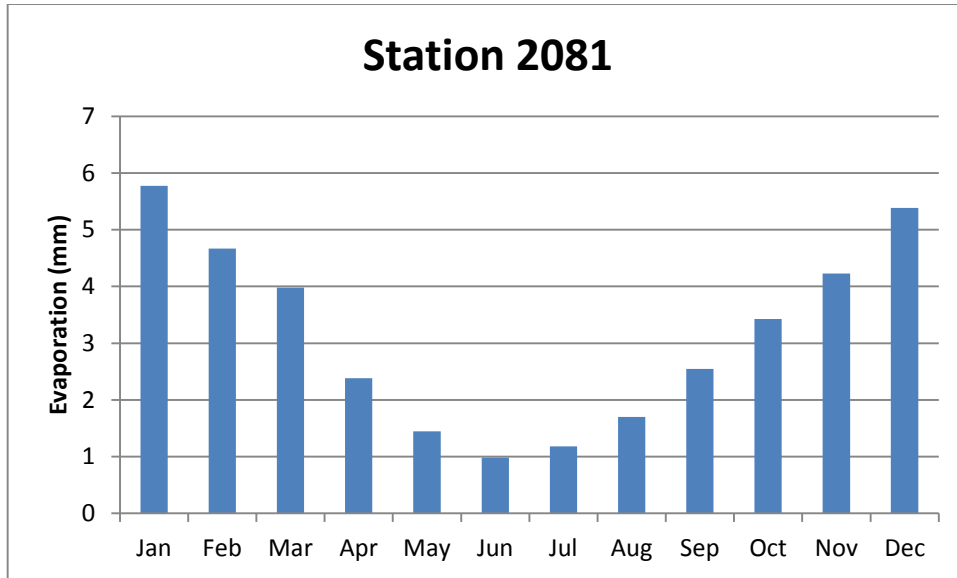


Figure B-3

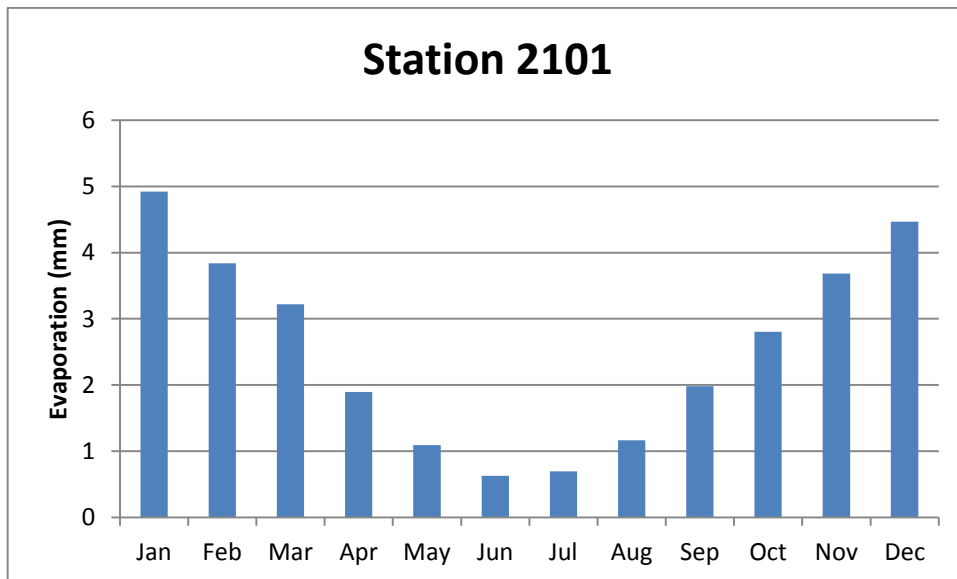


Figure B-4

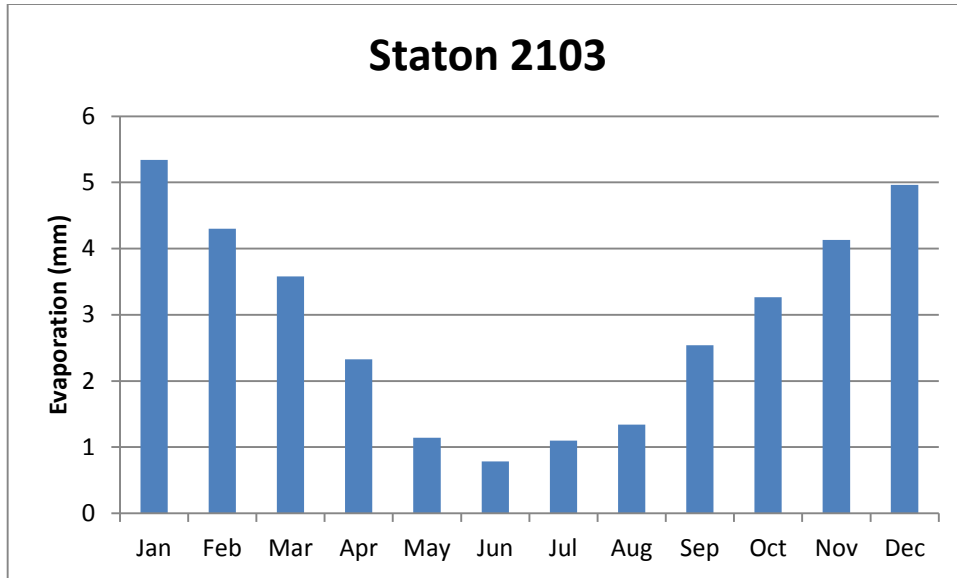


Figure B-5

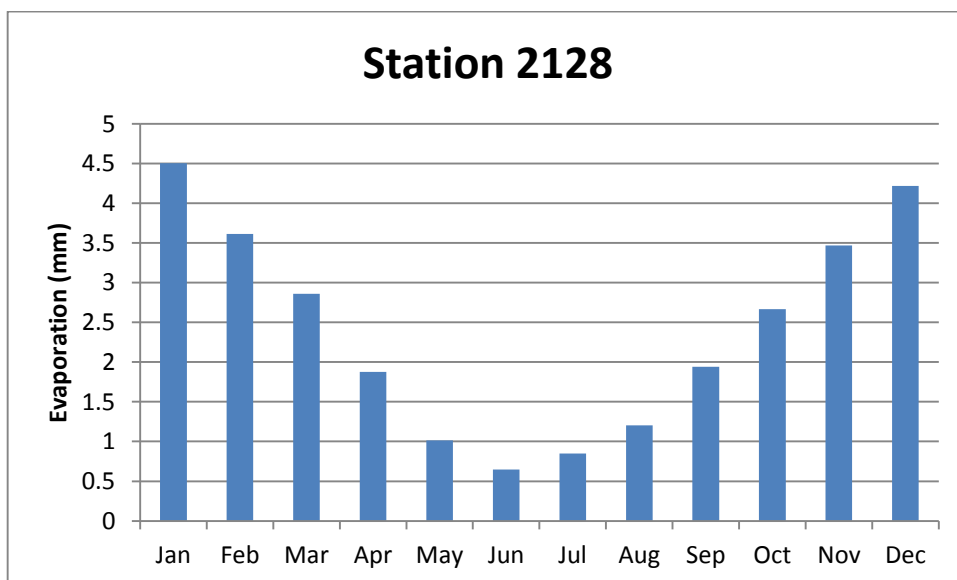


Figure B-6

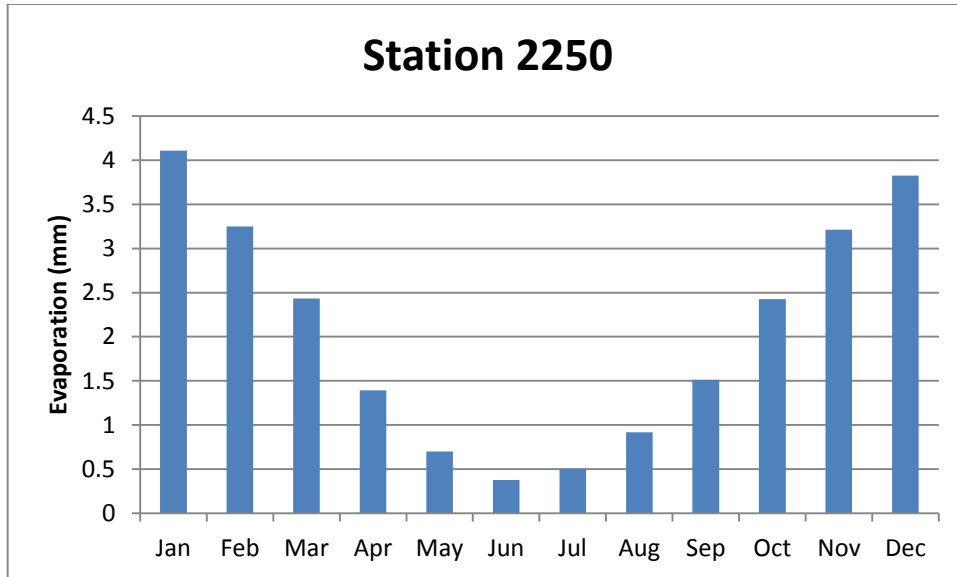


Figure B-7

# APPENDIX C.1

Predictor-predictand  $R^2$  values for 14 stations for  
CGCM3.1/T47 model

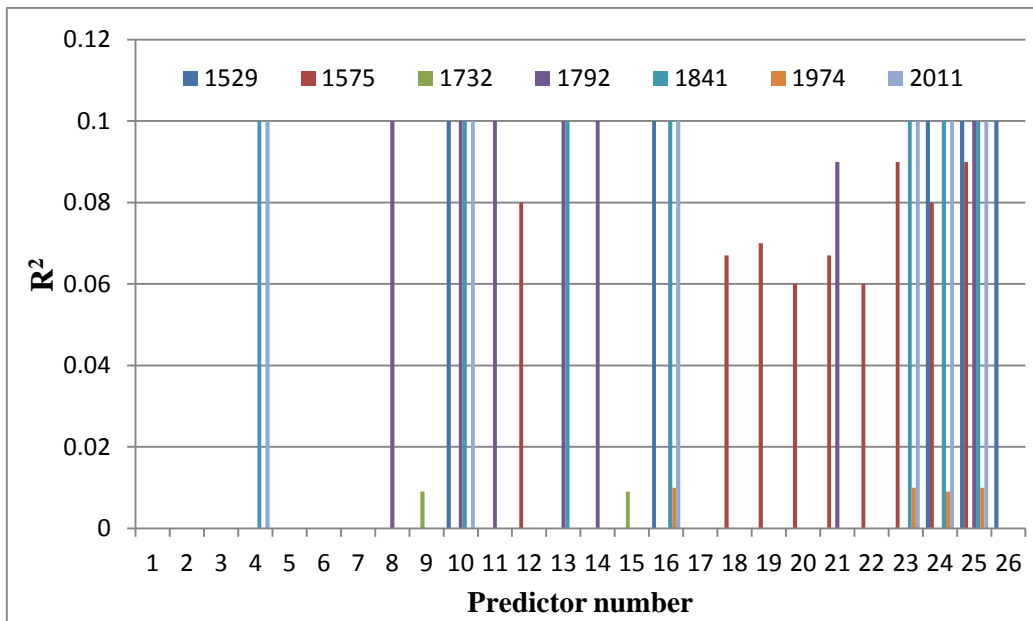


Figure C1 - 1

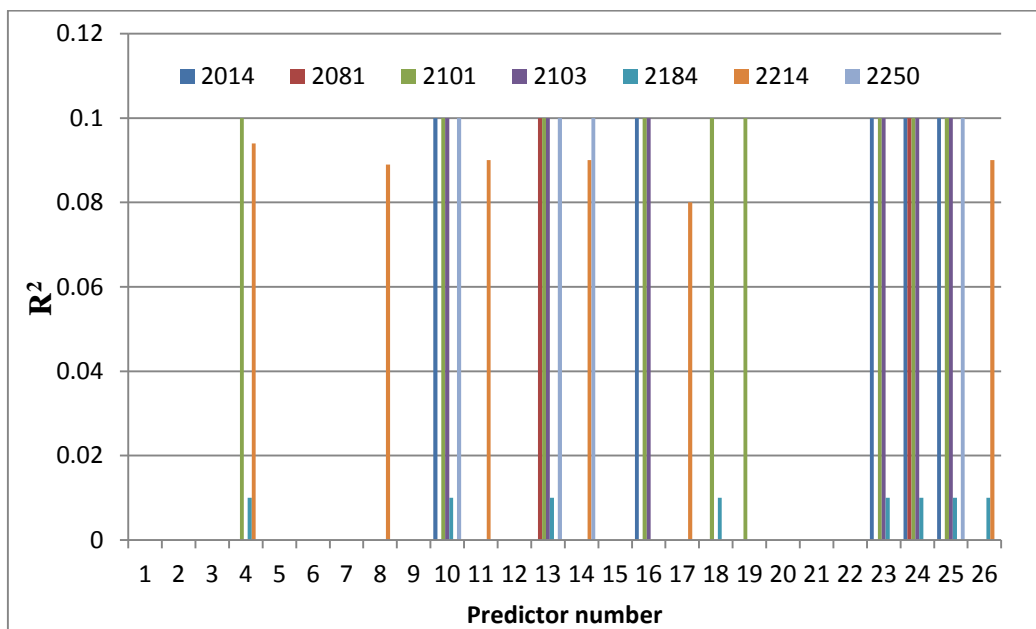


Figure C1 - 2

## APPENDIX C.2

Predictor-predictand  $R^2$  values for 5 stations for GCM  
HadCM3 model

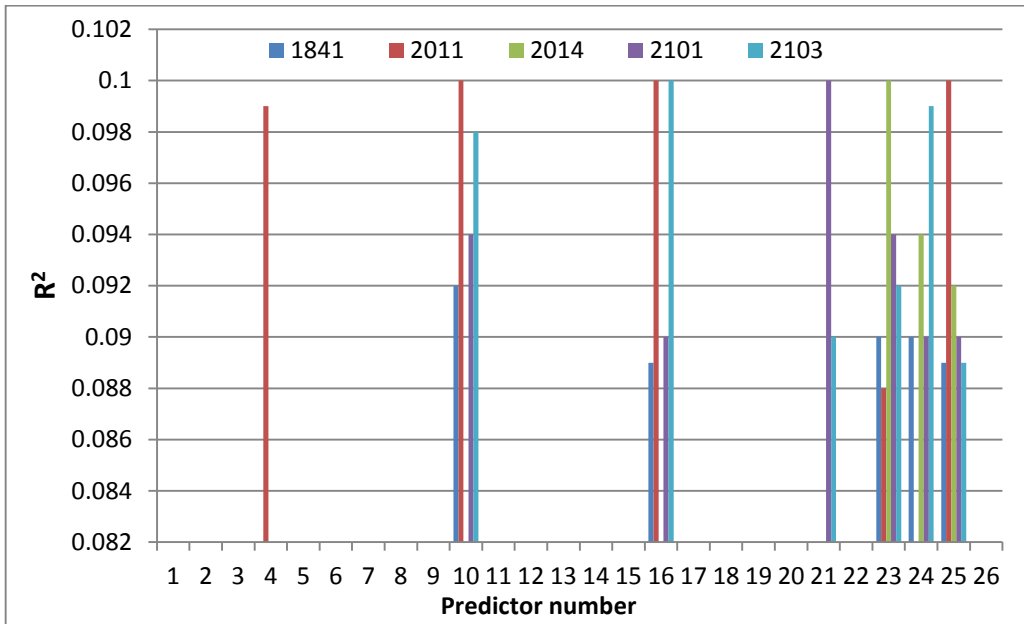
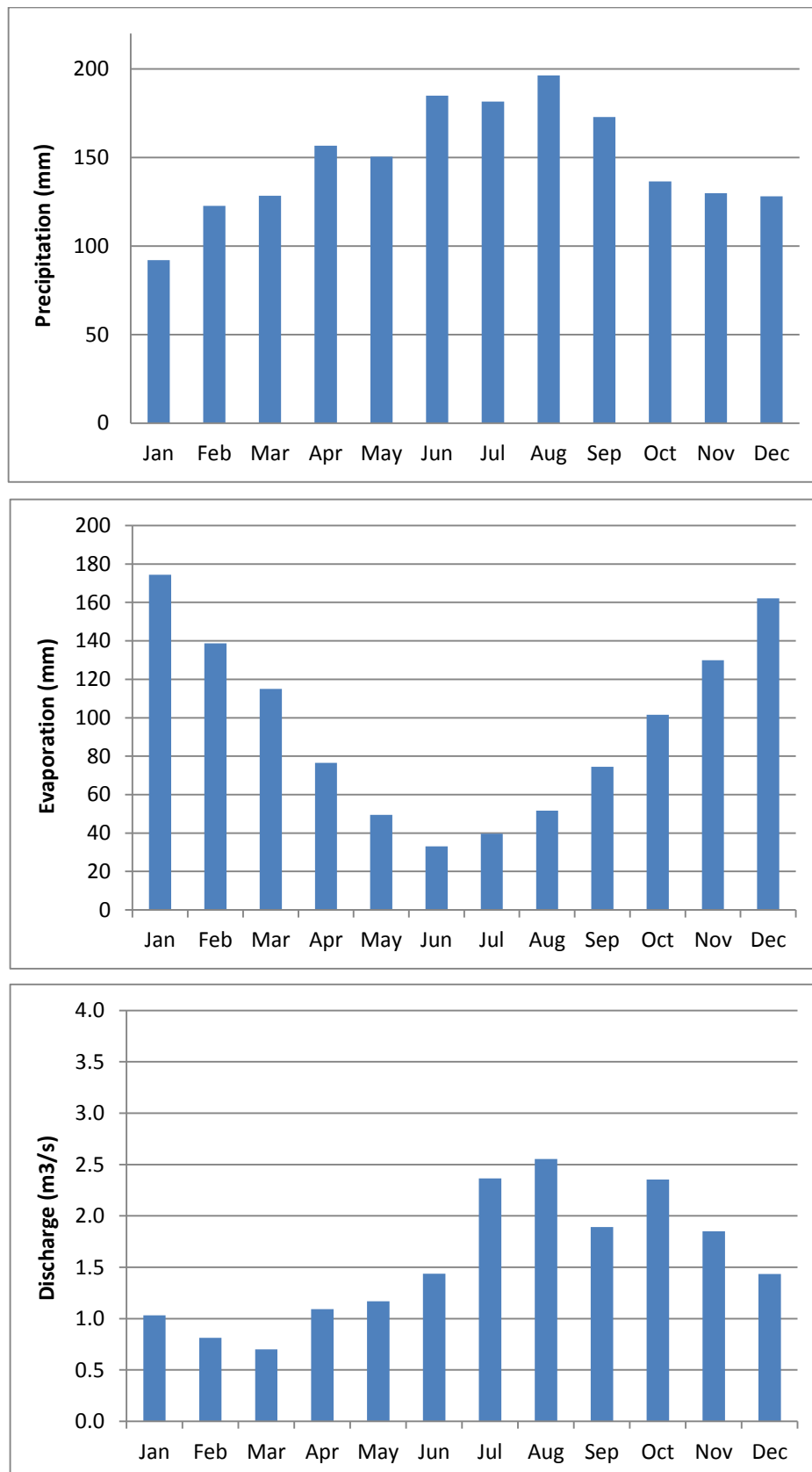


Figure C2 – 1

## APPENDIX **D**

### Monthly precipitation, evaporation and discharge observed in selected sub-catchments



**Fig. D-1** Precipitation, evaporation and flow pattern at selected station in Mangatawhiri catchment

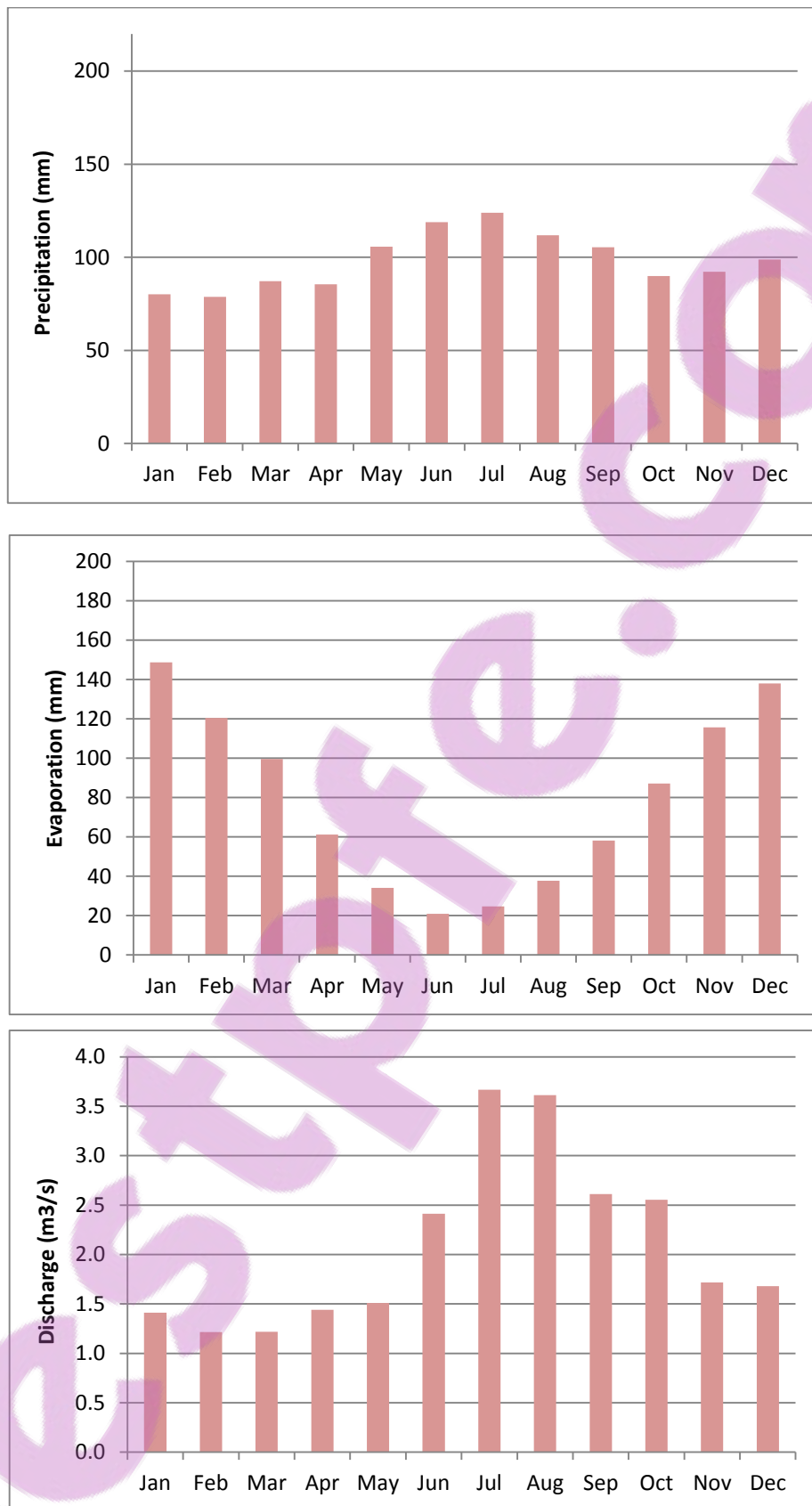
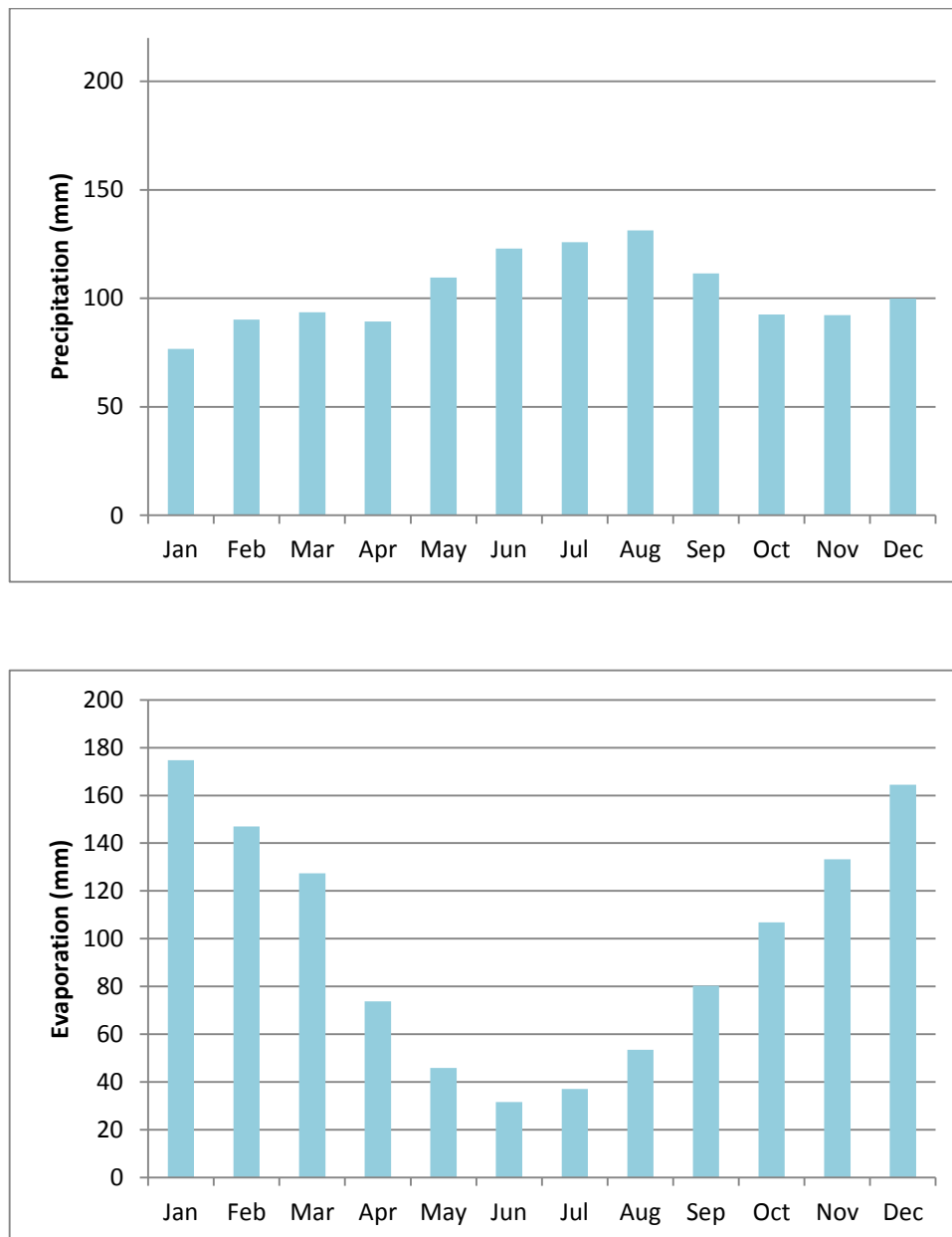


Fig. D-2 Precipitation, evaporation and flow pattern at selected station in Mangaonua catchment



**Fig. D-3** Precipitation and evaporation at selected station in Whangamarino catchment

---

## REFERENCES

1. Abtew, W., Obeysekera, J., and Iricanin, N. (2011). Pan evaporation and potential evapotranspiration trends in South Florida. *Hydrological Processes*, 25, 958-969.
2. Adamowski, K. et al. (2010). Influence of Trend on Short Duration Design Storms. *Water Resour. Manage.*, 24, 401–413.
3. Adamowski, K. (2009). Regional analysis of annual maximum and partial duration flood data by nonparametric and L-moment methods. *Journal of Hydrology*, 229, 219-231.
4. Andersen, F. H. (2008). *Hydrological modeling in a semi-arid area using remote sensing data*. PhD Thesis. University of Copenhagen, Denmark.
5. Andrew, R. M. and Dymond, J. R. (2007). A distributed model of water balance in the Motueka catchment, New Zealand. *Environmental Modelling & Software*, 22, 1519 - 1528.
6. Archer, D. R., Forsythe, N., Fowler, H. J. and Shah, S. M. (2010). Sustainability of water resources management in the Indus Basin under changing climatic and socio economic conditions. *Hydrol. Earth Syst. Sci.*, 7, 1883-1912.
7. Ashkar, F., and Rousselle, J. (1987). Partial duration series modelling under the assumption of a Poissonal flood count. *Journal of Hydrology*, 90, 135-144.
8. Baguis, P., Roulin, E., Willems, P. and Ntegeka, V. (2010). Climate change scenarios for precipitation and potential evapotranspiration over central Belgium. *Theor Appl Climatol*, 99, 273 - 286.
9. Bakker, A. M. R., Hurk, B. J. J. M. V., Bessembinder, J. J. E. and Kroon, T. (2011). Standard years for large-scale hydrological scenario simulations. *Environmental Modelling and Software*, 26, 797 - 803.
10. Bates, B.C., Z.W. Kundzewicz, S. Wu and J.P. Palutikof (2008). *Climate Change and Water*. Technical Paper. The Intergovernmental Panel on Climate Change, IPCC, Geneva, 210 pp.
11. Begueria, S. (2005). Uncertainties in partial duration series modelling of extremes related to the choice of threshold value. *Journal of Hydrology*, 303, 215 - 230.
12. Bell, V., Gedney, N., Kay, A. L. and et al. (2011). Estimating Potential Evaporation from Vegetated Surfaces for Water Management Impact Assessments Using Climate Model Output. *Journal of Hydrometeorology*, 12, 1127-1137.

13. Birikundavyi, S., and Rousselle, J. (1997). Use of partial duration series for single-station and regional analysis of floods. *Journal of Hydrologic Engineering*, 2(2), 68–75.
14. Bobee, B., Cavadias, G., Ashkar, F., Bernier, J., and Rasmussen, P. (1993). Towards a systematic approach to comparing distributions used in flood frequency analysis. *Journal of Hydrology*, 142, 121-136.
15. Boughton, W. (2004). The Australian water balance model. *Environmental Modelling & Software*, 19, 943-956.
16. Boughton, W. (2005). Catchment water balance modelling in Australia 1960–2004. *Agricultural Water Management*, 71, 91 - 116.
17. Boughton, W. (2006). Calibrations of a daily rainfall-runoff model with poor quality data. *Environmental Modelling and Software*, 21, 1114-1128.
18. Boughton, W., and Chiew, F. (2007). Estimating runoff in ungauged catchments from rainfall, PET and the AWBM model. *Environ Model Software*, 22, 476-487.
19. Brauer, C. (2007). *The Issel catchment: water balance study and rainfall-runoff modeling*. MSc Thesis. Department of Hydrology and Water Quality, Wageningen University, Germany.
20. Brazel, A. J., McCabe, G. J., and Verville, H. J. (1993). Incident solar radiation simulated by general circulation models for the southwestern United States. *Climate Research*, 2, 177 - 181.
21. Bronsterst, A., Kolokotronis, V., Schwandt, D. and Straub, H. (2007). Comparison and evaluation of regional climate scenarios for hydrological impact analysis: General scheme and application example. *International Journal of Meteorology*, 27, 1579-1594.
22. Buishand, T. A. (1989). The PDS method with a fixed number of peaks. *Journal of Hydrology*, 109, 1 - 9.
23. Castro-Diez, Y., Pozo-Vazquez, D. P., Rodrigo, F. S., and Esteban-Parra, M. J. (2002). NAO and winter temperature variability in southern Europe. *Geophysical Research Letters*, 29(0), X1-4.
24. Cavazos, T. (1998). Large-Scale Circulation Anomalies Conducive to Extreme Precipitation Events and Derivation of Daily Rainfall in Northeastern Mexico and Southeastern Texas. *Journal of Climate*, 12.

25. Charles, S. P., Bates, B. C., Whetton, P. H., and Hughes, J. P. (1999). Validation of downscaling models for changed climate conditions: case study of southwestern Australia. *Climate Research*, 12, 1-14.
26. Chen, H., Xu, C. Y. and Guo, S. (2012). Comparison and evaluation of multiple GCMs, statistical downscaling and hydrological models in the study of climate change impacts on runoff. *Journal of Hydrology* (434-435), 36-45.
27. Chen, J., Brissette, F. P., and Leconte, R. (2011). Uncertainty of downscaling method in quantifying the impact of climate change on hydrology. *Journal of Hydrology*, 401, 190-202.
28. Chiew, F. H. S., Kirono, D. G. C., Kent, D. M., Frost, A. J., Charles, S. P., Timbal, B. and et al. (2010). Comparison of runoff modelled using rainfall from different downscaling methods for historical and future climates. *Journal of Hydrology*, 387, 10-23.
29. Christensen, J., Hulme, M., Von Storch, H., Whetton, P., Jones, R., Mearns, L. and et al. (2001). Regional Climate Information - Evaluation and Projections. In Houghton, J.T. et al. (eds.), *IPCC Third Assessment Report Climate Change Working Group I: The Scientific Basis*. Cambridge, Great Britain: Cambridge University Press.
30. Chu, J. T., and Singh, V. P. (2010). Statistical downscaling of daily mean temperature, pan evaporation and precipitation for climate change scenarios in Haihe River, China. *Theor Appl Climatol*, 99, 149 - 161.
31. Chu, P.-S., Chen, Y. R., and Chroeder, T. A. (2010). Changes in Precipitation Extremes in the Hawaiian Islands in a Warming Climate. *American Meteorological Society*, 25.
32. Chun, K. P. (2010). *Statistical Downscaling of Climate Model Outputs for Hydrological Extremes*. PhD Thesis. Department of Civil and Environmental Engineering. Imperial College London, London, United Kingdom.
33. Chun, K. P., Wheeler, H. S., and Onof, C. J. (2010). *Potential evaporation estimates for 25 stations in the UK under climate variability*. Paper presented at the BHS Third International Symposium, Managing Consequences of a Changing Global Environment, Newcastle, UK.

34. Claps, P., and Laio, F. (2003). Can continuous streamflow data support flood frequency analysis? An alternative to the partial duration series approach. *Water Resources Research*, 39(8), 1-11.
35. Clause, B., and Pearsonb, C. P. (1995). Regional frequency analysis of annual maximum streamflow drought. *Journal of Hydrology*, 175, 111-130.
36. Comnalicer, E. A., Criz, R. V. O., Lee, S. and Im, S. (2010). Assessing climate change impacts on water balance in the Mount Makiling forest, Philipines. *J. Earth Syst. Sci*, 119(3), 256 - 283.
37. Cong, Z. T., and Yang, D. W. (2008). Does evaporation paradox exist in China? *Hydrol. Earth Syst. Sci.*, 5, 2111-2131.
38. Coulibaly, P., and Dibike, Y. B. (2004). *Downscaling global climate model outputs for flood frequency analysis in the Saguenay river system*. Project no.S02-15-01. McMaster University. Hamilton, ON.
39. Craig, I. P. (2006). Comparison of precise water depth measurements on agricultural storages with open-water evaporation estimates. *Elsevier Agricultural Water Management*, 85, 193-200.
40. Cunnance, C. (1973). A particular comparision of annual maximum and partial duration series metods of flood frequency prediction. *Journal of Hydrology*, 18, 257-271.
41. Cunnane, C. (1979). A note on the Poisson assumption in partial duration series models. *Water Resour Research*, 15(2), 489-494.
42. Cunnane, C. (1985). Factors affecting choice of distribution for flood series. *Hydrological Sciences Journal*, 30(1), 3 - 36.
43. Cunnane, C. (1988). Methods and merits of regional flood frequency analysis. *Journal of Hydrology*, 100, 269-290.
44. Das, S. and Cunnane, C. (2010). Examination of homogeneity of selected Irish pooling groups. *Hydrol. Earth Syst. Sci.*, 7, 5099-5130.
45. Davani, H. T., Nasser, M., and Zahraie, B. (2012). Improved statistical downscaling of daily precipitation using SDSM platform and data-mining methods. *Int. J. Climatol*. DOI: 10.1002/joc.3611.
46. Deidda, R. (2010). A multiple threshold method for fitting the generalized Pareto distribution and a simple representation of the rainfall process. *Hydrol. Earth Syst. Sci. Discuss*, 7, 4957-4994.

47. Deidda, R. and Puliga, M. (2009). Performances of some parameter estimators of the PP distribution over rounded-off samples. *Physics and Chemistry of the Earth*, 34, 626 - 634.
48. Denis, B., Laprise, R., Cote, J., and Caya, D. (2002). Downscaling ability of one-way nested regional models: The big-brother experiment. *Clim. Dyn.*, 18, 627-646.
49. DHI (2009). *MIKE 11: A modelling system for rivers and channels*. Reference manual. Copenhagen, Denmark: Danish Hydraulic Institute.
50. Dinpashoh, Y., Jhajharia, D., and Fard, A. F. (2011). Trends in reference crop evapotranspiration over Iran. *Journal of Hydrology*, 399, 422 - 433.
51. Douglas, E. M., Jacobs, J. M., Summer, D. M., and Ray, R. L. (2009). A comparison of models for estimating potential evapotranspiration for Florida land cover types. *Journal of Hydrology*, 373, 366-376.
52. Dravitzki, S. M. (2009). *Precipitation in the Waikato River Catchment*. PhD Thesis. The School of Geography, Environment and Earth Sciences. Victoria University of Wellington, Wellington, New Zealand.
53. Droogers, P. and Allen, R. G. (2002). Estimating reference evapotranspiration under inaccurate data conditions. *Irrigation and Drainage Systems*, 16, 33-45.
54. Drost, F., Renwick, J., Bhaskaran, B., Oliver, H., and McGregor, J. (2007). Simulation of New Zealand's climate using a high-resolution nested regional climate model. *Int. J. Climatol.*, 27, 1153-1169.
55. Dubrovsky, M. (2009). *Multi-GCM climate projections for Europe: GCMs performance and uncertainties*. Paper presented at the EMS Annual Meeting, Toulouse, France.
56. Engen-Skaugen, T., Roald, L. A., and Belgring, S. (2005). *Climate change impacts on water balance in Norway*. Report No. 1/2005. Norwegian Meteorological institute, Blindern, 82 pp.
57. Espadafor, M., Lorite, I. J., Gavilán, P., and Berengena, J. (2011). An analysis of the tendency of reference evapotranspiration estimates and other climate variables during the last 45 years in Southern Spain. *Agricultural Water Management*, 98, 1045 - 1061.
58. Esqueda, G. S. T., Norena, J. E. O., Garcia, C. G. and Conde, C. (2011). Vulnerability of water resources to climate change scenarios. Impacts on the irrigation districts in the Guayalejo-Tamesí river basin, Tamaulipas, México. *Atmosfera*, 24(1), 141-155.

- 
59. Fang Huang, Shuisen Zhou, Shaosen Zhang, Hongju Wang and Linhua Tang (2011). Temporal correlation analysis between malaria and meteorological factors in Motuo County, Tibet. *Malaria Journal* 2011, **10**:54. DOI: 10.1186/1475-2875-10-54.
  60. Ferrero, A. F., Saenz, J., Berastegi, G. I., and Fernandez, J. (2009). Evaluation of statistical downscaling in short range precipitation forecasting. *Atmospheric Research*, *94*, 448 - 461.
  61. Foley, A. M. (2010). Uncertainty in regional climate modelling: A review. *Progress in Physical Geography*, *34*(5), 647-670.
  62. Fowler, A. M., and Hennessy, K. J. (1995). Potential Impacts of Global Warming on the Frequency and Magnitude of Heavy Precipitation. *Natural Hazards*, *11*, 283-303.
  63. Fowler, H. J. and C. G. Kilsby (2003). *Extreme rainfall and flood risk in the UK*. Retrieved from <http://www.staff.ncl.ac.uk/h.j.fowler/extremerain.htm>.
  64. Fowler, H. J., and Kilsby, C. G. (2003). A regional frequency analysis of United Kingdom extreme rainfall from 1961 to 2000. *International Journal of Climatology*, *23*, 1313–1334.
  65. Fowler, H. J., and Kilsby, C. G. (2003). Implications of changes in seasonal and annual extreme rainfall. *Geophysical Research Letters*, *30*(13), 1720 - 1724.
  66. Fowler, H. J., Cooley, D., Sain, S. R., and Thurston, M. (2010). Detecting change in UK extreme precipitation using results from the climateprediction.net BBC climate change experiment. *Extremes*, *13*, 241 - 267.
  67. Francis, D., and Hengeveld, H. (1998). *Extreme Weather and Climate Change*. Environmenting report. Ontario, Canada - Authority of the Minister of the Environment.
  68. Friederichs, P. (2010). Statistical downscaling of extreme precipitation events using extreme value theory. *Extremes*, *13*, 109–132.
  69. Furcolo, P., Villani, P., and Rossi, F. (1995). *Statistical analysis of the spatial variability of very extreme rainfall in the Mediterranean area*. Paper presented at the US-Italia research workshop on the Hydrometeorology, Impacts, and Management of Extreme Floods. Perugia, Italia.
  70. García-Cueto, O. R., and Santillán-Soto, N. (2012). Modeling Extreme Climate Events: Two Case Studies in Mexico. In L. Druyan (eds.), *Climate Models*. InTech. DOI: 10.5772/31634.

71. Gibson, J. J., and Reid, R. (2010). Stable isotope fingerprint of open-water evaporation losses and effective drainage area fluctuations in a subarctic shield watershed. *Journal of Hydrology*, 381, 142-150.
72. Gifford, R. M. (2004). *Pan evaporation: An example of the detection and attribution of trends in climate variables*. Paper presented at the Australian Academy of Science, Canberra.
73. Giorgi, F. (2008). Regionalization of climate change information for impact assessment and adaptation. *WMO Bulletin*, 57(2), 86-92.
74. Gordon, N. D, McMahon, T. A., Finlayson, B. L., Gippel, C. J., and Nathan, R. J. (2004). *Stream hydrology: An introduction for ecologists*. England: John Wiley & Sons Ltd.
75. Gottschalk, L. and Krasovskaia, I. (2002). L-moment estimation using annual maximum (AM) and peak over threshold (POT) series in regional analysis of flood frequencies. *Norwegian Journal of Geography*, 56(2), 179-187.
76. Gleick, P (1993). *Water in Crisis: A Guide to the World's Fresh Water Resources*. New York: Oxford University Press, 473 pp.
77. Grimm, A. M. (2010). Interannual climate variability in South America: impacts on seasonal precipitation, extreme events, and possible effects of climate change. *Stoch Environ Res Risk Assess*, 25, 537 - 554.
78. Guhathakurta, P., Sreejith, O. P., and Menon, P. A. (2011). Impact of climate change on extreme rainfall events and flood risk in India. *J. Earth Syst. Sci*, 120(3), 359-373.
79. Guo, S., Wang, J., Xiong, L., Ying, A. and Li, D. (2002). A macro-scale and semi-distributed monthly water balance model to predict climate change impacts in China. *Journal of Hydrology*, 268, 1 - 5.
80. Gupta, H. V., Kling, H., Yilmaz, K. and Martinez, G. (2009). Decomposition of the mean squared error and NSE performance criteria: Implications for improving hydrological modelling. *Journal of Hydrology*, 377, 80-91.
81. Gutmann, E. D., Rasmussen, R. M. et al. (2012). A Comparison of Statistical and Dynamical Downscaling of Winter Precipitation over Complex Terrain. *Journal of Climate*, 25, 262-281.
82. Ha, N. T. T. (2009). *Water resources management in Ba river basin under future development and climate change scenarios*. ME thesis. Asian Institute of Technology, Bangkok, Thailand.

83. Habte, G. L. (2013). *Remote sensing and regionalization for integrated water resources modelling in upper and middle Awash river basin, Ethiopia*. MSc Thesis. Faculty of Geo-Information Science and Earth Observation. University of Twente, Enschede, the Netherlands.
84. Haddad, K., A. Rahman et al. (2011). Design Rainfall Estimation in Australia: A Case Study using L moments and Generalized Least Squares Regression. *Stochastic Environmental Research & Risk Assessment*, 25(6), 815-825.
85. Hafezparast, M., Araghinejad, S., Fatemi, S. E. and Bressers, H. (2013). A Conceptual Rainfall-Runoff Model Using the Auto Calibrated NAM Models in the Sarisoo River. *Hydrol Current Res*, 4(1), 2-6.
86. Hardy John (2003). *Climate change: Causes, effects and Solutions*. John Wiley & Sons Ltd, England.
87. Hashmi, M. Z. (2012). *Watershed Scale Climate Change Projections for Use in Hydrologic Studies: Exploring New Dimensions*. PhD thesis. The University of Auckland, Auckland, New Zealand.
88. Hashmi, M. Z., Shamseldin, A. Y., and Melville, B. W. (2011). Comparison of SDSM and LARS-WG for simulation and downscaling of extreme precipitation events in a watershed. *Stoch Environ Res Risk Assess*, 25, 475-484.
89. Helsel, D. and Frans, L. (2006). Regional Kendall Test for Trend. *Environmental Science and Technology*, 40(13).
90. Hobbins, M. T., and Rami'rez, J. A. (2004). Trends in pan evaporation and actual evapotranspiration across the conterminous U.S.: Paradoxical or complementary? *Geophysical Research Letters*, 31, 1-5.
91. Hosking, J. R. M. and Wallis, J. R. (1987). Parameter and Quantile Estimation for the Generalized Pareto Distribution. *Technometrics*, 29(3), 339-349.
92. Hosking, J. R. M. and Wallis, J. R. (1993). Some Statistic Usefui In Regional Frequency Analysis. *Water Resources Research*, 29(2), 271-281.
93. Hosking, J. R. M. and Wallis, J. R. (1997). *Regional frequency analysis: an approach based on L-moments*. Cambridge, UK: Cambridge University Press.
94. Hosking, J. R. M. and Wallis, J. R. (1993). Some Statistic Useful in Regional Frequency Analysis. *Water Resources Research*, 29(2), 271-281.

95. Hu, Y., Maskey, S. and Uhlenbrook, S. (2013). Downscaling daily precipitation over the Yellow River source region in China: a comparison of three statistical downscaling methods. *Theor Appl Climatol*, 112, 447-460.
96. Huang, J., Zhang, J., Zhang, Z., Sun, S. and Yao, J. (2012). Simulation of extreme precipitation indices in the Yangtze River basin by using statistical downscaling method (SDSM). *Theor Appl Climatol*, 108, 325-343.
97. Huntingford, C., Jones, R. G., Prudhomme, C., Lamb, R., Gash, J. H. C. and Jones, D. A. (2003). Regional climate-model predictions of extreme rainfall for a changing climate. *Quart. J. Roy. Met. Soc.*, 129, 1607-1621.
98. IIASA (1994). *Potential evapotranspiration methods and their impacts on the assessment of river basin runoff under climate change*. Working paper. International Institute for Applied System Analysis. Laxenburg, Austria.
99. Im, I. S., Jung, W., Chang, H., Bae, D. H. and Kwon, W. T. (2010). Hydroclimatological response to dynamically downscaled climate change simulations for Korean basins. *Climatic Change*, 100, 485–508.
100. IPCC (1999). *Guidelines on the use of scenario data for climate impact and adaptation assessment*. Task group on Scenarios for Climate Change Impacts. Intergovernmental Panel on Climate Change, Geneva, Switzerland, 77 pp.
101. IPCC (2000). *Emission scenarios*. A Special Report of IPCC Working Group III. Intergovernmental Panel on Climate Change, Geneva, Switzerland, 27 pp.
102. IPCC (2007). *Climate change 2007: Synthesis Report*. Contribution of Working Groups I, II and III to the Fourth Assessment Report of the Intergovernmental Panel on Climate Change. Intergovernmental Panel on Climate Change, Geneva, Switzerland, 104 pp.
103. IPCC (2008). *Climate Change and Water*. A Special Report of IPCC Working Group I. Intergovernmental Panel on Climate Change, Geneva, Switzerland, 214 pp.
104. Ishak, A., Bray, M., and Han, D. (2010). *Downscaling cumulative rainfall for comparison by four cumulus parameterization schemes in the Brue Catchment*. Paper presented at the BHS Third International Symposium, Managing Consequences of a Changing Global Environment, Newcastle.
105. Iturbe, I. R., Porporato, A., Ridolfi, L., Isham, V. S. and Coxi, D. R. (1999). Probabilistic modelling of water balance at a point: the role of climate, soil and vegetation. *Proceedings of the Royal Society*, 455, 3789-3805.

106. Jaiswal, R. K., Goel, N. K., Singh, P., and Thomas, T. (2003). L-Moment based Flood Frequency Modelling. *IE (I) Journal -CV*, 84, 6-10.
107. Jenkinson, A. F. (1955). The frequency distribution of the annual maximum (or minimum) values of meteorological elements. *Quart. J. Roy. Met. Soc*, 81, 158-171.
108. Jeong, D. I., St-Hilaire, A., Ouarda, T. B. M. J., and Gachon, P. (2012). CGCM3 predictors used for daily temperature and precipitation downscaling in Southern Québec, Canada. *Theor Appl Climatol*, 107, 389-406.
109. Jiang, T., Chen, Y. D., Xu, C. Y., Chen, X., Chen, X. and Singh, V. P. (2007). Comparison of hydrological impacts of climate change simulated by six hydrological models in the Dongjiang Basin, South China. *Journal of Hydrology*, 336, 316 - 333.
110. Jones, J et al. (1996) *Regional Hydrological response to climate change*. Netherlands: Kluwer Academic Publishers, 423 pp.
111. Jusoh, A. B. M. (2007). *Impact of Climate Change on Water Resources Availability in the Komati River Basin Using WEAP21 Model*. the UNESCO-IHE Institute for Water Education, Delft.
112. Kalnay, M., Kanamitsu, M., Kistler, R. and et al. (1996). The NCEP/NCAR 40-Year Reanalysis Project: Bulletin of the American Meteorological Society, Washington, US.
113. Katz, R. W. (2010). Statistics of extremes in climate change. *Climatic Change*, 100, 71-76.
114. Kay, A. L. and Davies, H. N. (2008). Calculating potential evaporation from climate model data: a source of uncertainty for hydrological climate change impacts. *Journal of Hydrology*, 358, 221 - 239.
115. Kaya, A. L., R. G. Jones and et al. (2006). RCM rainfall for UK flood frequency estimation. Climate change results. *Journal of Hydrology*, 318, 163–172.
116. Khan, M. S., Coulibaly, P. and Dibike, Y. B. (2006). Uncertainty analysis of statistical downscaling methods. *Journal of Hydrology*, 319, 357-382.
117. Kim, U. and Kaluarachchi, J. J. (2009). Climate change impacts on water resources in the upper Blue Nile river basin, Ethiopia. *Journal of the Amercian Water Resources Association*, 45(6).
118. Krause, P., Boyle, D. P. and Base, F. (2005). Comparison of different efficiency criteria for hydrological model assessment. *Advances in Geosciences*, 5, 89 - 97.

119. Kunkel, K. (2003). North American Trends in Extreme Precipitation. *Natural Hazards*, 29, 291–305.
120. Kutner MH, Nachtsheim CJ, Neter J. (2004). *Applied Linear Regression Models*, 4th edition, McGraw-Hill Irwin.
121. Lambert, J. H., Matalas, N. C., Ling, C. W. and Haimes, Y. Y. (1994). Selection of Probability distributions in characterizing risk of extreme events. *Risk Analysis*, 14(5).
122. Langa, M., Quardab, T. B. M. J. and Bobee, B. (1999). Towards operational guidelines for over-threshold modeling. *Journal of Hydrology*, 225, 103-117.
123. Lavers, D., Prudhomme, C. and Hannah, D. M. (2010). Large-scale climate, precipitation and British river flows: Identifying hydroclimatological connections and dynamics. *Journal of Hydrology*, 395, 242-255.
124. Li, K. and Qi, J. (2010). *Statistical Downscaling: a Powerful Tool for Estimating Global Change Impacts on Regional Scale*. Paper presented at the Conference on Environmental Science and Information Application Technology. Wuhan, China.
125. Li, Y., Horton, R., Ren, T. and Chen, C. (2010). Prediction of annual reference evapotranspiration using climatic data. *Agricultural Water Management*, 97, 300 - 308.
126. Liu, Z., Xu, Z., Charles, S. P., Fu, G. and Liu, L. (2011). Evaluation of two statistical downscaling models for daily precipitation over an arid basin in China. *International Journal of Meteorology*, 31, 2006-2020.
127. Lorenzoni et al. (2001) *Regional Environmental Change*. Springer-Verlag. ISSN: 1436-3798.
128. Madsen, H., Pearson, G. P. and Rosbjerg, D. (1997). Comparison of annual maximum series and partial duration series methods for modeling extreme hydrologic events: 2. Regional modeling. *Water Resources Research*, 33(4), 759--769.
129. Madsen, H., Rosbjerg, D. and Harremoes, P. (1993). Application of the partial duration series approach in the analysis of extreme rainfalls. *Proc., Int. Symp. on Extreme Hydrological events: Precipitation, Floods and Droughts, IAHS, Yokohama, Japan*, 213, 257-346.
130. Madsen, H., Rosbjerg, D. and Harremoes, P. (1994). PDS-Modelling and Regional Bayesian Estimation of Extreme Rainfalls. *Nordic Hydrology*, 25, 279-300.

131. Madsen, H., Wilsona, G. T. and Ammentorp, H. C. (2002). Comparison of different automated strategies for calibration of rainfall-runoff models. *Journal of Hydrology*, 261, 48-59.
132. Marks, D., King, G. A. and Dolph, J. (1993). Implications of climate change for the water balance of the Columbia river basin, USA. *Climate Research*, 2, 203 - 213.
133. Mason, S. J., Waylen, P., Mimmack, G. M., Rajaratnam, B., & Harrison, J. M. (1999). Changes in Extreme rainfall events in South Africa. *Climatic Change*, 41, 249–257.
134. Mauser, W. and Bach, H. (2009). PROMET – Large scale distributed hydrological modelling to study the impact of climate change on the water flows of mountain watersheds. *Journal of Hydrology*, 376, 362 - 377.
135. McKerchar, A. I. (1991). Regional flood frequency analysis for small New Zealand basins: Mean annual flood estimation. *Journal of Hydrology New Zealand*, 30(2), 65-75.
136. Mearns, L. O., Giorgi, F., Whetton, P., Pabon, D., Hulme, M. and Lal, M. (2003). *Guidelines for Use of Climate Scenarios Developed from Regional Climate Model Experiments*. DDC of TPCC TG CIA report at <http://www.ipcc-data.org/>.
137. Meng, F., Li, J. and Gao, L. (2007). ERM-POT model for quantifying operational risk for Chinese commercial banks. In Shi, Y. (eds.), *Lecture notes in computer science*. Berlin, Germany: Springer-Verlag Berlin Heildbreg.
138. Meszaros, I. and Miklanek, P. (2006). Calculation of potential evapotranspiration based on solar radiation income modeling in mountainous areas. *Biologia, Bratislava*, 61/Sppl.(19), S284-S288.
139. MfE (2008). *Climate change effects and impacts assessment: A Guidance Manual for Local Government in New Zealand*. 2<sup>nd</sup> Edition. Ministry for the Environment, Wellington, New Zealand.
140. Middelkoop, H., Daamen, K., Gellens, D., Grabs, W., Kwadijk, J. C. J., Lang, H. and et al. (2001). Impact of climate change on hydrological regimes and water resources management in the Rhine basin. *Climatic Change*, 49, 105 - 128.
141. Milly, P. C. D. and Dunne, K. A. (2011). On the Hydrologic Adjustment of Climate-Model Projections: The Potential Pitfall of Potential Evapotranspiration. *Earth Interactions*, 15.

142. Misra, V., DiNapoli, S. M. and Bastola, S. (2013). Dynamic downscaling of the twentieth-century reanalysis over the southeastern United States. *Reg Environ Change*, 13(Suppl), S15-S23.
143. Mitchell, J. (1989). The "greenhouse" effect and climate change. *Reviews of Geophysics* 27(1), 115-139.
144. Moreda, F. (1999). *Conceptual rainfall - runoff models for different time steps with special consideration for semi-arid and arid catchments*. PhD Thesis. Faculty of Applied Science. Vrije Universiteit Brussel, Brussels, Belgium.
145. Moreno, J. I. L., Vicente-Serrano, S. M., Mart'inez, M. A., Beguer'ia, S., and Kenawya, A. (2010). Trends in daily precipitation on the north eastern Iberian Peninsula, 1955–2006. *International Journal of Climatology*, 30, 1026–1041.
146. Mohsen, M. (2009). *Partial duration series in the annual domain*. Paper presented at the 18th World IMACS/MODSIM Congress. Cairns, Australia.
147. Mosley, M. P. (1981). Delimitation of New Zealand hydrologic regions. *Journal of Hydrology*, 49, 173-192.
148. Mpelasoka, F. S. (2000). *GCM-derived climate change scenarios and their impacts on New Zealand water resources*. PhD Thesis. Department of Science, Massey University, Palmerston North, New Zealand.
149. Mujumdar, P. P. and Ghosh, S. (2008). Modeling GCM and scenario uncertainty using a possibilistic approach: Application to the Mahanadi River, India. *Water Resour Research*, 44, 1-15.
150. Mullan A. B., Wratt, D. S., Renwick, J. A., 2001. Transient model scenarios of climate changes for New Zealand. *Weather and Climate*, 21, 3-34.
151. Mullan AB, Salinger MJ, Thompson CS, et al. 2001. The New Zealand climate: present and future, Warrick, RA, Kenny, GJ and Harman, JJ (eds) *The Effects of Climate Change and Variation in New Zealand: An Assessment Using the CLIMFACTS System*. Chapter 2. IGCI, University of Waikato, 11-31.
152. Naoum, S. and Tsanis, I. K. (2003). Hydroinformatics in evapotranspiration estimation. *Environmental Modelling and Software*, 18, 261-271.
153. Nayaka, P. C., Venkatesh, B., Krishna, B. and Jain, S. K. (2013). Rainfall-runoff modeling using conceptual, data driven, and wavelet based computing approach. *Journal of Hydrology*, 493.

154. Newsome, P.F.J, Wilde, R H and Willoughby, E J (2000). *Land resource information system spatial data layers – Volume 1 Label Format*. LRNZ report. Landcare Research New Zealand Ltd, Palmerston North, 73 pp.
155. Nichols, J., Eichinger, W., Cooper, D. I., Prueger, J. H., Hipps, L. E., Neale, C. M. U. and et al. (2004). *Comparison of evaporation estimation methods for a riparian area*. University of Iowa, Iowa.
156. NIWA (2005). *A methodology to assess the impacts of climate change on flood risk in New Zealand*. NIWA Client report: CHC2005-060. National Institute of Water & Atmospheric Research Ltd, Christchurch, 40 pp.
157. Norbiato, D., Borga, M., Sangati, M. and Zanon, F. (2007). Regional frequency analysis of extreme precipitation in the eastern Italian Alps and the August 29, 2003 - Flash flood. *Journal of Hydrology*, 345, 149– 166.
158. Obeysekera, J., Irizarry, M., Park, J. S., Barnes, J. and Dessalegne, T. (2011). Climate change and its implications for water resources management in south Florida. *Stoch Environ Res Risk Assess*, 25, 495 - 516.
159. Onoz, B. and Bayazit, M. (2001). Effect of the occurrence process of the peaks over threshold on the Flood estimates. *Journal of Hydrology*, 244, 86 - 96.
160. Onoz, B. and Bayazit, M. (2003). The power of statistical tests for trend detection. *Turkish J. Eng. Env. Sci*, 27, 247 - 251.
161. Palutikof, J. P., Brabson, B. B., Lister, D. H. and Adcock, A. T. (1999). A review of methods to calculate extreme wind speeds. *Meteoro. Appl*, 6, 119-132.
162. Palutikof, J. P., Goodess, C. M. and Guo, X. (1994). Climate change, potential evapotranspiration and moisture availability in the Mediterranean basin. *International Journal of Climatology*, 14, 853 - 869.
163. Park, J. S. and Jung, H. S. (2002). Modelling Korean extreme rainfall using a Kappa distribution and maximum likelihood estimate. *Theoretical and Applied Climatology*, 72, 55-64.
164. Pattanaika, D. R. and Rajeevanb, M. (2010). Variability of extreme rainfall events over India during southwest monsoon season. *Meteorol. Appl.*, 17, 88 - 104.
165. Pearson, C. P. (1991). New Zealand regional flood frequency analysis using L-moments. *Journal of Hydrology New Zealand*, 30(2), 53-64.

- 
166. Pearson, C. P. and Henderson, R. D. (1998). Frequency distributions of annual maximum storm rainfalls in New Zealand. *Journal of Hydrology New Zealand*, 37(1), 19-33.
  167. Pelt, S. C. v., Kabat, P., ter Maat, H. W., vanden Hurk, B. J. J. M. and Weerts, A. H. (2009). Discharge simulations performed with a hydrological model using bias corrected regional climate model input. *Hydrol. EarthSyst. Sci.*, 13, 2387 - 2397.
  168. Penman, H. L. (1947). Natural evaporation from open water, bare soil and grass. *Natural evaporation*.
  169. Pham, H. X., Shamseldin, A. Y. and Melville, B. W. (2013a). Statistical properties of partial duration series and its implication in frequency analysis. *J. Hydrol. Eng.* DOI: 10.1061/(ASCE)HE.1943-5584.0000916.
  170. Pham, H. X., Shamseldin, A. Y. and Melville, B. W. (2013b). Statistical downscaling of daily precipitation using UKSDSM model. Paper presented at the Thai-Japan International Academic Conference. Osaka, Japan.
  171. Pham, H., Shamseldin, A. and Melville, B. (2014). Statistical properties of partial duration series. Case study of North Island of New Zealand. *J. Hydrol. Eng.*, 19 (4), 807 - 815.
  172. Pielke, R. A. (2012). Regional Climate Downscaling: What's the Point? *Eos*, 93(5), 52-53.
  173. Pike, R. G., Bennett, K. E. and et al. (2010). *Climate Change Effects on Watershed Processes in British Columbia*. Chapter 19. Compendium of Forest Hydrology and Geomorphology in British Columbia.
  174. Pochop, L., Warnaka, K., Borrelli, J. and Hasfurther, V. (1985). *Design information for evapotranspiration ponds in Wyoming*. Report No. WWRC-85-21. Laramie: University of Wyoming.
  175. Pockley, P. (2009). The Evaporation paradox. *Australian Science*, Nov/Dec, 12-13.
  176. Prudhomme, C., Reynard, N. and Crooks, S. (2002). Downscaling of global climate models for flood frequency analysis: where are we now? *Hydrological Processes*, 16, 1137-1150.
  177. Qian, B., Gameda, S., Jong, R. and et al. (2010). Comparing scenarios of Canadian daily climate extremes derived using a weather generator. *Clim Res*, 41, 131 - 149.
  178. Randall, D. A., R. A. Wood and et al. (2007). Chapter 8 Climate Models and Their Evaluation. In S. Solomon, D. Qin, M. Manning (eds). *IPCC Fourth Assessment*

- 
- Report: Climate Change 2007, Working Group I (AR4 WGI)*. Cambridge, United Kingdom.
179. Riggs, H. C (1985). *Streamflow Characteristics*. Elsevier Sciences Publishers B. V. Amsterdam, the Netherlands.
180. Roderick, M. L. and Graham, D. F. (2002). The Cause of Decreased Pan Evaporation over the Past 50 Years. *Science*, 298(5597), 1410-1411.
181. Roderick, M. L., Hobbins, M. T. and Farquhar, G. D. (2009). Pan Evaporation Trends and the Terrestrial Water Balance. II. Energy Balance and Interpretation. *Geography Compass*, 3(2), 761 - 780.
182. Rosbjerg, D. and Madsen, H. (2004). Advanced approaches in PDS/POT modeling of extreme hydrological events. *Hydrology: Science & Practice for the 21st Century*, 1, 21.
183. Roy, L., Leconte, R., Brissette, F. P. and Marche, C. (2001). The impact of climate change on seasonal floods of a southern Quebec River Basin. *Hydro. Process*, 15, 3167–3179.
184. Rummukainen, M. (2010). State-of-the-art with regional climate models. *Advanced Review WIREs Climate Change*, 1, 82-96.
185. Saf, B. (2009). Regional Flood Frequency Analysis Using L-Moments for the West Mediterranean Region of Turkey. *Water Resource Manage*, 23, 531-551.
186. Saf, B. (2010). Assessment of the effects of discordant sites on regional flood frequency analysis. *Journal of Hydrology*, 380, 362-375
187. Salas, J. D. (1993). Analysis and modelling of hydrologic time series. *Handbook of Hydrology*, Maidment, D. R. (ed.). McGraw-Hill, New York, USA.
188. Sanderson, M. (2010). *Changes in the frequency of extreme rainfall events for selected towns and cities*: MetOffice, Devon, UK, 41 pp.
189. Schmidli, J. and Frei, C. (2005). Trends of heavy precipitation and wet and dry spells in Switzerland during the 20th century. *International Journal of Climatology*, 25, 753-771.
190. Schmidli, J., Goosse, H., Frei, C., Haylock, M., Hundercha, Y., Ribalaygua, J. and et al. (2007). Statistical and dynamical downscaling of precipitation: An evaluation and comparison of scenarios for the European Alps. *Journal of Geophysical Research*, 112, 1-20.
-

191. Shen, Y., Liu, C., Liu, M., Zeng, Y. and Tian, C. (2010). Change in pan evaporation over the past 50 years in the arid region of China. *Hydrological Processes*, 24, 225-231.
192. SHinYie, W. L and Ismail, N (2012). Analysis of T-Year Return Level for Partial Duration Rainfall Series. *Sains Malaysiana*, 41(11), 1389–1401
193. Silva, D., Meza, F. J. and Varas, E. (2010). Estimating reference evapotranspiration (ET<sub>0</sub>) using numerical weather forecast data in central Chile. *Journal of Hydrology*, 382, 64-71.
194. Sivakumar, M., and Stefanski, R. (2011). Chapter 2 Climate Change in South Asia. Lal, R. et al. (eds.), *Climate Change and Food Security in South Asia*. Geneva, Switzerland: Springer Science+Business Media B.V.
195. Stephen, G. F., Charles, P. and Yu, J. (2009). A critical overview of pan evaporation trends over the last 50 years. *Climate Change*, 97, 193 - 214.
196. Strzepek, K. and McCluskey, A. (2007). *The Impacts of Climate Change on Regional Water Resources and Agriculture in Africa*. Washington: The World Bank.
197. Sunyer, M. A., Madsen, H. and Ang, P. H. (2012). A comparison of different regional climate models and statistical downscaling methods for extreme rainfall estimation under climate change. *Atmospheric Research*, 103, 119 - 128.
198. Sweeney, J. C. (2009). *Climate Change*. National University of Ireland, Maynooth: Elsevier Ltd.
199. Szilagyi, J. and Jozsa, J. (2008). New findings about the complementary relationship based evaporation estimation methods. *Journal of Hydrology*, 354, 171-186.
200. Tait, A. and Woods, R. (2007). Spatial Interpolation of Daily Potential Evapotranspiration for New Zealand Using a Spline Model. *J. Hydrometeor*, 8, 430–438.
201. Takeuchi, K. (1984). Annual maximum series and partial duration series - Evaluation of langbien's formular and Chow's discussion. *Journal of Hydrology*, 68, 275-284.
202. Tanaka, N., Kume, T. and Yoshifuji, N. (2008). A review of evapotranspiration estimates from tropical forests in Thailand and adjacent regions. *Agricultural and Forest Meteorology*, 148, 807 - 819.
203. Teuling, A. J., Hirschi, M., Ohmura, A., Wild, M., Reichstein, M., Ciais, P. and et al. (2009). A regional perspective on trends in continental evaporation. *Geophysical Research Letters*, 36.

- 
204. Tian, D. and Martinez, C. (2012). Comparison of two analog-based downscaling methods for regional reference evapotranspiration forecasts. *Journal of Hydrology*, 475, 350-364.
  205. Timbal, B., Li, Z. L. and Fernander, E. (2008). *The Bureau of Meteorology Statistical Downscaling Model Graphical User Interface: User manual and software documentation*. CAWCR technical report No. 004. Australian Government Bureau of Meteorology, Melbourne, 98 pp.
  206. Thompson, C. S. and Tomlinson, A. I. (1993). Probable maximum precipitation in New Zealand for small areas and short durations. *Journal of Hydrology (NZ)*, 31(2), 78-90.
  207. Thornthwaite, C. W. (1948). An Approach toward a Rational Classification of Climate. *American Geographical Society*, 38(1).
  208. Timbal, B., Li, Z. L. and Fernandaer, E (2008). *The Bureau of Meteorology Statistical Downscaling Model Graphical User Interface: user manual and software documentation*. Australian Government Bureau of Meteorology.
  209. Trefry, C. M., Watkins, D. W. and Johnson, D. (2005). Regional Rainfall Frequency Analysis for the State of Michigan. *Journal of Hydrologic Engineering*, 10(6), 437-449.
  210. Vaitiekuniene, J. (2005). Application of rainfall-runoff model to set up the water balance for Lithuanian river basins. *Environmental research, engineering and management*, 1(31), 34 - 44.
  211. Von Storch, H. (1995). *Statistical Analysis in Climate Research*. Cambridge University Press. Cambridge, UK.
  212. Waikato Regional Council (2011). *Strategic assessment of the impacts of climate change on the Waikato region*. Technical report. Waikato Regional Council, Hamilton.
  213. Wang, Q. J., Pagano, T. C., Zhou, S. L., Hapuarachchi, H. A. P., Zhang, L. and Robertson, D. E. (2011). Monthly versus daily water balance models in simulating monthly runoff. *Journal of Hydrology* (in press).
  214. Wang, X., Yang, T., Shao, Q., Acharya, K., Wang, W. and Yu, Z. (2012). Statistical downscaling of extremes of precipitation and temperature and construction of their future scenarios in an elevated and cold zone. *Stoch Environ Res Risk Assess*, 26, 405 - 418.

215. Whetton P, Mullan AB, Pittock AB. 1996. Climate change scenarios for Australia and New Zealand. In WJ Bouma, GI Pearman, M Manning (eds). *Greenhouse '94: Coping with climate change*. Melbourne: CSIRO/DAR, 168 pp.
216. White, E. D., Easton, Z. M., Fuka, D. R., Collick, A. S. and et al. (2011). Development and application of a physically based landscape water balance in the SWAT model. *Hydrological Processes*, 25, 915 - 925.
217. Wilby, R. L., Charles, S. P. and et al. (2004). *Guidelines for use of climate scenarios developed from statistical downscaling methods*. Task Group on Data and Scenario Support for Impacts and Climate Analysis (TGICA), Intergovernmental Panel on Climate Change, Geneva.
218. Wilby, R. L., Hayc, L. E. and Leavesley, G. H. (1999). A comparison of downscaled and raw GCM output: implications for climate change scenarios in the San Juan River basin, Colorado. *Journal of Hydrology*, 225, 67-91.
219. Wilby, R. L., Hayc, L. E., and Leavesley, G. H. (1999). A comparison of downscaled and raw GCM output: implications for climate change scenarios in the San Juan River basin, Colorado. *Journal of Hydrology*, 225, 67-91.
220. Wilby, R., Dawson, C. and Barrow, E. (2002). SDSM - a decision support tool for the assessment of regional climate change impacts. *Environ Model Software*, 17(2), 145-157.
221. Wilks, D. S. (1993). Comparison of Three-Parameter Probability Distributions for Representing Annual Extreme and Partial Duration Precipitation Series. *Water Resources Research*, 29(10), 3543-3549.
222. Willems, P. and Vrac, M. (2011). Statistical precipitation downscaling for small-scale hydrological impact investigations of climate change. *Journal of Hydrology*, 402, 193 - 205.
223. WWF (2007). *Climate change impacts on APEC countries*. APEC Energy Working Group. World Wildlife Fund-Canon/Bruno, Pambour.
224. Xu, C. Y. and Singh, P. (1998). A Review on Monthly Water Balance Models for Water Resources Investigations. *Water Resour Manage*, 12, 31 - 50.
225. Xu, Z. and Yang, Z.-L. (2012). An Improved Dynamical Downscaling Method with GCM Bias Corrections and Its Validation with 30 Years of Climate Simulations. *American Meteorological Society*, 25, 6271-6286.

- 
226. Xue, Y., Vasic, R. and et al. (2007). Assessment of Dynamic Downscaling of the Continental U.S. Regional Climate Using the Eta/SSiB Regional Climate Model. *Journal of Climate*, 20, 4172-4193.
227. Yang, T., Li, H., Wang, W., Xu, C.Y. and Yi, Z. (2012). Statistical downscaling of extreme daily precipitation, evaporation, and temperature and construction of future scenarios. *Hydrol. Process.*, 26, 3510-3523.
228. Yang, T., Shao, Q., Hao, Z.-C., Chen, X., Zhang, Z., Xu, C.-Y. and et al. (2010). Regional frequency analysis and spatio-temporal pattern characterization of rainfall extremes in the Pearl River Basin, China. *Journal of Hydrology*, 380, 386-405.
229. Yates, D. (1994). *WatBal - An integrated water balance model for climate impact assessment of river basin runoff*: Working paper. International Institute for Applied Systems Analysis. Laxenburg, Austria.
230. Yoon, J.H., Leung, L. R. and Correia, J. (2012). Comparison of dynamically and statistically downscaled seasonal climate forecasts for the cold season over the United States. *Journal of Geophysical Research*, 117, 1-17.
231. Yuguo, D., Bingyan, C. and Zhihong, J. (2008). A Newly-Discovered GPD-GEV Relationship Together with Comparing Their Models of Extreme Precipitation in Summer. *Advances in Atmospheric Science*, 25(3), 507-516.
232. Zhang, J. (2010). Improving on Estimation for the Generalized Pareto Distribution. *Technometrics*, 52(3).
233. Zhang, L., Potter, N., Hickel, K., Zhang, Y. and Shao, Q. (2008). Water balance modeling over variable time scales based on the Budyko framework – Model development and testing. *Journal of Hydrology*, 360, 117 - 131.
234. Zhang, X., Wang, J., Zwiers, F. W. and Groisman, P. Y. (2010). The Influence of Large-Scale Climate Variability on Winter Maximum Daily Precipitation over North America. *Journal of Climate*, 23.
235. Zin, W. Z. W., Jamaludin, S., Deni, S. A. and Jemain, A. A. (2010). Recent changes in extreme rainfall events in Peninsular Malaysia: 1971–2005. *Theor Appl Climatol*, 99, 303–314.
236. Zotarelli, L., Duckes, M. D., Romero, C. C., Migliaccio, K. W. and Morgan, K. T. (2010). Step by Step Calculation of the Penman-Monteith Evapotranspiration (FAO-56 Method). *FAO*, Italia.

237. Zvi, A. B. (2009). Rainfall intensity–duration–frequency relationships derived from large partial duration series. *Journal of Hydrology*, 367, 104-114.